Two methods of modelling electric current systems by analysis of magnetic field data, with particular reference to the quasi-dc magnetic field of the human leg

Thesis

TWO METHODS OF MODELLING ELECTRIC CURRENT SYSTEMS BY ANALYSIS OF MAGNETIC FIELD DATA, WITH PARTICULAR REFERENCE TO THE QUASI-DC MAGNETIC FIELD OF THE HUMAN LEG

submitted for the degree of PhD by David Grimes BSc, MSc

July, 1989

Date of Submission: July 1989
Date of Award: 13th October 1989

"Life is about....trying to get a partially inflated rubber lilo into a suicase which is just too small for it even when uninflated."

N.F. Simpson

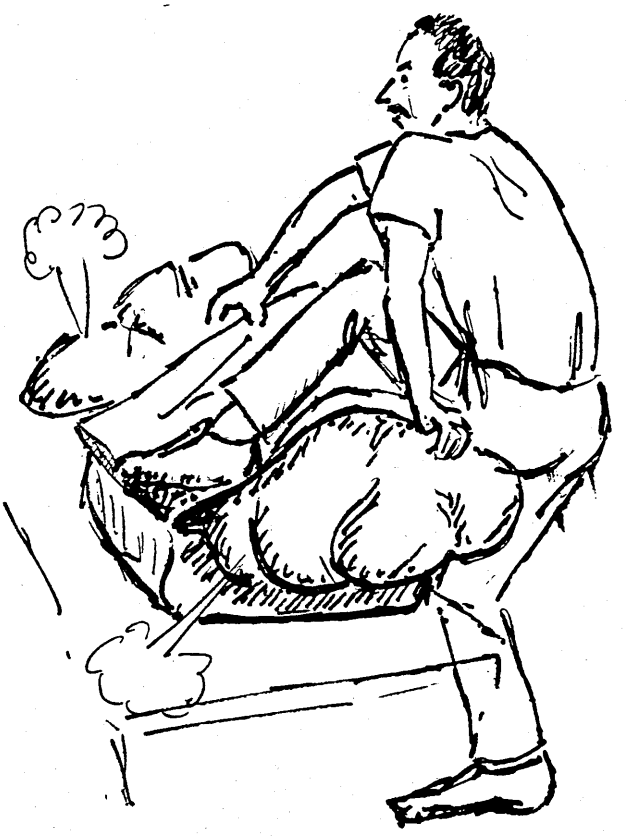

ABSTRACT

This thesis deals with two approaches to the problem of obtaining information about electric current distributions by analysing the associated magnetic field. Both methods have been developed within the context of a particular biomagnetic study, the analysis of the quasi dc magnetic field of the human leg. The techniques have been designed to deal with data sensed by a gradiometer in a series of horizontal scans above the current-carrying region and take full account of the gradiometer configuration.

Method 1, the line-dipole technique, analyses each scan individually and calculates the dipole term of a multipole expansion which best characterises the current distribution cross-section immediately below the line of scan. Method 2, the line current loop iterative-perturbative algorithm, uses data from all the scans to compute the coordinates of the best fit line current loop for the whole data map.

Both methods have been extensively tested with computer simulated data and with real data from current-carrying wire loops and the results show that both methods are capable of producing an accurate replication of the target system provided it satisfies the initial model assumptions.

The dc magnetic field of the human leg has been investigated for a number of normal subjects. The line-dipole technique provides a useful method of characterising the data and indicates regions of high current density which

allow inferences to be drawn about the physiological nature of the current generators. Analysis of the field from a leg with a fibula fracture shows significant differences from the normal pattern, although a direct, causal connection with the fracture is not necessarily implied.

The line current loop technique has been less successful in achieving a high quality fit to the leg data but this lack of success is consistent with a physiologically reasonable model of the source currents.

Although both methods have been designed for this rather specialised biomagnetic inverse problem, they are of more general applicability and may be useful in other fields such as geophysics or non-destructive testing.

ACKNOWLEDGEMENTS

First and foremost, I would like to take the opportunity of thanking Steve Swithenby for initiating the biomagnetism project of which this work forms a part, for his help and tuition during my time at the Open University and for his support and encouragement during the long period of gestation of this thesis.

I also owe a debt of gratitude to Rosemary Lennard for educating me in the complexities of biology and physiology and for sharing many hours of potentially tedious experimentation.

Tom Smith and Andy Ioannides contributed much to the methods of mathematical analysis I have used here and I wish to express my thanks for many hours of discussion and instruction.

My time at the Open University was both enjoyable and productive and for that I would like to thank all the people with whom I worked, ran, socialised, played cricket or otherwise associated. Finally I would like to thank Sheila Wilson for helpful comments on the thesis and Alison Campbell for moral support.

CONTENTS

LIST OF FIGURES

to the boundary are shown dashed.

Figure 3.5 Current dipoles in a conducting sphere. Dipole (1) is radial; dipole (2) has both radial and tangential components (shown dashed).

Figure 3.6 Current dipoles in a conducting cylinder. Dipole (1) is radial, dipole (2) is axial, dipole (3) is off-axial and non-radial. The radial field outside the cylinder will only register the effect of dipole (3).

Figure 3.7 Determination of the location of a current dipole in a conducting half-space from a contour map of the normal component of the field in a plane parallel to the half-space boundary. The contour values are given as a fraction of the maximum field strength. (After Williamson and Kaufman, 1981, figure 12).

Figure 3.8 The spread of electrical activity in the heart represented by moving sheets of dipoles. (After Tripp, 1983, p111).

Figure 3.9 Examples of multipole terms based on infinitessimal current elements. **a)** dipole **b,c)** quadrupole **d,e)** octupole.

Figure 4.1 Comparison of leg field and field from a pair of oppositely oriented, parallel, line currents in 4 different orientatiions.

Figure 4.2 Axially uniform current distribution suitable for modelling with line multipole expansion. Shaded areas represent current in +y direction. Unshaded areas represent current in -y direction.

Figure 4.3 Examples of line multipole terms. **a)** monopole, **b)** dipole, **c,d)** quadrupole.

Figure 4.4 Alternative representation of line multipole terms **a)** monopole, **b)** dipole, **c)** quadrupole.
Shading indicates current in +y direction. No shading indicates current in -y direction.

Figure 4.5a) Parameters specifying line dipole.
b) coordinate system used in line dipole location.

Figure 4.6 Parameters used in numerical integration over sensing coil.

Figure 4.7 Structure of program LSWADX.

Figure 5.1 Coordinate system for parallel line current pair.

Figure 5.2 Line dipole parameter discrepancies for parallel line current pair plotted against angle Ø.
δl = 45mm, z_1 = -50mm.

Figure 5.3 Comparison of scans from pure line dipole source (solid line) and parallel line current pair (dashed line).

l = 50mm. I l for current pair = m for line dipole. z_1 = -60mm in all cases. **a)** Ø = 90°, **b)** Ø = 180°, **c)** Ø = 135°.

a**Figure 5.4a)** Line dipole parameter discrepancies for parallel wire pair plotted against depth ($-z_1$) for 3 different values of δl. Ø = 0° **b)** Line dipole parameter discrepancies for parallel wire pair plotted against depth ($-z_1$) for 3 different values of δl. Ø = 45°. **c)** Line dipole parameter discrepancies for parallel wire pair plotted against depth ($-z_1$) for 3 different values of δl. Ø = 90°.

Figure 5.5 Line dipole parameter discrepancies for parallel wire pair plotted against wire separation (δl). The horizontal dashed line indicates the criterion of acceptability for x,z. **a)** z_1 = -30mm, **b)** z_1 = -40mm **c)** z_1 = -80mm **d)** z_1 = -100mm.

Figure 5.6 Experimental arrangement for measuring field generated by a parallel line current pair.

Figure 5.7 Current configurations used in the tests described in section 5.3.2.

Figure 5.8 Variation of parameter discrepancy with Ø for the current configuration shown in figure 5.3b at y = 50mm, z_1 = -80mm.

Figure 5.9 Variation of parameter discrepancies with y for the current configurations of figure 5.3. Ø = 70°, z_1 = -80mm in all cases.

Figure 5.10 Truncated current distribution, axially uniform with respect to the y-axis, extending between y = ±L. Shading indicates current in the +y direction, no shading indicates current in the -y direction.

Figure 5.11 Physical representation of a truncated line dipole.

Figure 6.1a) Anterior scans positions 1 to 7 subject BD. Asterisk indicates position of tibial crest. **b)** Anterior scans positions 1 to 7 subject AG. Asterisk indicates position of tibial crest.

Figure 6.2 Anterior scans for subject JM left leg compared with best fit line dipole signal.
Crosses indicate experimental data. Solid line is best fit model signal.

Figure 6.3a) Measured signal and best fit line dipole signal for 4 different aspects at position 3 (subject RL).
Crosses indicate experimental data. Solid line is best fit model signal. **b)** Best fit line dipoles and leg profiles for data in figure 6.3a **c)** Profiles and dipoles from figure 6.3b redrawn so that tibiae and fibulae coincide. **d** Line dipole vectors from figure 6.3c corrected for δl = 60mm.

Figure 6.4a) Measured signal and best fit line dipole signal

for 4 different aspects of position 3 (subject BJ). Crosses indicate experimental data. Solid line is best fit model signal. **b)** Best fit line dipoles and leg profiles for data in figure 6.4a superimposed so that tibiae and fibulae coincide. **c)** Line dipole vectors from figure 6.4b corrected for δl = 30mm.

Figure 6.5a) Anterior scans and best fit line dipole signals for positions 1 to 7 subject DG left leg. Crosses indicate experimental data. Solid line is best fit model signal. **b)** Line dipole vectors and leg profiles for data in figure 6.5a. Open circles show dipole positions corrected for δl = 50mm.

Figure 6.6 Cross section of human left leg showing main anatomical features **a)** 100mm below the knee joint **b)** 60mm above the ankle joint

Figure 6.7 Line dipole vectors for subject DG at position 3 for 20 separate scans. From Grimes et al (1985).

Figure 6.8 Line dipole vectors **a)** position 3 for 12 normal subjects **b)** position 7 for 10 normal subjects. From Grimes et al (1985).

Figure 6.9 Change in line dipole vector with movement of posterior muscle bulk. From Grimes et al (1985)

Figure 6.10 Possible leg current configurations.

Figure 6.11 Anterior scans positions 1 to 6 for subject TR with a fibula fracture. Fracture is located in the vicinity of position 3, right leg.

Figure 6.12 Line dipole vectors related to approximate tibia and fibula positions for subject TR.

Figure 7.1 Coordinate system used for the line current loop model.

Figure 7.2 The effect of adding a perturbation to a loop. The original, circular loop is indicated by a solid line, the loop shape after the perturbation has been added is shown dashed. The perturbation centre is marked *, other knots are marked x. **a)** σ = 0.5 **b)** σ = 1.0.

Figure 7.3 Positions of zero B_x (marked x) for a field scan above a horizontal loop.

Figure 7.4a) A set of field scans in a plane above a horizontal loop. The field zero positions are marked with open circles. The interpolated loop is shown dashed. **4b)** Comparison of the SRL (dashed line) obtained in figure 7.4a with the actual target loop (solid line). Perturbation centres are marked x. The loop point number (t) at each perturbation centre is also indicated.

Figure 7.5 Field ratio scans ($B_{oz}/B_{Tz}-1$) for the target and reference loops of figure 7.4. For clarity of presentation,

each scan has been scaled down by a factor F. The value of F is shown on the right of each scan.
Field points used in the inversion are shown *. Field point pairs are joined by dashed lines.

Figure 7.6 The structure of the inversion program.

Figure 7.7 Example 1.
a) Target loop (solid line) and SRL computed from field zeroes (dashed line). **b)** Target field from loop in figure 7.7a. **c)** Field ratio map with inversion points and pairs for the target and reference loops shown in 7.7a. **d)** Target and reference loops after 1 iteration. **e)** Target and reference loops (indistinguishable from each other) after 4 iterations. **f)** Field ratio map after 4 iterations.

Figure 7.8 Example 2
a) Narrow target loop (solid line) and SRL (dashed line). **b)** Target field for the loop in figure 7.8a. **c)** Reference loop and target loop after 7 iterations **d)** Field ratio map after 7 iterations.

Figure 7.9 Example 3
a) Figure of eight target loop (solid line) and SRL (dashed line) **b)** Target loop and final reference loop after 6 iterations. Inversion points and pairs are also indicated.

Figure 7.10 Example 4
a) Target loop (solid line) and SRL (dashed line) **b)** Target field with random noise added. **c)** Field ratio map with inversion points and pairs. **d)** Comparison of reference loop and target after 6 iterations **e)** Final reference loop after 10 iterations

Figure 8.1 Comparison of maximum V_z vectors (arrows) and x-y projection of target loop (solid line). The vectors were derived from the set of scans in figure 8.3b. The limb of the target loop running from bottom right to top left is nearest to the scanning plane. It can be seen that the vectors are very close to the actual loop in this region.

Figure 8.2 The structure of the full, three dimensional fitting program. Dashed boxes correspond to dashed sections in figure 7.6.

Figure 8.3 Example 1. Modelling a three dimensional figure of eight loop (simulation). **a)** Comparison of target loop (solid line) and initial SRL (dashed line) (x-y projection). **b)** Comparison of target loop (solid line) and initial SRL (dashed line) (y-z projection). **c)** Simulated gradiometer signal from the target loop in figure 8.3a,b. **d)** Simulated gradiometer signal from the SRL in figure 8.3a,b. **e)** Field ratio map ($B_{oz}/B_{Tz}-1$) also showing inversion points and pairs. **f)** Comparison of target loop (solid line) and final reference loop (dashed line) after 6 iterations, before smoothing (x-y projection). **g)** Comparison of target loop (solid line) and final reference loop (dashed line) after 6 iterations, before smoothing (y-z projection). **h)** Comparison of target loop (solid line) and final reference

loop (dashed line) after 6 iterations, after smoothing (x-y projection). **i)** Comparison of target loop (solid line) and final reference loop (dashed line) after 6 iterations, after smoothing (y-z projection). **j)** Comparison of target field (solid line) and final reference loop signal(dashed line).

Figure 8.4 Example 2. Modelling a three dimensional figure of eight loop (experimental data).
a) Target scans **b)** Initial SRL. Perturbation centres are shown as crosses. **c)** Field ratio map ($B_{oz}/B_{Tz}-1$) also showing inversion points and pairs. **d)** Comparison of target loop (solid line) and final reference loop (dashed line) after 8 iterations, (x-y projection). **e)** Comparison of target loop (solid line) and final reference loop (dashed line) after 8 iterations, (y-z projection). **f)** Comparison of target loop scans (solid line) and final reference loop scans (dashed line)

Figure 8.5 Example 3. Modelling the leg data.
a) Set of scans in a plane above the lateral surface of the leg for subject DG. **b)** Initial SRL derived from the data in figure 8.5a. **c)** Field ratio map ($B_{oz}/B_{Tz}-1$) showing inversion points and pairs. **d)** Best fit loop for leg data (x-y projection). z coordinates are given at various points to indicate the three dimensional nature of the loop. Arrows indicate current direction. Approximate leg outline is shown dashed.**e)** Best fit loop for leg data (y-z projection). **f)** Comparison of leg data with best fit loop signal.

INTRODUCTION

1 The scope of the thesis

This thesis deals with two approaches to a particular electromagnetic inverse problem, the description of a current system by analysis of the associated magnetic field. Although, in a general sense, this problem has no unique solution, that is not to say it is insoluble. One may proceed by adopting a simple source model specified by a small number of parameters. Available information about the system may be used to further restrict the set of allowable solutions so that, hopefully, it is possible to arrive at a single, best fit current configuration.

The two techniques described here are concerned with this restricted problem. Both have been developed within the context of a specific biomagnetic investigation. They were devised as a means of analysing gradiometer measurements of quasi dc fields generated by ionic currents within the human leg. Consideration of the leg geometry and physiology has influenced the design of the models and may be used to limit both the spatial extent and the current strength in the modelled current system.

This does not mean that the applications need be restricted to biomagnetism. Either method may be used in any situation where currents are to be mapped but where direct current measurement is either impractical or undesirable. Possible examples include geomagnetism and non-destructive

testing.

2 Biomagnetic considerations

The study of biomagnetic phenomena has expanded rapidly in the last decade due largely to the increasing availability of ultrasensitive SQUID magnetometers and the development of sophisticated data analysis techniques often based on powerful computer algorithms.

During this period most of the research effort has gone into the investigation of the magnetic fields of the human heart and brain. Little attention has been paid to fields associated with biological regeneration and growth mechanisms, although many electrical measurements suggest that currents which would give rise to measurable fields play an important role in these phenomena.

This association between electric currents and biological development has led to the suggestion that electrical techniques may be used to stimulate regeneration of tissue. One medical application is the use of electric currents to treat cases of non-union in limb fractures. While there is a considerable body of literature indicating that the some of the techniques used may be effective, little progress has been made in understanding the mechanism and many clinical trials have lacked adequate controls. Even less is known about the possible role of endogenous currents in natural fracture healing.

One reason for this lack of knowledge is the difficulty of making in vivo, electrode measurements of very small, quasi-dc currents. An alternative approach is to try and measure the magnetic field associated with any such

currents. In 1980, a biomagnetism project was initiated at the Open University with the purpose of detecting and analysing fields associated with naturally healing fractures in the lower leg.

An unexpected result of these investigations was the observation that all healthy, non-fractured legs had associated field patterns consistent with quasi-dc currents within the limb. This was felt to merit further analysis as the presence of these endogenous currents could well have a bearing on the use of applied currents in the treatment of non-union.

The two methods of analysis presented in this thesis were developed with the goal of modelling the leg field data. The line current dipole technique, uses the 2nd order term in a multipole expansion to characterise the current pattern at various positions along the leg. The current loop model attempts the more ambitious task of finding the shape of the line current loop which best fits the field data.

3 Structure of the the thesis

Present knowledge of the role of electric and magnetic fields in biological systems is reviewed in chapter 1 with particular reference to the use of electrical methods in the treatment of non-union.

In chapter 2, I describe the design of the experimental system and the protocols for the collection of magnetic field data in the vicinity of the human leg.

Methods of solving the biomagnetic inverse problem are discussed in chapter 3. Standard techniques exist, however they have been designed with reference to the likely current

generators and the specific geometries of the human heart and brain. These techniques are not appropriate to the analysis of the leg data and, for that reason, the two techniques mentioned above have been developed.

Chapters 4 to 6 are concerned with the line dipole approach. Chapter 4 develops the theory and describes the algorithm for finding the best fit parameters. Chapter 5 is concerned with tests on the model. These were designed to ascertain the extent to which the model parameters are likely to reflect the reality of the current distribution. The analysis of the leg data is described in chapter 6.

The current loop model is discussed in chapters 7 and 8. Chapter 7 deals with the detailed theory of the model and gives the results of computer simulations for some simple cases. The application of the line dipole algorithm to three dimensional current systems and the analysis of the human leg data is described in chapter 8.

4 Convention regarding magnetic field terminology

Problems sometimes arise in discussions of magnetic phenomena over the name used for the magnetic field vector $\underset{\sim}{B}$. Usually $\underset{\sim}{B}$ is referred to as the 'magnetic induction'. This can occasionally cause difficulty if it is confused with the process of Faraday induction. On the other hand the term 'magnetic field' is ambiguous as it may be taken to mean the magnetic field intensity $\underset{\sim}{H}$.

This thesis deals almost exclusively with the quantity $\underset{\sim}{B}$. Hence 'magnetic field' may be taken to mean $\underset{\sim}{B}$ unless otherwise stated. Where there is any possibility of

ambiguity, I will adopt the terminology of Tripp (1982) and use the term 'B-field' to distinguish $\underset{\sim}{B}$ from $\underset{\sim}{H}$.

CHAPTER 1

A REVIEW OF BIOELECTRIC PHENOMENA AND THEIR MEASUREMENT WITH SPECIAL REFERENCE TO FRACTURE HEALING

1.1 Endogenous and applied bioelectric fields

It is possible to distinguish two themes in the study of bioelectricity. One is the investigation of the role played by innate electric currents and fields in metabolic processes and the other is the effect of externally applied electric fields on these processes.

It is not surprising either that applied electric fields have some effect on organisms or that many internal processes of organisms involve endogenous electrical activity. Most of the molecules that make up cells are electrically charged and the movement of these charged particles constitutes an electric current which may arise from or give rise to an electric field.

The most obvious instance of endogenous electrical activity is the 'action potential' by which information is transmitted along nerve fibres. The interior of a nerve cell has a negative potential with respect to its external environment, the potential difference being maintained by means of pumps and ion-specific leakage channels in the cell membrane. If this voltage decreases by more than a specified amount, there is a change in the activity of some channels causing a potential pulse to propagate along the cell.

As a further example, consider the situation when a cell membrane is ruptured. Free flow of ions can now take place

into and out of the cell, the net effect being an influx of positive charge at the site of injury. It is believed that such 'injury currents' may be involved in the mechanisms by which the repair of the damaged membrane takes place.

Conversely, the application of external electric fields may be expected to influence the behaviour of charged species within an organism and thus affect metabolic processes. Applied fields have been shown to stimulate regeneration of nerves and influence the location of growth tips in plant embryos (see section 1.4 for a more detailed discussion). The exact mechanism is poorly understood but in both cases, the fields may enhance existing, natural effects.

These two themes in bioelectricity are intimately linked. Knowledge of the effects and causes of endogenous currents and fields is a necessary prerequisite for learning how applied fields can be used most effectively to stimulate desirable processes such as healing and regeneration.

1.2 Early history of bioelectricity

The Greeks are credited with the first recorded observations of bioelectric phenomena some 2600 years ago when Thales of Miletus commented on the severe shocks produced by electric fish but not until Galvani at the end of the eighteenth century was there any significant progress in understanding the link between biology and electricity.

Galvani's results showed firstly that muscle contractions could be stimulated by electric fields and secondly that the same stimulation could be effected without external electricity by inserting a damaged nerve into the

muscle (Geddes and Hoff, 1981). In fact Galvani was demonstrating simultaneously the electrical nature of muscle contraction and the presence of injury currents, although this interpretation was not available to him at the time.

Given the complexity of biological systems and the low sensitivity of available instrumentation, it is not surprising that subsequent progress in understanding bioelectrical phenomena was slow. In 1828, Nobili developed a galvonometer sensitive enough to make more precise measurements of currents in frog preparations (again these were injury currents) and, around 1840, Matteucci demonstrated the existence of a transient potential associated with muscle contraction. DuBois-Reymond (1843) made the first measurement which indicated that potential differences were also associated with injuries in humans. The first electrical recording of heart activity (the electrocardiogram or ecg) was made in 1856 and electrical signals from the brain were also measured in the latter half of the 19th century.

In this century, most of the effort in bioelectric research has gone into the study of transient and repetitive phenomena. In particular, the ecg and eeg are now standard medical tools and have been invaluable in the analysis of brain and heart function and the diagnosis of abnormal conditions.

1.3 Bioelectrical measurements relating to development and growth

In most organisms, development occurs over a time scale of hours or days, so that associated electrical effects tend to be dc or quasi-dc. This considerably exacerbates the problems involved in making electrode measurements. Electrolytic effects may occur at metal-fluid interfaces and instrumental drift can distort and obscure the measured voltage. Furthermore, electrodes inserted into an organism to measure potentials are invasive and will alter the target system to an unknown and unknowable extent.

Nevertheless, pioneering work was carried out in the early years of this century by Hyde (1905) who recorded potential differences across fish eggs and by Lund (1925) who showed that a section of hydroid stem about to grow a head developed a longitudinal potential difference. The positive end predicted the position of eventual head formation.

These early measurements are open to criticism in that they were made with surface electrodes on organisms which had been removed from their natural, aqueous environment. More recently, however, Jaffe (1966) was able to measure a voltage across normally developing fucoid eggs in seawater. He arranged several hundred of the eggs in series inside a loose fitting capillary tube and recorded the potential difference between the ends of the tube.

Measurements have also been made on the alga Acetabularia under normal developmental conditions (eg Novak and Bentrup, 1972). In this case, a segment of Acetabularia

regenerated naturally in seawater in a container compartmentalised in such a way that the ends of the segment were electrically insulated from each other. The measured voltage pulses indicated a current entering the end of the stem about to form a cap.

A major breakthrough in non-invasive measurement came with the introduction of the vibrating probe developed by Jaffe and Nucitelli (1974). The probe consists of an electrode forced to vibrate at several hundred Hertz by a piezoelectric element, the amplitude of vibration being of the order of 15μm.

The probe is positioned in an aqueous medium close to the organism under investigation. Measuring the peak to peak amplitude of the voltage variation relative to a reference electrode gives the the potential difference between the extremities of movement of the probe tip. Knowing the resistivity of the medium, the current density at that point can be calculated from Ohm's law. Thus a map of the current through the medium in the vicinity of the organism can be constructed.

Using this technique, the currents associated with various developmental and regenerative processes have been investigated. Nucitelli (1978) mapped currents in the vicinity of a fucoid embryo and showed that the point of entry of the current into the embryo predicted the position at which the growth tip would develop. Various experiments quoted by Borgens (1979) show current entering the presumptive growth tip of other plant cells, while in 1979 Stern and Jaffe measured large currents leaving the primitive streak of the developing chick embryo.

Although in all of these cases the current precedes other signs of development, it is difficult to establish a causal relationship. One hypothesis suggested by Stern (1984) is that essentially random processes trigger a small, transmembrane current which initiates a positive feedback cycle. The current causes membrane changes which act so as to amplify the current which in turn stimulates further membrane changes and so on. Once established, it is possible that the current generates potential differences along the membrane, causing the reorganisation of molecules necessary to trigger the next stage of development (Jaffe, 1981).

Currents associated with limb regeneration in the red spotted newt Notophthalmus iridescens are reported by Borgens (1982). These amphibians naturally regrow limbs after amputation. Measurements with a vibrating probe showed large currents ($\sim 100 \mu A\ cm^{-2}$) leaving the cut surface of the limb stump. The current consisted of a Na^+ ion flux and appeared to be generated by the skin, pumping through Na^+ ions from the external environment.

Again, the precise role of the current in the regeneration process is not well understood but it has been shown that regeneration can be halted by interrupting the current. This may be done by closing the wound or removing Na^+ ions from the environment. In the latter case it is interesting to note that both current and regeneration are eventually reestablished with Ca^{2+} ions as the charge carriers.

The same experiments have been performed on frogs which do not normally regenerate limbs (Borgens, 1982).

Again, large currents were measured leaving the stumps of amputated limbs; however in this case, the currents were concentrated around the periphery of the limb in the highly conducting lymph space, bypassing the core tissues. This peripheral conducting region is absent in the newt and Borgens postulates that it is the action of the currents on the central tissue of the limb and in particular on the nerves that stimulate the regeneration process. This argument is supported by the observation also reported by Borgens that currents artificially driven through the centre of frog limb stumps appear to initiate some regeneration.

1.4 Bioelectric measurements in bone and muscle

Yasuda (1953) demonstrated the existence of stress induced potential differences in bone. When a section of bone is flexed, the part of the bone under tension becomes electropositive, while that under compression becomes electronegative. It was hypothesised by Fukada and Yasuda in 1957 that these potentials could be responsible for the ability of bone to remodel itself in response to applied forces. This property of bone (known as Wolff's law) arises from the fact that bone which is repeatedly compressively stressed thickens, while bone which is not stressed in this way atrophies.

Initially, the piezoelectric behaviour of collagen was held resposible for the observed potential difference. However this would be expected to give rise only to a transient effect in wet bone, whereas the observed potential difference is of longer duration. A more probable cause suggested by other authors (e.g. Pienkovsky and Pollack,

1983) is a 'streaming potential' mechanism.

Streaming potentials arise when an ionic fluid is forced through channels (formed in this case by the collagen matrix) which preferentially bind charges of one sign. The fluid movement causes a separation of bound and unbound charges and hence gives rise to a potential difference.

These stress-related potentials are a mechanical property of bone independent of cell viability. Another effect which has been observed is the relative electronegativity of areas of bone involved in growth or repair. Friedenberg and Brighton (1966) found the epiphysis in normally growing bone to be electronegative with respect to the rest of the bone while Friedenberg et al (1971) report the same effect at the site of injury in fractured bone. However Lokietek et al (1974) have queried this latter finding and suggest that the voltage may arise from injury currents in damaged tissue close to the fracture.

Overall, the experimental evidence indicates that bone is relatively electronegative in regions where growth is occurring. It is primarily this observation which has led to the suggestion that bone growth can be stimulated by applied electric fields.

Steady currents have also been observed around muscle fibres by Betz et al (1980). Using a vibrating probe, they detected currents leaving the endplate region of rat lumbrical muscle. In a later paper (Betz et al, 1984) they attribute the currents to an inhomogeneous distribution of Cl^- leakage channels in the cell membranes. Cl^- ions enter

the fibre uniformly along its length, but leave through channels which are concentrated away from the endplate region. The result is an apparently positive outward current close to the endplate.

1.5 The effects of applied electric fields on biological tissue

Lund in 1923 showed that the polarity of fucoid eggs could be controlled by a potential difference of a few mV across each egg. Jaffe and Nucitelli (1977) quote other examples of development axes being influenced by fields of similar size. Once more the probable explanation is that the applied field gives rise to potential differences in the membrane which initiate organisation of important molecules.

As far as regeneration is concerned, as well as the evidence already mentioned in section 1.3 relating to electrically stimulated limb regrowth in frogs, Borgens (1982) has reported evidence of the regeneration of lamprey giant axons under the action of an applied field. Here the migration of Ca^{2+} ions into the cut end of the axon appears to be a crucial factor.

Less convincing are attempts which have been made to stimulate limb regeneration in mammals. For example Becker (1972) claimed some success in regrowth of amputated forelimbs in rats. However the extent to which regrowth in the electrically treated limbs exceeds that in the controls is at best marginal.

The application of ac fields also has detectable effects although the mechanism is more complex and even less well understood. Examples are cited by Barker and Lunt (1983) of

experiments on a variety of organisms from chick embryos to bacteria and slime moulds. In most cases some effects were observed although these ranged from increased growth to tissue necrosis. The results appear to be frequency specific and also dependent on the shape of the applied wave form.

1.6 The effect of applied fields on fracture healing

1.6.1 Non-union in fractures

The evidence of potential differences in bones related to both mechanical stress and growth (section 1.4) coupled with the evidence sited in the previous section for the influence of electric fields on regeneration and development has led to much interest in the electrical stimulation of fracture healing in cases of non-union. This is a condition in which the normal process of bone repair becomes permanently arrested, perhaps due to poor immobilisation, inadequate reduction or insufficient blood supply because of damage to the surrounding tissue.

Often the problem can be dealt with by improved immobilisation and reduction, in some cases involving pins or plates fixed directly to the bone. Sometimes bone grafting is necessary if the fracture gap is too great. In some cases, none of these treatments work and the last resort, if the fracture is in a limb bone, is amputation. Occasionally, a false joint forms at the fracture site; this is known as a pseudarthrosis.

1.6.2 DC techniques in the treatment of non-union

A number of experiments performed on animals indicate

that dc currents reliably cause osteogenesis (Brighton, 1981 and others reviewed by Barker and Lunt, 1983). Typically current is introduced via an electrode inserted into the bone cortex and bone regrowth is stimulated if this electrode is used as a cathode. The optimum current is of the order of 10 to 20μA but varies depending on cathode material. It seems that the effect may be partly due to an electrolytic reaction at the cathode decreasing oxygen tension and increasing hydroxyl radical concentration (Brighton et al, 1977). The experiments of Brighton (1981) and others provide sufficiently good controls to conclude that it is, in fact, the electrical stimulation which enhances the bone growth in these cases.

The first successful dc treatment of non-union involving implanted electrodes was performed by Friedenberg et al (1971). A full clinical trial was subsequently reported by the same group (Brighton et al, 1981). The treatment involved the implantation of 4 cathodes at the fracture site receiving current from a surface anode. The current to each cathode was 20μA and was maintained for a period of up to 12 weeks with no weight bearing. Brighton claims a success rate of 79% for early attempts and 89% in later trials. Many of the failures had formed pseudarthroses which appear to be resistant to the treatment unless the membrane which forms over the fracture surface is removed.

Although double blind trials yielding impressive statistics have been performed with animals showing that dc currents stimulate fracture repair (eg Fuentes et al, 1984), no such work has been carried out with human subjects. It is therefore difficult to say to what extent results in the

clinical trials are influenced by other aspects of the treatment regime, such as the long period of immobilisation - or even the psychological benefit of the increased patient care.

1.6.3 AC techniques in the treatment of non-union

The use of an ac approach to non-union stimulation follows from the idea that the stress related potentials mentioned in section 1.4 initiate healing in normal circumstances. In natural healing then, the normal movement of the person would tend to deliver the current as a series of pulses. The use of time-varying pulses has the added advantage that the current can be induced magnetically using coils mounted outside the body and is thus mechanically noninvasive.

Unfortunately, the efficacy of pulsed field treatment appears to be less certain and the mechanism is even less well understood than in the dc case. Experiments on animals have yielded conflicting results. For example, two trials involving dogs (Enzler et al, 1980 and Blumlein et al, 1978) showed no significant difference between electrically stimulated fractures and controls. However, in a third study, Sturmer and Schmit-Neuerberg (1985a) achieved a much higher success rate for their electrically treated cases.

Detailed comparison is difficult as the treatment regimes differed as did the frequencies and waveforms used. Both Sturmer and Blumlein used the Kraus-Lechner technique described below. In Sturmer's trial, the treated animals had artificially induced pseudarthroses and the electrical

treatment was used in conjunction with bone grafts and fixing plates. The control limbs had the same fixings and grafts but dummy coils were fitted. This combination of treatments may account for their high success rate, or it may be that the differences in applied frequency and waveform were significant. The ac approach is reported to be very sensitive to these parameters (Bassett, 1985).

Most of the treatment of human non-unions has been carried out on tibial fractures using the methodology described by Bassett (1985). A pair of coaxial, current-carrying coils are mounted on the cast on either side of the fracture. The coils are individually designed for each patient to ensure a spatially uniform magnetic field in the vicinity of the fracture and the time-varying current is adjusted to induce electrical fields of about 0.1 - 0.15 mV mm^{-1} at the fracture site parallel to the bone axis. The exact pulse shape and frequency are not clearly indicated in the literature. During the treatment, which may be for 12 to 16 hours per day, the treated limb is completely immobilised.

With this regime a success rate greater than 90% is claimed. Bassett postulates that the induced currents effect calcification of the fibrocartilage in the fracture gap, however in the absence of definitive animal experiments and double blind trials it is difficult to be sure that the currents are a causal factor.

A slightly different ac method in present use is that developed by Kraus and Lechner in 1972. Here a secondary coil is implanted close to the fracture and the coil terminals are arranged so that the induced current is forced

through the fracture site. Sturmer and Schmit-Neuerberg (1985b) report on the successful treatment of 36 out of 37 pseudarthroses that have shown poor reaction to other forms of treatment. Again the electrical treatment was used in conjunction with fixation and bone grafting. In spite of the remarkable success of the regime, the authors are careful to point out that they cannot be sure of the causal effect of the currents without a double blind trial.

One such trial of the Bassett technique has been attempted by Barker and co-workers in Sheffield. A preliminary report on 16 patients (Barker et al, 1984) shows worse results for the electrically treated subjects than for the controls, however the statistical significance of such low numbers is questionable.

1.7 Biomagnetic measurements of currents associated with fracture healing

1.7.1 Principles of biomagnetic measurement

From the foregoing discussion, it seems likely that endogenous currents play an important role in the natural healing of fractures, even if the exact mechanism remains unclear. Likewise, the way in which artificial currents influence healing is imperfectly understood, although it seems plausible that they enhance or replicate endogenous effects. Obviously, a more detailed knowledge of any current patterns which occur during natural healing is desirable, both from the point of view of understanding that process better and of improving electrical treatment techniques.

I have already mentioned (section 1.3) the difficulties

inherent in trying to make electrical measurements of such currents. One way around these problems is to detect the currents magnetically. All electrical currents give rise to magnetic fields. Biological tissue is essentially transparent to these fields so that they can be sensed from outside the organism producing them with little or no distortion. In principle then biomagnetic measurements provide a completely noninvasive method of monitoring biological currents.

1.7.2 Biomagnetic measurements at the Open University

This approach has formed the basis of a research program at the Open University with the long term goal of the making magnetic measurements of currents associated with fracture healing. It was found, however, that a control group of subjects with normal, healthy limbs produced magnetic signals consistent with a dc current pattern with a strength of the order of microamps. The biological function of these currents is not fully understood but they appear to be related to muscle action and are unaffected by mechanical stressing of the bone.

In terms of fracture healing, their significance lies in the fact that they exist at all. It would appear that stress generated potentials are not the only electrical effects associated with leg movement and this needs to be borne in mind if treatment regimes are set up which attempt to enhance or replicate endogenous current systems.

The measurement and analysis of these signals, together with a preliminary analysis of a single fibula fracture are discussed in the following chapters.

CHAPTER 2

EXPERIMENTAL PROCEDURE AND DATA COLLECTION

2.1 Experimental considerations

2.1.1 Overall experimental design

The equipment used for the mapping of the magnetic field in the vicinity of the human leg is shown in figure 2.1. The subject lies on the bed which is free to move in the horizontal plane. A SQUID magnetometer is supported in a wooden cradle over the bed and measures, to a first approximation, the change in the vertical component of the magnetic field as the bed is moved. Also shown in figure 2.1 is the coordinate system used throughout this work. The x and y axes are in the horizontal plane, respectively perpendicular and parallel to the long dimension of the bed; the z axis points vertically upwards.

Three mutually perpendicular sets of Helmholtz coils surround the magnetometer. Their purpose is to null the ambient field in the vicinity of the magnetometer and subject. The position of the bed in the x and y directions is monitored by potentiometers linked to the bed movement. Output from both potentiometers and the magnetometer is fed to the A/D port of a MINC 11-03 computer.

The usual procedure for obtaining a field map is to pass the subject under the magnetometer in the x direction. As the bed moves, the computer continuously samples simultaneous values of magnetometer output and bed position. Several such passes are averaged for the purpose of noise

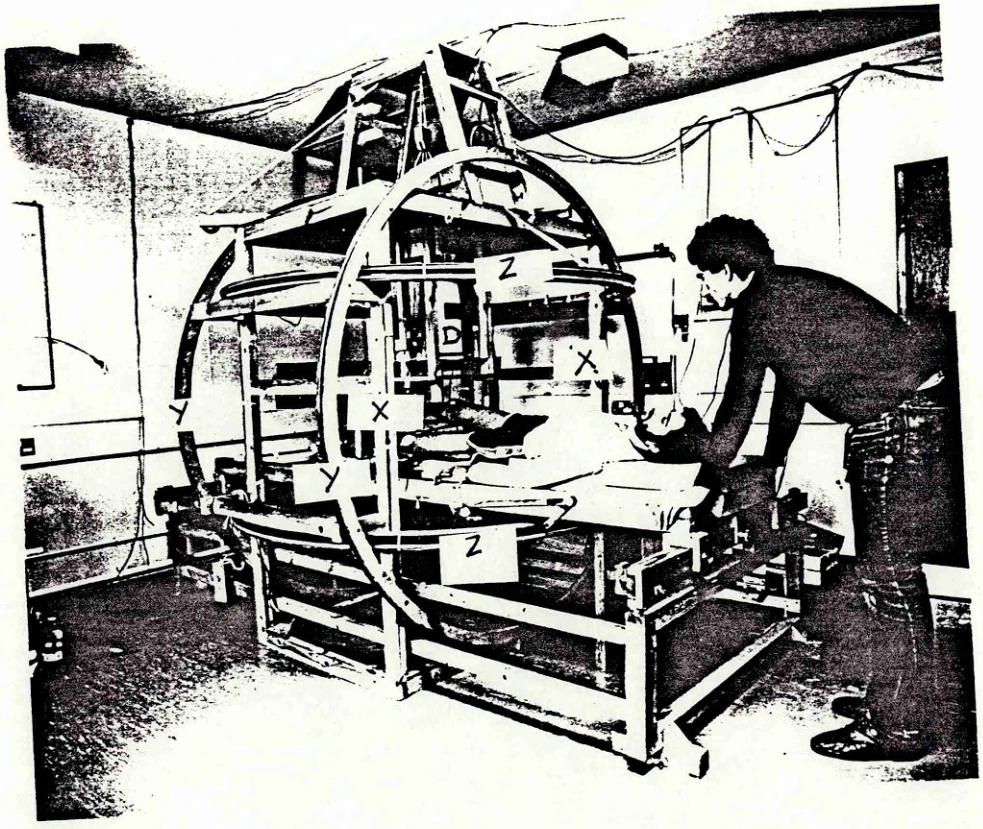

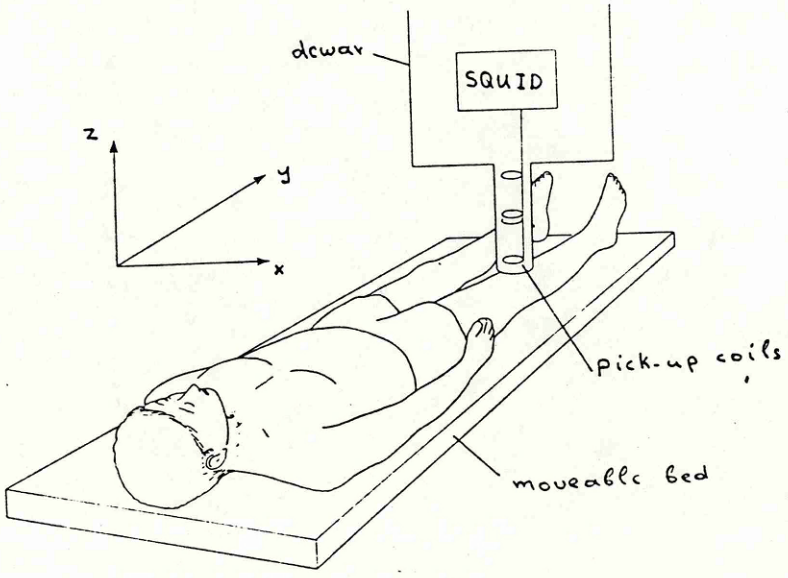

Figure 2.1a) The arrangement for measuring the dc magnetic field of the human leg. X, Y and Z Helmholtz coils are labelled, as is the dewar, D. **b)** The coordinate system for magnetic field measurements.

reduction. These averaged data constitute a single 'scan'. A field map in an x-y plane above the leg is constructed by performing a number of scans at different y positions.

Obviously, the greater the number of scans, the more detailed the field map. In fact, the leg signal was found to vary only slowly in the y-direction, so 7 scans between knee and ankle provided adequate resolution. They could also be completed in a time (~15 minutes) during which the signal remained approximately constant. The scans were normally performed at positions 1 to 7 of the anatomical scale defined in section 2.4.1.

Exactly the same procedure was used for collection of field data in the vicinity of other current sources such as the current loops described in chapters 5 and 8.

2.1.2 The SQUID magnetometer

The magnetometer used for these experiments was a commercial, 2nd order (d^2B/dz^2) gradiometer based on an rf SQUID and built by the BTi corporation. Details of the functioning of rf SQUID magnetometers can be found in many references (e.g Giffard et al 1972 and Swithenby 1980) and it is my intention here only to discuss those operational features which have a direct bearing on data collection and analysis.

The SQUID magnetometer is based on a superconducting ring containing a 'Josephson junction' or narrow, resistive gap. It is a property of a superconducting ring that the total magnetic flux threading it must be an integral number of flux quanta (one flux quantum is 2.07×10^{-15} Wb). Any attempt to change this condition by application of flux from an external source causes a compensating supercurrent to

appear in the ring which acts so as to exactly counterbalance the external flux change. Thus the relationship between externally applied flux Φ_a and flux threading the ring Φ_i is:

$$\Phi_i = \Phi_a - Li \qquad (2.1a)$$

$$\Phi_i = n\Phi_o \qquad (2.1b)$$

where L is the ring inductance

i is the compensating supercurrent

n is an integer

Φ_o is the flux quantum

The inclusion of the Josephson junction modifies the relationship between Φ_i and Φ_a to that shown in figure 2.2. In order to measure changes in Φ_a, an rf current in a tank circuit inductively linked to the SQUID is used to drive the SQUID around a hysteresis loop such as ABCDEFGHIB in figure 2.2. Any change in Φ_a alters the symmetry of the loop so that it is no longer centred at A (figure 2.2).

This distortion of the hysteresis loop can be monitored and used to control a feedback current (again inductively linked to the SQUID via the tank circuit) which maintains the loop symmetry. The output voltage is derived from the feedback current and is thus directly proportional to the change in externally applied flux.

It should be stressed that the SQUID magnetometer only measures change in flux through the ring and not the absolute value of the flux. This is because the baseline for the output voltage is determined by the value of n in equation (2.1b).

appear in the ring which acts so as to exactly counterbalance the external flux change. Thus the relationship between externally applied flux Φ_e and flux threading the ring Φ_i is:

$$\Phi_i = \Phi_e - L\dot{i} \qquad (2.1a)$$

$$\Phi_i = n\Phi_o \qquad (2.1b)$$

where L is the ring inductance

i is the compensating supercurrent

n is an integer

Φ_o is the flux quantum

The inclusion of the Josephson junction modifies the relationship between Φ_i and Φ_e to that shown in figure 2.2. In order to measure changes in Φ_e, an rf current in a tank circuit inductively linked to the SQUID is used to drive the SQUID around a hysteris loop such as ABCDEFGHIB in figure 2.2. Any change in Φ_e alters the symmetry of the loop so that it is no longer centred at A (figure 2.2).

This distortion of the hysteresis loop can be monitored and used to control a feedback current (again inductively linked to the SQUID via the tank circuit) which maintains the loop symmetry. The output voltage is derived from the feedback current and is thus directly proportional to the change in externally applied flux.

It should be stressed that the SQUID magnetometer only measures change in flux through the ring and not the absolute value of the flux. This is because the baseline for the output voltage is determined by the value of n in equation (2.1b).

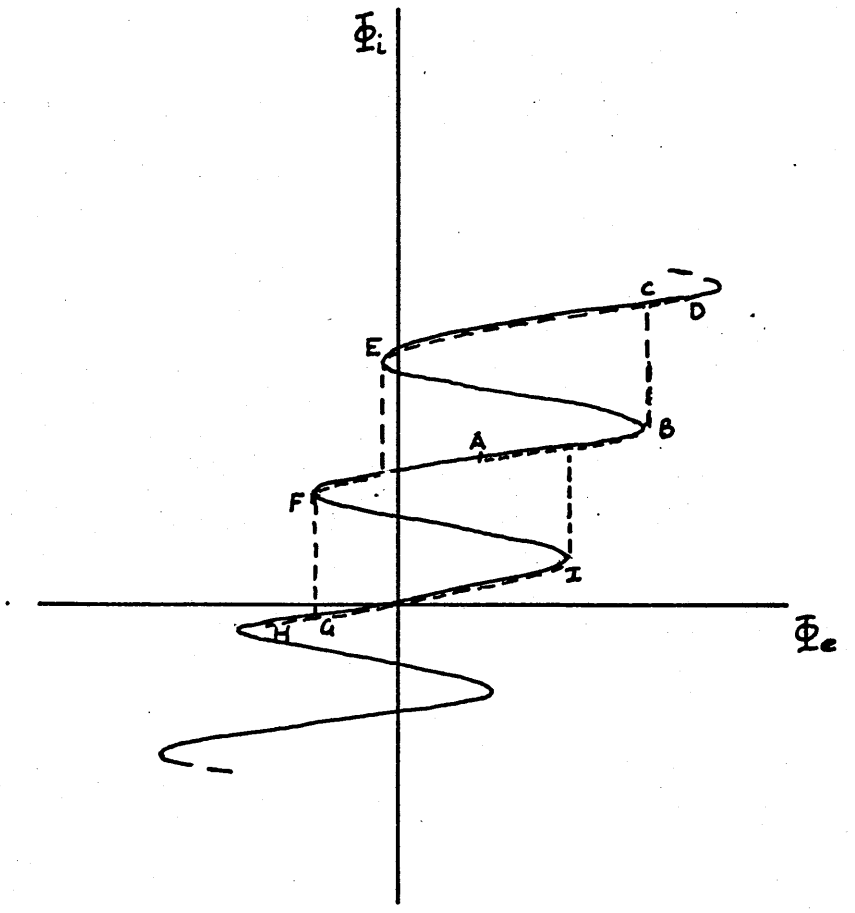

Figure 2.2 Relationship between externally applied flux (Φ_e) and flux threading SQUID ring (Φ_i). Dotted line shows hysteresis loop when ac field is applied to SQUID initially at A.

In most standard SQUID magnetometers, the external field is not sensed directly by the SQUID ring. The sensing unit comprises an ensemble of series-wound coils. Any attempt to change the flux linking the ensemble gives rise to a compensating supercurrent in the coils. This current acts to maintain the net flux through the ensemble as described for the SQUID ring. Inductive coupling between the sensing coils and the SQUID ensures a change in flux at the SQUID proportional to the net change through the sensing ensemble. Thus the output voltage signal may be represented as:

$$V_{out} = \sum_{i=1}^{n} k_i \int_{S_i} \Delta \underset{\sim}{B} \cdot d\underset{\sim}{S_i} \qquad (2.2)$$

where n is the number of sensing coils

S_i is a surface bounded by the ith sensing coil

k_i is a calibration factor relating output voltage to applied average flux density for the ith coil. It depends on the number of turns in the coil, the sense of the windings and the inductive coupling between the ensemble and the SQUID ring.

In our case the sensing coil ensemble is a stack of 3 circular, coaxial coils. The middle coil is equidistant from the other two, contains twice as many turns and is wound in the opposite sense. Dimensions are as given in figure 2.3. This arrangement ensures that fields which are constant or of uniform gradient produce no net flux change. The system thus effectively discriminates against distant (i.e. noise-causing) sources.

Standard BTi electronics modules were used to provide the magnetometer voltage output. These allow three possible

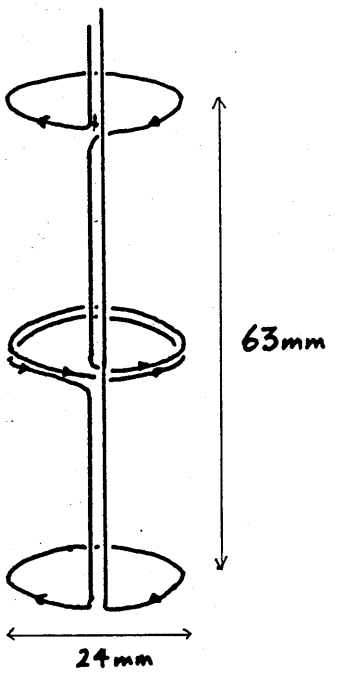

Figure 2.3 Second order (d^2B/dz^2) gradiometer sensing coil configuration used for all experimental measurements in this thesis.

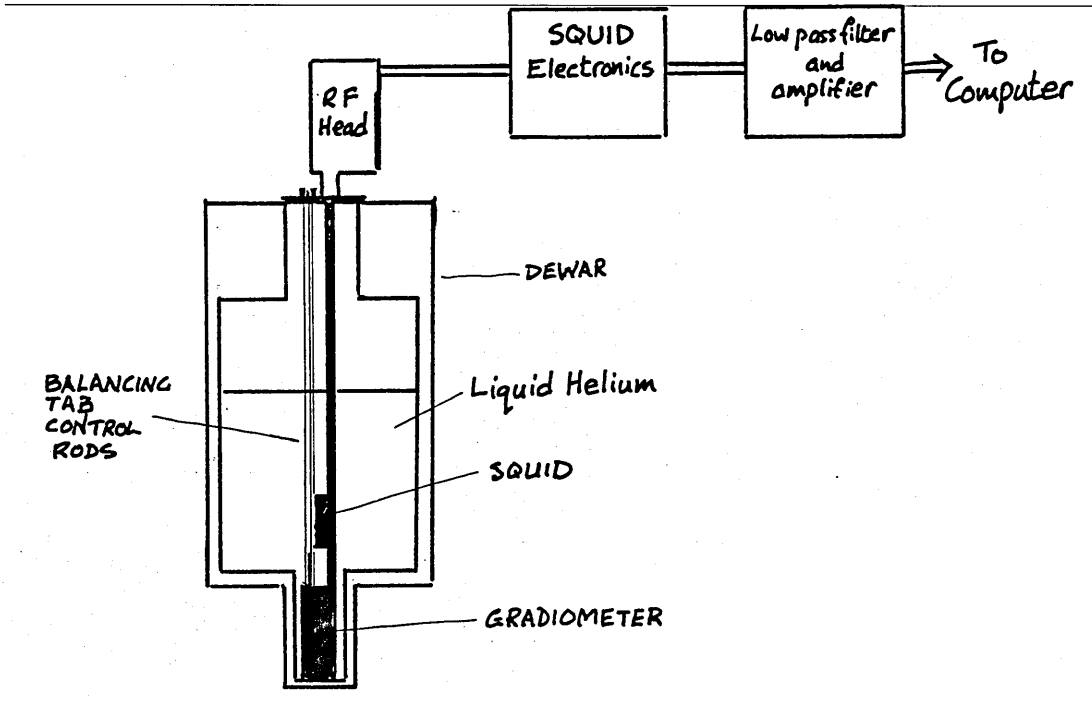

Figure 2.4 The magnetometer system.

amplifications (x1, x10, x100). The calibration for each amplification as given by the supplier is shown in table 2.1. In the table, the column headed Φ_c gives the net flux change through the ensemble corresponding to 1 volt at output. The column headed B_{zc} gives the change in strength of a z directed uniform B-field which would produce a flux change of Φ_c through the gradiometer if the field was acting at the bottom coil alone.

Throughout the remainder of this work the field measured by the magnetometer will be assumed to mean this equivalent field at the bottom coil unless otherwise stated.

TABLE 2.1

Amplification	Φ_c /Wb	B_{zc} /T
x1	9.05×10^{-12}	2.0×10^{-8}
x10	9.05×10^{-13}	2.0×10^{-9}
x100	9.05×10^{-14}	2.0×10^{-10}

Because of the reliance on superconductivity, the gradiometer and SQUID must be kept immersed in a large dewar of liquid helium. As a result the system is somewhat cumbersome and needs to be kept approximately upright. In the experiments described here, the dewar was always kept vertical with the common axis of the gradiometer coils in the z direction. Its height relative to the plane of the bed could, however, be adjusted. Figure 2.4 is a schematic representation of the whole magnetometer system.

2.1.3 Coil balancing

The successful functioning of the gradiometer design described above depends on the net flux through the coils

from spatially uniform or uniform gradient fields being zero. In principle, this could be achieved by manufacturing the coils to very high tolerances to ensure equal area and accurate alignment. However, this is not a practicable proposition, particularly as dimensions may be altered during repeated thermal recycling. An alternative approach is to have small superconducting tabs positioned close to the coils. The tabs are used to distort the field and thus alter the amount of flux threading the coils. The usual arrangement is to have three tabs, each tab being positioned so that its adjustment 'fine tunes' the response of the magnetometer to one of the three (x,y,z) field components.

In the case of the gradiometer described here, the tab positions were controlled by long rods passing through the mouth of the dewar. The balancing operation was performed using spatially uniform ac fields generated by the Helmholtz coils. Frequencies of 30, 65 and 80 Hz were used for the x,y and z directed fields respectively. This allowed the effect of each tab adjustment on all 3 component directions to be monitored simultaneously. The magnetometer output was fed to the computer which produced a frequency spectrum after every adjustment.

Ideally, this balancing procedure should minimise the heights of the three peaks corresponding to the applied ac signal together with that due to 50 Hz mains-derived noise. In practice it was usually not possible to minimise all 4 peaks simultaneously, but a compromise position with minimum average peak height gave a sufficiently high signal to noise ratio for our measurements.

Using this method, the ambient noise level was typically

80fT $Hz^{-1/2}$ in a frequency band from 0.2 to 50Hz. To maintain this noise level, the procedure was repeated every two or three months.

2.1.4 Position of the conducting body

The experimental procedure as outlined in section 2.1.1 gives magnetometer and potentiometer outputs which relate the magnetic B-field to a coordinate system fixed to the bed. It is also necessary to locate the body containing the currents (e.g. the human leg) in the same coordinate system. To achieve this the location device shown in figure 2.5 was used.

Two horizontal rods A and B parallel to the x axis are mounted on a column fixed to the magnetometer cradle. The column and rods can be moved up and down manually by means of a small rack and pinion. When not in use the rods are raised clear of the dewar tail. The position of a point on the body can be determined by lowering the device and moving the bed until one of the rods touches the required point. The computer can then calculate the x-coordinate from the x-potentiometer reading, while the z-coordinate is read manually from a scale fixed to the column.

This system could be used to identify the location of a specific feature (such as the position of the tibia during a leg measurement or the location of a wire in a model line-current loop). It could also be used to obtain a complete cross-sectional profile of a leg as a series of x,z coordinates. An example of such a profile is shown in figure 2.6. Both possibilities were built into the data acquisition programs described in section 2.3.

2.2 Noise considerations

The noise affecting the magnetic field data in these experiments may be conveniently categorised either as 'subject noise' arising from sources within the system under investigation or 'external noise' produced by other sources. Both categories are discussed below.

2.2.1 External noise sources

Because the position of the magnetometer remained fixed during the experiments, the spatial variation in the ambient field caused by nearby ferromagnetic objects had no effect, provided of course they remained stationary during data collection.

External sources which produce time-varying noise include mains-borne ac currents, vibrating or moving ferromagnetic objects and eddy currents in nearby conductors. To minimise eddy current or vibrational noise within the experimental apparatus, the entire structure was made from wood or plastic with brass or aluminium fixings where necessary.

Although the fields measured were dc or quasi dc, the method of measurement (moving the subject and averaging the field data into preselected distance intervals) gives an effective frequency bandwidth of 0.3 - 20 Hz (see section 2.3). Significant noise appears within this band due to aliasing of higher frequency sources; however much of this was eliminated by the use of low pass analogue filters as described in section 2.3.

The choice of sampling interval in the time domain was also found to be important. Empirical tests showed a

distinct minimum in background noise at a sampling rate of 200 Hz. The exact reason for this is not clear, although it may be due to the presence of an undetected noise source at some harmonic of that frequency. Triggering the data collection directly from the mains was also tried but with no detectable improvement in noise reduction.

All of the experimental work described here was carried out within 20 metres of an access road. Moving cars and other large ferromagnetic objects caused detectable magnetometer responses. Fortunately these transient disturbances were usually much larger than the expected signal and had a recognisably different shape. Records containing such disturbances were easily identified and were rejected. Procedures for filtering out noise transients were built into the computer code where appropriate (see section 2.3.3).

2.2.3 Subject noise

For experiments involving current through copper wires, possible artefacts due to the magnetic properties of the wire and its supports were avoided by using large currents (of the order of mA) with the magnetometer set to its lowest sensitivity (see table 2.1).

In the case of a human subject, disentangling a specific signal from the other magnetic fields generated within the body is potentially more problematic. In particular the heart produces large, varying magnetic fields. However, the distance of the lower leg from the heart, combined with the attenuation due to the gradiometer arrangement, renders its contribution insignificant in comparison with the expected signal.

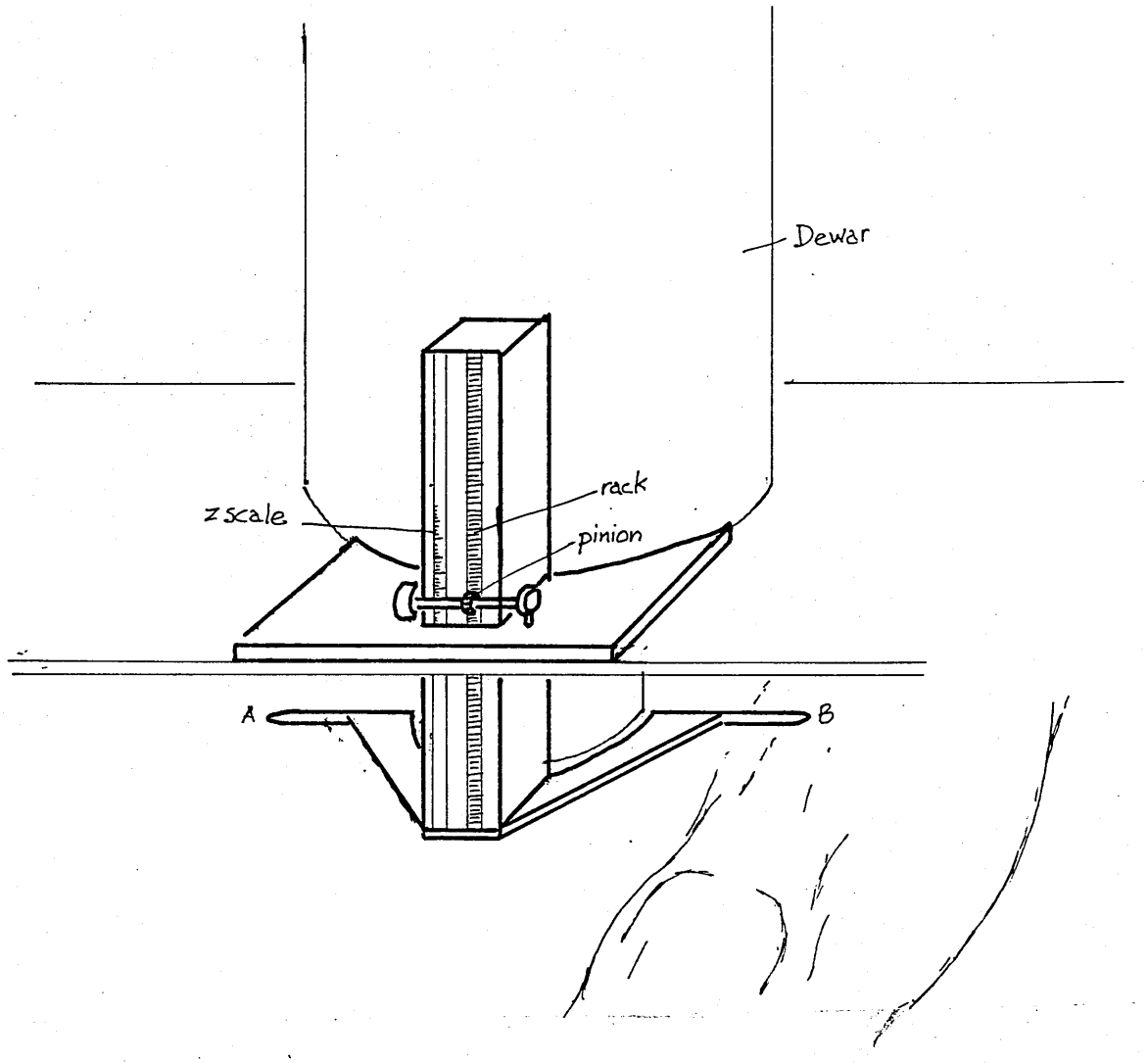

Figure 2.5 The location device used to determine the position of objects in the laboratory reference frame.

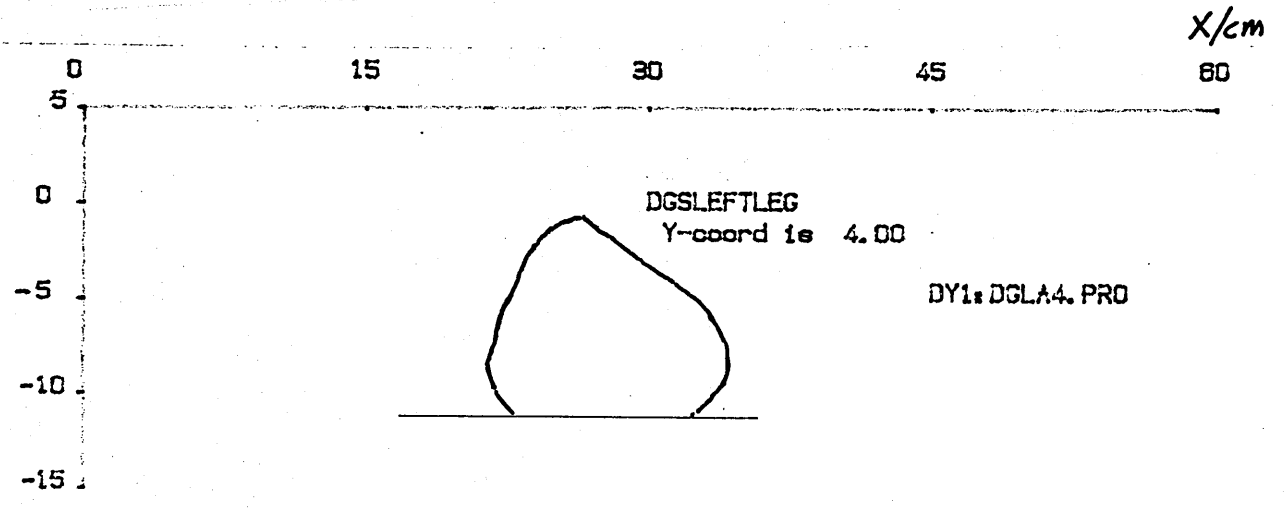

Figure 2.6 Leg profile obtained using the device in figure 2.5.

Of more concern in these experiments were the bulk magnetic properties of human tissue. The magnetic susceptibility of the tissue causes a distortion of the surrounding field. Movement of the subject in the earth's field produces flux changes at the sensing coils much larger than the expected signal.

The ambient field close to the gradiometer was greatly reduced by passing dc currents through the three orthogonal sets of Helmholtz coils. The current strengths were adjusted until all components of the ambient field, as measured by a fluxgate magnetometer placed directly below the dewar tail, were $< 10^{-8}$ Tesla.

The field produced by Helmholtz coils of this size is constant to within 10% inside a volume of 0.01m diameter. However the remainder of an extended structure (such as the human body) lying under the magnetometer will still be situated in a field of considerable strength. The overall signal at the magnetometer can be easily computed using the concept of the gradiometer 'lead field' as described by Tripp (1983). The lead field $\underset{\sim}{B}_L$ at a point may be thought of as the field produced at that point by unit current in the gradiometer coils. With this definition, the net flux through the gradiometer ensemble due to a volume element δv with susceptibility χ at position $\underset{\sim}{r}$ is given by:

$$\delta \Phi_r = \frac{\chi}{\mu} \underset{\sim}{B}_L(\underset{\sim}{r}) \cdot \underset{\sim}{B}_a(\underset{\sim}{r}) \delta v \qquad (2.3)$$

where $\underset{\sim}{B}_a(\underset{\sim}{r})$ is the ambient field at $\underset{\sim}{r}$.

The flux due to a body with susceptibility χ occupying volume V is then

$$\Phi = \frac{\chi}{\mu_0} \int \underset{\sim}{B}_1 \cdot \underset{\sim}{B}_a \, dv \qquad (2.4)$$

As a rough approximation of the effect of a human body lying along the y-axis of the Helmholtz coils under the conditions described above, I have carried out a computer simulation of the magnetometer response for a rectangular slab lying between x = ±0.30m, y = ±1.0m, z = ±0.05m with the origin of coordinates at the centre of symmetry of the Helmholtz arrangement. A value of $\chi = -9\times10^{-6}$ (the approximate, average susceptibility of human tissue) was used for the slab. Dimensions of gradiometer and coils were as in the actual laboratory arrangement and the centre of the gradiometer bottom coil was at (0,0,0.06)m.

The ambient field $\underset{\sim}{B}_a$ was set at $(0,5\times10^{-5},-5\times10^{-5})$Tesla and the Helmholtz coils adjusted to reduce the field at the origin to 0.1% of $\underset{\sim}{B}_a$. This is a factor of 5 greater than the actual maximum allowable ambient field amplitude mentioned above. Φ was computed via equation (2.4) at 10mm intervals and summed over the whole volume.

The simulated gradiometer signal calculated with these parameters was -14 fT. As might be expected, the dominant contribution comes from the volume closest to the sensing coils. In fact the gradiometer field from a cube of side 50mm directly below the gradiometer is -87 fT (This is greater than the overall response because the z component of field from the Amperian surface current of the remainder of the slab will be in the opposite direction to that from the section immediately beneath the gradiometer). This figure is well below the background noise level of 800 fT for an individual pass (section 2.2.4).

As an empirical check before experiments, a polystyrene beaker of diameter 50 mm and depth 100mm containing $CuSO_4$ was passed under the magnetometer as close to the bottom surface of the dewar as possible. For $CuSO_4$ $\chi = 8 \times 10^{-6}$, so that the net flux through the gradiometer should be an order of magnitude bigger than that for the human body or just below the background noise level. No signal was in fact observed for correctly adjusted Helmholtz coils. Hence it can be concluded that the Helmholtz coil arrangement is a satisfactory method of eliminating effects due to the bulk magnetic properties of human tissue.

2.2.4 Typical noise values

A typical noise spectrum for the magnetometer in our laboratory is shown in figure 2.7a. It can be seen that within the frequency band 0.3 to 50Hz,the spectrum is approximately flat at 80fT $Hz^{-1/2}$.

A typical background noise signal obtained by moving the bed (without subject) under the magnetometer is also shown. Fig 2.7b shows a single pass. The maximum noise amplitude is ~1 picotesla, corresponding to ~200fT $Hz^{-1/2}$ in a 20Hz bandwidth. Figure 2.7c shows a scan averaged over 5 passes. This reduces the noise amplitude to ~300fT (equivalent to 70fT $Hz^{-1/2}$).

2.3 Data collection

2.3.1 Data acquistion hardware

The SQUID output is connected to the standard SHE electronics module which gives a voltage output calibrated as described in section 2.1.2. The electronics module also

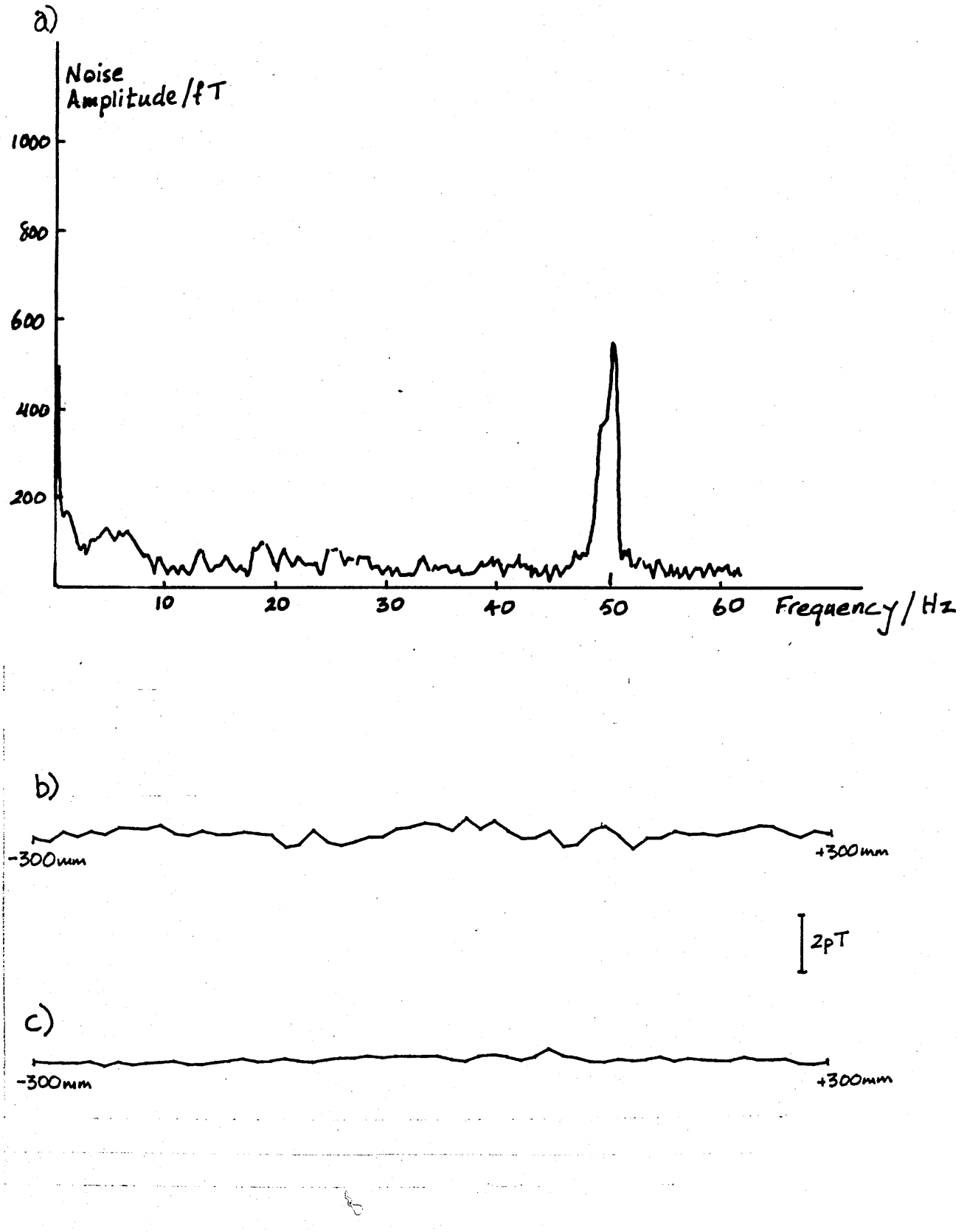

Figure 2.7a) Typical noise spectrum from magnetometer system b) Typical noise level for scan (1 pass, no subject). c) Typical noise level for scan (5 passes, no subject).

incorporates a notch filter set to 50Hz to suppress mains derived noise. In addition, for these experiments the output voltage was fed through two, in-series, low pass filters each with a 40Hz cut off. The filtered signal was then directed to the A/D input of a dedicated DEC MINC 11-03 minicomputer.

The MINC computer has 64k of RAM and 2 floppy disc drives capable of storing 0.5Mb each. The A/D converter distinguishes 4096 voltage levels between ±5.12V, giving a resolution of 2.5mV. An additional x3 amplifier built into the low-pass filter improved the effective resolution to 0.8mV (= 160fT measured at the bottom sensing coil).

Although the A/D converter can in principle accept data at sampling rates up to 10kHz, in practice the data acquisition rate was limited by software error checking to 400 Hz. For the reasons noted in section 2.2.1, the actual rate used was in fact 200Hz.

2.3.2 Data averaging

For the purposes of noise reduction it is desirable to average over as much data as possible. This can be carried out either spatially or temporally. Spatial averaging is appropriate in situations where data can be collected at a finer spatial resolution than the smallest significant detail in the signal. The criterion for temporal averaging is that the signal be reliably constant over the time necessary to collect several data samples from each data point.

The programs were designed to be used in various experimental situations and hence both options were built into the code. Within an individual pass, spatial averaging

was achieved by simultaneously collecting field and position data at the optimal rate (200Hz) and then averaging the field data over predetermined distance intervals. A time average of the signal could be obtained simply by repeating the pass an appropriate number of times.

For data from the human leg, a distance interval of 10mm with 3 passes per scan produced an acceptable spatial resolution while allowing the whole field map to be completed in about 15 minutes, over which time the leg signal did not alter appreciably.

The time taken to make an individual pass was approximately 3 seconds. The length of the scan (600mm) and the spatial averaging interval (10mm) then give an effective lower and upper frequency limit for the signal of 0.3 and 20Hz respectively. Thus the analogue low pass filters described above could be expected to produce negligible distortion of the signal.

2.3.3 Data collection programs

All programs were written in FORTRAN under an RT-11 operating system. Two main versions of the data collection program were produced entitled BEDWIZ and BEDZIP. Diagrams summarising the structure of these programs are presented in figure 2.8.

Program BEDWIZ operates in the following manner. Initial parameters relating to length of scan, number of passes per scan and size of averaging interval are input by the operator. The calibration of x and y potentiometers is performed by moving the bed to standard positions at which the computer reads the potentiometer voltages. During each

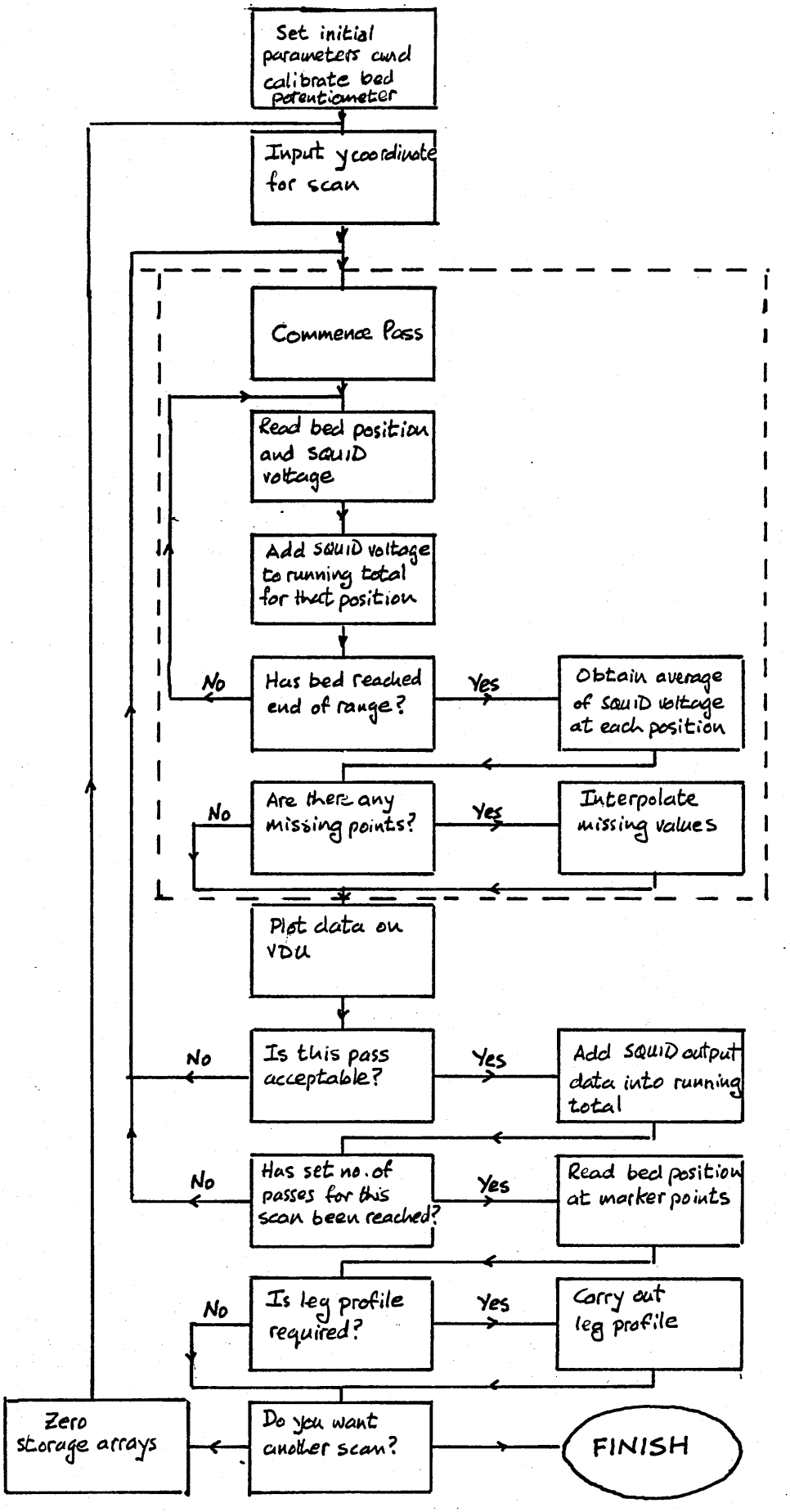

Figure 2.8a) Structure of data collection program BEDWIZ.

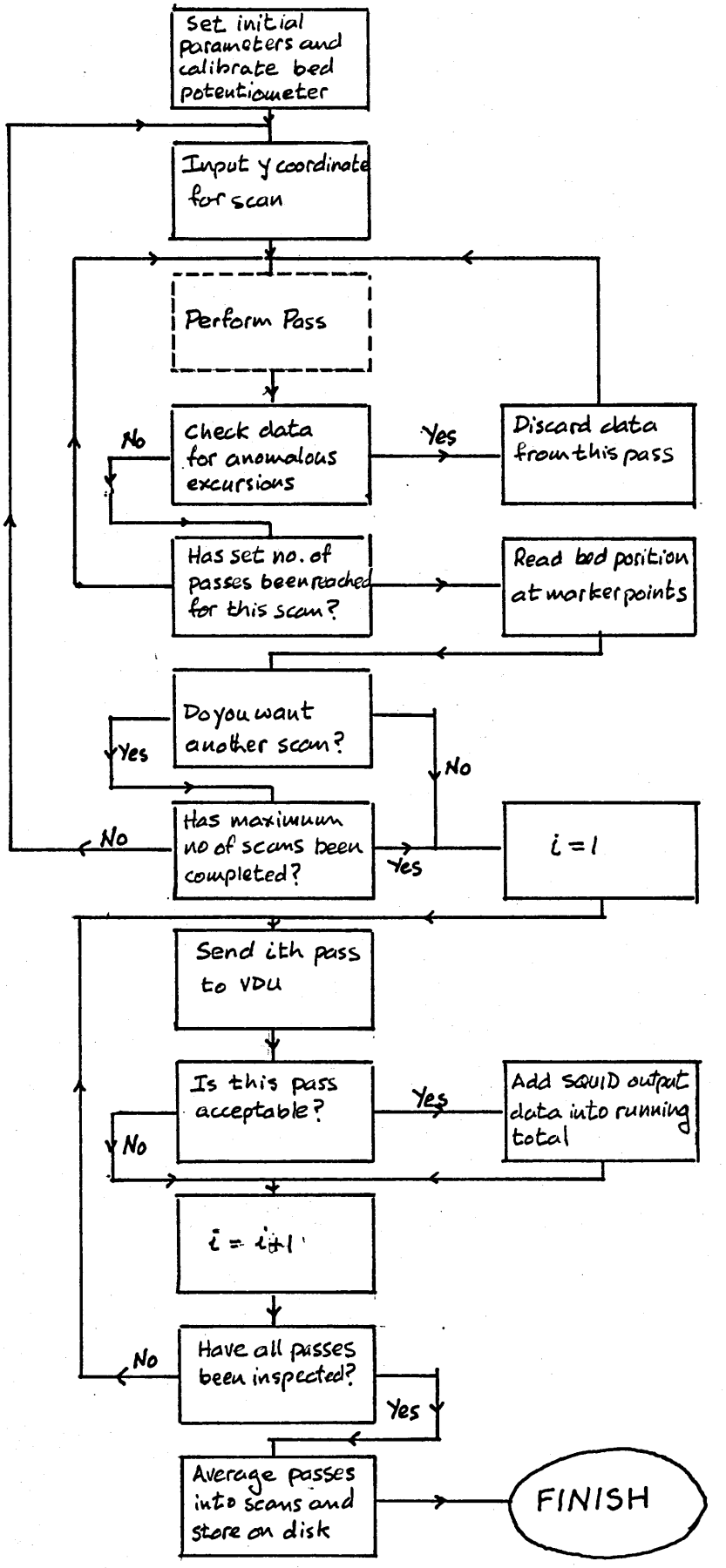

Figure 2.8b) Structure of data collection program BEDZIP. Dashed box contains same logic as dashed section in figure 2.8a

pass, position and field data are automatically sampled and the field data are averaged over the preset spatial interval.

A visual display of the data on the VDU then allows the operator to accept or reject the pass. This prevents unacceptably noisy passes or those containing transients from being included in the final average. Data from the requisite number of successful passes is averaged and reduced to zero mean to give a final data set at each y-position. Finally, at the end of the scan, a representative x-coordinate for the conducting body (e.g the position of the tibia in the case of leg measurements) is stored using the location device described in section 2.1.3. The corresponding z-coordinate is read in manually.

At this point a profile of the leg can also be stored, again as described in section 2.1.3 and figure 2.6. Finally the scan data, averaged over the appropriate number of passes is stored on disc and sent to an online digital plotter (Hewlett Packard HP7470A).

The interactive features of BEDWIZ are useful in that they allow operator intervention to reject noisy or dubious data. The disadvantage is that the intervention slows the data collection procedure. Program BEDZIP allows for situations in which the rapid collection of data is of greater importance than interactive checking. BEDZIP has the same structure as BEDWIZ but there is no visual display at the end of each pass. A trap within the code can be set to automatically reject signals above a given amplitude. This provides crude but effective discrimination against signals from passing cars and other moving magnetic objects. All passes are stored without averaging into scans until the

whole data map is complete. The passes can then be retrospectively examined by the operator to reject spurious signals. The drawback of this approach is that rejected passes cannot be repeated, so reducing the amount of averaging for that scan.

2.4 The magnetic field of the human leg

2.4.1 Anatomical leg position

In order to allow comparison of scans for subjects with different leg lengths, a relative scale was used for leg measurements assigning the value zero to the knee crease and 10 to the base of the heel as shown in figure 2.9.

2.4.2 Collection of leg data

A typical field map for the both legs of a healthy, normal subject is shown in figure 2.10. The field plots are superimposed on approximate leg outlines. The horizontal line through each scan is at the position of the appropriate y-coordinate (as defined above). It also marks the zero field position for that scan.

For reasons of comfort, most data were collected with the subject lying on his/her back, thus presenting the anterior aspect of the leg to the gradiometer. The position of the gradiometer could be adjusted between scans to allow the closest possible approach to the leg surface in each case.

In all anterior scans, the position of the crest of the tibia was recorded using the leg location device described in section 2.1.4. This could then be used as a reference position to relate the scan x-coordinates to the leg

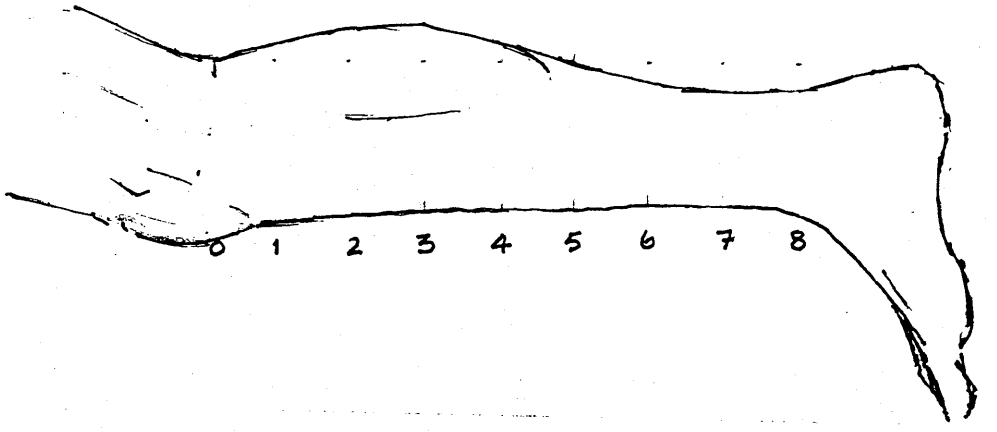

Figure 2.9 Anatomical scale for leg measurement.

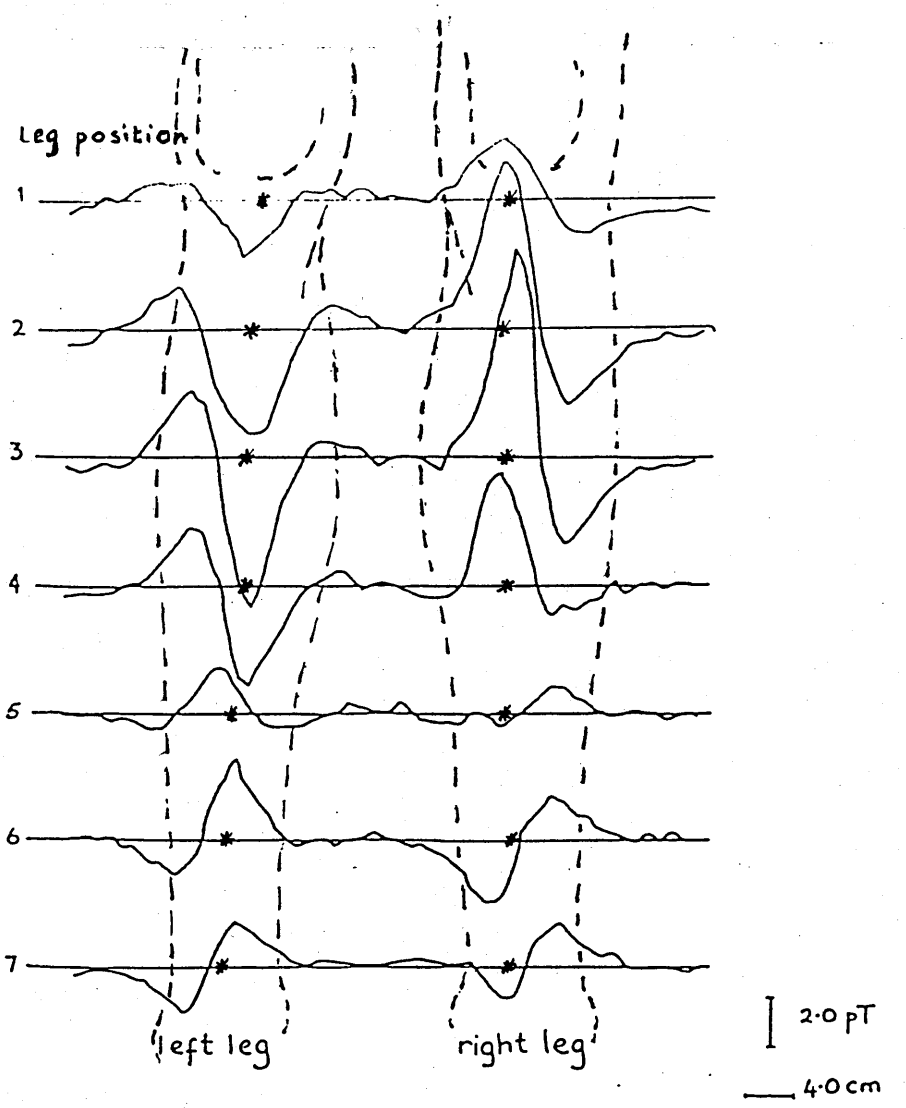

Figure 2.10 Set of gradiometer scans for subject JM.

anatomy. The tibial positions are indicated by the asterisks in figure 2.10. Although the location device could also be used to obtain a complete leg cross-section outline (section 2.1.4), this was not adopted as standard procedure as it was time consuming and led to patient discomfort.

In some cases, field maps were produced for all four aspects of the leg (anterior, medial, posterior and lateral surfaces being successively uppermost). The positioning of the subject for these scans is shown in figure 2.11.

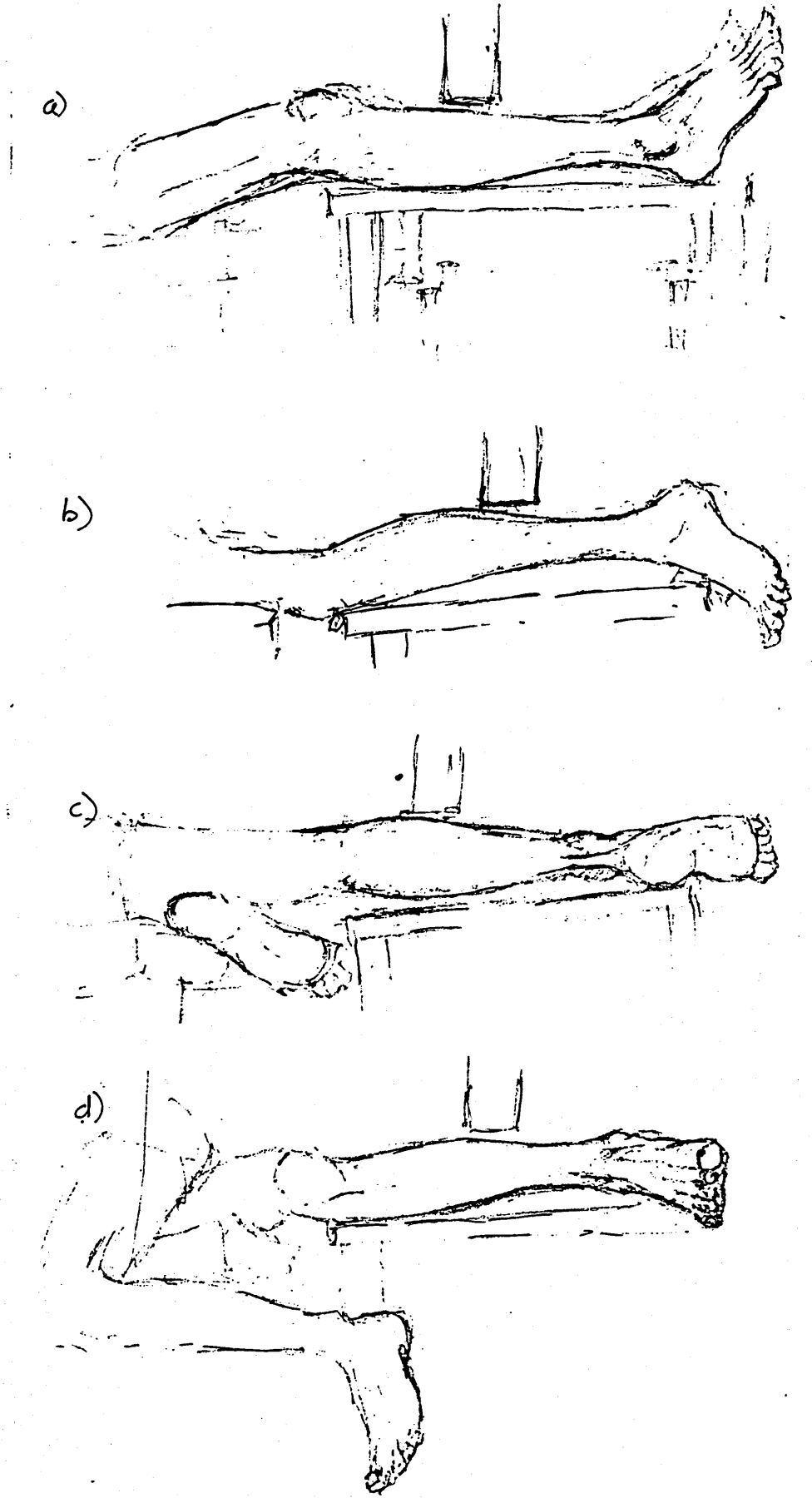

Figure 2.11 Position of subject's leg during scans **a)** anterior **b)** posterior **c)** lateral **d)** medial.

CHAPTER 3

METHODS OF MODELLING BIOMAGNETIC CURRENT SOURCES

3.1 The inverse problem

3.1.1 General approaches to inverse problem solving

The subject of physics is broadly concerned with developing mathematical models of physical systems. A mathematical model of a particular system will usually specify that system in terms of a finite number of parameters which can be related in some well defined way to a set of measurable quantities, the experimental data.

There are two kinds of calculation which can be performed with such a model. We may input values for the system parameters and attempt to compute a simulated set of experimental data. This is the '**forward problem**'. Alternatively we may input the experimental data and try to calculate the system parameters which give rise to them. This is the '**inverse problem**'. In most situations, the inverse problem is of more interest and its solution is of greater practical value. Unfortunately it is usually more difficult to solve.

Ideally one would wish a model to represent exactly the important features of the target system but this is not always possible. The data may be insufficient or an exact model may be too complex or contain too many parameters. One may circumvent this problem by recasting the model in a form which asks 'good' questions as defined by Sabatier (1985).

That is to say, the reformulated model should present an easily soluble inverse problem the solutions of which, while not necessarily providing an exact description of the physical system, nevertheless yield useful information about it. The multipole analysis described in section 3.8 provides an example of this approach.

A difficulty which frequently arises is that, even if the inverse problem is technically soluble, a large (perhaps infinite) number of possible solutions may exist. Here it may be possible to make use of other information about the system to reduce the set of possible solutions to a more manageable size. One may then hope to select a 'best' solution from the reduced set by applying some specified criterion.

3.1.2 The biomagnetic inverse problem

In the context of biomagnetism, the chosen model must relate experimental data consisting of a spatial map of the magnetic B-field integrated over a sensing coil ensemble (as described in chapter 2) to a set of parameters which describe the biological current sources. Such a model must be based on the general relationship between electric currents and magnetic fields defined by Maxwell's equations. This relationship is discussed in detail in section 3.2.

It is easy to show that the electromagnetic inverse problem does not have a unique solution. One only needs to consider the fact that current configurations exist which are magnetically silent (Helmholtz 1853, Sarvas 1987). Any combination of such configurations may be added to a particular solution for a given set of magnetic field data

thus giving rise to an infinite number of theoretically possible solutions.

In order to restrict the number of possible solutions, other information as to the likely nature of the source currents must be employed. Fortunately with biologically generated magnetic fields, it is often reasonable to approximate the source current distribution with a simple model specified by only a small number of parameters. In particular, models based on a current dipole are used by many workers in biomagnetism. Specific models of this type are reviewed in section 3.5.

Other constraints on possible solutions arise from a knowledge of the anatomy and physiology of the system in question. As a simple example, there is an upper limit to the current strength which can be supported by biological tissue without incurring severe damage. It is also self-evident that all currents must lie within the physical boundaries of the conducting body. These considerations and others can be used to reject physically improbable solutions. A 'best fit' solution may then be sought by applying standard minimisation techniques such as the method of least squares.

Although most biomagnetic modelling has been carried out using the models described in section 3.5, these techniques have not been found appropriate for the field in the vicinity of the human leg. Other methods have therefore been sought and these are outlined in section 3.4 and discussed in detail in chapters 4 to 8.

3.2 Electric currents and magnetic fields

The relationship between magnetic B-field $\underset{\sim}{B}$ and current density $\underset{\sim}{J}$ is defined by Maxwell's equation:

$$\nabla \times \underset{\sim}{B} = \mu\left(\underset{\sim}{J} + \varepsilon \frac{\partial \underset{\sim}{E}}{\partial t}\right) \qquad (3.1a)$$

where μ = magnetic permeability

ε = electric permittivity

$\underset{\sim}{J}$ = current density

$\underset{\sim}{E}$ = electric field

The second term on the right hand side of (3.1a) is the contribution to the magnetic field from a changing electric field. This so-called 'displacement current' is negligible in biological tissues for frequencies less than a few hundred Hz (Tripp, 1983) and, as I am considering quasi-dc conditions in this thesis, I will not consider it further. Thus for the present discussion it is sufficient to write:

$$\nabla \times \underset{\sim}{B} = \mu \underset{\sim}{J} \qquad (3.1b)$$

From this may be derived a further equation (Tripp, 1983):

$$\underset{\sim}{B}(\underset{\sim}{r}) = \frac{\mu}{4\pi} \int_{v'} \frac{\underset{\sim}{J}(\underset{\sim}{r}') \times \underset{\sim}{R}}{R^3} \, dv' \qquad (3.2)$$

where $\underset{\sim}{r}$ is the point of measurement of $\underset{\sim}{B}$ (the field point) relative to some origin O. $\underset{\sim}{r}'$ defines a position of current density $\underset{\sim}{J}$ and $\underset{\sim}{R} = \underset{\sim}{r} - \underset{\sim}{r}'$. v' is the volume containing the currents. The whole arrangement is shown in figure 3.1.

Equation (3.2) is of course the Biot-Savart law. It is of great importance here as it can be used to describe the magnetic field outside a conducting body in terms of the

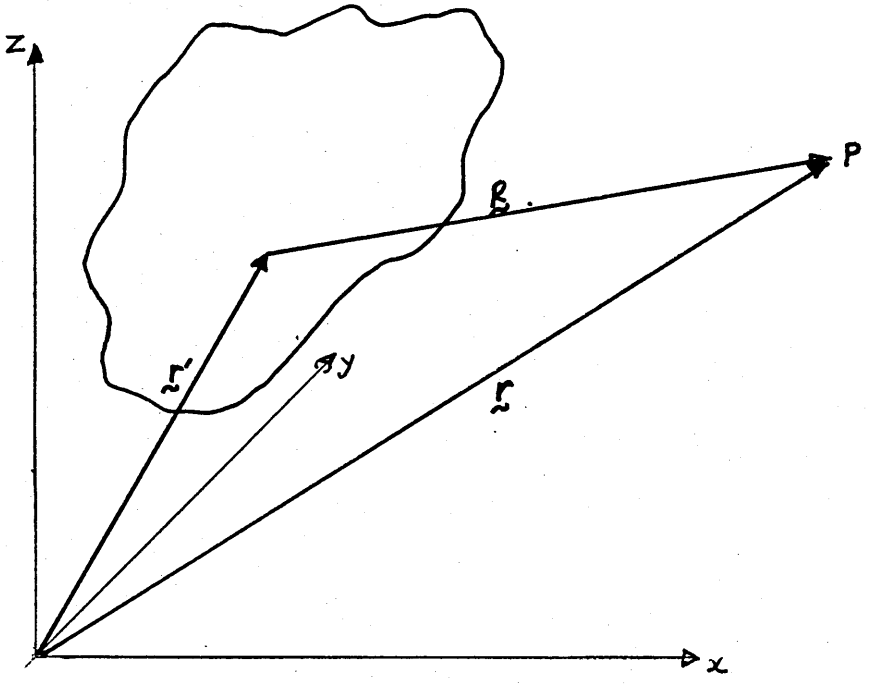

Figure 3.1 The coordinate system used in equation (3.2).

current distribution within. $\underset{\sim}{B}$ can be determined at any point provided the integral of $\underset{\sim}{J}$ over the volume can be performed. It thus defines the forward problem in biomagnetism.

3.3 The current dipole as a model of biological current sources

The biomagnetic inverse problem in general consists of inverting equation (3.2) and finding a distribution of $\underset{\sim}{J}(\underset{\sim}{r})$ which reproduces the experimental data. As discussed in the preceding section, there is no unique solution to the inversion of (3.2) and a simplifying model needs to be defined which restricts the number of possible solutions. The technique which has proved most useful in a variety of biological contexts has been to model the system as a **current dipole** or dipoles in a conducting volume of some simple geometry.

The current dipole can be thought of as an infinitessimal element of current with length and orientation defined by the vector $\underset{\sim}{\delta l}$ and with current strength I. The dipole is a current generator and the circuit is completed by the 'volume current' in the conducting medium (figure 3.2a). The strength of the dipole is characterised by the dipole moment $\underset{\sim}{Q}$ where

$$\underset{\sim}{Q} = I\,\underset{\sim}{\delta l} \qquad (3.3)$$

This model is particularly useful both because of its simplicity (the field due to a dipole is seen to be

$$\underset{\sim}{B}_D = \frac{\mu}{4\pi}\frac{\underset{\sim}{Q}\times\underset{\sim}{R}}{R^3} \qquad (3.4)$$

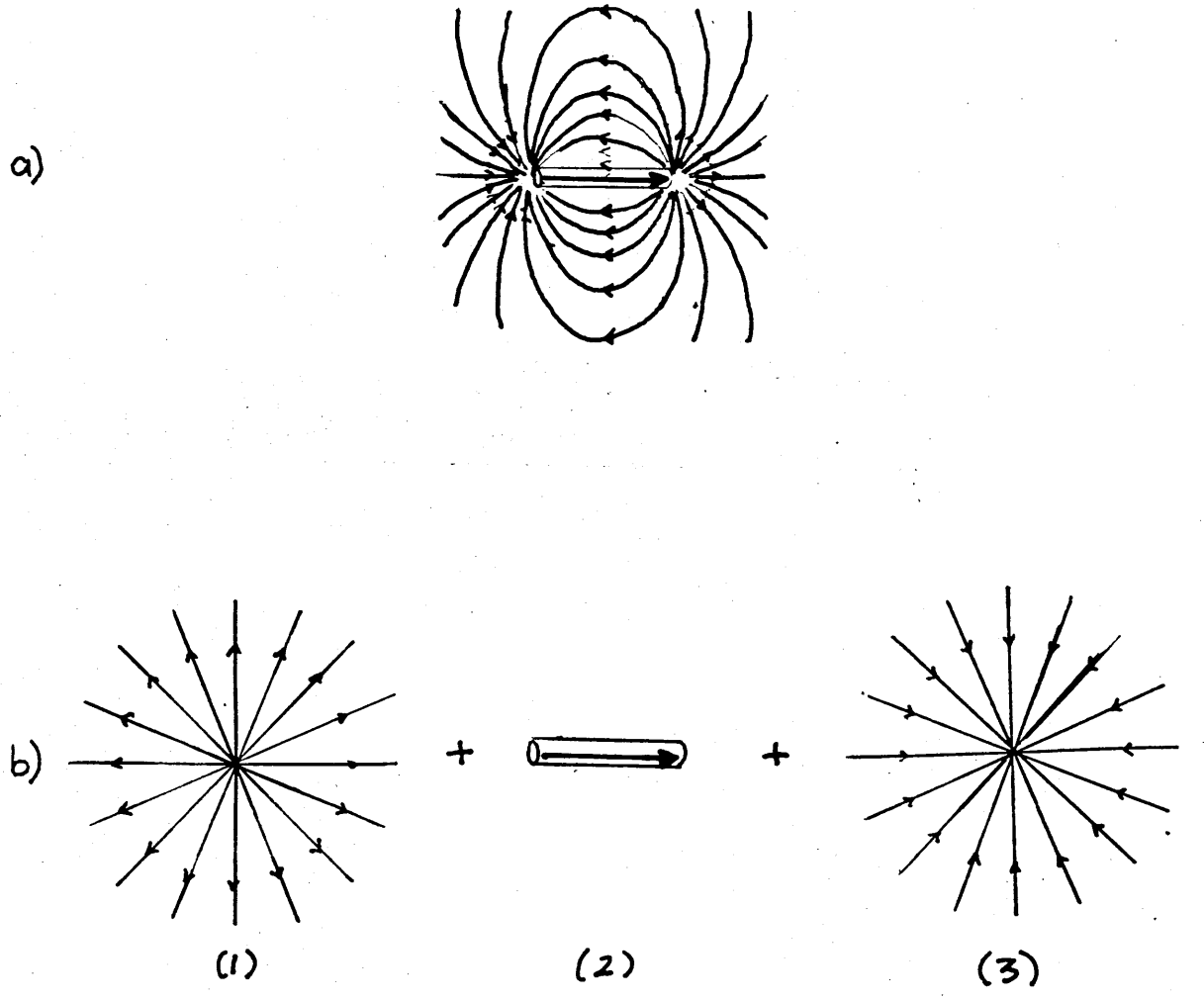

Figure 3.2a) Current dipole and return current streamlines in an infinite conducting medium. **b)** Decomposition of the currents in figure 3.2a into (1) a current source, (2) an isolated dipole, (3) a current sink.

from Biot Savart) and also because it is an accurate physical picture of many biological current sources. For example, the passage of an action potential along a nerve or muscle fibre may be represented by a pair of current dipoles (Tripp, 1983) and the electrical excitation of such fibres is the basis of all signals observed in magnetocardiography and magnetomyography. Similarly the intracellular currents which dominate the measured magnetic field of the brain have a strongly dipolar form (Okada, 1983).

Okada (1985) has also shown that even if the volume of excited tissue is of the order of 10mm in extent, the approximation of an infinitessimal dipole still gives an accurate localisation of the source.

3.4 The current dipole in an infinite conducting volume

Another important feature of the current dipole model is that, in conducting regions of particular geometry, the contribution of the volume current to the externally measured normal field component is zero. To arrive at this conclusion one first needs to consider a current dipole in an infinite conducting medium.

The streamlines of volume current in such a medium form the pattern shown in figure 3.2a. This pattern can be thought of as the sum of the (physically impossible) separate parts shown in figure 3.2b, namely a current dipole, a point source projecting current radially into the infinite medium and a point sink absorbing current in an identical manner. The two radial current patterns ((1) and

(3) in figure 3.2b) sum to give the total volume current. The magnetic B-field of both of these patterns is zero as may be shown by taking the curl of equation (3.1b) written for (3) in figure 3.2b, the source radiating outwards into the conducting volume.

$$\nabla\times\nabla\times\underset{\sim}{B}_s = \mu(\nabla\times\underset{\sim}{J}_s) \tag{3.5}$$

where the subscript 's' denotes quantities relating to the currents from the point source

Now

$$\nabla\times\nabla\times\underset{\sim}{B}_s = \nabla(\nabla\cdot\underset{\sim}{B}_s) - \nabla^2\underset{\sim}{B}_s \tag{3.6}$$

And

$$\nabla\cdot\underset{\sim}{B}_s = 0 \tag{3.7}$$

from Maxwell's equations.

Hence

$$\nabla^2\underset{\sim}{B}_s = -\mu(\nabla\times\underset{\sim}{J}_s) \tag{3.8}$$

which is a Poisson-type equation. The solution to this is:

$$\underset{\sim}{B}_s = \frac{\mu}{4\pi}\int_{V'}\frac{\nabla'\times\underset{\sim}{J}_s(\underset{\sim}{r}')}{R}\,dv' \tag{3.9}$$

where as before the prime denotes the position of current elements and $\underset{\sim}{R} = \underset{\sim}{r}-\underset{\sim}{r}'$.

Now

$$\underset{\sim}{J}_s(\underset{\sim}{r}') = \frac{S}{4\pi r'^3}\underset{\sim}{r}' \tag{3.10}$$

where S is the rate of flow of charge from the point source.

Hence

$$\nabla \times \underset{\sim}{J}_s = 0 \qquad (3.11)$$

everywhere. It follows that at all points

$$\underset{\sim}{B}_s = 0 \qquad (3.12)$$

The same arguments apply to the current sink in figure 3.2b, thus the volume current does not contribute to the field measured at $\underset{\sim}{r}$. Only the dipole itself has any effect and equation (3.4) exactly describes the situation whether the dipole exists in free space or in a conducting volume. It is worth noting that this conclusion does not depend on the dipole being of vanishingly small length. It is true whatever its size.

3.5 The dipole in finite conducting volumes

If discontinuities in conductivity are introduced into the volume conductor, the volume current pattern is altered so that, in general, it does contribute to the measured field. To show this, we can consider a finite conducting volume made up of a number of regions of different conductivities. Embedded within the conducting body is a distribution of current sources giving rise to a source current density $\underset{\sim}{J}_s(\underset{\sim}{r}')$. The arrangement is shown in figure 3.3. Geselowitz (1970) shows that in such a case the magnetic field measured in the region outside the conducting body is:

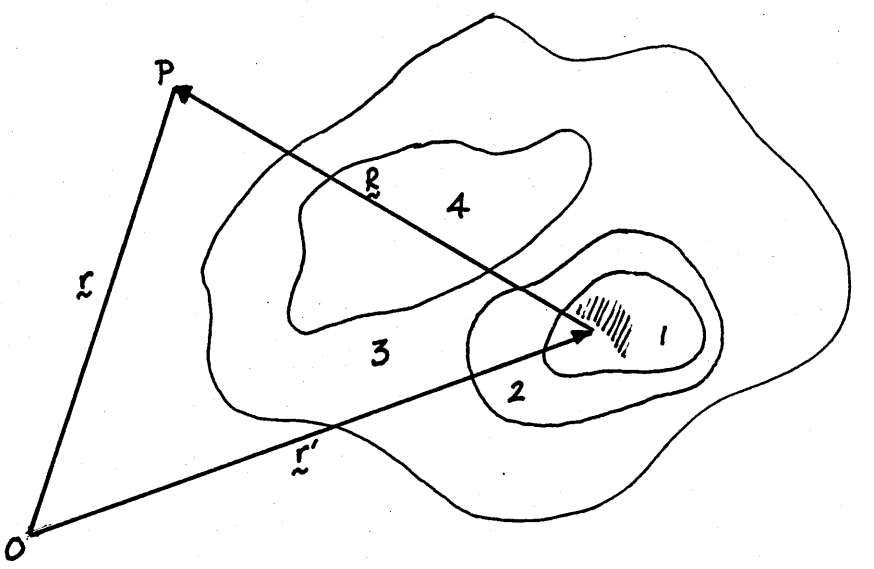

Figure 3.3 Current sources in regions of differing conductivities. Regions 1, 2, 3, 4 have conductivities σ_1, σ_2, σ_3, σ_4 respectively. Current sources are shown shaded.

$$\underset{\sim}{B}(\underset{\sim}{r}) = \frac{\mu}{4\pi}\left\{\int_{v'}\underset{\sim}{J}_s(\underset{\sim}{r}')\times\nabla\left(\frac{1}{R}\right)dv' + \sum_{(ij)}(\sigma_i-\sigma_j)\int_{S_{ij}}V_{ij}(\underset{\sim}{r}')\,\hat{\underset{\sim}{n}}_{ij}\times\nabla\left(\frac{1}{R}\right)dS_{ij}\right\} \qquad (3.13)$$

where S_{ij} represents the boundary between the ith and jth regions, $\hat{\underset{\sim}{n}}_{ij}$ is the unit vector normal to the surface S_{ij}, V_{ij} is the electric potential on the boundary S_{ij} and σ_i is the conductivity of the ith region.

The 1st term on the right hand side of equation (3.13) is the contribution from the current dipole source distribution exactly as for an infinite region of constant conductivity. The second term represents the field due to the volume currents.

Comparison of the two terms shows that the volume current contribution is equivalent to a distribution of dipole sources on the surfaces S_{ij}. The strength of these fictitious, secondary dipoles is determined by the potential on S_{ij} and the difference in conductivity between the regions, while their orientation is everywhere normal to S_{ij}. The field is calculated via the cross product of the normal vector $\hat{\underset{\sim}{n}}_{ij}$, so it will always be directed parallel to the local boundary surface. This leads to the conclusion that, if $\hat{\underset{\sim}{n}}_{ij}$ does not vary too rapidly the field component perpendicular to the conductivity boundaries will contain information only about the dipole sources and not their associated volume currents.

A second simplification in analysis can be introduced by noting the result of Grynszpan and Geselowitz (1973) showing that, for a volume conductor with axial symmetry, any dipole

located on and oriented along the axis will produce zero field outside the conductor. This is because the field from the dipole is everywhere exactly cancelled by the field from its associated volume currents.

I will illustrate the application of these results by considering a current dipole in 3 simple volume conductor geometries: the infinite half-space, the sphere and the cylinder.

3.5.1 The infinite conducting half space

Figure 3.4 shows a single dipole in an infinite conducting half-space. In the light of the preceding discussion, it is clear that, if the magnetic field is sampled perpendicular to the bounding surface S, only the effect of the dipole itself will be measured. The field of the volume current, being parallel to S, will be undetected.

Furthermore, any component of the dipole perpendicular to S will give rise to a field which is exactly cancelled by its own volume currents. Thus the measured data will contain information which relates solely to the component of the dipole source parallel to S.

3.5.2 The conducting sphere

Applying similar arguments to a dipole in a conducting sphere (figure 3.5), it may be deduced that the radial component of any dipole will be magnetically silent (the field being balanced by that due to its own volume currents). Additionally the volume currents arising from a dipole will not contribute to the externally measured radial field. Thus measurements of the radial field component will

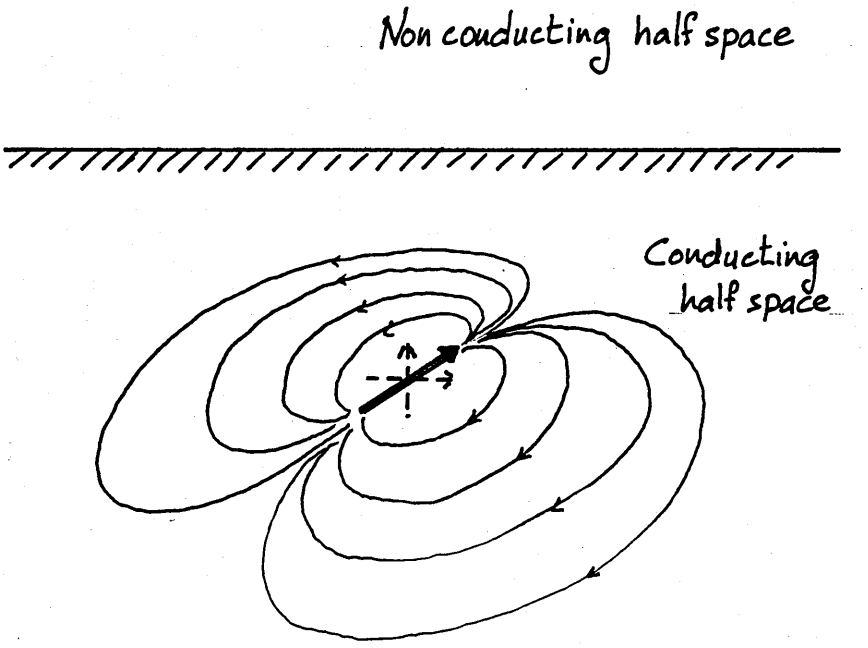

Figure 3.4 Current dipole in an infinite conducting half space. Components of the dipole parallel and perpendicular to the boundary are shown dashed.

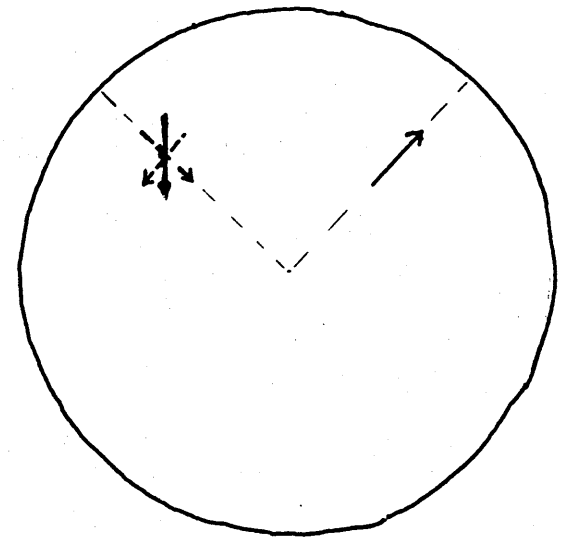

Figure 3.5 Current dipoles in a conducting sphere. Dipole (1) is radial; dipole (2) has both radial and tangential components (shown dashed).

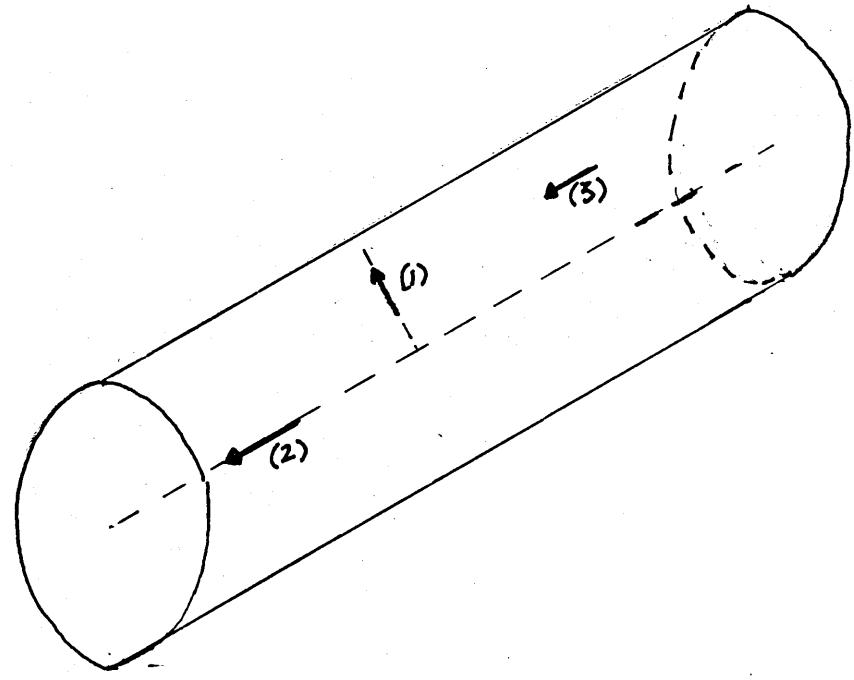

Figure 3.6 Current dipoles in a conducting cylinder. Dipole (1) is radial, dipole (2) is axial, dipole (3) is off-axial and non-radial. The radial field outside the cylinder will only register the effect of dipole (3).

register the effect of tangential dipole sources alone.

3.5.3 The conducting cylinder

For a cylindrical conductor, the symmetry is such that both axial and radial dipoles (such as (a) and (b) in figure 3.6) produce no field outside the cylinder. The radial B-field will thus be due to the non-axial and non-radial dipole components, their volume currents once again not contributing.

3.6 The inverse problem for single dipoles

The analysis presented in the previous section shows that field patterns due to current dipoles in conducting volumes of simple symmetrical shape are remarkably uncomplicated. This makes the solution of the inverse problem relatively easy to deal with. In all the cases described in section 3.5 the position, strength and orientation of a single dipole can be accurately determined from the map of the field component normal to the conductor's bounding surface.

For example Tripp (1983) shows that, in the case of an infinite half space, the depth of the dipole below the measurement plane is given by:

$$h = \frac{D}{\sqrt{2}} \qquad (3.14)$$

where D is the distance between extrema of the normal field component. The position of the dipole projected onto the plane of measurement is midway between the extrema and its orientation is perpendicular to a line joining the extrema (see figure 3.7). The dipole moment can then be

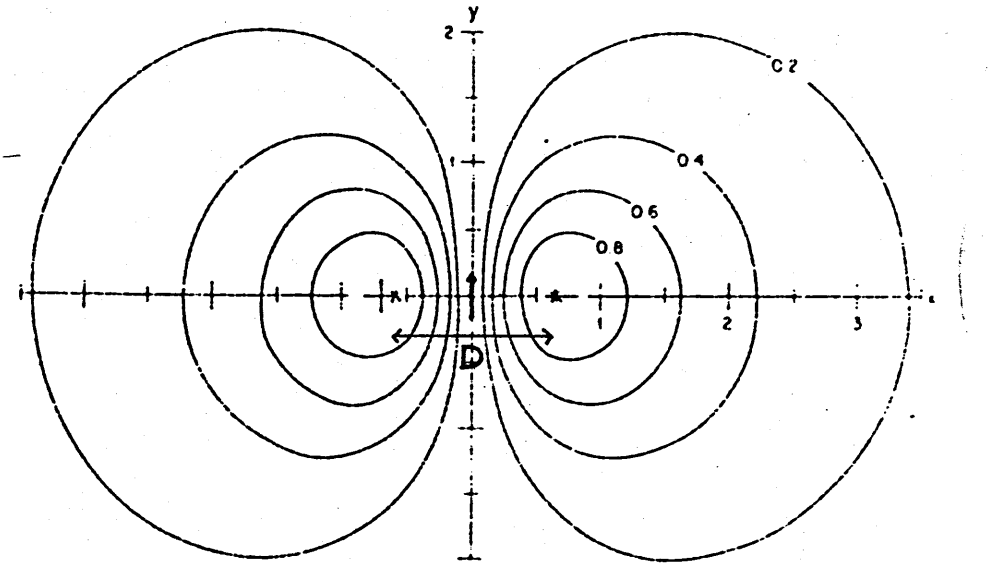

Figure 3.7 Determination of the location of a current dipole in a conducting half-space from a contour map of the normal component of the field in a plane parallel to the half-space boundary. The contour values are given as a fraction of the maximum field strength. (After Williamson and Kaufman, 1981, figure 12).

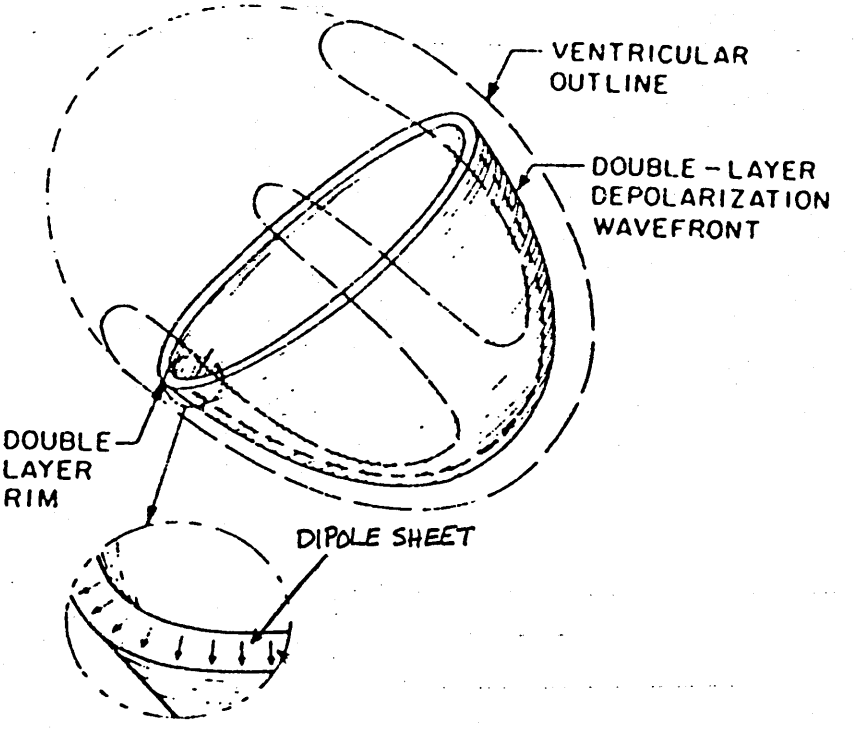

Figure 3.8 The spread of electrical activity in the heart represented by moving sheets of dipoles. (After Tripp, 1983, p111).

determined from the signal amplitude. Similar formulae can easily be derived for a dipole in a conducting cylinder or sphere (Williamson and Kaufman, 1981).

The convenience of these calculations has led to the widespread use of a 'dipole in a sphere' model for the interpretation of MEG signals. This model has proved extremely useful in cases where the following conditions are met:

(1) The conducting volume can be reasonably modelled as a sphere

(2) The experimental signals arise from a single, dipole-like source.

(3) The dipole source is approximately tangential to the surface of the model sphere.

Fortunately, these conditions are fulfilled in the case of many sources of cortical activity. Although the brain is by no means a sphere, cortical sources are sufficiently close to the brain surface that a local estimate of curvature can be used as the basis of a spherical model which provides accurate localisation (Romani, Williamson and Kaufmann, 1982).

For deeper sources or where local curvature changes rapidly more accurate geometries are needed. This has been attempted by several workers (Nicolas et al, 1985, Swithenby and Janday, 1987, Meijs and Peters, 1988). However the trade off is an increase in the complexity of the calculations and a loss of the simplifying assumptions associated with spherical symmetry.

The second proviso, that the magnetic field data arises predominantly from a single source, is true in several areas

of brain research. Evoked responses relating to visual, auditory and somatic stimuli have all been successfully modelled using the single dipole method. The calculated location of the model dipole shows good agreement with other information relating to the expected area of cortical activity (Williamson and Kaufman, 1981).

The fact that only tangential dipole components can be registered would appear to be a severe restriction. Fortunately, much important cortical activity takes place in fissures and sulci where the dendrites of pyramidal cells which approximate to dipole sources lie tangential to the cranial surface.

A single dipole in a conducting volume has also been used to model magnetic field data from the heart (Gonelli and Siavo, 1987). Notwithstanding the greater complexity of the signal, the dipole model still provides accurate localisation of the primary current source over much of the cardiac cycle, although the inclusion of higher order multipole terms improves the fit (Gonelli and Siavo, 1987).

3.7 The inverse problem for multiple dipoles

Many experimental field maps do not conform to the simple symmetry expected from a single dipole. However, attempting to build a model with more than one dipole, greatly complicates the fitting procedure. A system of n dipoles increases the number of equations to be solved by a factor of n. As the number of computational operations required to solve a system of n equations goes as n^3 (Davis, 1986), computing time escalates rapidly. Even then solutions may converge only weakly towards a fit (Weinberg et al, 1985).

Over the last few years, more attention has been given to solving the multiple dipole case. Chapman et al (1984) have used a 2 dipole model for the location of alpha rythm activity, although other workers have pointed out the problems of weak convergence for such models. Recently more novel strategies have been suggested such as the use of Bayesian parameter estimation (Sarvas et al, unpublished), data partitioning (Ioannides et al, 1987) and 'expert system' computing methods (Palfreyman and Ioannides, 1987).

As far as MCG data is concerned the situation is even more complex. The repolarisation and depolarisation wavefronts of the cardiac signal can be thought of in terms of sheets of dipoles as shown in figure 3.8 (Tripp, 1983). Cuffin and Cohen have developed analytical expressions for dipole sheets of simple geometry, however the morphology of the cardiac wavefront is considerably more complex than this. The most successful approach has been to characterise the signal in terms of a multipole expansion (described below).

3.8 Multipole methods

As discussed in section 3.1, if a physically realistic decription of a system is too complex to present a readily soluble inverse problem, it may be possible to reformulate the problem in terms of a simpler description which, while not as realistic, provides stable solutions and yields useful information.

An example of such an appropriate model is a multipole analysis based on small current elements. The first term in this analysis (the monopole) is an isolated current source

or sink. This, of course, would violate charge conservation, and so cannot exist. The 2nd order term, the current dipole, has already been discussed in detail in the preceding sections. Successively higher order terms are then the quadrupole (2 oppositely oriented dipoles separated by an infinitessimal distance) and the octupole (2 oppositely oriented quadrupoles with infinitessimal separation). Examples of these terms are shown in figure 3.9.

It is possible to show (Katila, 1983) that the magnetic field due to an arbitrary arrangement of current sources within a bounded, conducting volume can be simulated by a multipole expansion containing a series of terms as described above based at some origin O. The simulation is good for any point P outside a sphere centred on O containing all the source currents. Provided sufficient terms are included, any degree of accuracy can be achieved.

Such a multipole analysis is only of practical value if a good fit can be achieved with a reasonably small number of terms and if useful information (in a characterisation or diagnostic sense) is contained in the best fit model parameters. This is in fact the case for the MCG data. Katila et al (1987) have shown that dipole and quadrupole terms together provide a much better fit to cardiac data than a dipole alone.

An interesting feature of the multipole analysis is that it clearly shows up the difference between the information contained in electrical potential data and magnetic field data. The quadrupole tensor can be broken down into a symmetric and an antisymmetric component. Katila and Karp (1983) show that both components are present in the magnetic field data, whereas only the symmetric portion contributes

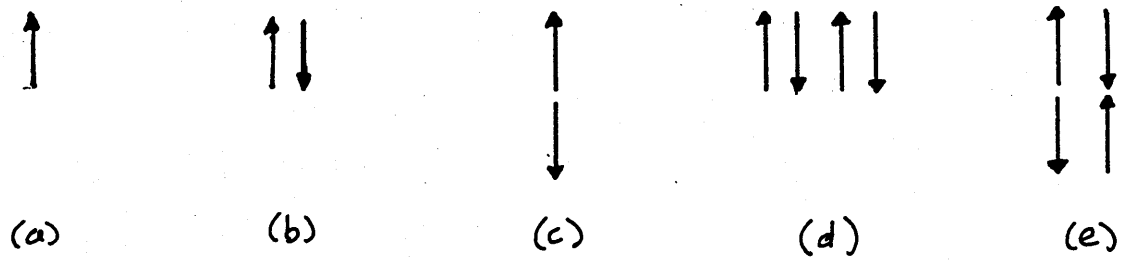

Figure 3.9 Examples of multipole terms based on infinitessimal current elements. **a)** dipole **b,c)** quadrupole **d,e)** octupole.

to the electric potential.

3.9 Modelling methods applicable to human leg data

The preceding discussion summarises the techniques used to model the magnetic fields due to ionic currents within the human body. It will be observed that they all assume infinitessimal current generators acting within a conducting volume. These models are useful because of their relative simplicity and because they closely approximate the reality of many physiological situations.

The data which form the subject of this thesis are somewhat different. The current pattern appears to extend over a considerable volume (the lower leg) and there is no evidence, either from inspection of the data or from consideration of the physiology, to suggest that there is a specific localised source for the current. Thus a model based on a single current dipole or a multipole expansion at a particular point does not seem suitable. The most likely sources for the current are either the bone (perhaps via some kind of piezoelectric effect or streaming potential as described in chapter 1) or the muscle. In both cases a physically realistic model would seem to suggest a large number of dipoles situated in a volume with a very complex conductivity structure. It is extremely doubtful whether useful solutions could be extracted from a model of such complexity.

A fundamentally different approach to the analysis of these data has therefore been adopted. Guided by the principles outlined in section 3.1.1, we have attempted to formulate models which pose 'good questions'. That is to

say that, although the models are not expected to provide a physiologically exact picture of the leg currents, they should generate useful information and be readily soluble. Two such models are described in the following chapters. They both provide a convenient system of characterisation of the leg signal and allow some conclusions to be drawn about the nature of the current sources.

The first method takes advantage of the fact that the variation of the signal along the leg axis is gradual. This, coupled with the rapid fall off in sensitivity of the gradiometer with distance, suggests that each scan may be treated independently and modelled by an axially uniform current pattern. Thus the problem is reduced to a 2-dimensional one. This approach is described in chapters 4 to 6.

The fit to the individual scans with this model is excellent, however its applicability is somewhat limited. Only currents parallel to the y-axis are considered and these must not change too rapidly with y. There is no requirement of current continuity from scan to scan and the centres of +y directed and -y directed current must not be too far apart. These points are discussed in more detail in the following chapters.

The second modelling approach is based on a line current loop. Here the fitting procedure involves using the whole field map to predict the shape and current strength of the 'best-fit' loop. The fit to the data is not quite as good as with the first method and the quality of data required to achieve a convergent solution is somewhat higher, however the best fit current configuration is 3-dimensional and satisfies current continuity. This model is described in

CHAPTER 4

THE THEORY OF THE LINE CURRENT DIPOLE MODEL

4.1 Justification of the line dipole model

As discussed in the preceding chapter, the slow variation of the leg signal in the y direction (figure 2.8) coupled with the discrimination of the gradiometer in favour of local sources suggests the possibility of modelling the signal at each leg position separately. As will be seen, this has the advantage of restricting the model to two dimensions, thus reducing the number of parameters needed to describe the source configuration and considerably simplifying the flux integration over the sensing coils.

As far as the choice of an appropriate model is concerned, Lennard (1984) has suggested that the measured leg signal is similar to the field produced by a pair of parallel line currents. This is illustrated in figure 4.1. A set of scans from position 3 of a typical, normal subject is shown in figure 4.1a. The leg was rotated by 90° between each scan so that in turn anterior, medial, posterior and lateral surfaces were presented to the gradiometer. The experimental procedure for obtaining the scans is described in section 2.4.

Figure 4.1b shows a computer simulation of a similar set of scans across a pair of infinitely long line currents of equal and opposite current strength running parallel to

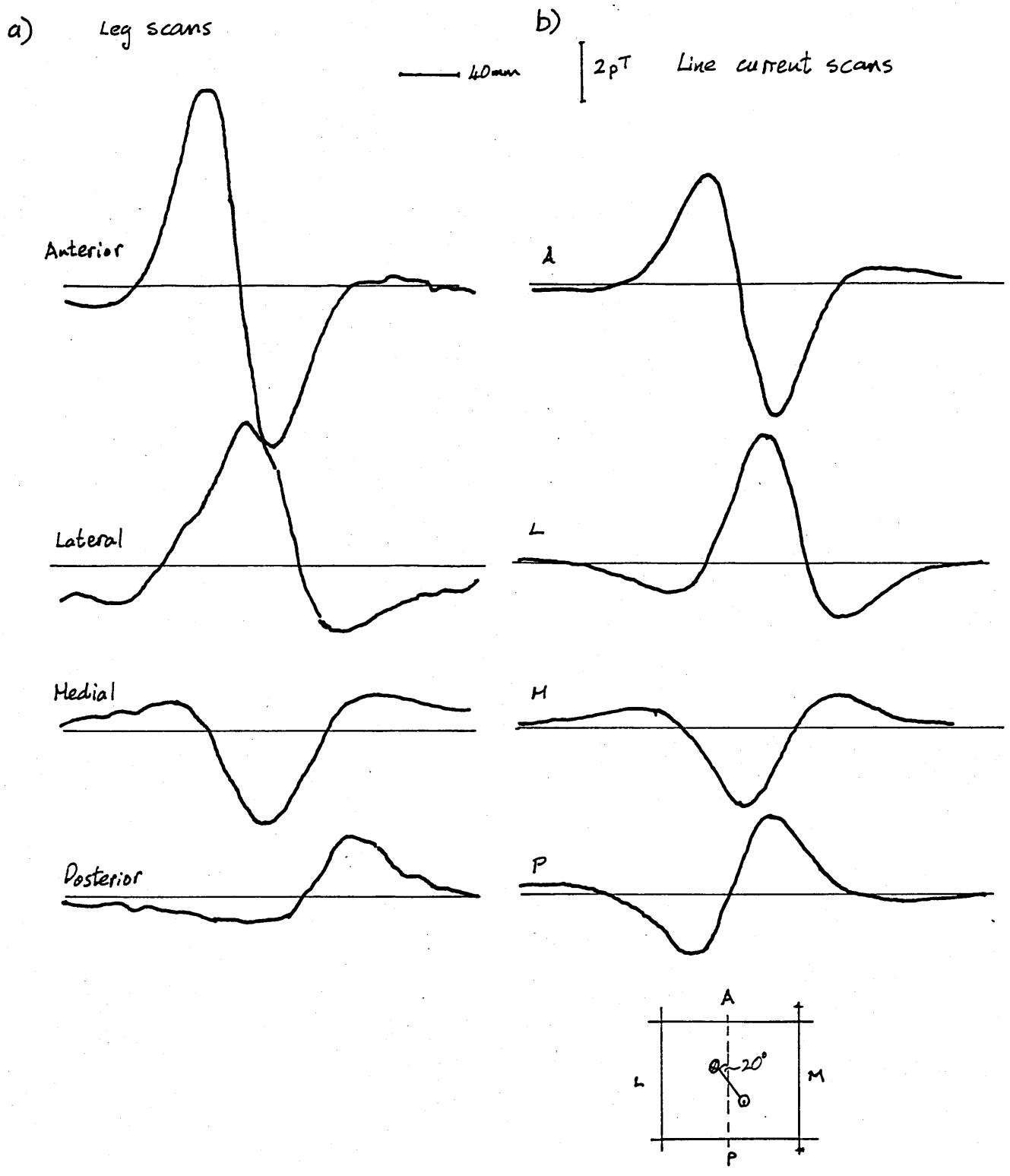

Figure 4.1 Comparison of anterior, lateral, medial and posterior scans of the human leg with 4 equivalent scans of a pair of antiparallel line currents. The approximate relation of the position of the scans to the line currents is shown inset.

the y-axis. The separation of the line currents is small compared to the distance between the currents and the scanning plane. As in figure 4.1a, the line currents have been rotated through 90° between each scan. The similarity between the two sets of scans suggests that a line current pair would indeed be a suitable model for the leg data. The parameters to be found would then be the current strength and x,z coordinates of each line current. The solution to the inverse problem expressed in this form is, however, only weakly convergent as an increase in current strength can be almost exactly compensated for by a decrease in separation between the currents.

To overcome this problem an alternative approach has been adopted. This involves describing the current system in terms of a multipole expansion for an axial current distribution. As mentioned in section 3.9, the idea is not necessarily to provide an exact replication of the current system. Rather we seek to develop a model which is simple enough to present a tractable inverse problem while still generating useful information about the source current structure.

Within this model, the pair of line currents described above, correspond to the dipole term of the expansion and the product of current strength and current separation appear as a single parameter, the dipole moment. Using the dipole term alone as a model requires the specification of only 4 parameters corresponding to the position, strength and orientation of the dipole.

This line current multipole expansion is described formally in the next section and the procedure for finding

the 'best fit' parameter values is discussed in section 4.3.

4.2 Line current multipole analysis

4.2.1 Description of the line current multipole expansion

Consider a current distribution as shown in figure 4.2. The current density vector $\underset{\sim}{J}(\underset{\sim}{r}')$ is always parallel to the y-axis and independent of y ($\underset{\sim}{J}(\underset{\sim}{r}') = J(\underset{\sim}{r}')\hat{\underset{\sim}{j}}$ and $\underset{\sim}{r}' = x'\hat{\underset{\sim}{i}} + z'\hat{\underset{\sim}{k}}$). J is any function of x',z'. I will show that the magnetic B-field measured at some position $\underset{\sim}{r}$ can be reproduced by a multipole expansion based on a line current infinite in extent and centred at some origin O. As with other multipole expansions the technique is only of value if an acceptable fit to the data can be accomplished with a small number of terms. In fact for the leg data it is possible to achieve such a fit with the dipole term alone.

The appropriate multipole expansion can be physically pictured as follows. The monopole term is a line current infinite in extent, parallel to the y-axis and passing through O. The higher order terms are then formed in the usual manner from the monopole. The dipole term consists of two equal but oppositely oriented monopoles separated by an infinitessimal displacement $\delta\underset{\sim}{l}_1$. The quadrupole is formed from two equal and opposite dipoles separated by $\delta\underset{\sim}{l}_2$ and so on. Examples of these physical representations are shown in figure 4.3. It should be noted that $\delta\underset{\sim}{l}_1$ is defined as pointing <u>from</u> the negative monopole <u>to</u> the positive monopole. $\delta\underset{\sim}{l}_2$, $\delta\underset{\sim}{l}_3$ etc are similarly defined.

In order to derive expressions for the magnetic B-field corresponding to the various multipole elements, it is

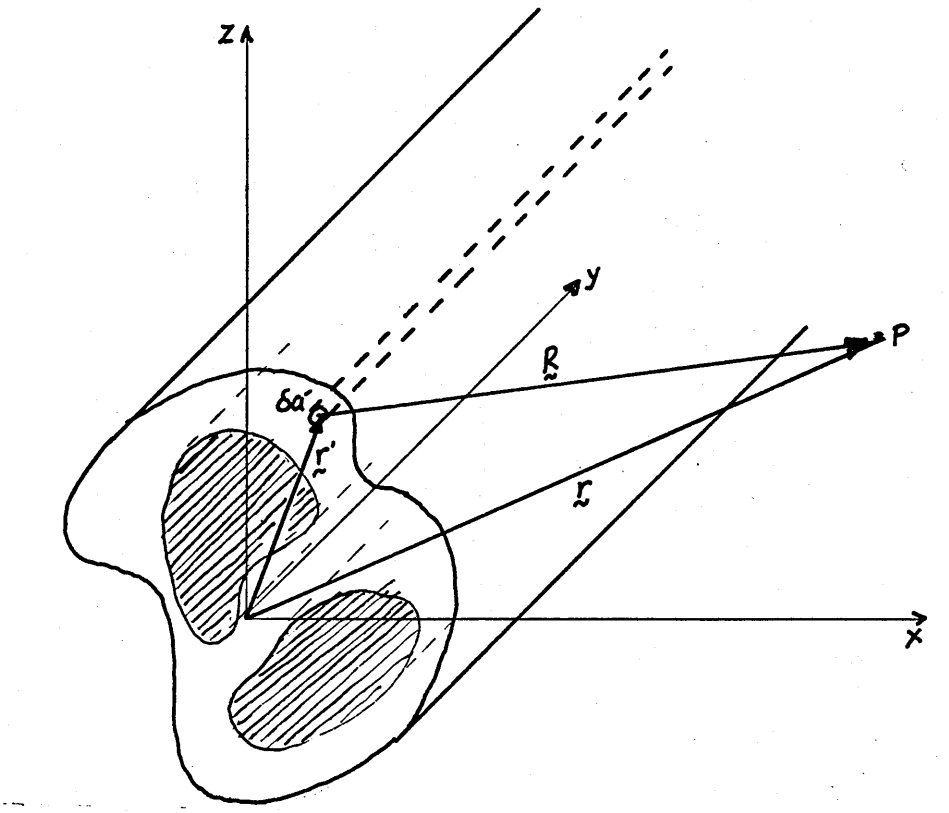

Figure 4.2 Axially uniform current distribution suitable for modelling with line multipole expansion. Shaded areas represent current in +y direction. Unshaded areas represent current in -y direction.

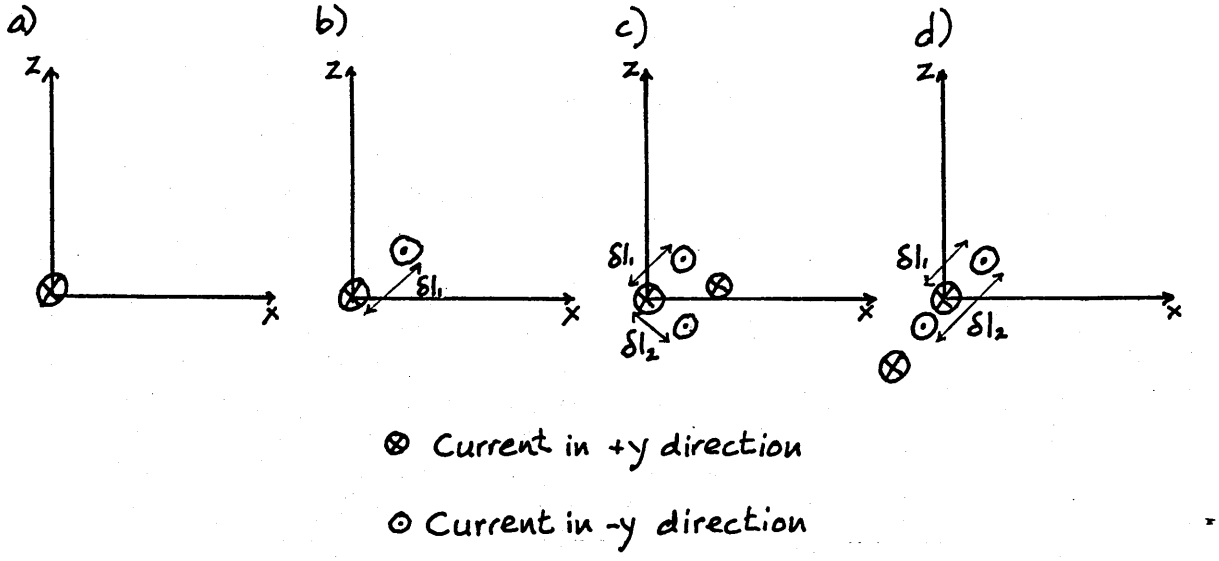

Figure 4.3 Examples of line multipole terms. a) monopole, b) dipole, c,d) quadrupole.

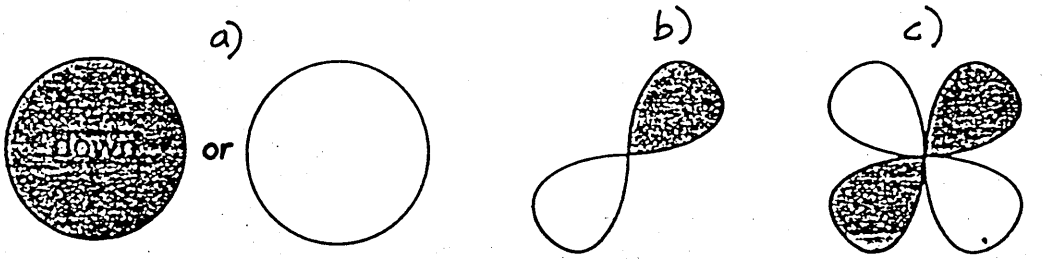

Figure 4.4 Alternative representation of line multipole terms a) monopole, b) dipole, c) quadrupole.
Shading indicates current in +y direction. No shading indicates current in -y direction.

easier to work with the vector potential $\underset{\sim}{A}$ and then obtain $\underset{\sim}{B}$ by the defining relationship:

$$\underset{\sim}{B} = \nabla \times \underset{\sim}{A} \qquad (4.1)$$

As the B-field for currents parallel to the y-axis will only have x,z components, it is possible to construct an appropriate vector potential function which satisfies (4.1) in which only the y-component is non-zero.

Thus:

$$\underset{\sim}{A}_n(\underset{\sim}{r}) = A_n(\underset{\sim}{r})\hat{j} \qquad (4.2)$$

where $\underset{\sim}{A}_n(\underset{\sim}{r})$ is the vector potential of the nth order multipole at field point $\underset{\sim}{r}$.

If the monopole term has magnitude $A_0(\underset{\sim}{r})$, then, from fiqure 4.3, the dipole term can be written as:

$$A_1(\underset{\sim}{r}) = A_0(\underset{\sim}{r}) - A_0(\underset{\sim}{r} + \underset{\sim}{\delta l_1})$$

$$A_1(\underset{\sim}{r}) = (-\underset{\sim}{\delta l_1} \cdot \nabla) A_0(\underset{\sim}{r}) \qquad (4.3a)$$

Similarly, the quadrupole term can be expressed in the form:

$$A_2(\underset{\sim}{r}) = (-\underset{\sim}{\delta l_2} \cdot \nabla)(-\underset{\sim}{\delta l_1} \cdot \nabla) A_0(\underset{\sim}{r}) \qquad (4.3b)$$

and in general the vector potential of the nth order multipole is:

$$A_n(\underset{\sim}{r}) = (-\delta l_n \cdot \nabla) \cdots (-\delta l_2 \cdot \nabla)(-\delta l_1 \cdot \nabla) A_0(\underset{\sim}{r}) \qquad (4.3c)$$

As this model deals for the most part with the dipole term, it will be useful to derive an expression for $A_1(r)$ explicitly. Working from equation (4.3b) we first need to evaluate the monopole term $A_0(r)$.

The monopole term is in fact a line current so:

$$A_0(\underset{\sim}{r}) = -\frac{\mu I}{2\pi} \int_{-\infty}^{\infty} \frac{dy}{r} \qquad (4.4)$$

where I is the current strength (Lorrain and Corson, 1979). Performing the integration:

$$A_0(\underset{\sim}{r}) = -\frac{\mu I}{2\pi} \ln(r) \qquad (4.5)$$

The dipole vector potential $A_1(\underset{\sim}{r})$ can now be calculated from equations (4.3a) and (4.5).

$$A_1(\underset{\sim}{r}) = -\frac{\mu I}{2\pi} (-\delta \underset{\sim}{l}_1 \cdot \nabla) \ln(r)$$

$$= \frac{\mu I}{2\pi} \frac{\delta \underset{\sim}{l}_1 \cdot \underset{\sim}{r}}{r^2}$$

Defining the dipole moment m as:

$$\underset{\sim}{m} = I \delta \underset{\sim}{l}_1 \qquad (4.6)$$

gives:

$$\delta A(\underset{\sim}{r}) = \frac{-\mu}{2\pi} \frac{\underset{\sim}{m} \cdot \underset{\sim}{r}}{r^2} \qquad (4.7)$$

4.2.2 The multipole expansion for an arbitrary current distribution

I will now show that the vector potential of the arbitrary current distribution shown in figure 4.2 can be written in terms of the multipole elements defined above.

Consider an element of area $\delta a'$ at position $\underset{\sim}{r}'$. The current through $\delta a'$ is $J(\underset{\sim}{r}')\delta a'$ and its contribution to the vector potential at field point $\underset{\sim}{r}$ is:

$$\delta A(\underset{\sim}{r},\underset{\sim}{r}') = -\frac{\mu}{2\pi} J(r')\,\delta a' \ln(R) \qquad (4.8)$$

where $\underset{\sim}{R} = \underset{\sim}{r} - \underset{\sim}{r}'$

Equation (4.8) can be expanded as a McLaurin series.

$$\delta A(\underset{\sim}{r},\underset{\sim}{r}') = \left(1 + (-\underset{\sim}{r}'\cdot\nabla_r) + \frac{(-\underset{\sim}{r}'\cdot\nabla_r)^2}{2!} + \cdots\right)\delta A(\underset{\sim}{r},0) \qquad (4.9)$$

Integrating over area a' gives:

$$A(\underset{\sim}{r}) = -\frac{\mu}{2\pi}\int_{a'} da'\left(1 + (-\underset{\sim}{r}'\cdot\nabla_r) + \frac{(-\underset{\sim}{r}'\cdot\nabla_r)^2}{2!} + \cdots\right) J(\underset{\sim}{r}')\ln(r) \qquad (4.10)$$

The terms in this expansion can be seen to be of the same form as the multipole elements defined in equations (4.3).

The 1st term is:

$$A_o(\underset{\sim}{r}) = -\frac{\mu}{2\pi} I \ln(r) \qquad (4.11)$$

where

$$I = \int_{a'} da' J(\underset{\sim}{r}') \tag{4.12}$$

Thus the 1st term represents the field which would be produced if all the current passed through the multipole origin.

The 2nd term is:

$$A_1(\underset{\sim}{r}) = \frac{\mu}{2\pi} \int_{a'} da' J(\underset{\sim}{r}') (\underset{\sim}{r}' \cdot \nabla_r) \ln(\underset{\sim}{r}) \tag{4.13}$$

which is identical to equation (4.7) provided we take

$$\underset{\sim}{m} = \int_{a'} da' J(\underset{\sim}{r}') \underset{\sim}{r}' \tag{4.14}$$

Equation (4.14) will be used as the definition of the line dipole moment or line dipole strength.

In similar fashion, higher order terms in the expansion can be shown to be equivalent to higher order multipole elements.

Thus the vector potential of an arbitrary current density distribution may be reproduced by a suitably chosen set of multipole elements located at the origin. The B-field of the multipole elements may be found via equation (4.1). Again we are mainly interested in the dipole term, so taking the curl of $A_1(\underset{\sim}{r})\hat{\jmath}$

$$\underset{\sim}{B}_1(\underset{\sim}{r}) = \frac{\mu_0}{2\pi r^4} (r^2 \underset{\sim}{m} - 2\underset{\sim}{r}(\underset{\sim}{m} \cdot \underset{\sim}{r})) \times \hat{\jmath} \tag{4.15}$$

Two points about the expansion are worthy of note.

Firstly $\underset{\sim}{B}_0(\underset{\sim}{r})$ falls off as 1/r and $\underset{\sim}{B}_1(\underset{\sim}{r})$ falls off as r'/r^2. In general $\underset{\sim}{B}_n(\underset{\sim}{r})$ falls off as r'^n/r^{n+1}. From D'Alambert's rule it follows that the series is only necessarily convergent provided $r > r'$. That is the model is only strictly applicable provided the field point is farther from the origin than any region of non-zero current density. This point will be discussed further in chapter 5.

The second point is that the physical representation of the multipole elements used in figure 4.3 is not unique. In particular, a cylinder coaxial with the y-axis and with a radially symmetric current distribution is a pure monopole provided $r' < r$ (figure 4.4a) and, similarly, an axially uniform distribution with the cross-section shown in figure 4.4b is a pure dipole. A pure quadrupole cross-section is shown in figure 4.4c. While bearing in mind this alternative physical description of the multipole elements, I will continue to refer to line dipole, line quadrupole etc. in order to distinguish these concepts from the elemental current multipoles used by many workers in biomagnetism and discussed in chapter 3.

4.3 The line dipole inverse problem

4.3.1 Formulation of the inverse problem

With regard to the relationship between the axial currents in the leg and their associated magnetic fields, the multipole expansion as defined above constitutes a description of the forward problem. To solve the inverse problem, we need to be able to calculate the best fit multipole parameters from the field data.

Charge conservation requires that the monopole term is zero. The similarity between the leg data and the field from a pair of line currents (see section 4.1) suggests fitting with the dipole term alone. This involves the determination of 4 parameters: the dipole strength m, its location in 2 dimensions (x_1,z_1) and its orientation ϕ. The information is most conveniently represented by the '**line dipole vector**' as shown in figure 4.5a. The centre of the vector arrow is the x,z location of the dipole. The length of the arrow is proportional to the dipole strength m (and not the separation between currents which may be infinitessimal). The 'centre of gravity' of current in the +y direction is in the region towards the head of the arrow and the 'centre of gravity' of current in the -y direction is in the region towards the tail of the arrow.

Of these 4 parameters, it is possible to show that best fit estimates for two (m,ϕ) can be found analytically leaving the location (x_1,z_1) to be found by numerical methods. The fitting procedure outlined below follows that in Grimes et al (1985) and is based on a general approach to a class of inverse problems described by Smith (1985).

4.3.2 The simulated gradiometer signal from a line dipole

Equation (4.15) gives the magnetic B-field for a line dipole located at the origin of coordinates. This equation needs to be adapted to fit the experimental situation in which we measure the vertical field component B_z averaged over the sensing coils for a dipole located at (x_1,z_1). This is shown in figure 4.5a. Now B_{1z} for a line dipole at this location is:

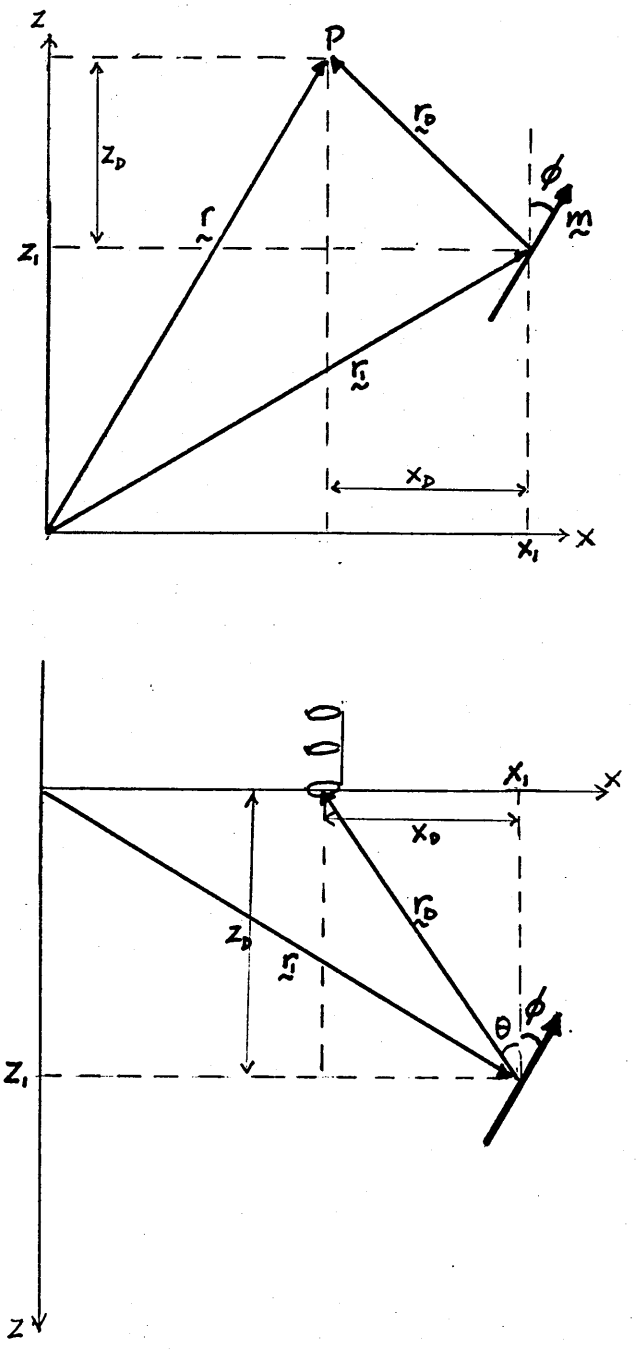

Figure 4.5a) Parameters specifying line dipole.
b) coordinate system used in line dipole location.

$$B_{1z} = \frac{\mu}{2\pi r_D^4}\left[r_D^2 \underset{\sim}{m} - 2\underset{\sim}{r_D}(\underset{\sim}{m}\cdot\underset{\sim}{r_D}) \times \hat{\underset{\sim}{j}} \right]\cdot\hat{\underset{\sim}{k}}$$

$$= \frac{\mu}{2\pi r_D^4}\left[r_D^2 \underset{\sim}{m} - 2(\underset{\sim}{m}\cdot\underset{\sim}{r_D})\underset{\sim}{r_D} \right]\cdot\hat{\underset{\sim}{i}} \qquad (4.16)$$

where $\underset{\sim}{r_D} = (x_D, z_D) = \underset{\sim}{r} - \underset{\sim}{r_1}$

and $\underset{\sim}{r_1} = (x_1, z_1)$

The dependence on the dipole parameters m, ϕ, x_1, z_1 can be written explicitly using the notation of figure 4.5a.

$$\left.\begin{aligned} \hat{\underset{\sim}{i}}\cdot\underset{\sim}{m} &= m\sin\phi \\ \hat{\underset{\sim}{i}}\cdot\underset{\sim}{r_D} &= x_D \\ \underset{\sim}{m}\cdot\underset{\sim}{r_D} &= m r_D \cos(\theta-\phi) \\ &= m(z_D\cos\phi + x_D\sin\phi) \end{aligned}\right\} \qquad (4.17)$$

Substituting in (4.16) gives:

$$B_{1z} = \frac{m\mu}{2\pi}\left[\frac{(z_D^2 - x_D^2)\sin\phi - 2x_D z_D\cos\phi}{(x_D^2 + z_D^2)}\right] \qquad (4.18)$$

Now this expression for B_{1z} must be integrated over the sensing coils to give the total flux. Combining equations (4.18) and (2.2) and assuming all coils are circular with radius c and common axis in the z direction we get an expression for the gradiometer signal S_1:

$$S_1 = \frac{1}{\pi c^2}\frac{m\mu}{2\pi}\sum_{i=1}^{n} k_i \iint_{\text{coil ensemble}} dx\,dy \left(\frac{(z_D^2 - x_D^2)\sin\phi - 2x_D z_i\cos\phi}{(x_D^2 + z_D^2)}\right) \qquad (4.19)$$

where n = no. of sensing coils

k_i is a calibration factor relating the flux through the ith detection coil to magnetometer output

z_{Di} = height of ith coil above the dipole

For the gradiometer used in our experiments

$n = 3$

$k_1 = k_3 = k$; $k_2 = -2k$

where k is a constant

$z_{D2} = z_{D1}+d$

$z_{D3} = z_{D1}+2d$

where d is the intercoil separation.

The double integral in equation (4.19) is not soluble analytically. However it can be reduced to a single integration by noting that B_z is independent of y. If the coil area is divided into a series of strips of width dx parallel to the y axis (as in figure 4.6.), the flux through each strip is simply $B_z h dx$. The total flux through the coil is then $\int_{-c}^{c} hB_z dx$ where h is the strip length. Equation (4.19) then becomes:

$$S_1 = \frac{1}{\pi C^2}\frac{m\mu_0}{2\pi}\sum_{i=1}^{n} k_i \int_{-c}^{c} h\left\{\frac{(Z_{Di}^2-(s+X_D)^2)}{(X_D^2+Z_{Di}^2)}\sin\phi - 2\frac{(s+X_D)Z_{Di}}{(X_D^2+Z_{Di}^2)}\cos\phi\right\} ds \qquad (4.20)$$

where x_D defines the x-coordinate of the geometric centre of the coil and s is used as the integration variable.

With this notation $h = 2\sqrt{c^2-s^2}$.

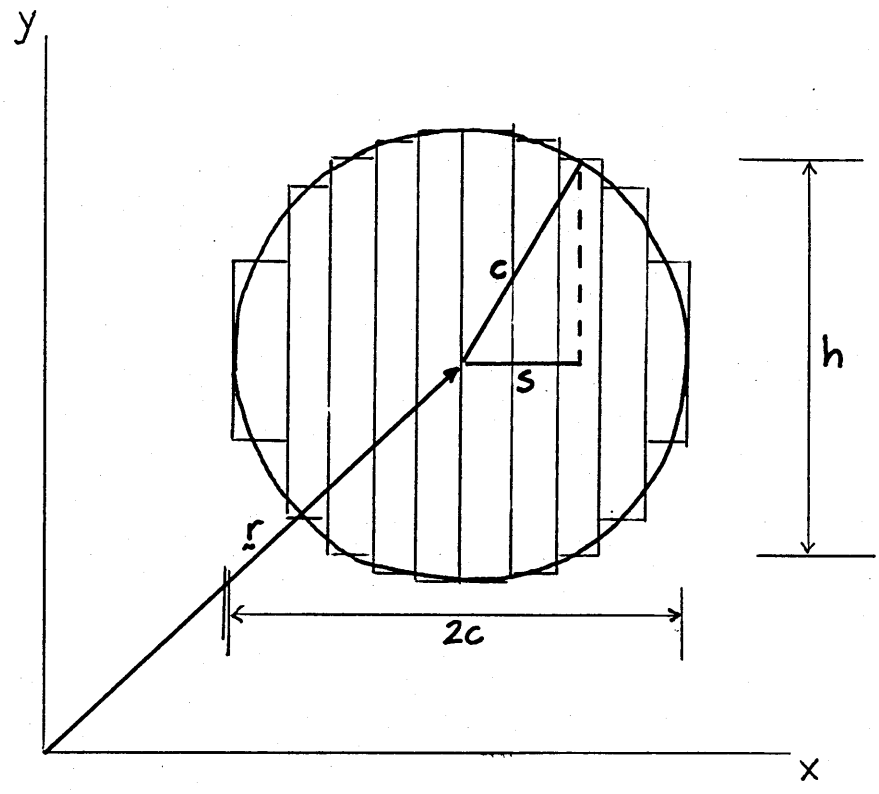

Figure 4.6 Parameters used in numerical integration over sensing coil.

S_i in equation (4.20) now represents the response of a gradiometer with coil centres at (x,z_{Di}) to a dipole at position (x_i,z_i).

4.3.3 The laboratory coordinate system

As mentioned in chapter 2, field scans are actually performed by passing the subject in the x direction under a fixed magnetometer. In terms of data analysis, it is easier to consider the subject to be stationary while the magnetometer moves. Computation is further simplified if we assume the gradiometer bottom coil moves in the plane z = 0 The origin of coordinates is also in this plane and lies on the axis of the z directed Helmholtz coils. This system is depicted in figure 4.5b.

4.3.4 Determination of the best fit dipole

Given a set of experimental data S(x), we now need to determine the parameters of the dipole which best fits the data.

I will define the 'best fit' parameter estimates (written as m^*,ϕ^*,x_i^*,z_i^*) to be those which minimise the integral:

$$E = \int (S-S_i)^2 dx \qquad (4.21)$$

I will now show that it is possible to perform the minimisation with respect to m,ϕ analytically, leaving x_i^*,z_i^* to be found by numerical methods. Again following Grimes et al (1985), I will simplify the algebraic notation

as follows. Firstly equation (4.20) is rewritten as:

$$S_i = m\beta \tag{4.22}$$

where

$$\beta = a\sin\phi + b\cos\phi \tag{4.23}$$

$$a = \frac{1}{\pi C^2}\frac{\mu}{2\pi}\sum_{i=1}^{n} k_i \int_{-c}^{c} 2\sqrt{c^2-s^2}\cdot\frac{(z_{Di}^2-(x_D+s)^2)}{(z_{Di}^2+(x_D+s)^2)}\,ds \tag{4.24}$$

$$b = \frac{-1}{\pi C^2}\frac{\mu}{2\pi}\sum_{i=1}^{n} k_i \int_{-c}^{c} 2\sqrt{c^2-s^2}\,\frac{2z_{Di}(x_D+s)}{(z_{Di}^2+(x_D+s)^2)}\,ds \tag{4.25}$$

Equations (4.22), (4.23) emphasise the nature of the dependence of S_i on m and ϕ.

Secondly, as the integral along the x-axis of the product of two functions of x occurs frequently, I will use the notation

$$(f,g) = \int_{-\infty}^{\infty} f(x)\,g(x)\,dx \tag{4.26}$$

Note that:

$$(f,g) = (g,f) \tag{4.27}$$

Now differentiating E in equation (4.22) with respect to m, we get:

$$\frac{\partial E}{\partial m} = \frac{\partial}{\partial m}(S-m\beta, S-m\beta) \tag{4.28}$$

$$\frac{\partial E}{\partial m} = -2(S,\beta) + 2m(\beta,\beta) \qquad (4.29)$$

And at a minimum:

$$m^* = \frac{(S,\beta)}{(\beta,\beta)} \qquad (4.30)$$

The minimisation of E with respect to ϕ is most easily carried out by first substituting for m in (4.22) from (4.30). This gives:

$$E = (S,S) - \frac{(S,\beta)^2}{(\beta,\beta)} \qquad (4.31)$$

Then:

$$\frac{\partial E}{\partial \phi} = -\frac{\partial}{\partial \phi}\left[\frac{(S,\beta)^2}{(\beta,\beta)}\right]$$

For a minimum:

$$\left(S,\frac{\partial \beta}{\partial \phi}\right)(\beta,\beta) = (S,\beta)\left(\beta,\frac{\partial \beta}{\partial \phi}\right) \qquad (4.32)$$

Now

$$\frac{\partial \beta}{\partial \phi} = a\cos\phi - b\sin\phi \qquad (4.33)$$

Substituting from (4.33) and (4.23) into (4.32) yields eventually:

$$\tan\phi^* = -\frac{(S,a)(b,b)-(S,b)(a,b)}{(S,a)(b,a)-(S,b)(a,a)} \qquad (4.34)$$

Combining the above expression for ϕ with (4.30) and (4.31) then gives finally:

$$m^* = \frac{\left\{\left[(S,a)(b,b)-(S,b)(a,b)\right]^2\left[(S,a)(a,b)-(S,b)(a,a)\right]^{-2}\right\}^{1/2}}{(a,a)(b,b)-(a,b)^2} \qquad (4.35)$$

and

$$E = (S,S)-\frac{(S,a)^2(b,b)+(S,b)^2(a,a)-2(S,a)(S,b)(a,b)}{(a,a)(b,b)-(a,b)^2} \qquad (4.36)$$

The expression on the right of (4.36) is a function of x_1, z_1 only, so the residual E can be computed for any dipole position without actually calculating m^*, ϕ^*. The most efficient method for determining x_1^*, z_1^* is to systematically search the x,z plane, calculating E at each point until a minimum is found. Only then is it necessary to use equations (4.35) and (4.34) to evaluate m^* and ϕ^*.

4.4 Considerations concerning discretely sampled data

The data S(x) are sampled at discrete intervals. The values a(x) and b(x), on the other hand are obtained from exact, analytical functions and can be calculated to arbitrary accuracy. Consideration of equations (4.24) and (4.25) shows that a is an even function and b is an odd function of x. It follows that (a,b) = 0. It can also be shown that (a,a) = (b,b) (Grimes et al, 1985). If these

properties of a and b are incorporated in the preceding analysis, equations (4.34) to (4.36) become:

$$\tan\phi^* = \frac{(S,a)}{(S,b)} \qquad (4.34a)$$

$$m^* = \left[\frac{(S,a)^2 + (S,b)^2}{(a,a)}\right]^{1/2} \qquad (4.35a)$$

$$E = (S,S) - \frac{(S,a)^2 + (S,b)^2}{(a,a)} \qquad (4.36a)$$

This appears to be a useful simplification. In fact it leads to inaccurate results. This is because the analysis is, in effect, a comparison between the measured data and the model data. Thus it is important that the integrals in both cases are calculated in the same way. As the integrals containing S(x) have to be determined by discrete summation, the integrals containing combinations of a and b should be evaluated by an identical summation procedure. In other words, a consistent approach to the integration must be adopted throughout the analysis.

4.5 Considerations concerning the line quadrupole term

One more subtlety of the line multipole system needs to be considered. It is possible to show (Grimes et al, 1985) that for a line multipole expansion of any axial current distribution, there exists a multipole origin at which the quadrupole term vanishes. Thus the system may be exactly represented by dipole, octupole and higher order terms.

Now consider a set of magnetic field data corresponding to a simple system in which only a few, lower order terms

are non-zero (dipole and quadrupole, say). If we attempt to determine the best fit dipole parameters for these data, it is likely that the best fit location will be found at just that point for which the quadrupole term vanishes. However, this may not be the true location of the dipole component of the current system.

This consideration may help to explain some of the results for test data discussed in the following chapter in which there is a very good fit between target and modelled data but a considerable mismatch between the best fit dipole parameters and the parameters of the target system.

4.6 Computational procedure for determining the best fit line dipole

Given a set of data for a scan across a current source, the fitting procedure is as follows:

(1) Select initial estimates (x_{1e}, z_{1e}) of x_1 and z_1 defining the dipole position.

(2) Calculate E at x_{1e}, z_{1e}. Then, keeping x_{1e} fixed, search adjacent values of z_{1e} until a local minimum E is found.

(3) Now, keep z_{1e} fixed and search for a minimum E by varying x_{1e}.

(4) Repeat steps 2 and 3 until no further improvement in E is made.

(5) If desired, at this point the step size between adjacent values of x_{i*} or z_{i*} can be reduced and the whole process repeated. The final position is x^*, z^*.

(6) Calculate m^* and $\emptyset^*$ for the position (x^*, z^*).

In the program used in this analysis, the integration of the calculated field over the sensing coils was performed using Simpson's rule. This can be carried out to any required accuracy by reducing the strip width (figure 4.6). For our coil dimensions, a strip width of 1mm was found to give adequate precision while allowing reasonably rapid computation. Integrals along the x-axis between $\pm\infty$ were replaced by summations of the appropriate values over the x data range (typically 31 or 61 data values at 1cm intervals).

In searching the x,z plane, a step size of 1cm was used initially. When a minimum position was found, the step size was reduced to 1mm and the process repeated.

Figure 4.7 shows a block diagram of the computer program.

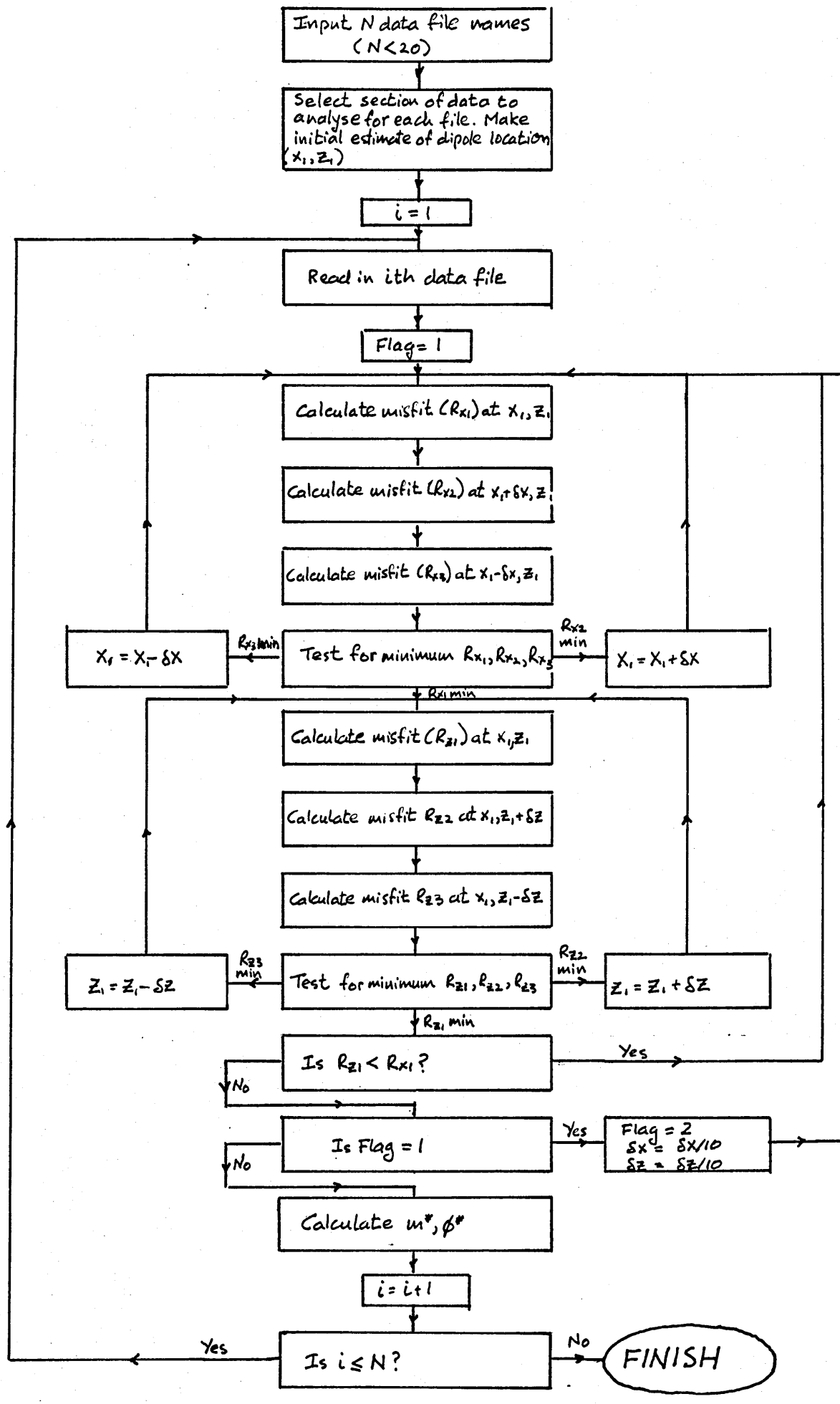

Figure 4.7 Structure of program LSWADX.

CHAPTER 5

TESTS ON THE LINE DIPOLE MODEL

5.1 Introduction

In this chapter I wish to discuss various tests carried out on the line dipole modelling technique described in section 4.5. The purpose of the tests was firstly to determine the accuracy of the method when applied to 'pure' line dipole data and secondly to examine to what extent useful information may be obtained from the best fit parameters in cases where the current configuration is only approximately line dipolar.

These latter tests are significant as the main purpose of the modelling technique is to analyse magnetic field data from the human leg and it is obvious that the leg current distribution cannot be purely line dipolar. The currents are not infinite in extent and are unlikely to be exactly dipolar in cross section.

The tests were carried out using data either from computer simulations or from actual measurements made on current carrying wire loops. The results are described below.

5.2 Computer simulations

5.2.1 Pure line dipole simulation

In order to check the internal consistency of the inversion procedure, simulated data for a pure line dipole

were generated via equation (4.20). The input data set consisted of 31 signal estimates at 10mm intervals. The best fit dipole parameters were determined as described in section 4.5 and these were compared with the known, original input parameters. An estimate of the overall quality of fit was obtained by computing a misfit parameter defined by:

$$R = (E/(S,S))^{1/2}. \qquad (5.1)$$

A number of input data sets were used with a wide variety of input parameters. The following results were obtained:

1) x_1* and z_1* were accurate to better than ±0.05mm. It is notable that this is much less than either the sensing coil diameter or the data sampling interval. Indeed better accuracy might have been achievable but this was not pursued further as physical measurements with our laboratory system can only be made to ±2mm. The best fit estimates m* and Ø* were accurate to within 0.4% and 0.02° respectively. R was typically < 10^{-3}%.

2) Addition of white noise with amplitude up to 5% of the peak to peak signal did not significantly affect the accuracy of the results. The noise level expected from leg measurement data is well within this range.

3) The addition of a dc offset of up to 8% of the peak to peak signal likewise produced no significant effect. Table 5.1 summarises these results.

It will be recalled (section 4.3.3) that the plane z = 0 passes through the gradiometer bottom coil. Thus z_1 is always negative; $-z_1$ represents the depth of the dipole

were generated via equation (4.20). The input data set consisted of 31 signal estimates at 10mm intervals. The best fit dipole parameters were determined as described in section 4.5 and these were compared with the known, original input parameters. An estimate of the overall quality of fit was obtained by computing a misfit parameter defined by:

$$R = (E/(S,S))^{1/2}. \qquad (5.1)$$

A number of input data sets were used with a wide variety of input parameters. The following results were obtained:

1) x_1* and z_1* were accurate to better than +0.05mm. It is notable that this is much less than either the sensing coil diameter or the data sampling interval. Indeed better accuracy might have been achievable but this was not pursued further as physical measurements with our laboratory system can only be made to ±2mm. The best fit estimates m* and ϕ* were accurate to within 0.4% and 0.02° respectively. R was typically < 10^{-3}%.

2) Addition of white noise with amplitude up to 5% of the peak to peak signal did not significantly affect the accuracy of the results. The noise level expected from leg measurement data is well within this range.

3) The addition of a dc offset of up to 8% of the peak to peak signal likewise produced no significant effect. Table 5.1 summarises these results.

It will be recalled (section 4.3.3) that the plane z = 0 passes through the gradiometer bottom coil. Thus z_1 is always negative; $-z_1$ represents the depth of the dipole

below the bottom coil.

While these results are encouraging and show that the method is internally consistent and relatively robust, they should be treated with some caution. High accuracy might be expected from data which are purely dipolar, particularly as the same algorithm was used in both the forward and inverse calculations.

TABLE 5.1

m/ Amx10^{-8}	m_1*/ Amx10^{-8}	Ø/ deg	Ø*/ deg	x_1/ mm	x_1*/ mm	z_1/ mm	z_1*/ mm	R/ %
10.00	10.04	-60.0	-60.0	0	0	-50	-50	0.00
10.00	10.04	-60.0	-60.0	-100	-100	-50	-50	0.00
1.000	1.000	-60.0	-59.98	0	0	-10	-10	0.01
1000	1000	-60.0	-60.0	0	0	-300	-300	0.0
10.00(1)	10.05	-60.0	-60.04	0	0	-50	-50	32.8
10.00(2)	9.89	-60.0	-61.51	0	-1	-50	-50	14.5

(1) dc offset = 8% of peak to peak height

(2) noise amplitude = 5% peak to peak height

5.2.2 Parallel wire pair simulation

To investigate the performance of the model when the source is not a pure dipole, a second set of tests was performed using the simulated gradiometer measurements for a pair of oppositely oriented, infinite length line currents parallel to the y-axis and separated by a distance δl. Referring to figure 4.3, this configuration will tend to a pure line dipole when $\delta l/z \rightarrow 0$.

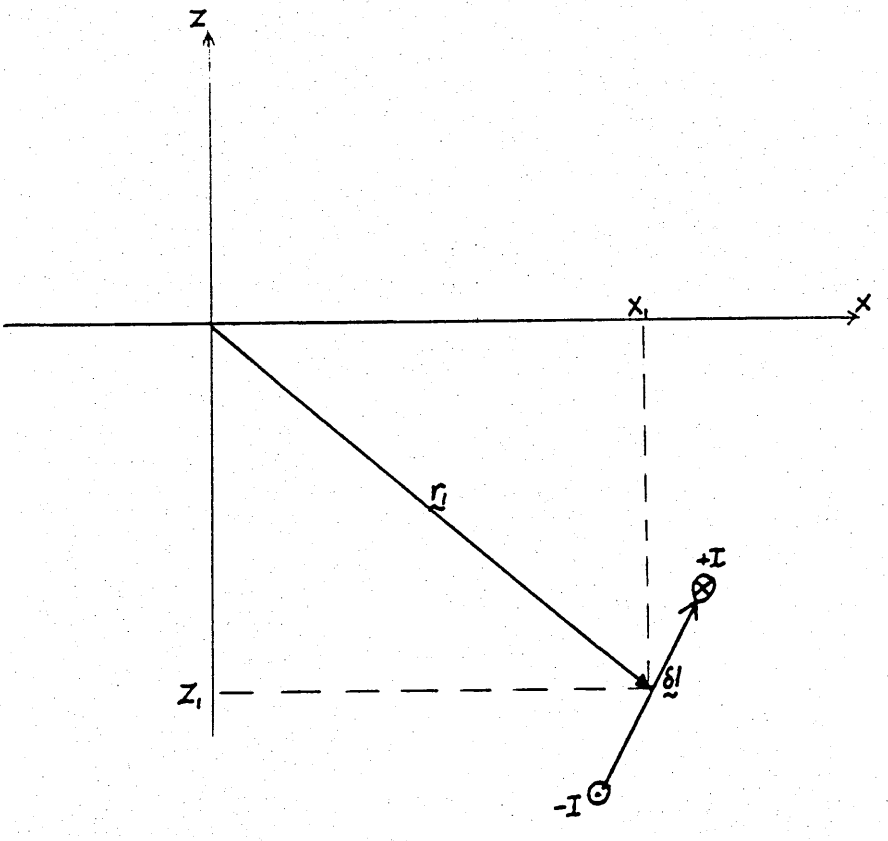

Figure 5.1 Coordinate system for parallel line current pair.

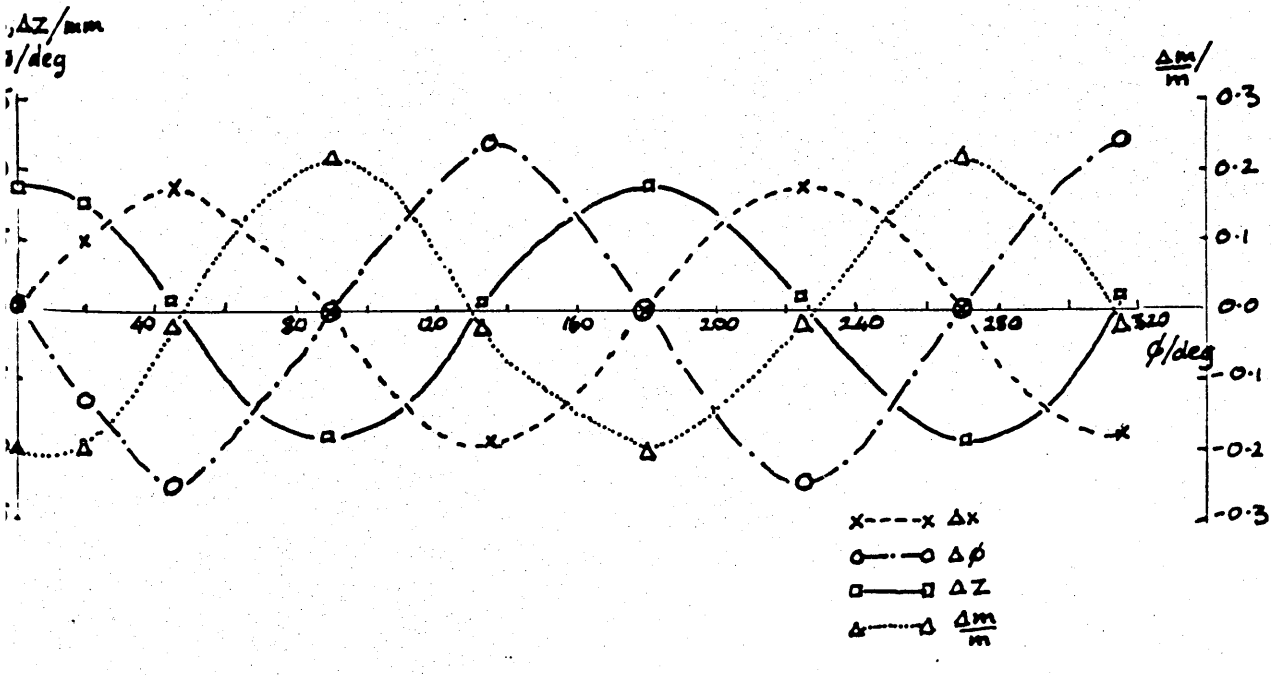

Figure 5.2 Line dipole parameter discrepancies for parallel line current pair plotted against angle Ø.
δl = 45mm, z_1 = -50mm.

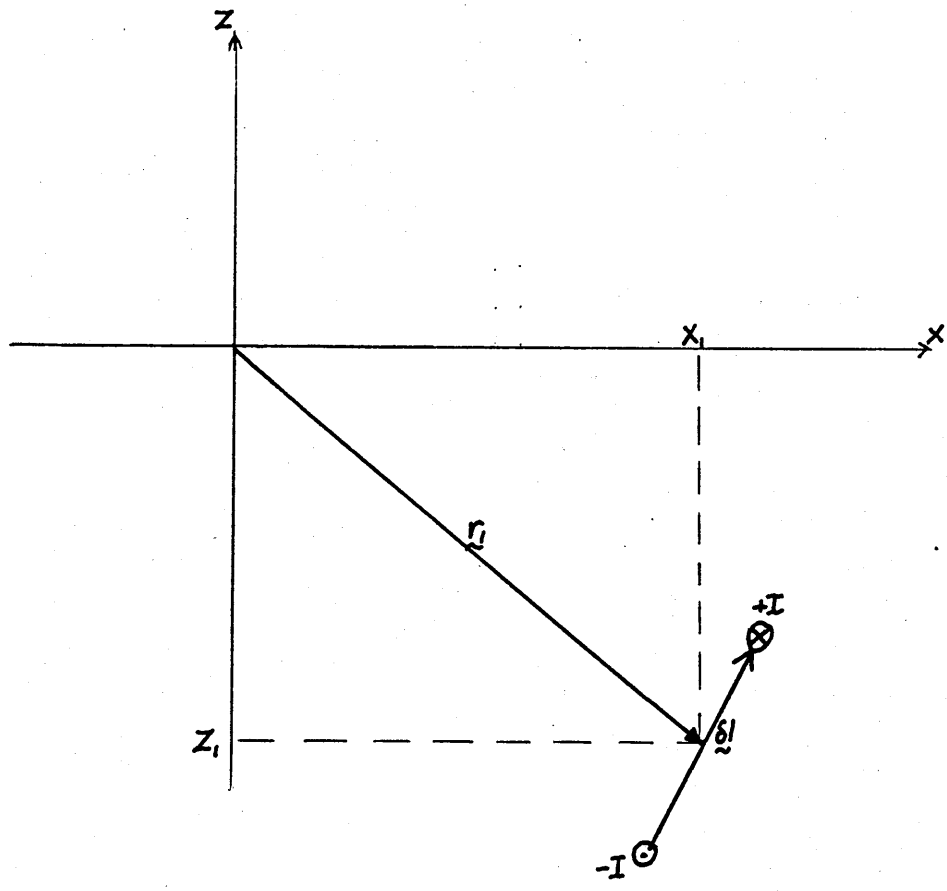

Figure 5.1 Coordinate system for parallel line current pair.

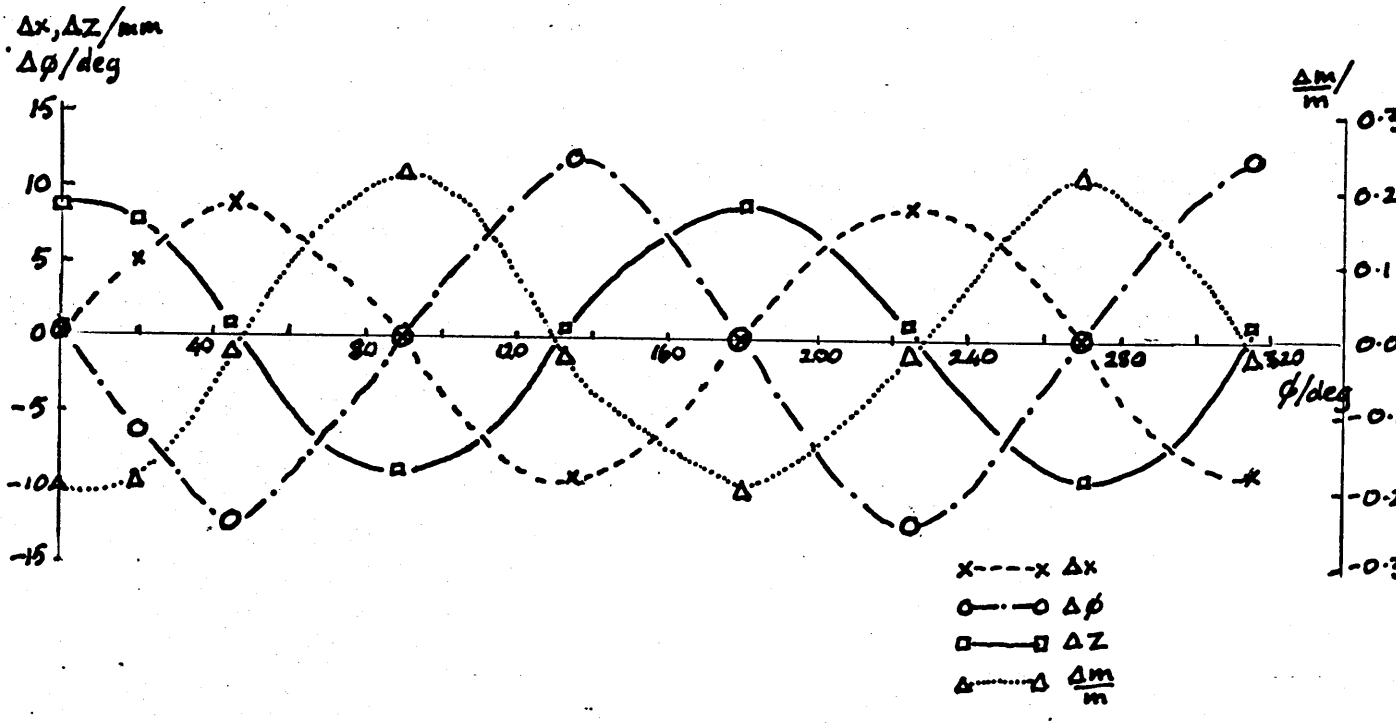

Figure 5.2 Line dipole parameter discrepancies for parallel line current pair plotted against angle Ø.
δl = 45mm, z_1 = -50mm.

The dipole location is taken as the average (x,z) position of the currents and the dipole strength is $I\delta l$ where I is the current magnitude. As before, the dipole vector points from the negatively oriented current to the positively oriented current. ϕ is the angle between a line perpendicular to the currents and the z axis. The situation is illustrated in figure 5.1.

Simulations were performed for a range of depths ($-100mm \leqslant z \leqslant -10mm$) and a range of δl ($10mm \leqslant \delta l \leqslant 100mm$) which might reasonably be expected to occur in the human leg. Best fit dipole parameters were calculated and compared with the input parameters. The results are most conveniently presented in terms of parameter discrepancies Δx, Δz, $\Delta\phi$, m, which are defined as follows:

$$\Delta x = x^* - x_1$$

$$\Delta z = z^* - z_1$$

$$\Delta\phi = \phi^* - \phi_1$$

$$\Delta m = m^* - m_1$$

The discrepancies all show a periodic variation with angle ϕ. Figure 5.2 demonstrates this for the particular case of $\delta l = 45mm$ and $z_1 = 50mm$. In fact, the form of the variation is the same for all z_1 and δl, only the amplitude changes (increasing as $\delta l/z_1$ increases).

From figure 5.2, it can be seen that Δx, $\Delta\phi$ are zero at $\phi_1 = n\pi/2$ and Δm, Δz are maximum at these angles. Conversely Δm, Δz are zero for $\phi_1 = (2n+1)\pi/4$ where Δx, $\Delta\phi$ are maximum.

This angular dependency can be qualitatively explained by examining figure 5.3 which compares the scan for a pure

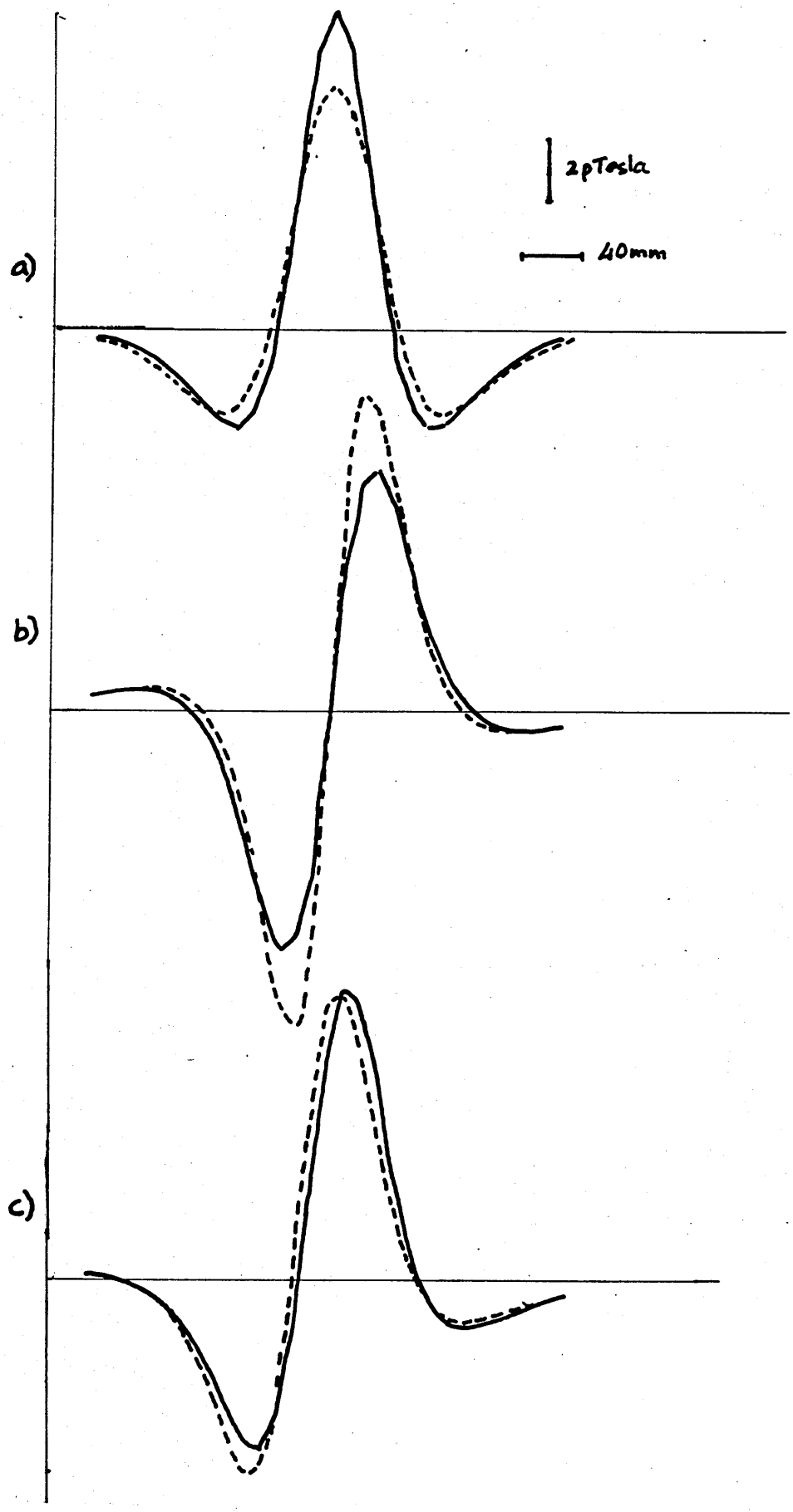

Figure 5.3 Comparison of scans from pure line dipole source (solid line) and parallel line current pair (dashed line). δl = 50mm. I δl for current pair = m for line dipole. z = -60mm in all cases. a) $\phi = 90°$, b) $\phi = 180°$, c) $\phi = 135°$.

dipole and the scan for a line current pair with identical dipole moment at the same depth. At $\phi = n\pi/2$ we may expect the algorithm to locate x and ϕ precisely because of the signal symmetry. At $\phi = (2n+1)\pi/2$ (dipole vector horizontal, figure 5.3a), the separation of the currents in the current pair causes an increased spread in the signal peak but a decreased amplitude.

The model can compensate for the increased spread by finding a best fit solution at a greater depth (z more negative). Because the signal amplitude decreases rapidly with increasing depth, m must now be overestimated to fit the data.

Conversely at $\phi = n\pi$(dipole vertical, figure 5.3b), the signal spread of the wire pair is reduced compared to the dipole but its amplitude is increased (figure 5.2b). This is because the uppermost line current passes closer to the sensor and thus dominates the signal. The model matches the smaller spread with a reduced depth (z less negative). At the new depth, m must be underestimated to achieve a fit.

At intermediate angles ($\phi = (n+1/2)\pi/2$, figure 5.3c) the two competing effects tend to cancel so that m and z are accurately estimated. However the lack of signal symmetry means that the calculation of x and ϕ is less straightforward. Figure 5.3c illustrates the case for $\phi = 135°$. It can be seen that the negative peak for the current pair is enhanced and the whole signal is shifted in the negative x direction. Once more this is due to the increased contribution from the uppermost current. The fit can now be optimised by reducing x (Δx positive) and increasing ϕ ($\Delta\phi$ negative.

Figure 5.4 shows the variation of parameter discrepancy with z_1 for 3 values of δl (10mm, 50mm, 100mm). For convenience, here and in subsequent plots, $z < 0$ (increasing depth) is plotted to the right of the origin. The values of ϕ are chosen to maximise the parameter discrepancies and the z range exceeds the likely dimensions of the human leg. It can be seen that all discrepancies decrease with increasing depth and increase with increasing δl (as they should).

The misfit parameter R is also plotted in figure 5.4. It will be noted that it is not always a reliable guide to parameter accuracy. In general, $R > 10\%$ implies an unacceptable fit but for large δl, the fit may appear good (small R) while giving unacceptable parameter estimates, particularly for $\phi = 90^\circ$ or 270°.

The purpose of the tests is to investigate the reliability of the model parameters. Of particular interest is whether the best fit parameters are sufficiently accurate to allow us to distinguish between specific anatomical sources for the leg currents. With this in mind, I will, somewhat arbitrarily, regard as acceptable model fits which reproduce the target parameters to within the following limits:

$$\Delta x < 10\text{mm}$$

$$\Delta z < 10\text{mm}$$

$$\Delta \phi < 15^\circ$$

No limit is given for m as its accurate determination is of minor significance.

As the accuracy of fit depends on both δl and z. It is of interest to calculate the maximum value of δl (δl_{max})

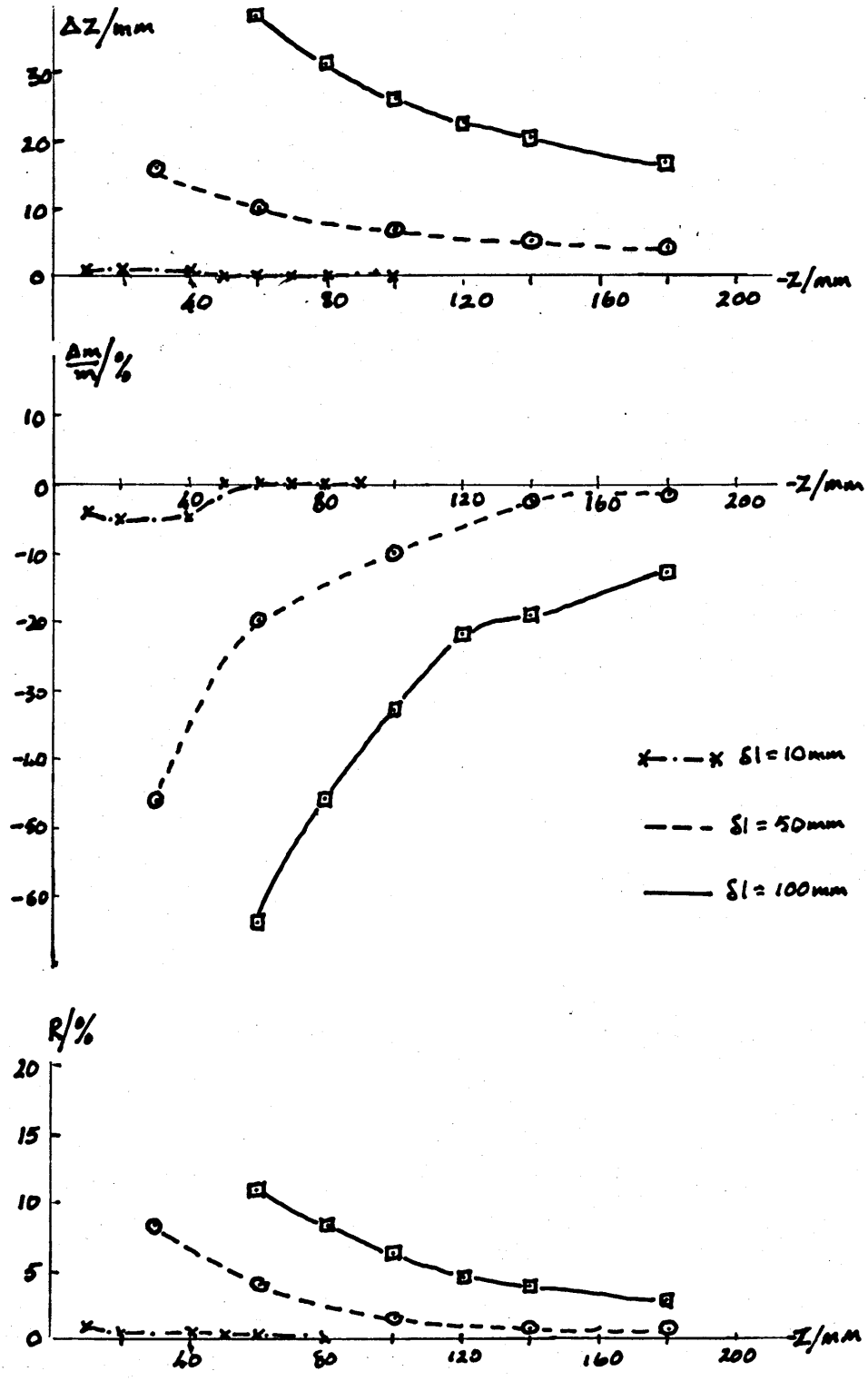

Figure 5.4a) Line dipole parameter discrepancies for parallel wire pair plotted against depth (-z) for 3 different values of δl.
$\emptyset = 0^{\circ}$.

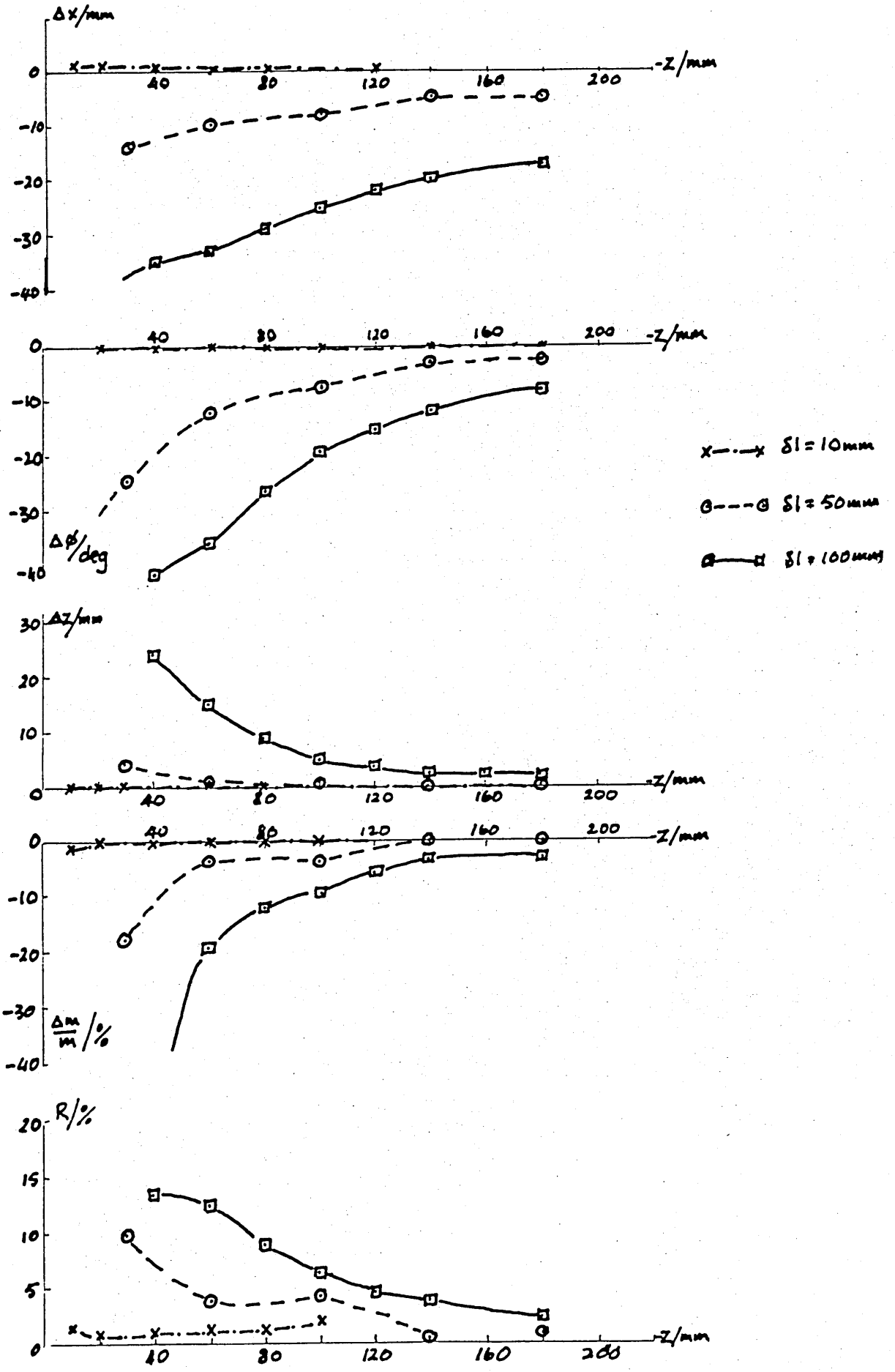

Figure 5.4b) Line dipole parameter discrepancies for parallel wire pair plotted against depth ($-z_1$) for 3 different values of δl.
$\phi = 45°$.

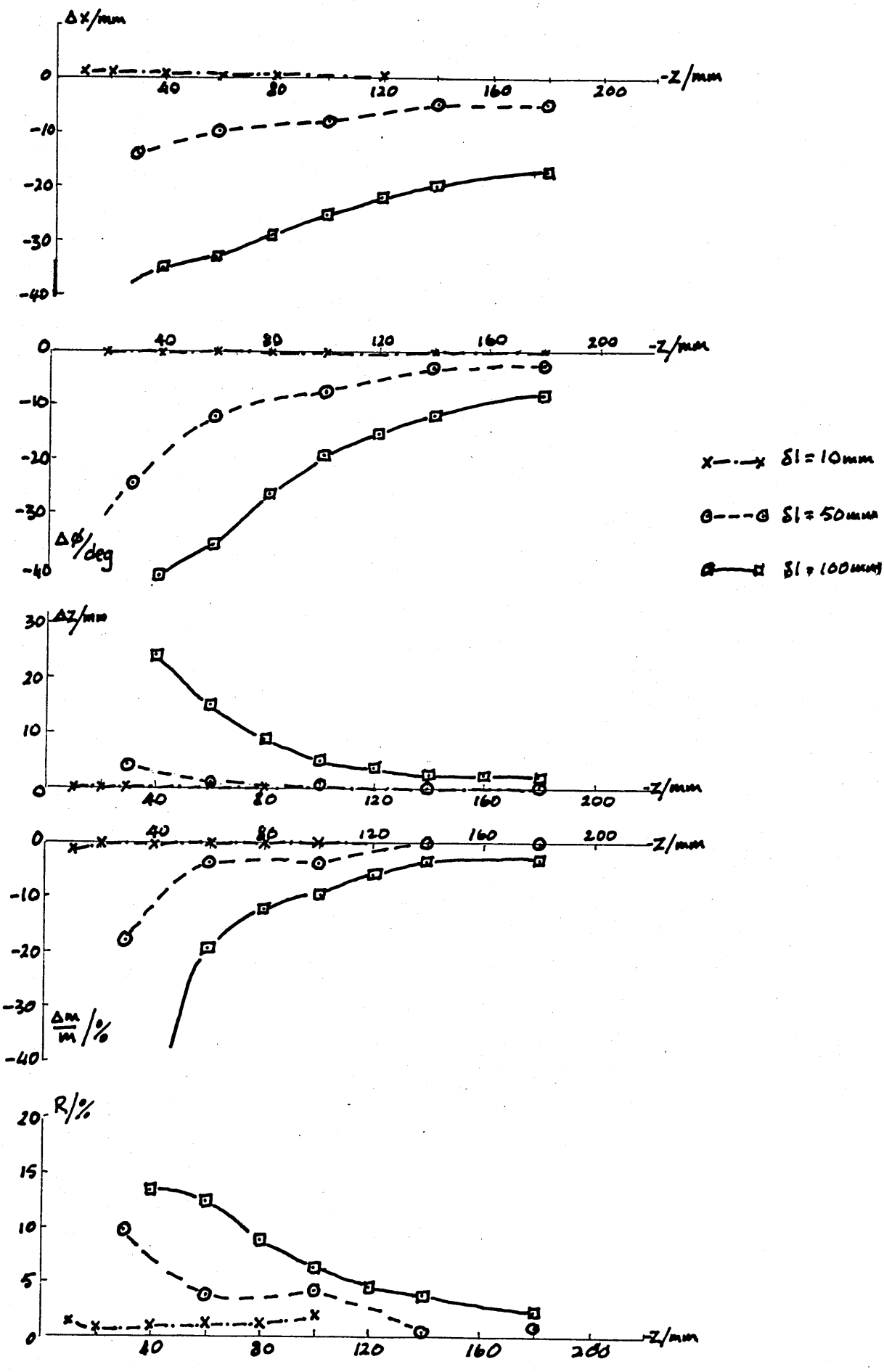

Figure 5.4b) Line dipole parameter discrepancies for parallel wire pair plotted against depth ($-z_1$) for 3 different values of δl.
$\emptyset = 45°$.

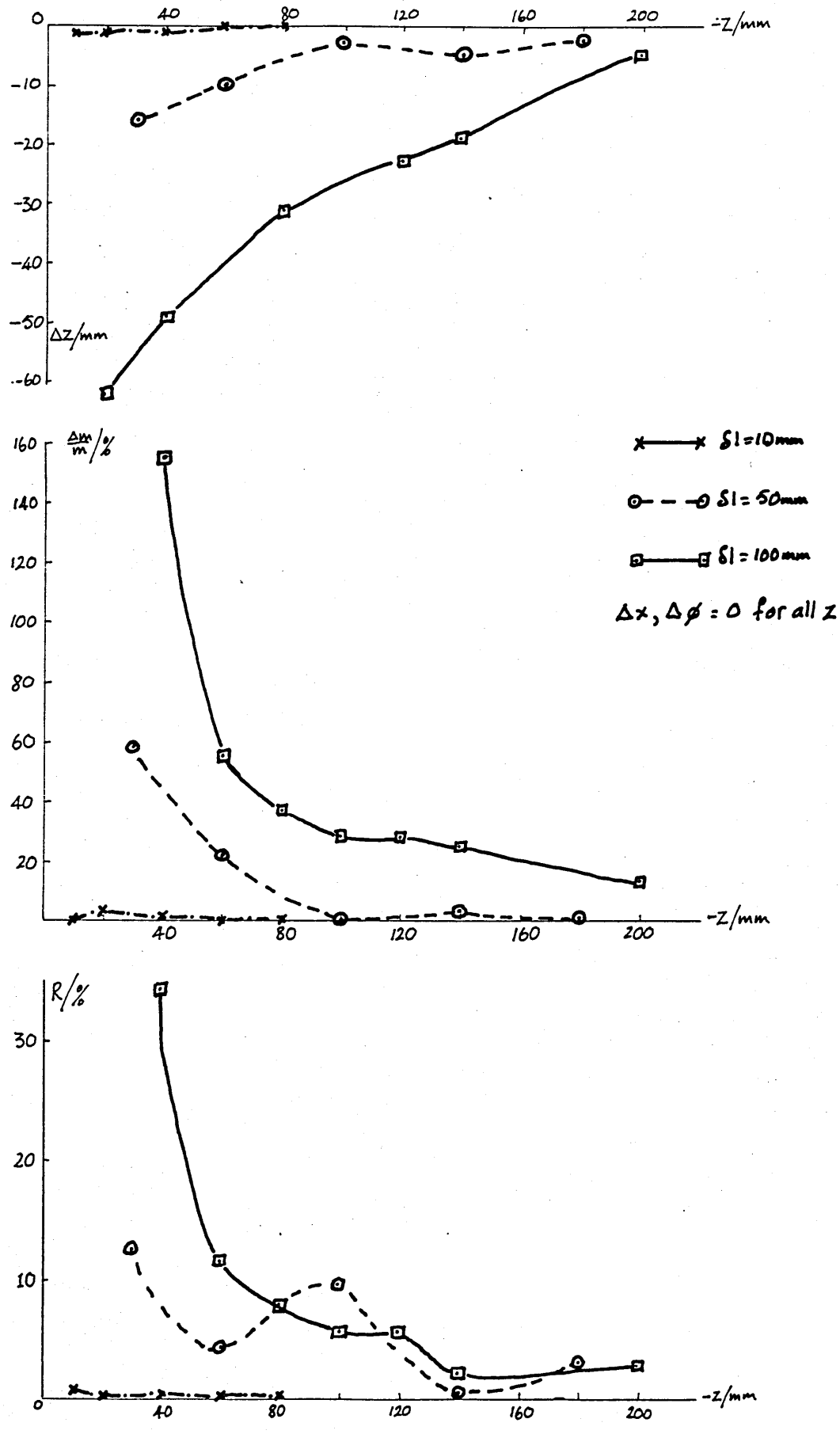

Figure 5.4c) Line dipole parameter discrepancies for parallel wire pair plotted against depth (-z) for 3 different values of δl.
$\phi = 90°$.

for a given z which would give acceptable results according to the 'criterion of acceptability' defined above.

This is done in figure 5.5 which shows the modulus of parameter discrepancies v. δl at 3 different depths. Once again the plotted discrepancies correspond to the least favourable value of ϕ in each case and the z range encompasses the likely range of dipole depths for the human leg (z = -30mm to z = -80mm). The figure shows that δl_{max} increases from 35mm at z = -30mm to δl_{max} = 55mm at z = -100mm. It can also be seen that, if the criteria for $\Delta x, \Delta z, \Delta \phi$ are met, then $\Delta m/m < 30\%$.

The results of the parallel line current simulations for the range of depths corresponding to the human leg may be summarised as follows:

1) For δl < 10mm, the dipole is located to better than 1mm and 2°.

2) For δl < 35mm, the dipole is located to better than 10mm and 15°.

3) For 35mm < δl < 55mm, the acceptability of the fit depends on depth as indicated in figure 5.5.

4) For δl > 55mm the parameter discrepancies are not within the limits of the 'criterion of acceptability' in the depth range of interest.

It should be stressed that the designation of the line dipole parameters as not 'acceptable' simply implies that they are outside the arbitrarily specified limits of accuracy, however useful information may still be obtained by considering the dependency of the parameters on ϕ as illustrated in figure 5.2.

This shows that line current pairs with dipole vectors

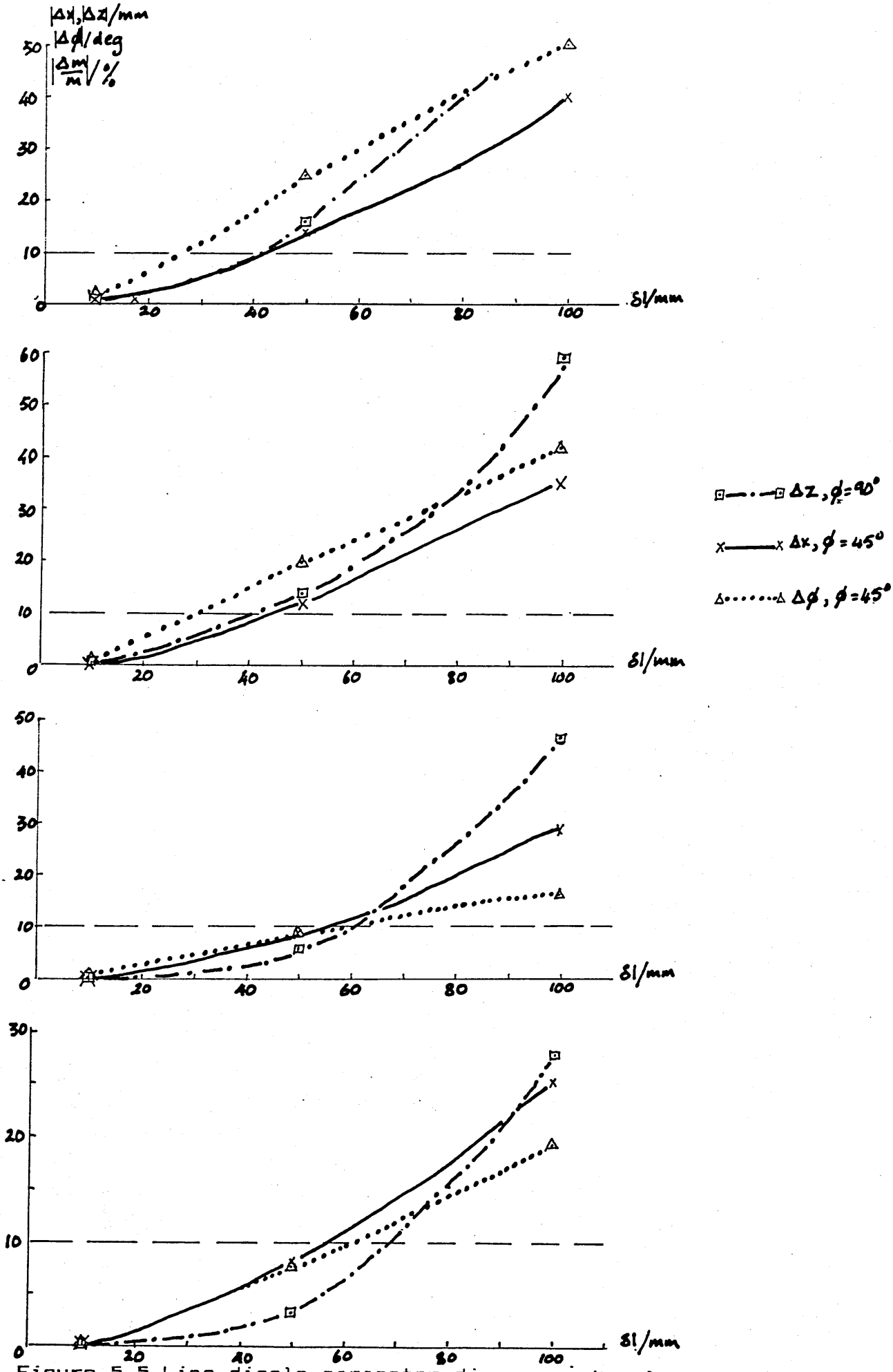

Figure 5.5 Line dipole parameter discrepancies for parallel wire pair plotted against wire separation (δl). The horizontal dashed line indicates the criterion of acceptability for x,z. a) $z_1 = -30mm$, b) $z_1 = -40mm$ c) $z_1 = -80mm$ d) $z_1 = -100mm$.

which are approximately horizontal or vertical should give accurate values of x^* and $\emptyset^*$ irrespective of δl. Furthermore, m^* and z^* will be overestimated if the dipole vector is roughly horizontal and underestimated if it is roughly vertical. Similarly for dipole vectors with $\emptyset$ close to 45°, 135°, 225°, 315°, estimates of m^*, z^* are likely to be accurate with x^* and $\emptyset^*$ over or underestimated as shown by figure 5.2.

Finally it should be observed that figure 5.5 imposes a more restrictive limit on δl than that for multipole series convergence discussed in section 4.2.2. This would simply imply $\delta l_{max} < 2z$.

5.3 Tests using current carrying wires

5.3.1 The parallel wire pair

To verify that the computer simulations accurately represent the true gradiometer response, scans were performed in the laboratory on a parallel pair of current carrying wires with a separation of 10mm for $-100mm < z_1 < -30mm$.

The wires were supported on a long, wooden beam which had been tested for magnetic contamination. The beam could be rotated about its long axis so as to vary the angle $\emptyset$. Positions of individual wires were determined using the location device described in section 2.1.4. The angle $\emptyset$ was either calculated from the positions of the wires or from a protractor attached to the end of the beam. The arrangement is shown in figure 5.6.

Measurements were made with the SQUID set to x1

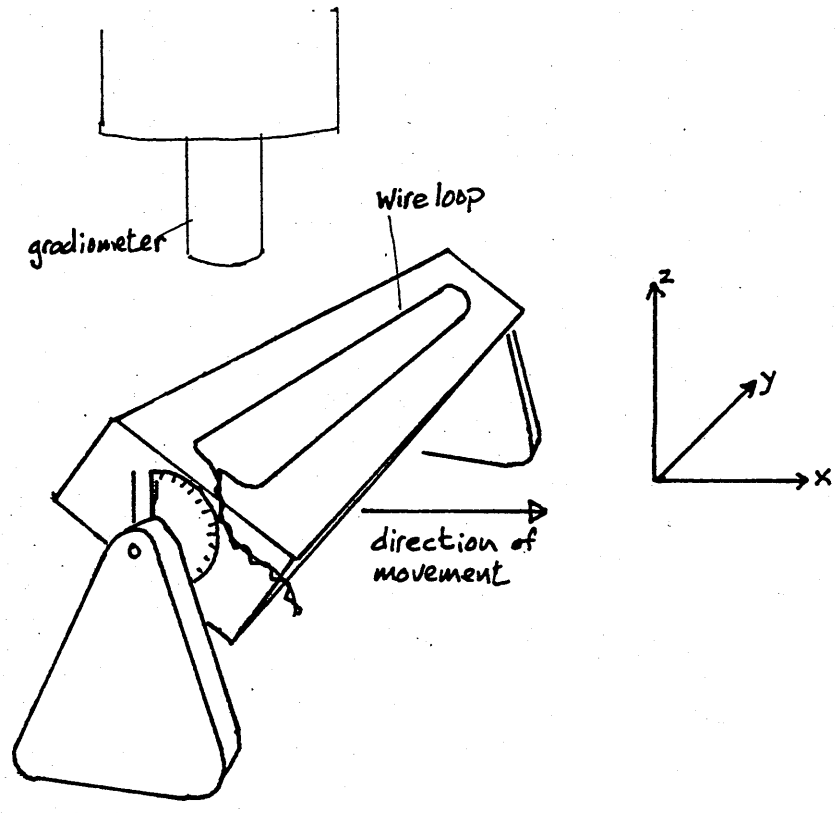

Figure 5.6 Experimental arrangement for measuring field generated by a parallel line current pair.

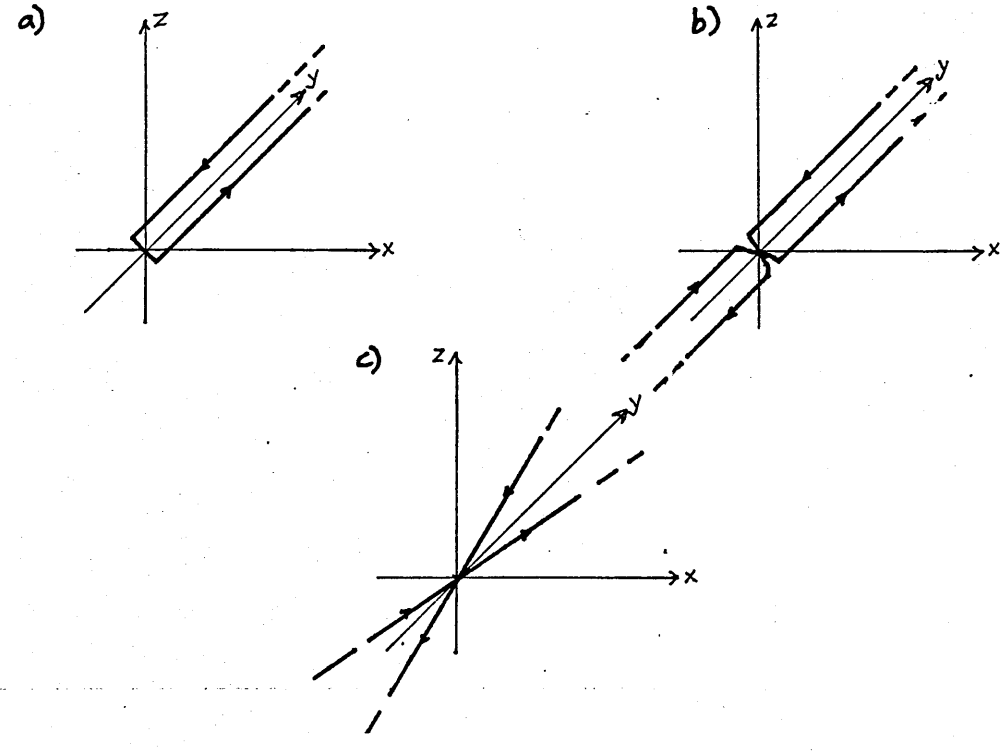

Figure 5.7 Current configurations used in the tests described in section 5.3.2.

sensitivity and a current of ~10mA. This gave a signal of similar amplitude to the leg data and rendered insignificant the magnetic effects of the wires themselves. It also reduced background noise to negligible levels.

Some variability of the initial scans was found to be due to the effect of low pass filtering the SQUID output (described in chapter 2). Ensuring that the bed moved slowly (at speeds < 80mms^{-1}) avoided this problem.

TABLE 5.2

a) Experimental parameters

Scan	m/ Amx10^{-5}	Ø/ deg	x_1/ mm	z_1/ mm
1	88	90	-1	-88
2	90	180	-11	-67
3	92	69	-23	-58

b) Best fit to experimental data

Scan	m*/ Amx10^{-5}	Ø*/ deg	x_1*/ mm	z_1*/ mm
1	106	89	-1	-89
2	111	179	-8	-66
3	102	66	-24	-59

c) Best fit to computer simulation data

Scan	m*/ Amx10^{-5}	Ø*/ deg	x_1*/ mm	z_1*/ mm
1	88	90	-1	-88
2	89	180	-11	-67
3	91	69	-23	-58

The modelling program was applied to the experimental data and also to data from a computer simulation of the same parallel wire arrangement. Results for 3 sets of data are shown in table 5.2. Table 5.2a shows the experimentally measured input parameters; table 5.2b shows the best fit model parameters and table 5.2c shows the best fit model parameters for the computer simulation.

For x,z and Ø, both sets of best fit parameters agree to within the limits of measurement error (+5° for Ø and +2mm for x,z). The values of m* for the experimental data however are substantially overestimated.

These large values for m* are puzzling. Experimentally, this is the least accurately measured parameter as the wire positions are only measured to ±2mm, however this does not account for a systematic overestimate of up to 25%. Subsequent measurements using completely different modelling techniques have given similar results and we have concluded that the calibration figure provided by the manufacturer is in error by about 15%. This scaling factor has been allowed for in the remainder of the thesis.

5.3.2 Three dimensional current configurations

To test the success of the model when the current configuration varies with y, three sets of experiments were performed using the configurations shown in figure 5.7. These were (a) the region close to the end of a long, narrow rectangular loop (long side parallel to the y axis), (b) a long, narrow rectangular loop with an abrupt 180° twist and (c) a pair of non parallel wires with a crossover point. For (a) and (b) the separation between the wires in the x

direction was 3mm. For (c) the included angle at the crossover point was approximately 4°.

The purpose of the tests was to determine how closely the crossover or termination could be approached while still producing dipole parameters which accurately reflect the configuration directly below the magnetometer. This information can then be used to as a rough guide to the reliability of leg model parameters for individual scans. Within this context, case (b) represents a rather severe test as it is unlikely that such an abrupt change occurs within the leg. Case (c) is a more realistic scenario with a gradual variation in current configuration along its entire length.

The parameter discrepancies (Δm, $\Delta \phi$, Δx, Δz) were measured as a function of y position for each configuration. For configuration (a), y = 0 represents the end of the loop, in the other two cases, y = 0 is the crossover point. In all cases the wires were close enough together to give results indistinguishable from a pure dipole for measurements made far from the anomaly. The range over which the parameter discrepancies are discernible increases with depth as might be expected. Results quoted here are for z_1 = -80mm, which is close to the maximum observed depth for leg dipoles.

The situation is also complicated by the fact that discrepancies vary with Ø. The form of the variation in all 3 cases is similar to that shown in figure 5.2 for the infinite line current pair. The dependence on Ø is most extreme for the abrupt twist and figure 5.8 shows the

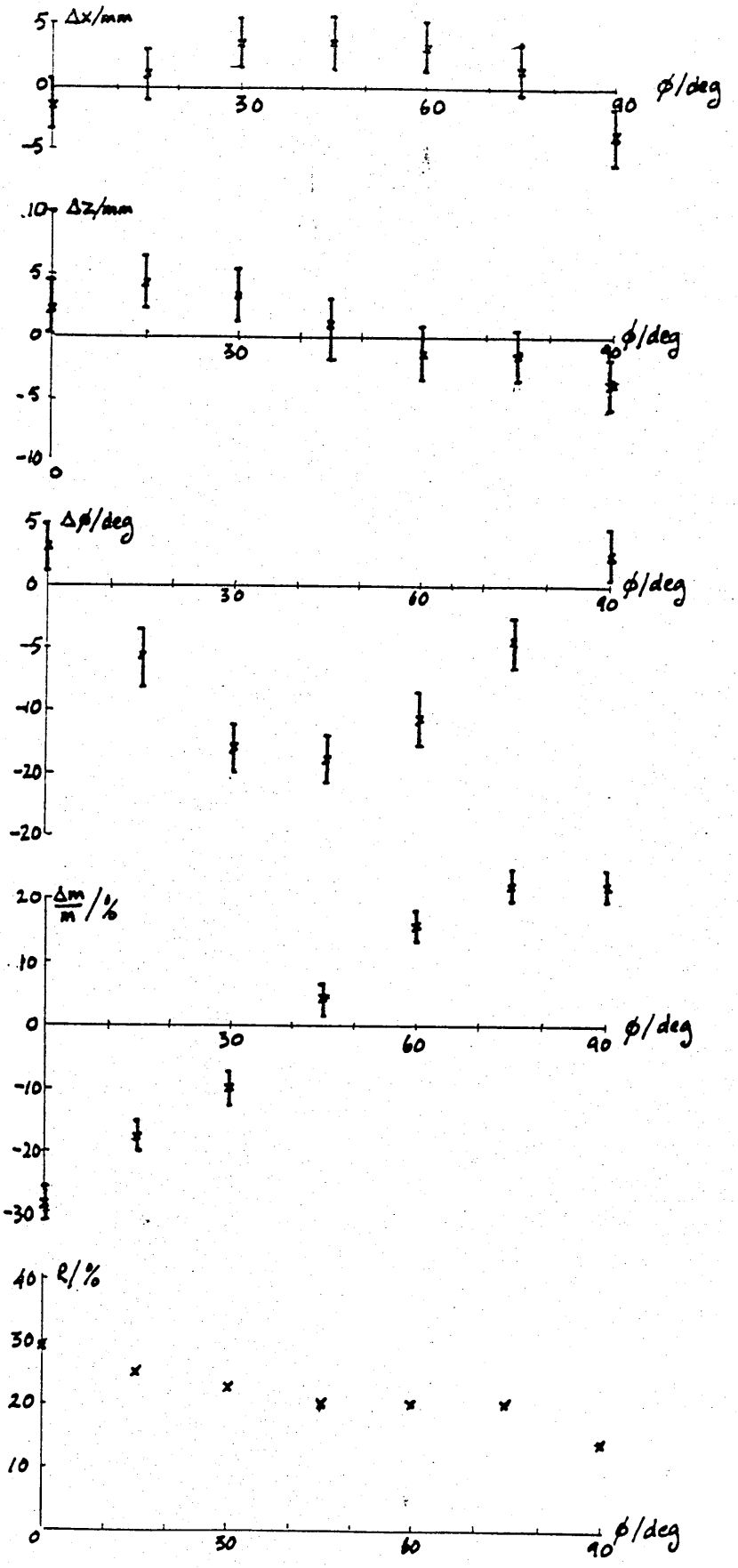

Figure 5.8 Variation of parameter discrepancy with Ø for the current configuration shown in figure 5.3b at y = 50mm. z_1 = -80mm.

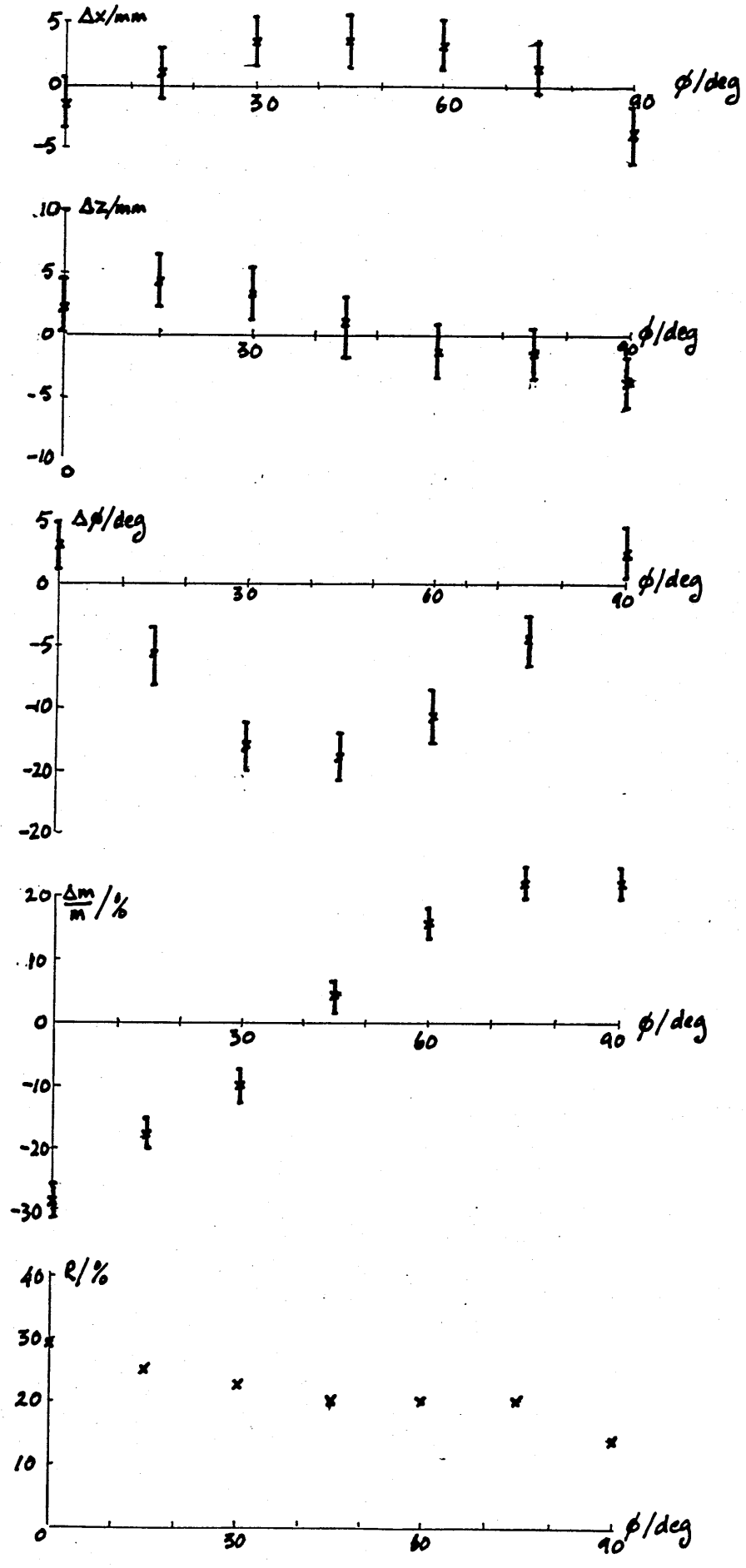

Figure 5.8 Variation of parameter discrepancy with Ø for the current configuration shown in figure 5.3b at y = 50mm, z_1 = -80mm.

variation of discrepancy with Ø for this case at y = 50mm. The values of R at each angle are also plotted. It should be observed that the values of R here are significantly larger than in cases of comparable accuracy when a parallel current pair is modelled (cf figure 5.4).

It may seem surprising that a small value of R is obtained at Ø = 90, where Δz and Δm are both large. However this is illustrative of the fact already mentioned in section 5.2.2 that changes in m and z can compensate for each other. It also emphasises the point that a small R does not necessarily mean accurate parameter values.

Figure 5.9 shows the parameter discrepancy variation with y. Ø = 70° has been used as an illustrative angle as this is relatively unfavourable with respect to all parameters (figure 5.8). As might be expected case (b) shows the greatest deviation from the experimental figures, however even in this case Δx is within the limits of acceptability for y > 10mm while $\Delta Ø$ is acceptable for y > 50mm. z and m are the least accurate parameters, only becoming acceptable 70mm from the twist.

For case (a), z meets the acceptability criterion for all y. x and Ø once more fit well to within 10mm of the end of the loop.

The non parallel wire pair (case (c)) is matched extremely well for all parameters to within 10mm of the crossover. As this is the configuration which produces a field pattern most closely resembling the actual leg data, this is encouraging.

To summarise, the parameters are accurate provided:

(i) abrupt twists do not occur within 70mm of the scan

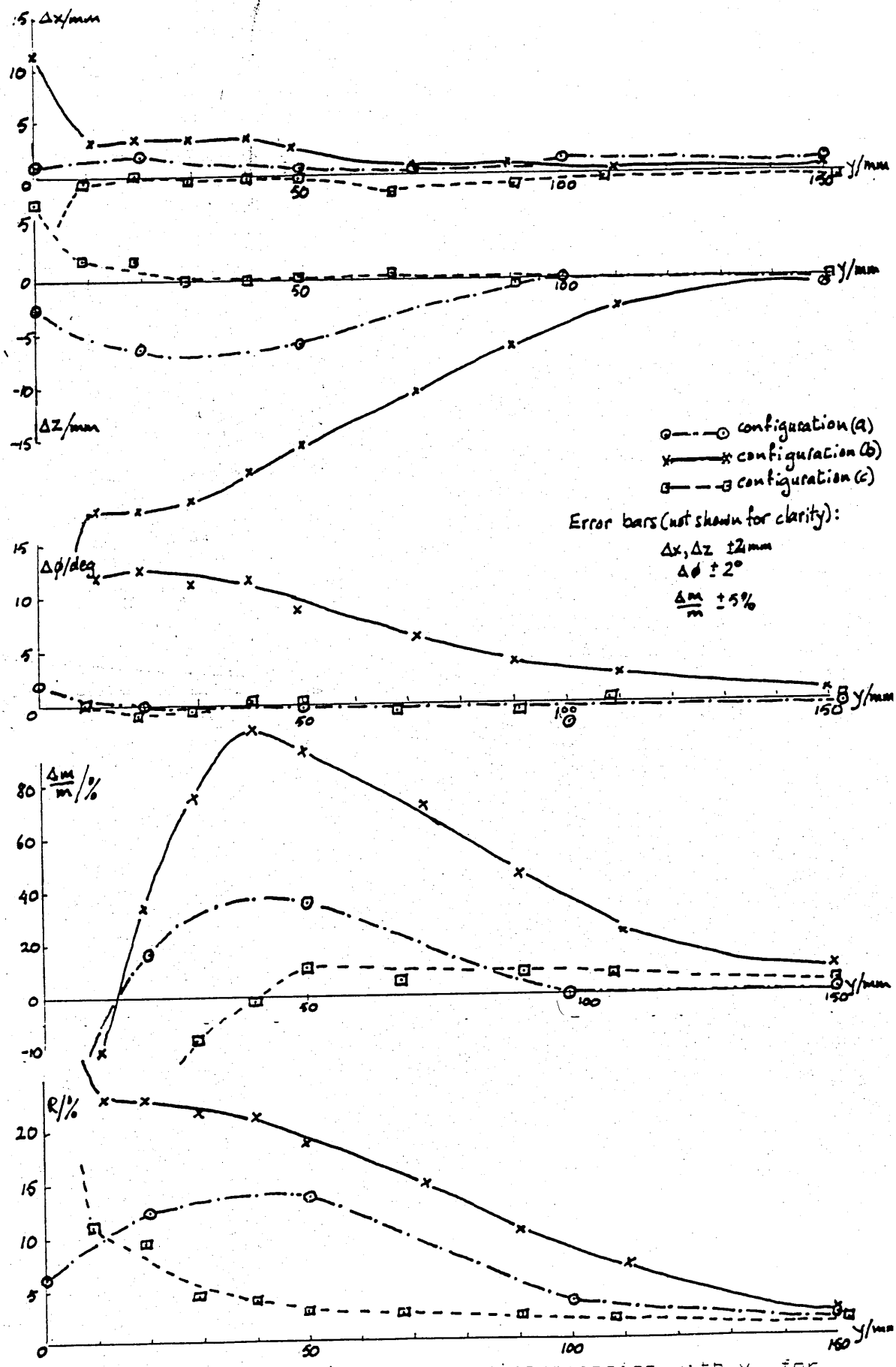

Figure 5.9 Variation of parameter discrepancies with y_1 for the current configurations of figure 5.3. $\phi = 70°$, $z_1 = -80mm$ in all cases.

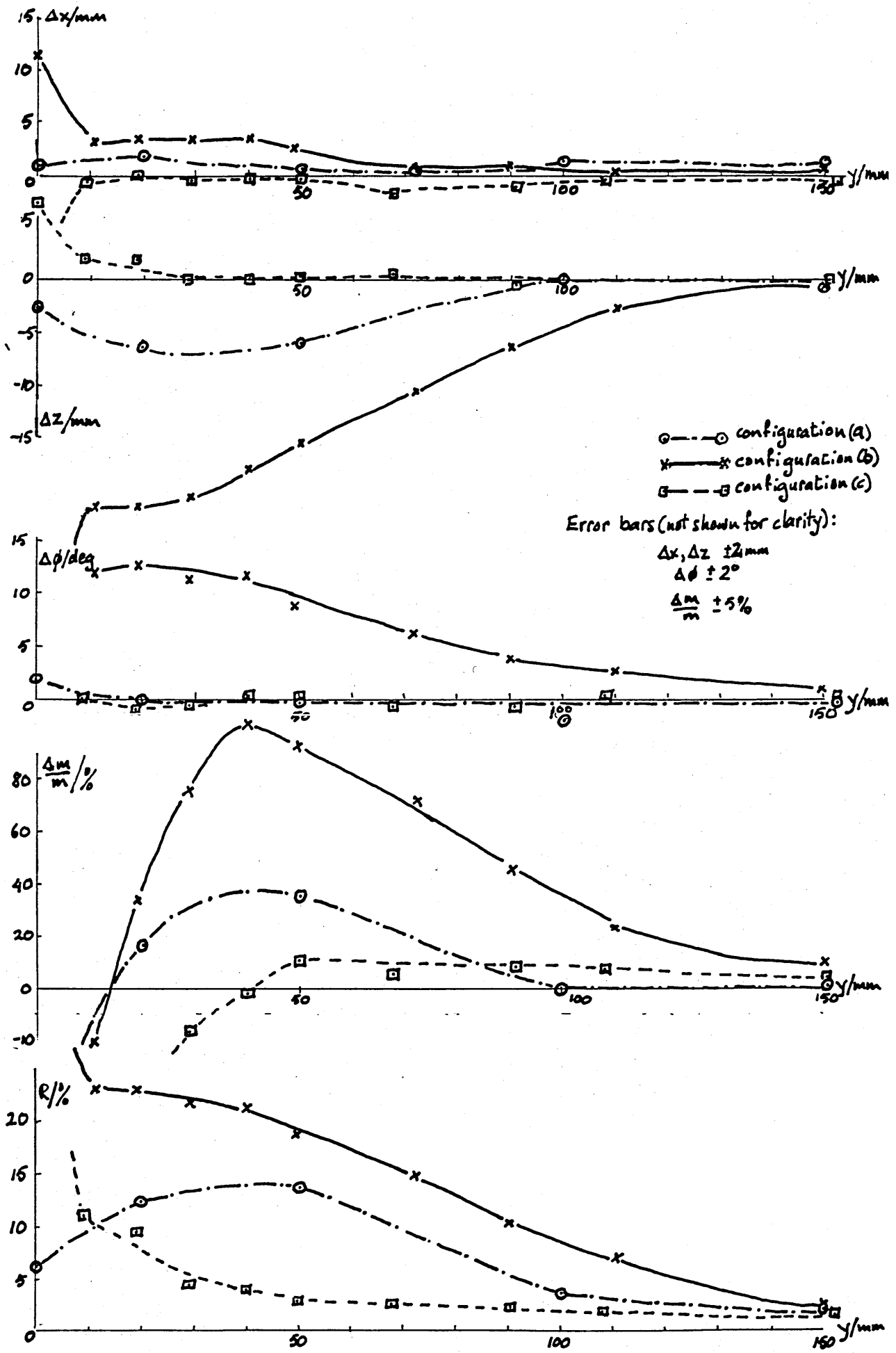

Figure 5.9 Variation of parameter discrepancies with y for the current configurations of figure 5.3. Ø = 70°, z_1 = -80mm in all cases.

(ii) ends of loops or crossovers do not occur within 10mm of the scan

(iii) Deviations of a few degrees from parallel for the currents have little effect.

For depths less than 80mm, these restrictions would of course be reduced.

Although different values of Ø would produce some variations in the y distances quoted above, Ø = 70° is close to a worst case for all parameters. Hence the overall conclusion is that current patterns at depths typical of those found in the leg and which are line-dipolar in a local sense only can be accurately modelled using the line dipole technique.

The values of R in figure 5.9 are greater than for comparable parallel wire pair results. Inspection of figure 5.9 suggests that R > 15% is an indication of unreliable model parameters, although it should be noted that these data are effectively noise free.

5.4 The truncated line dipole

The results of the previous section support the idea that the modelling of scans on an individual basis can yield meaningful results provided the variation of current pattern with y is not too rapid. Theoretical support for this conclusion can be obtained by considering a 'truncated line dipole'. As the name implies, it is equivalent to the line dipole discussed in section 4.2 but with the extent of the currents in the y direction reduced from $\pm\infty$ to $\pm L$. This is ilustrated in figure 5.11.

It is possible to show that the magnetic field of any

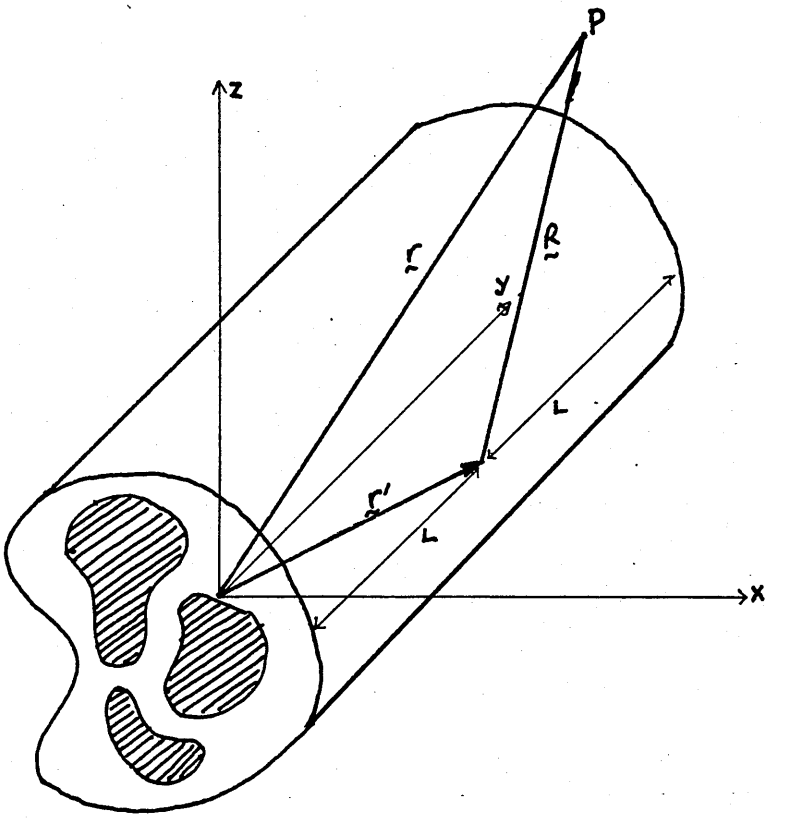

Figure 5.10 Truncated current distribution, axially uniform with respect to the y-axis, extending between y = ±L. Shading indicates current in the +y direction, no shading indicates current in the -y direction.

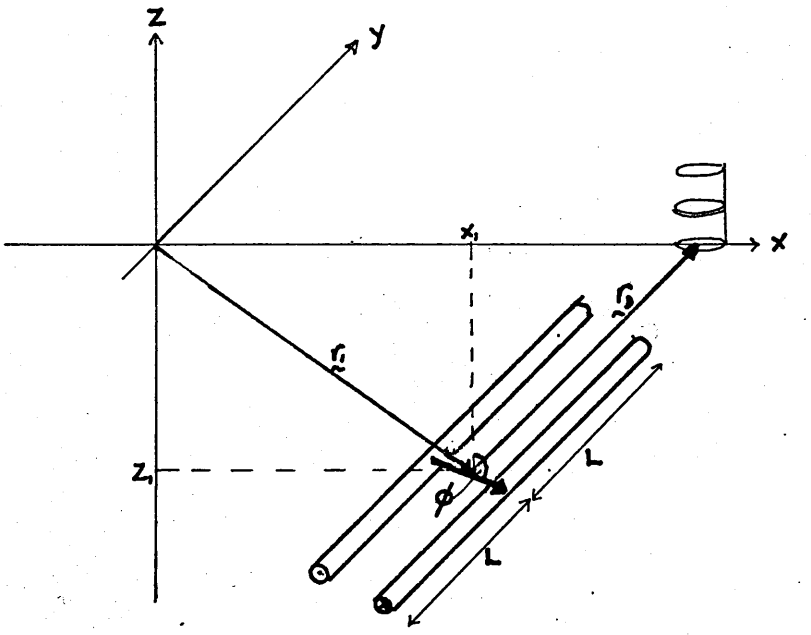

Figure 5.11 Physical representation of a truncated line dipole.

truncated current system which is axially uniform for $-L < y < L$ (figure 5.10) can be reproduced by a multipole expansion at some arbitrarily chosen origin in which the truncated line dipole is the 2nd term.

A full derivation of the gradiometer signal for the truncated line dipole is given in appendix 1. Here I will quote the final result:

$$S_{T_i} = -\frac{\mu m}{2\pi}\frac{1}{\pi c^2}\sum k_i \int_{-c}^{c} \frac{ds}{\left[(s+x_{iD})^2+z_{iD}^2\right]}\left\{\left[\frac{(z_{iD}^2-(x_{iD}+s)^2)(L+h)^2+z_{iD}^2(z_{iD}^2+(x_{iD}+s)^2)}{\left[(x_{iD}+s)^2+z_{iD}^2+(L+h)^2\right]^{\frac{1}{2}}}\right.\right.$$

$$\left.-\frac{(z_{iD}^2-(x_{iD}+s)^2)(L-h)^2+z_{iD}^2(z_{iD}^2+(x_{iD}+s)^2)}{\left[(x_{iD}+s)^2+z_{iD}^2+(L-h)^2\right]^{\frac{1}{2}}}\right]\sin\phi$$

$$\left.-(x_{iD}+s)z_{iD}\left[\frac{((x_{iD}+s)^2+z_{iD}^2+2(L+h)^2)}{\left[(x_{iD}+s)^2+z_D^2+(L+h)^2\right]^{\frac{3}{2}}}-\frac{((x_{iD}+s)^2+z_{iD}^2+2(L-h)^2)}{\left[(x_{iD}+s)^2+z_{iD}^2+(L-h)^2\right]^{\frac{3}{2}}}\right]\cos\phi\right\} \quad (5.2)$$

where S_{Ti} is the required gradiometer signal and other terms are as defined in chapter 4.

Equation (5.2) reduces to equation (4.20) as $L/z_D \rightarrow \infty$.

This equation can now be used to simulate scans across a truncated dipole. The scans can be compared with corresponding scans for the infinite dipole in order to determine how large L must be before the approximation to the infinite dipole is good.

One way to do this is to calculate the misfit parameter R for the two sets of data according to equation 5.1. This has been done and the results are presented in table 5.3 for various values of L and z_1. The calculations were based on scans of 61 data points at 10mm intervals with $x_1 = 0.0$ and $\phi_1 = 65°$. In fact variations in x_1 and ϕ_1 made little

difference to the misfit values.

As might be expected, increasing L or decreasing depth below the sensing coils decreases the misfit. The maximum likely depth of leg dipoles is 80mm. At this depth the misfit is < 7% for L > 90mm. That is to say that 93% of the infinite line dipole signal is produced by currents within 90mm of the detector centre measured along the y axis.

TABLE 5.3

z/mm \ L/mm	30	50	70	90	110	130	150
20	12	3	1	0.6	0.4	0.2	0.2
40	27	9	4	2	1	0.7	0.5
60	39	18	8	4	2	1	1
80	48	26	14	7	4	2	2
100	55	34	20	11	7	4	3
120	61	41	26	16	8	6	4

It is also possible to look at the truncated line dipole in terms of the previously defined criterion of acceptability and determine the minimum L at a given z for which acceptable best fit parameters are computed by the infinite line dipole method. Of particular interest is the minimum L at the maximum likely depth for leg dipoles. As before I will take this to be 80mm. Best fit model parameters have been computed for truncated line dipole scans at this depth. Once more these scans consisted of 61 data points at 10mm intervals with x_1 = 0.0 and $\emptyset_1$ = 65°. Parameter discrepancies are summarised in table 5.4. It can be seen that acceptable fits are obtained for L > 10mm.

The low value for minimum L is encouraging. It arises

because the shape of the signal is maintained down to L = 10mm even though the amplitude decreases. The parameters x*, z* and Ø* are dependent only on the signal shape and are therefore computed accurately. Only m* depends on the amplitude and thus decreases with decreasing L.

Overall, the truncated line dipole calculations show that the signal is dominated by currents within a few cm of the detector and that accurate position and angle parameters may be obtained from very short sections of dipole-like current.

TABLE 5.4

L/ mm	x/ mm	z/ mm	m/m/ %	Ø/ deg
10	9	11	76	14
30	3	5	55	11
50	3	3	32	9
70	2	2	18	6
90	2	1	8	5
110	1	1	5	3

These results are consistent with the experimental data discussed in the last section. The broad conclusion from both experimental and theoretical results is that, provided the current configuration is approximately line dipolar in cross section and reasonably constant over a y range of the order of 10mm either side of the sensing coils, one may expect the line dipole parameters to provide reliable information as to the underlying current structure.

5.5 Summary of results of tests on the line dipole model

The main results of tests described in this chapter may be summarised as follows:

1) 'Pure' line dipole data as generated by equation (4.20) can be modelled essentially perfectly.

2) Using the line dipole algorithm to model a pair of infinite length, oppositely oriented line currents parallel to the y axis locates the line currents' position (x_1, z_1) and orientation $\emptyset_1$ with an accuracy dependent on z and δl, the line current separation.

At depths corresponding to human leg currents, the position parameters x*, z* are accurate to within +10mm and $\emptyset$* to within $\pm 15^\circ$ provided $\delta l < 35$mm.

For $\delta l > 35$mm, the model parameters may be in error by more than these amounts.

3) The line dipole model gives accurate results for three dimensional current patterns, provided the current system in the vicinity of the gradiometer is approximately line dipolar. For example, at $z_1 = -80$mm and $\emptyset_1 = 70^\circ$, the accuracy is better than ±10mm for x,z and $\pm 15^\circ$ for $\emptyset$ provided the gradiometer is at least 70mm away from a sudden 180° twist or ~10mm away from the end of a loop or gradual crossover. Small deviations from parallel ($\sim 5^\circ$) have little effect.

4) The above results are in agreement with simulations using a truncated line dipole which show that more than 93% of the infinite line dipole signal is generated within 90mm of the gradiometer and that a truncated, dipolar configuration with half-length > 10mm can be accurately modelled by the line dipole technique.

The acceptability criteria defined in this chapter are stringent and rather arbitrary. They are meant to give an indication of situations in which the model parameters may be used without correction. However, even where current configurations are such that the parameter discrepancies are not 'acceptable' in terms of the above definition, they may still be useful.

For example figure 5.2 shows that the parameter discrepancies vary cyclically with angle Ø. Knowledge of this variation may be used to correct raw parameter estimates so that accurate information about the current pattern may be obtained. This is discussed further in section 6.3.2.

CHAPTER 6

THE LINE DIPOLE MODEL APPLIED TO LEG DATA

6.1 The leg experiments

Leg signals were measured as described in chapter 2 for a group of 25 subjects with no leg fractures. These subjects define the 'normal' group. Initially the data were intended as a control for measurements made on subjects with fractured fibulae. The fact that the normal limbs consistently produced large, quasi-dc signals was entirely unexpected and merited investigation in its own right. This is particularly so as preliminary analysis of the data indicated currents on the scale of μA which is of the same order as the implanted currents used in the fracture healing techniques described in chapter 1.

A detailed analysis of the signal characteristics, the variation with time and the intersubject variability is given by Lennard (1984) and Grimes, Lennard and Swithenby (1985). Here I wish to concentrate on the application of the line dipole analysis to the data and the information concerning the currents which may be obtained from this analysis.

6.2 The normal leg signal

Figure 6.1 shows a set of scans across the anterior surface of the legs for positions 1 to 7 of subjects BD and

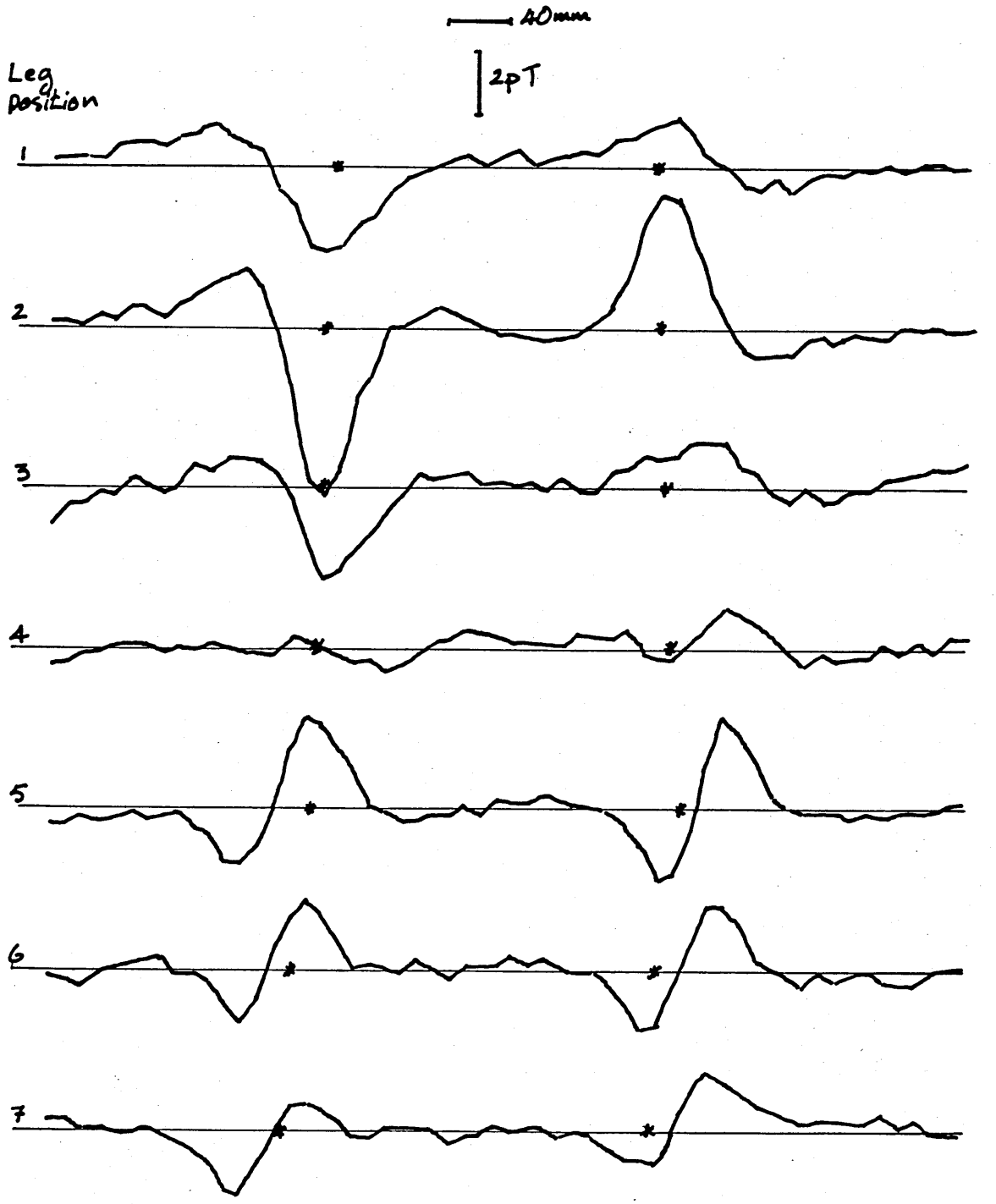

Figure 6.1a) Anterior scans positions 1 to 7 subject BD. Asterisk indicates position of tibial crest.

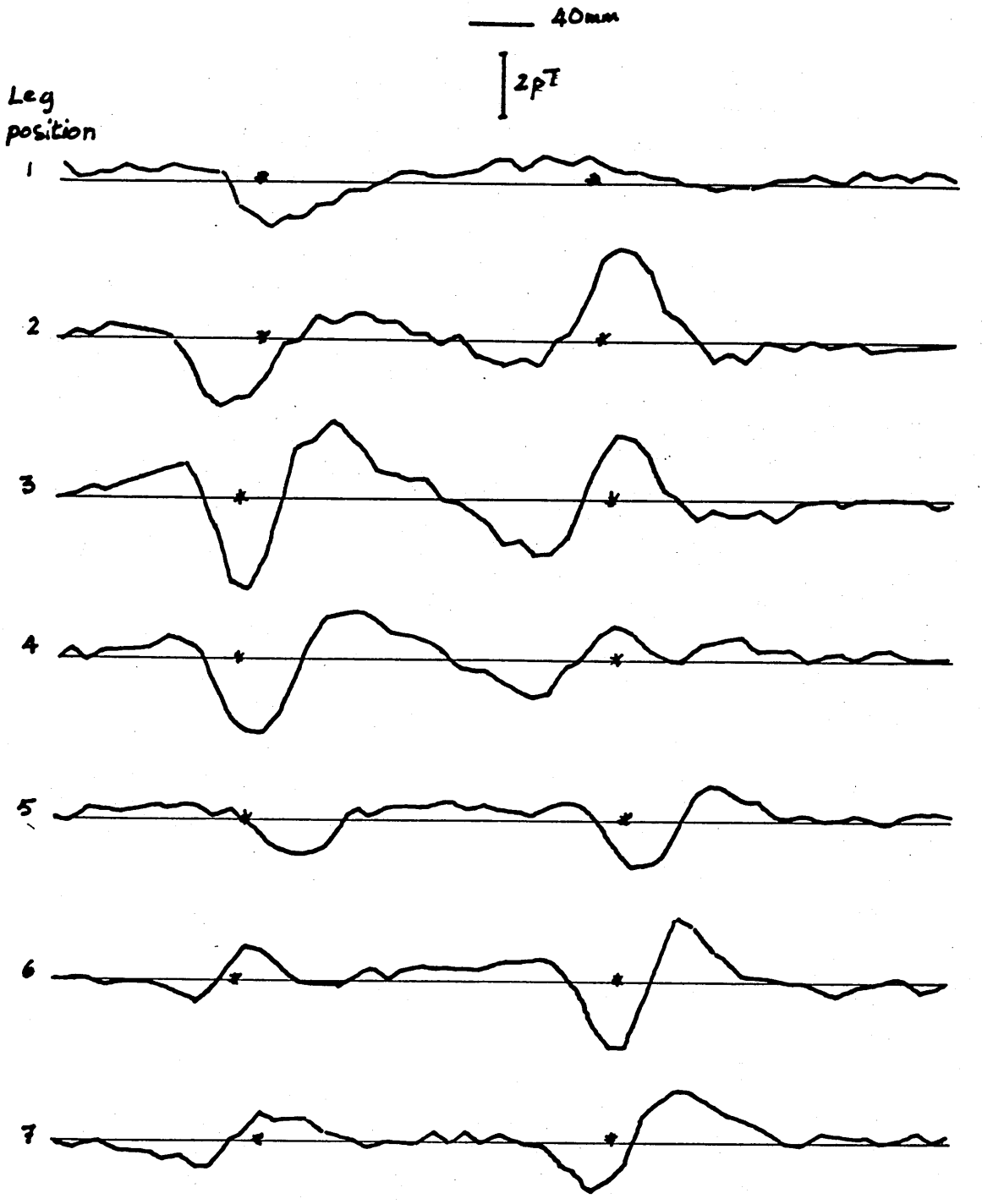

Figure 6.1b) Anterior scans positions 1 to 7 subject AG. Asterisk indicates position of tibial crest.

AG. The leg positions are as defined in section 2.4 and correspond approximately to a spacing of 50 - 60mm. All the data in figure 6.1 were obtained within 15 minutes of the subject getting onto the bed. During this time there was no significant alteration in the signal.

Both sets of scans show a strong signal at positions 2 and 3. In the left leg, this is roughly consistent with a dipolar angle in the range 0° to -90°. The signal decreases or becomes confused at position 4 or 5 and shows a polarity reversal around position 6 or 7. As might be expected the right leg scans were consistent with a current system showing mirror symmetry with the left leg.

For the other subjects investigated the pattern was similar. There was a variability of a factor of 2 or 3 in signal amplitude and some variation in the position corresponding to polarity reversal. Otherwise the scans shown in figure 6.1 are typical.

Superficial injuries such as abrasions or cuts appeared to have no effect on the signal. Neither did a sprained ankle (subject DG) or a chronic leg ulcer (subject JG). The age range of the subjects was 9 years to 73 years. There was no apparent correlation between age and amplitude or structure of signal.

The variation of signal with time was investigated for a subgroup of 12 adult subjects. For these, the signal amplitude decreased significantly over a time period of 1 hour and in 5 out of the 12 it reversed in polarity in this time. Subject discomfort prevented us from ascertaining whether all signals would reverse if given sufficient time.

Active dorsiflexion of the foot brought the signal back to its original amplitude.

An analysis was carried out of the day to day variation of 3 subjects SS, DG and RL. Measurements were made at the same time morning and afternoon for 2 periods of one week. For all 3 subjects, the signals showed no significant variation either from day to day or between morning and afternoon.

6.3 The suitability of the line dipole model applied to the leg signal

In the light of the tests described in chapter 5, it is necessary to consider whether the line dipole method is appropriate to the analysis of the leg signal. Two points need to be considered. Firstly, is the variation in the y direction slow enough to justify the 2-dimensional approximation? Secondly, is the current pattern approximately line dipolar in cross section as defined in section 4.2.2?

6.2.1 The variation with y

Figure 6.2 shows a set of scans from subject JM (left leg). The measured data and field values reconstructed from the best-fit dipole are shown. Best fit parameters are also given. The first 4 scans show only slow variation, with Ø changing between -80° and -30°. From positions 4 to 6 there is a swing through 180° to Ø = 140°. Positions 6 and 7 show a return to a more stable current pattern. Although there is a large change between positions 4 and 6, it occurs over a distance of 100mm.

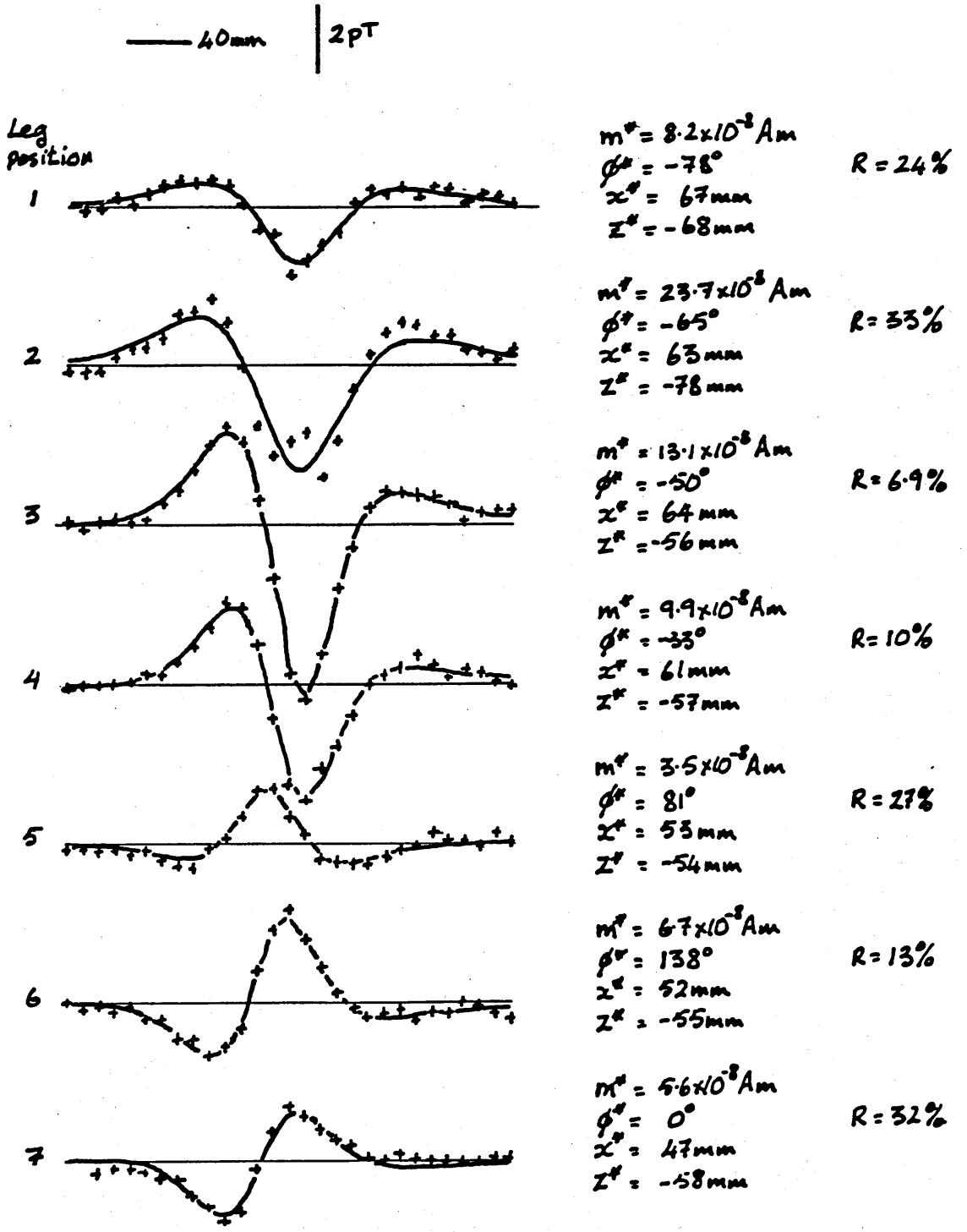

Figure 6.2 Anterior scans for subject JM left leg compared with best fit line dipole signal.

Crosses indicate experimental data. Solid line is best fit model signal.

Referring to section 5.3.2, the change in the leg signal most closely resembles that of the non-parallel wire pair (figure 5.9c). This would suggest that the calculated leg parameters are indeed acceptable unless the scan is within 10mm of a crossover. On this basis only for scan 5 in figure 6.2 would the analysis be suspect, although positions 1 and 7 may well lie close to the end of a loop.

6.3.2 The current cross section

The second question is whether the current pattern is dipolar in cross section. Some guidance here can be obtained from the value of R. Again referring to section 5.3.2, a value of R > 15% appeared to indicate an unacceptable fit. However this was with negligible noise. Table 5.1 shows that a noise with a p to p amplitude which is 5% of the p to p signal can produce a misfit of 15% without significantly affecting the parameters. I will therefore, again rather arbitrarily, use an upper limit of R = 30% as a basis on which to reject line dipole fits. With this criterion, scans 2 and 7 in figure 6.2 would be rejected, although the large R in scan 2 seems mainly due to an anomalous event in the centre of the scan. In scan 7 there appears to be a linear trend superimposed on the signal.

In fact most scans analysed from most subjects have R < 30%. For positions 2 to 4, where the signal to noise ratio is high, R is often < 10%. Positions 5 to 7 generally gave more variable results, occasionally with R > 30%. This can be ascribed partly to a low signal to noise ratio and partly

to the proximity of a crossover or the end of the loop.

As pointed out in chapter 4, a low R value is a necessary but not a sufficient indicator of reliable parameter estimates. For example a large separation between the centres of oppositely directed currents (δl) can generate an inaccurate dipole position with a small R (Section 5.2.2). One way of testing this possibility is to look at the variation of parameter estimates with angle $\emptyset_1$. This variation should be large for large δl.

If this experiment were performed on a pair of antiparallel line currents of fixed geometry, it would be possible to generate a graph of variation of parameter values with $\emptyset_1$ (similar to figure 5.2) and hence deduce δl from the amplitude of the parameter variation. Unfortunately, the effect of gravity on the relaxed, human leg muscle means that its shape does not remain constant under rotation. It is thus not possible to determine δl accurately in this fashion, however a rough estimate may be attempted.

I have chosen to demonstrate this for 2 subjects at position 3. This position reliably gives large signals with small misfit values and is sufficiently far from either the putative crossover region or the possible loop termination close to the knee.

Figure 6.3a shows a set of scans at position 3 for subject RL with respectively anterior, lateral, medial and posterior surfaces uppermost (ie nearest the detector). Figure 6.3b shows the leg profiles obtained during the scans. Superimposed on each profile is the best fit line dipole. The approximate positions of tibia and fibula are

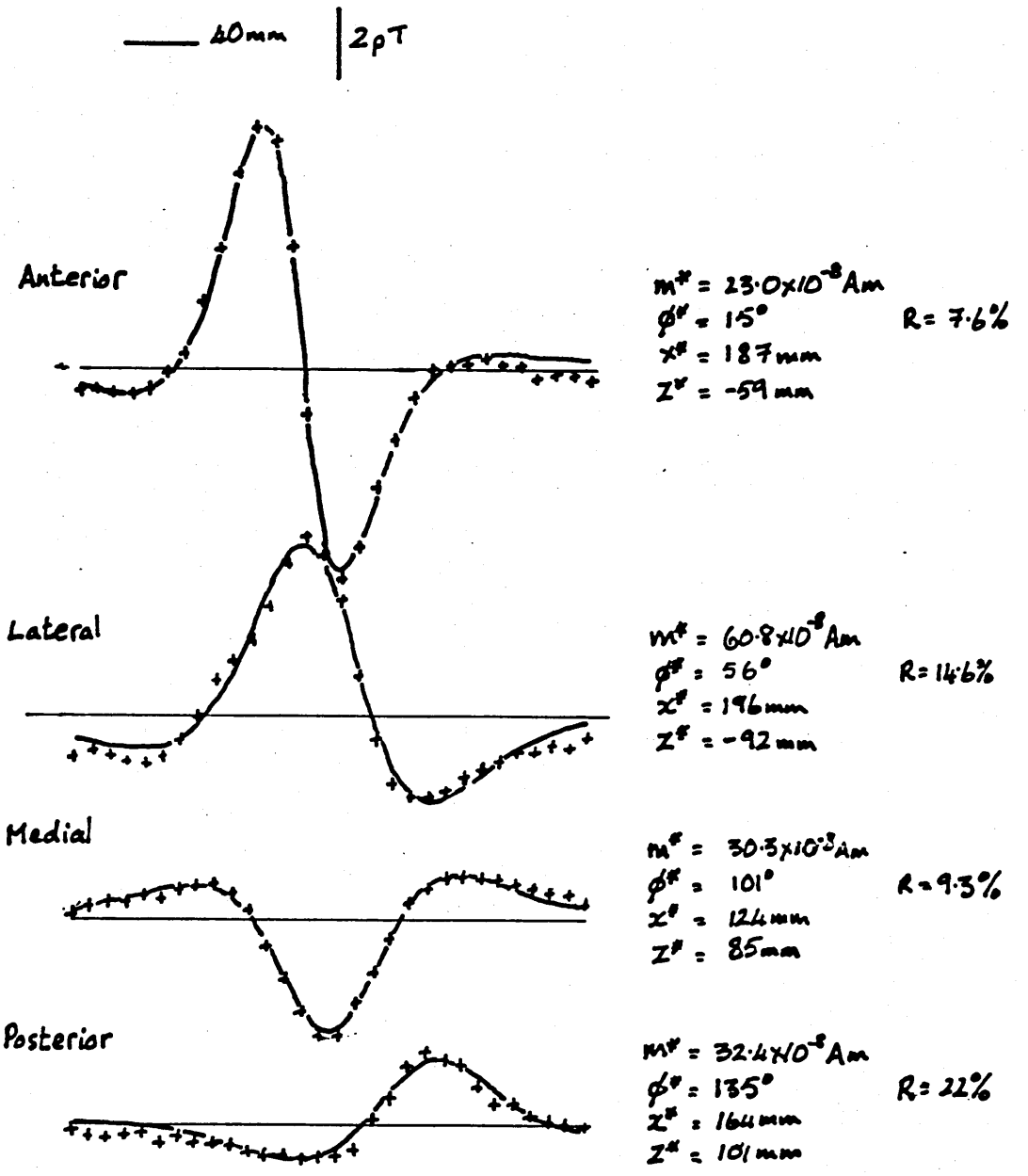

Figure 6.3a) Measured signal and best fit line dipole signal for 4 different aspects at position 3 (subject RL).

Crosses indicate experimental data. Solid line is best fit model signal.

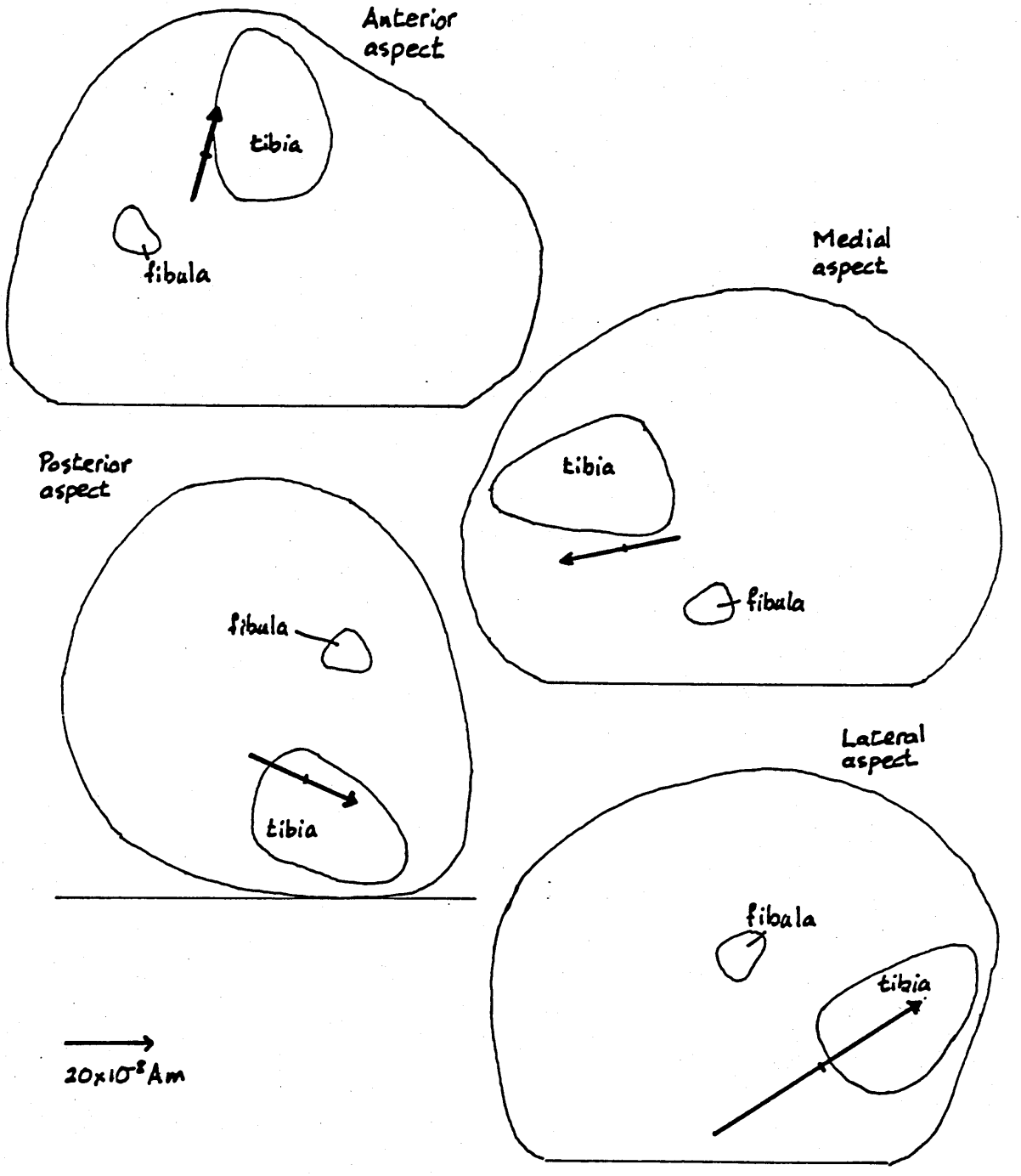

Figure 6.3b) Best fit line dipoles and leg profiles for data in figure 6.3a

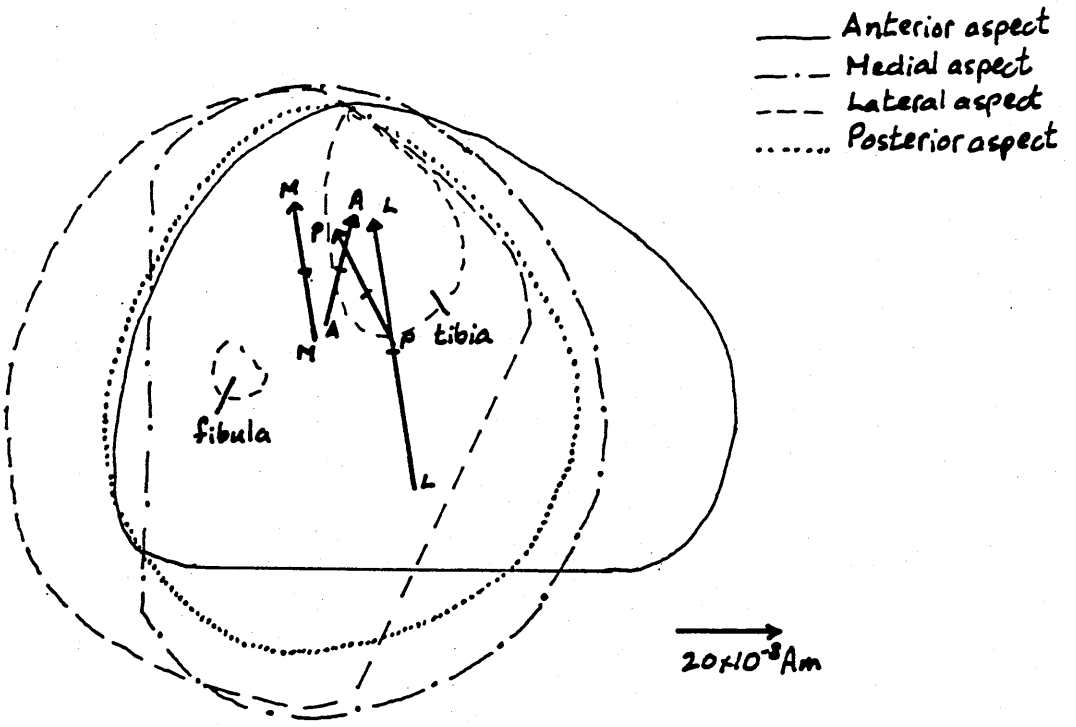

Figure 6.3c) Profiles and dipoles from figure 6.3b redrawn so that tibiae and fibulae coincide.

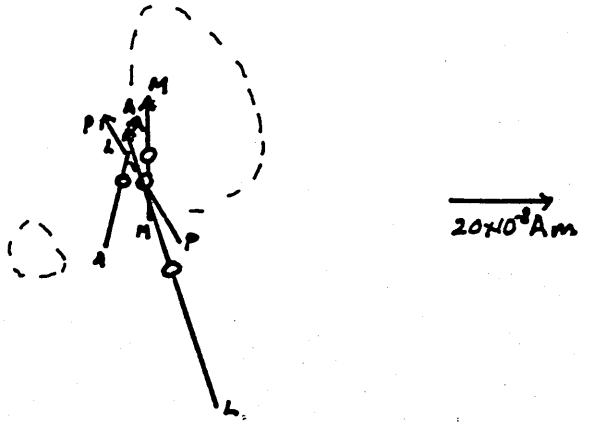

Figure 6.3d Line dipole vectors from figure 6.3c corrected for δl = 60mm.

also included for each case. These were drawn in by comparison with Computer Assisted Tomography (CT) cross sections of a human leg in the same positions.

The difference in leg geometry in the 4 orientations can clearly be seen from the leg outlines. It can also be seen that the best fit dipoles show a degree of consistency. All are near the lateral edge of the tibia and point towards the leg's anterior surface.

This is shown more clearly in figure 6.3c where the leg outlines have been superimposed on each other ensuring that tibiae and fibulae coincide. The dipole vectors do not exactly match, although they all lie within a circle of radius 15mm. It can be seen that the lateral scan dipole is slightly anomalous, being deeper in the leg and much larger than the others.

It is not clear how much of the difference between dipoles is due to a non-negligible current separation and how much is due to the shift in muscle bulk under rotation of the leg, however, using figures 5.2 and 5.3, it is possible to estimate the change in parameters due to an assumed δl and replot the vectors on the diagram. The 'best' δl is then the value which most nearly causes the dipoles to coincide.

In this case the best value is δl = 60mm. The corrected vectors are shown in figure 6.3d. The picture is improved with the exception of the lateral scan vector which has actually moved farther away and deeper into the leg. The anterior, medial and posterior dipole positions now fit within a circle of radius 10mm just on the lateral edge of

the tibia.

Figure 6.4 shows the same process repeated for subject BJ. Figure 6.4a gives the measured and best-fit field data for anterior, lateral, posterior and medial scans and the dipole vectors are superimposed on the appropriate leg outlines in figure 6.4b. The medial scan dipole is clearly anomalous and I will disregard it for the moment. Anterior, posterior and lateral vectors form the same pattern as in figure 6.3c with the lateral vector being larger and deeper. This time an assumed δl of 30mm brings the anterior and posterior dipoles closest together; again the lateral dipole moves deeper. Figure 6.4c gives the corrected vectors.

For the two cases presented, it is not possible to give a precise figure for δl, however if we disregard the medial vector for subject BJ and assume that the lateral scan is influenced by a change in muscle shape, the remaining data are consistent with a current separation of a few cm at position 3 (~60mm for RL, ~30mm for BJ). The assumption regarding the lateral scan is reasonable as, in this position, the calf muscle is supporting the weight of the leg and is displaced from its relaxed configuration.

If these values for δl are assumed correct, the size of the associated leg currents would be ~5 to 10μA. This is consistent with a physiologically reasonable current density in the leg muscle tissue of $0.5\mu Acm^{-2}$ (Lennard 1984).

The medial scan dipole for BJ remains unexplained. Such a shift has not been observed in other subjects and there is no obvious explanation for its occurrence here.

A similar analysis at position 7 on the other side of the crossover did not produce consistent results. As already

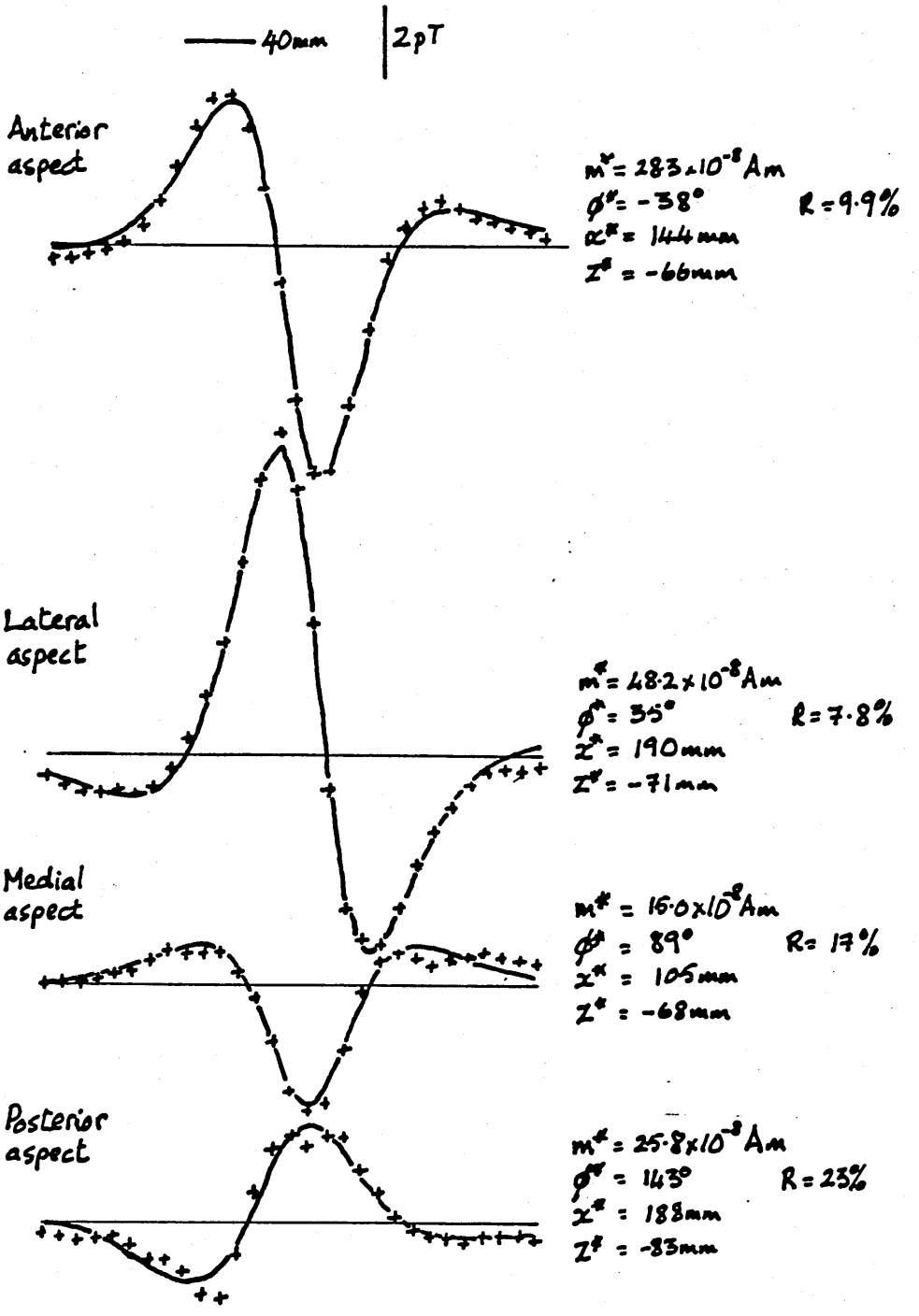

Figure 6.4a) Measured signal and best fit line dipole signal for 4 different aspects of position 3 (subject BJ). Crosses indicate experimental data. Solid line is best fit model signal.

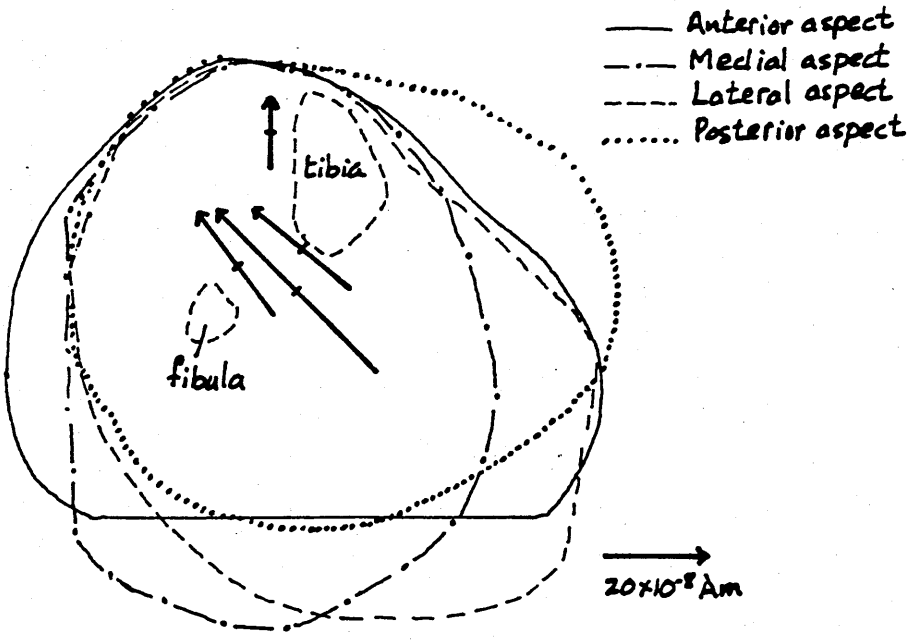

Figure 6.4b) Best fit line dipoles and leg profiles for data in figure 6.4a superimposed so that tibiae and fibulae coincide.

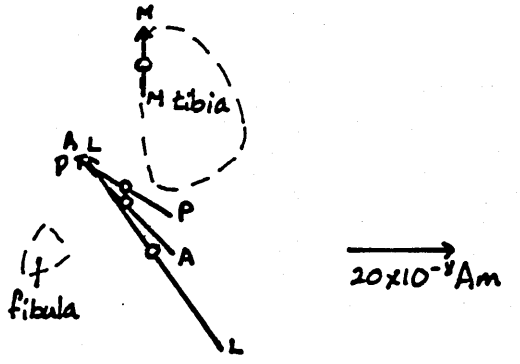

Figure 6.4c) Line dipole vectors from figure 6.4b corrected for δl = 30mm.

mentioned, dipole vectors from positions 5 to 7 are generally less consistent. This may be due to the proximity of the crossover or a loop termination. It may also be simply that the more distal current pattern changes more markedly with leg rotation.

The conclusion to be drawn from the preceding discussion is that the line-dipole is a useful model for describing the leg data. The results of the application of the technique to a full set of scans are described in the next section.

6.4 Detailed analysis of the normal leg signal

Figure 6.5a shows a set of scans for subject DG together with the best fit model signal. Figure 6.5b shows the best fit dipole vectors superimposed on leg profiles which were recorded at each position during the experiment. CT scans were also made of the same leg at approximately the same positions and the tibia and fibula cross sections are taken from these. Figure 6.6 illustrates the main anatomical features of the leg cross section for comparison.

Scans 1 to 4 all have acceptable values of R (R < 30%) and show a consistent picture with the dipole located close to the posterior edge of the tibia. This would indicate a region of current in the positive y direction (i.e. distally directed or down the leg) either in the tibia or immediately anterio-lateral with respect to it. The return current path (proximally directed or up the leg) is quite clearly in the gastrocnemious or soleus muscle compartments. Performing a correction for δl of ~50mm as described in the last section would push the dipole locations anteriorly and laterally as

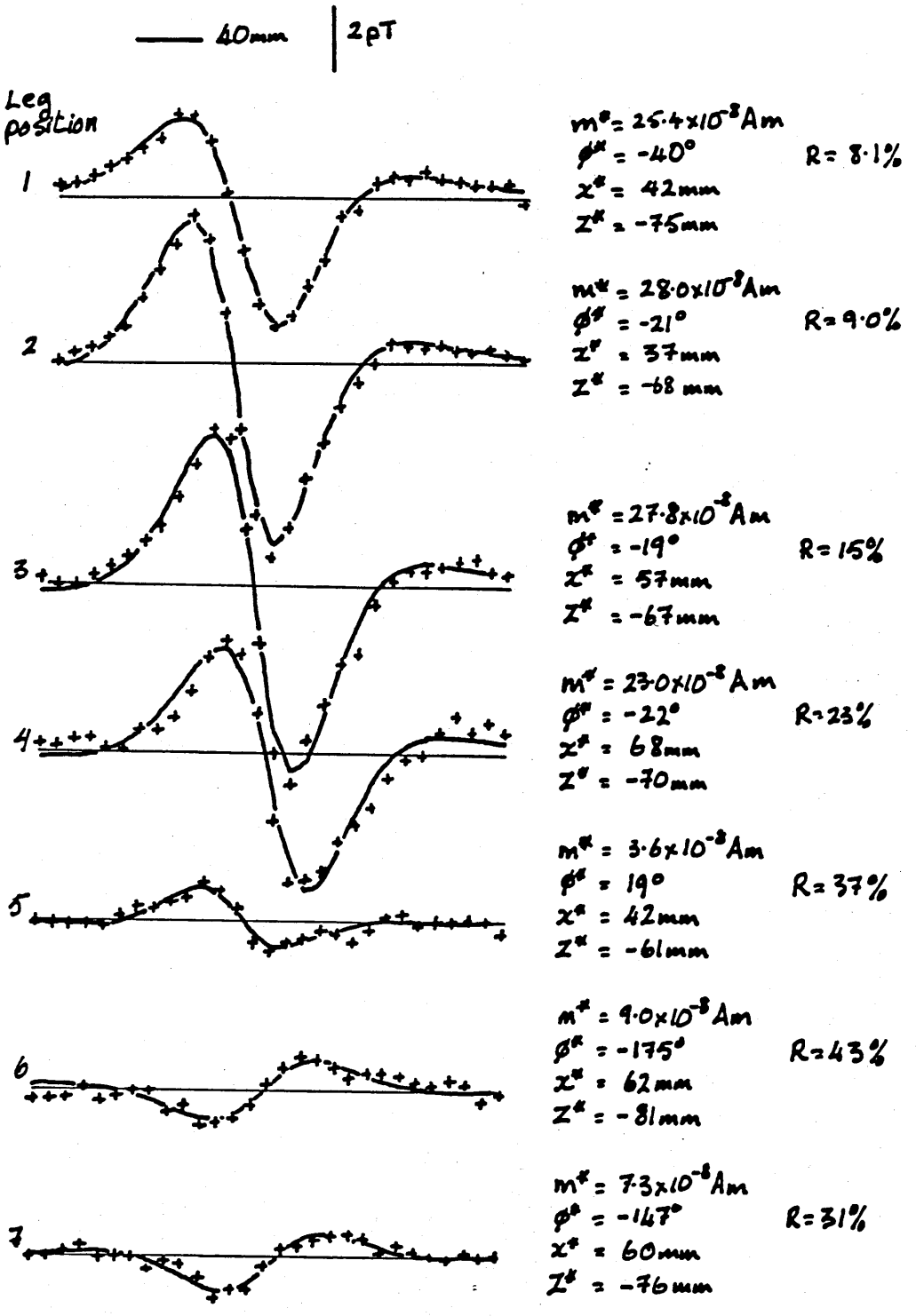

Figure 6.5a) Anterior scans and best fit line dipole signals for positions 1 to 7 subject DG left leg.
Crosses indicate experimental data. Solid line is best fit model signal.

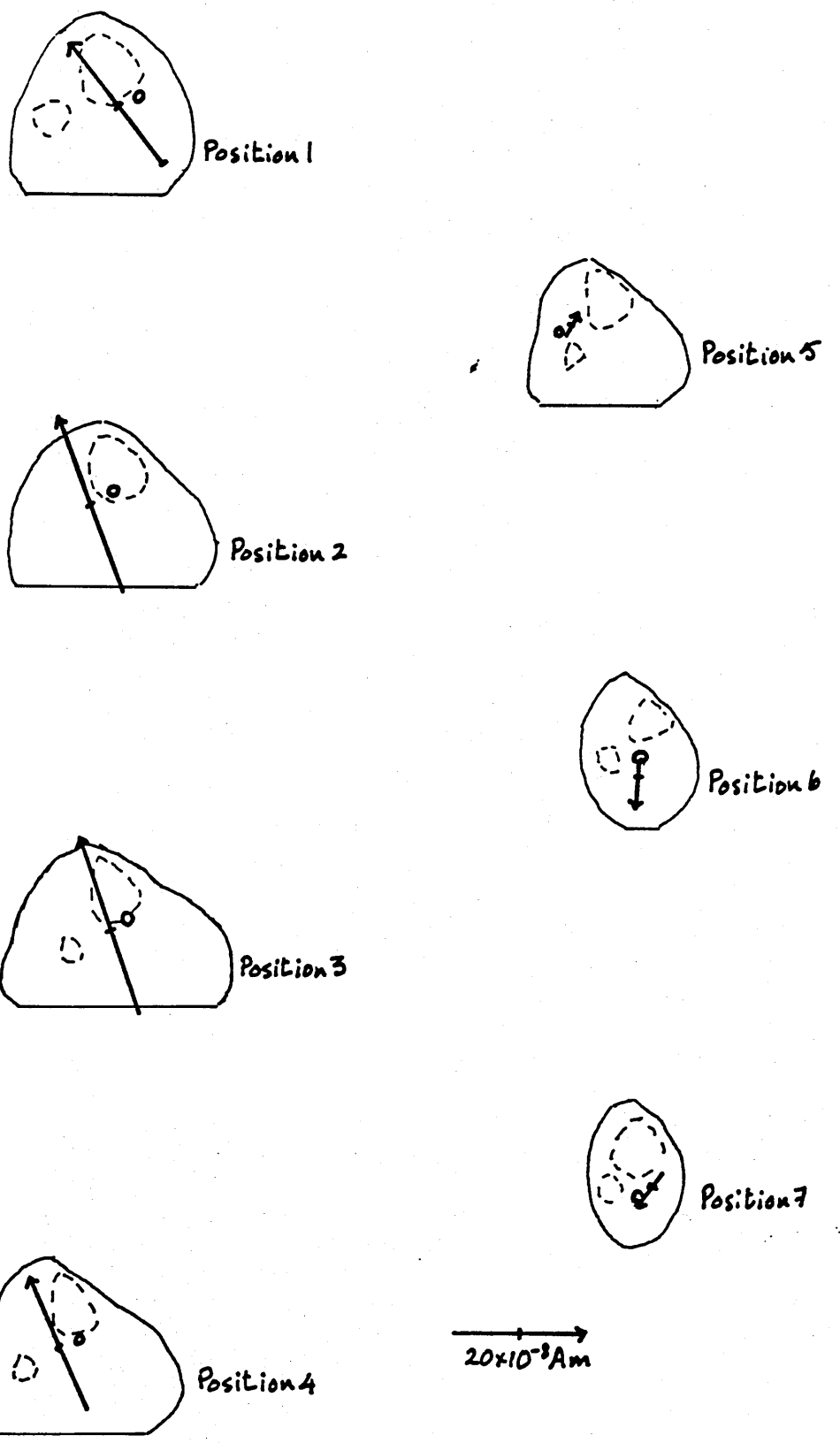

Figure 6.5b) Line dipole vectors and leg profiles for data in figure 6.5a. Open circles show dipole positions corrected for δl = 50mm.

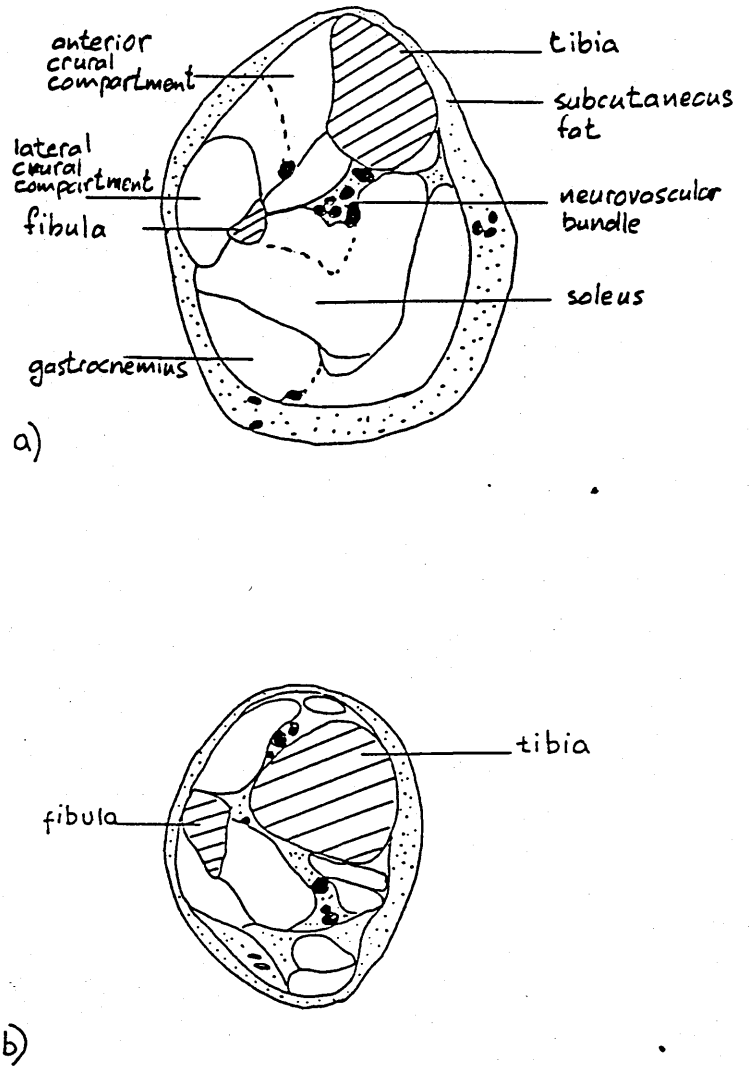

Figure 6.6 Cross section of human left leg showing main anatomical features **a)** 100mm below the knee joint **b)** 60mm above the ankle joint

shown by open circles in the figure. This does not materially alter the possible anatomical locations of high current density.

Scans 5,6 and 7 all show high values of R and are therefore less reliable. However they are consistent with a rotation of the dipole vector so that by position 7 the proximally directed current is uppermost. All currents now appear to be in the posterior muscle compartments. Once more the dipole locations corrected for a non-negligible δl are shown by open circles.

6.5 Variability of the dipole vectors

The scans in figure 6.5 are the only set which can be compared directly with the corresponding leg outlines and CT information, however a comparison may be made with dipole vectors from the same subject at different times and with dipole vectors from other subjects.

Figure 6.7 (from Grimes et al 1985) shows line dipole vectors for subject DG position 3 for 20 different scans. The vectors are superimposed on a typical leg outline using the tibial position as a fixed reference point. There is a variation of ~15mm in the dipole location, however the indicated regions of high current density are in agreement with figure 6.5.

The dipole vectors at postions 3 and 7 for 12 and 10 normal subjects respectively are shown in figures 6.8a and b. The positions are shown relative to the position of the tibial crest. An average leg outline is included to give an idea of the leg shape at each position. More variation is apparent here as might be expected from the variety of leg

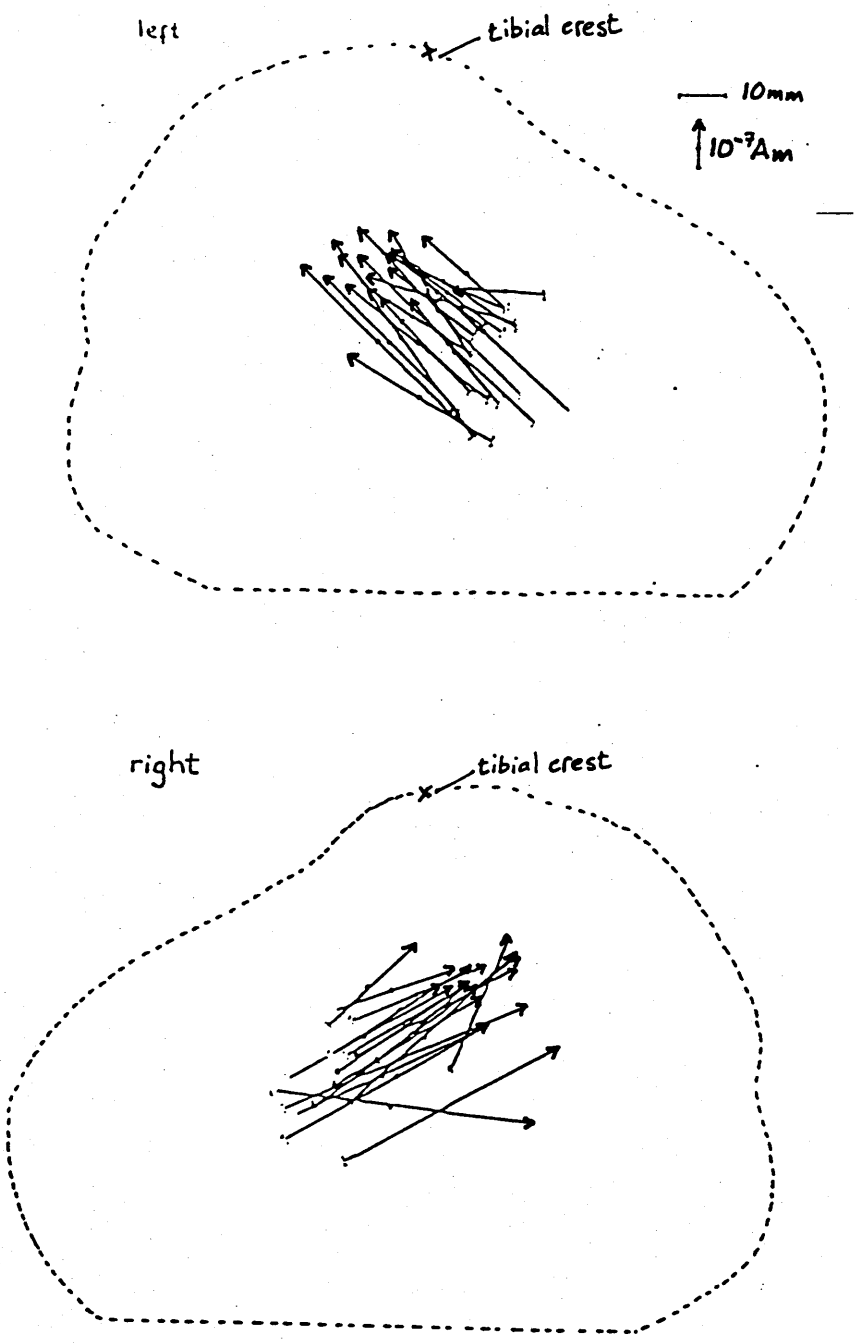

Figure 6.7 Line dipole vectors for subject DG at position 3 for 20 separate scans. From Grimes et al (1985).

shape and size but the orientation of the vectors at position 3 is still broadly consistent with those in figures 6.5 and 6.7.

Comparison of figures 6.8b and 6.5 shows a greater discrepancy at position 7. The average dipole vector appears to be more laterally placed and closer to the anterior surface than is the case for subject DG and it is likely that figure 6.5 is anomalous in this respect. Figure 6.8 suggests that in the more distal leg positions, the currents may be located entirely within the anterior and lateral crural muscle compartments.

6.6 Variation of dipole vectors with movement of muscle bulk

Confirmation that the proximally directed current location is in the posterior muscle compartments is given by the results of a further experiment. Three scans were performed at position 3 for subject RL over a period of 10 minutes. Between successive scans the calf muscle was moved manually in a lateral direction while still remaining relaxed. The positions of the resultant dipole vectors are shown in figure 6.9. They clearly indicate that the centre of proximal current shifts with the muscle bulk.

6.7 Possible current configurations within the leg

The dipole vectors indicate regions of high current density directed parallel to the leg axis at each leg position, however they must correspond to a 3 dimensional current distribution in the leg as a whole. Two current patterns consistent with the results discussed in the

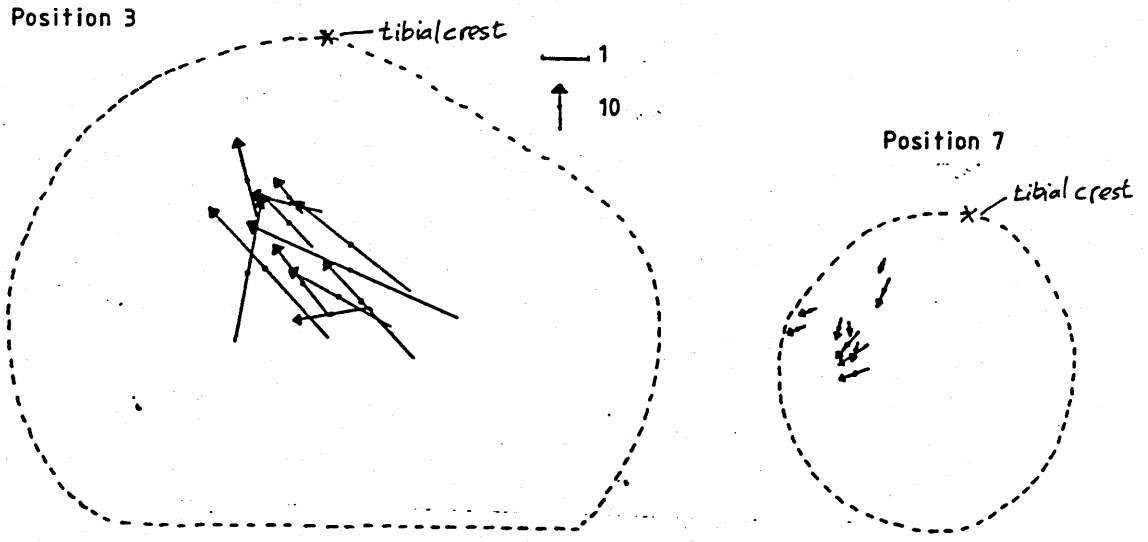

Figure 6.8 Line dipole vectors **a)** position 3 for 12 normal subjects **b)** position 7 for 10 normal subjects. From Grimes et al (1985).

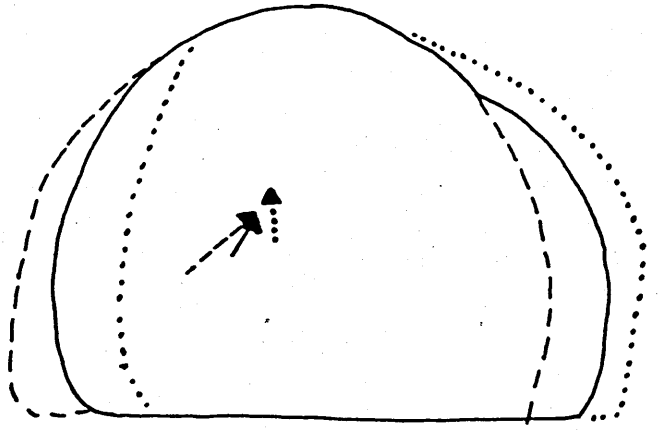

Figure 6.9 Change in line dipole vector with movement of posterior muscle bulk. From Grimes et al (1985)

previous sections are shown in figure 6.10.

For positions 1 to 3, the proximally directed currents are located in the posterior muscle bulk and the distal flow is either in the anterior crural compartment or possibly in the tibia. For positions 6 and 7, the pattern is less certain, as the fit to the data is in general less good. It seems, however that the downward current is still in the anterior or lateral crural regions but the upward current is now much closer - either also in the anterior crural compartment or in the tibia.

It is not clear whether we are looking at a single,'figure of eight' pattern or two separate loops. In the case of a single loop, the decrease in size of the dipole moment in the more distal positions would have to be due to a decrease in current separation. This would be consistent with upward and downward flows being compressed into the anterior and lateral crural compartments. If the pattern consists of two separate loops, then the decrease in vector size could be either due to a smaller separation or a smaller current strength.

6.8 Physiological mechanism for currents in a normal subject

The above analysis suggests that the leg currents occur predominantly in the muscle compartments and perhaps also in the tibia. The variation of signal structure with muscle activity described in section 6.1 points towards a current source in the muscle cells, however there are other possibilities which need to be considered. These are:

1) Currents may occur in response to potential

differences caused by mechanical stresses in bone (see section 1.4).

2) The observed field may be due to the flow of ionic species in the blood stream.

3) The observed field may be due to movement of ionic species along nerve cells.

If the fields were due to ionic transport in the nerves, one would expect a major part of the current to be in the neurovascular bundle at the posterior edge of the tibia. Comparing figures 6.5 and 6.6, it is not likely that this is a region of high current density.

Lennard (1984) describes experiments to investigate the possibilities of the currents being related to blood flow or tibial stress. The results show that mechanical stressing of the tibia while the leg muscle is relaxed produced no signal variation. Likewise prevention of blood flow by arterial occlusion had no discernible effect. It is therefore highly probable that the currents are generated within the muscles themselves.

As mentioned in section 1.4, there is some evidence that inhomogeneous distribution of Cl^- leakage channels in the muscle cell membranes of rats gives rise to dc currents along cell membranes acting to re-equilibrate ionic concentrations (Betz et al, 1984). It may be that an aggregation of such currents occurs in the human leg muscle giving rise to the measured effects. The signal change after dorsiflexion would be consistent with increased ionic activity after an action potential.

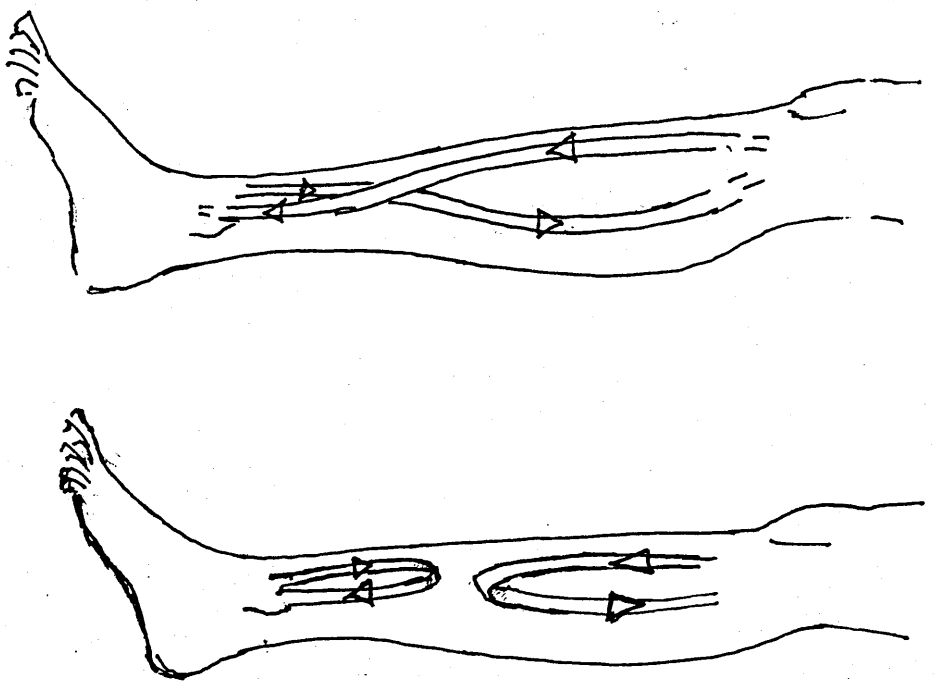

Figure 6.10 Possible leg current configurations.

6.9 Line dipole analysis of data from a fibula fracture

The main aim of the biomagnetic project with which these modelling techniques are associated is to investigate the possibility of currents associated with healing fractures. As described in the preceding pages, the line dipole approach has been successfully applied to the data from normal (i.e. unfractured) legs and a variety of other simple current structures. If currents associated with fractures give rise to detectable fields, it is to be expected that they could be mapped using the same technique.

Initially, the intention was to analyse tibial fractures as they are relatively common and the majority of non-unions occur here. Unfortunately, it has not yet been possible to overcome problems of magnetic contamination of leg casts. All cast materials so far investigated have contained ferromagnetic contaminants in sufficient quantity to make reliable data analysis impossible.

Consequently, the opportunity to apply my techniques to fractured legs has been limited to the investigation of a single fibula fracture (subject TR). The fibula is non-weight bearing so a cast is usually unnecessary. Unfortunately fibula fractures are not common.

For TR, a fracture was evident from X-ray photographs approximately in the middle of the right fibula at position 3 on our anatomical scale. Scans made across the anterior surfaces of both legs 15 days after the fracture are presented in figure 6.11.

Comparison with figure 6.1 shows that the right leg field has abnormally high amplitudes at position 6 and 7. It may also be noted that the signals are not consistent

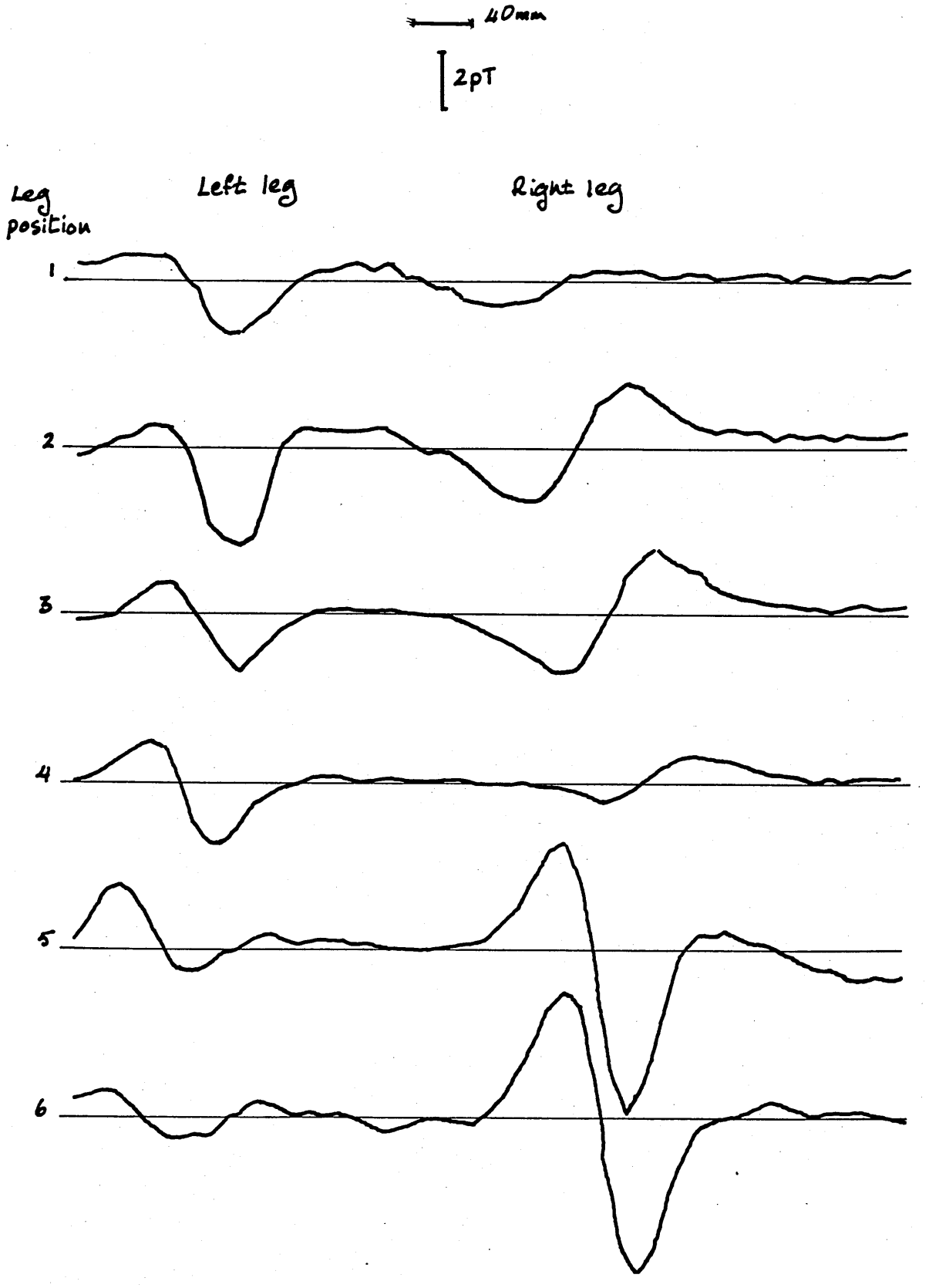

Figure 6.11 Anterior scans positions 1 to 6 for subject TR with a fibula fracture. Fracture is located in the vicinity of position 3, right leg.

with the expected mirror symmetry between right and left leg current patterns.

Figure 6.12 shows the line dipole vectors for the data fom TR. Owing to subject discomfort, leg profiles were not taken during the measurements so that the positions of tibia and fibula in the figure have been estimated from the location of the tibial crest.

The left leg vectors have one or two anomalous features. At positions 1 and 2, they appear very medial. The reason for this is not clear. At position 6, the vector is reversed with respect to the normal orientation, however the value of R indicates a very poor fit.

The right leg vectors are significantly different to those from any other subject. At positions 2 and 3 they are large and downward pointing, indicating a distally directed current in the posterior muscle compartments. There is an abrupt 180° shift in orientation between positions 4 and 5 and the vectors at positions 5 and 6 are abnormally large and appear to be more centrally located in the leg than usual. Apart from position 1, the fit to the data is everywhere excellent.

It is clear that the current configuration in the fractured leg is highly anomalous and the orientation of the vectors again suggests charge flow predominantly in the muscle bulk. Beyond that, the lack of anatomical information makes it difficult to determine the reason for the different pattern.

It is certainly interesting that the data relating to a leg fracture are also the only data in which such marked

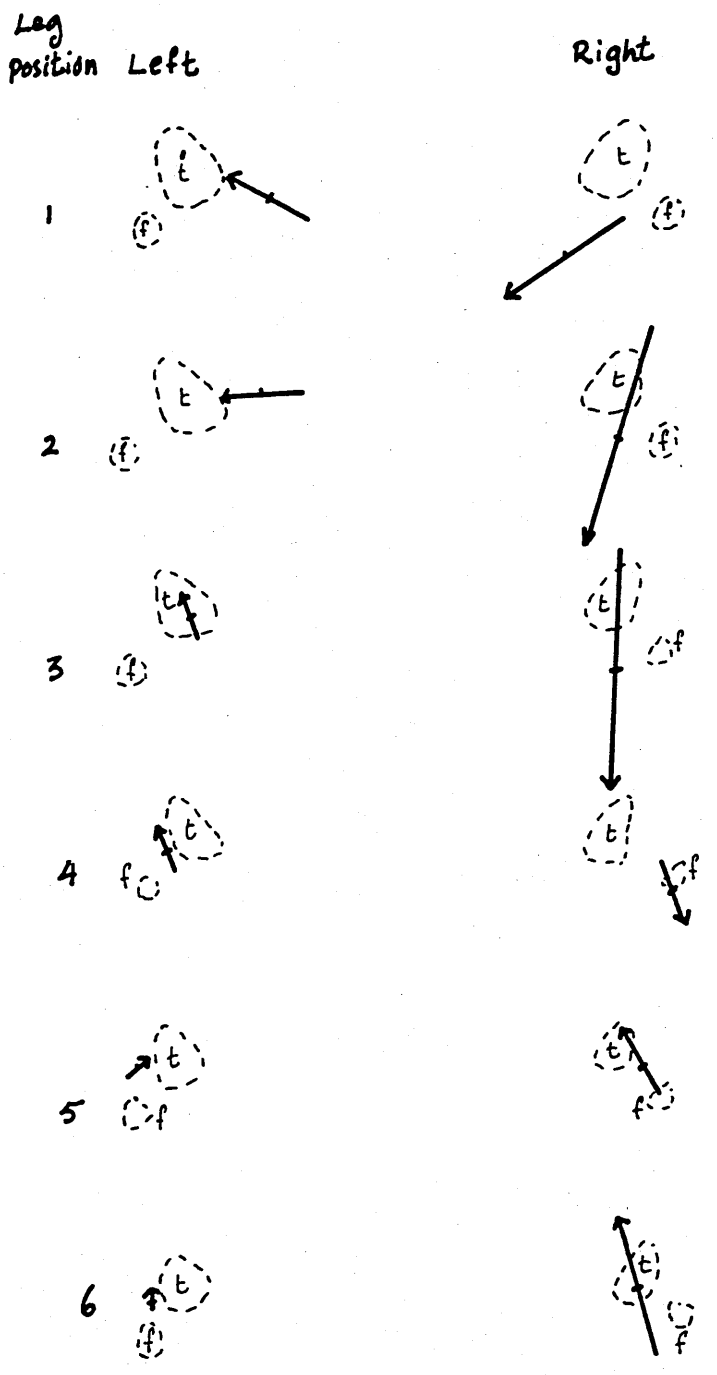

Figure 6.12 Line dipole vectors related to approximate tibia and fibula positions for subject TR.

differences exist between the legs and where such large fields have been measured in the vicinity of the distal part of the lower leg. Other subjects with minor leg injuries such as abrasions, bruising, sprains and ulcers have been investigated. None of these injuries had any noticeable effect on the signal.

This does not necessarily imply a causal relationship between the fracture and the anomalous signal. If the hypothesis attributing the normal currents to Cl^- channels in muscle fibres is correct, it could be that the severe damage to the muscle adjacent to the fracture site causes an alteration in current pattern. On the other hand, injury currents associated with the fracture or the damage in the surrounding tissue could be superimposed on the normal currents. More experimental evidence is needed to resolve this issue.

6.9 Summary of results

The line dipole analysis has been applied to leg field data from a number of normal, healthy subjects and one subject with a fibula fracture. Inspection of the data indicates that the signal variation in the y direction is slow enough for the line dipole method to be applicable. The variation of parameter values as the leg is rotated about its long axis are consistent with upward (proximally directed) and downward (medially directed) currents of 5 to 10 μA, the centres of current being separated by a few centimetres. There is also evidence that a change in muscle geometry alters the current pattern.

The fit to the data is generally good and the modelling

technique is successful in that it provides a useful method of characterising leg signals. It also gives the relative location of upward and downward current densities and points to the currents being predominantly in the muscle bulk of the leg.

The analysis of the fractured leg data indicates a current pattern which is significantly different from all normal subjects although the physiological significance of this is not clear. More studies of subjects with fractures are needed to clarify this point.

CHAPTER 7

THE LINE CURRENT LOOP ITERATIVE-PERTURBATIVE MODEL - THEORY AND 2-DIMENSIONAL LOOPS

7.1 Introduction

The line dipole model discussed in the preceding chapters succeeds in its primary goal of characterising the field pattern and providing useful information about current structure for current loops and the endogenous currents of the human leg. It suffers from certain limitations already discussed at some length in chapters 5 and 6. These are:

1) there is no requirement for current continuity from scan to scan

2) all currents are assumed to be parallel to the y axis

3) best fit parameter values may become inaccurate if the current distribution changes rapidly with y or if there is an appreciable separation between the centres of oppositely directed currents.

The line current loop model described in this chapter has been developed in an attempt to overcome these limitations. As the name implies, the aim is to fit the target data with the field generated by a line current forming a closed loop of arbitrary shape. Both spatial and current continuity are inbuilt requirements which the best fit loop must satisfy, thus avoiding the discontinuous

solutions of a scan by scan approach. The loop model also removes the restriction on current direction. An individual loop segment may have any orientation.

As far as the human leg data are concerned, the model is still somewhat nonphysiological in that the conductivity structure of the leg suggests that any current path should have a finite cross-section. However actually modelling such a diffuse system would represent an enormous increase in complexity and it is not unreasonable to expect that the best fit line current loop will define some average current path through the leg. The line current loop model is thus a compromise between the physically realistic and the computationally feasible.

As for the line dipole technique, this model has been developed with a view to solving a specific biomagnetic inverse problem but it is, of course, quite generally applicable and may be used in any situation where currents approximating to a line current loop are to be determined from the magnetic field map. My aim in this chapter is to describe the technique and illustrate its application to actual line current loops and to magnetic field data from the human leg.

7.2 An overview of the iterative perturbative method

The approach adopted here for determining the best fit loop is similar to an iterative perturbative algorithm used by Mackintosh and Ioannides (1985) in relation to the inverse problem for nuclear scattering.

There are two stages. In stage 1 all available

information is used to make a first estimate of the loop shape (the starting reference loop or SRL) and the current strength. In stage 2, a set of perturbations is superimposed on the SRL and the amplitudes of the perturbations are adjusted so as to reproduce the target data as closely as possible. This new loop is then used as the SRL for a second iteration and the process is repeated until a stable solution is reached or until the fit to the data achieves some predetermined level of acceptability.

An important feature of the method is its interactive nature. The inversion is performed on a computer in real time and the program allows the operator to intervene at certain stages and adopt various strategies to optimise the fitting procedure. These strategies are discussed in more detail in subsequent sections.

7.3 Theoretical considerations

7.3.1 The loop geometry

We assume that the target field $\underset{\sim}{B}_T(\underset{\sim}{r})$ can be reproduced by a line current loop L described by the vector $\underset{\sim}{L}(t)$, where t is a parameter which defines the locus of points on the loop. L is then the target loop which must be determined. The model or reference loop l is denoted by $\underset{\sim}{l}(t)$ and the difference between the two loops is $\underset{\sim}{p}(t)$. The arrangement is shown in figure 7.1. Thus:

$$\underset{\sim}{p}(t) = \underset{\sim}{L}(t) - \underset{\sim}{l}(t) \qquad (7.1)$$

A field point at position $\underset{\sim}{r}$ has displacements $\underset{\sim}{R}(t)$ and $\underset{\sim}{R}_0(t)$ from $\underset{\sim}{L}(t)$ and $\underset{\sim}{l}(t)$ respectively. So we also have:

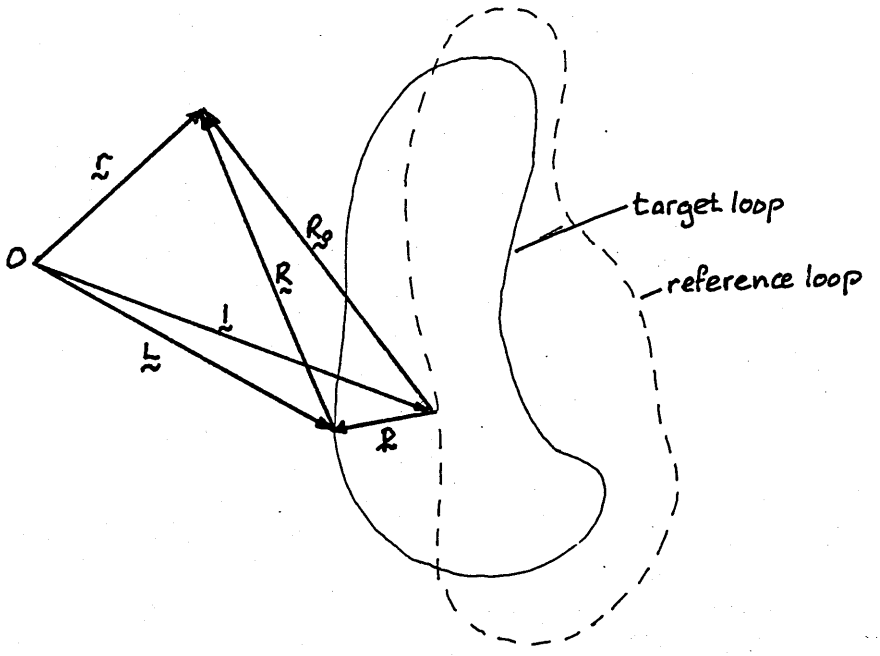

Figure 7.1 Coordinate system used for the line current loop model.

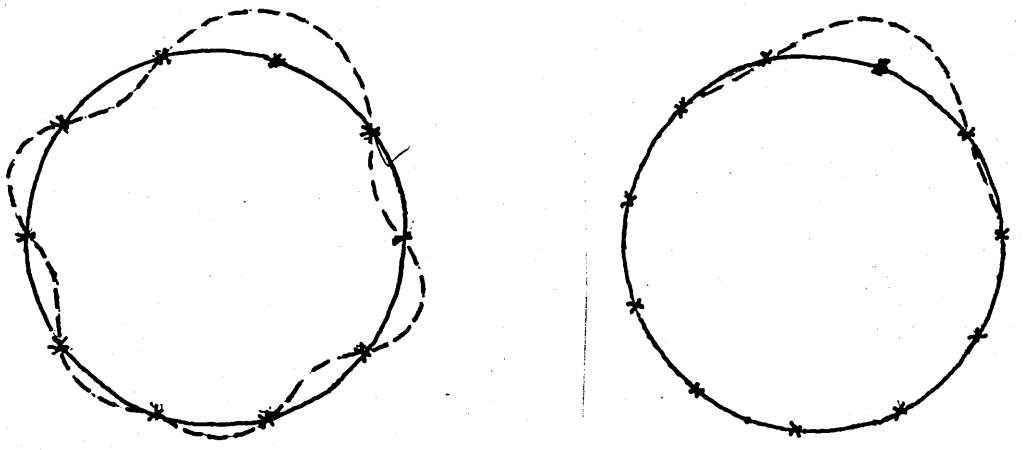

Figure 7.2 The effect of adding a perturbation to a loop. The original, circular loop is indicated by a solid line, the loop shape after the perturbation has been added is shown dashed. The perturbation centre is marked *, other knots are marked x. **a)** $\delta = 0.5$ **b)** $\delta = 1.0$.

$$\underset{\sim}{p}(t) = \underset{\sim}{R}_0(t) - \underset{\sim}{R}(t) \qquad (7.2)$$

For each value of t, $\underset{\sim}{p}$ can be specified in terms of a linear sum of vector functions which describe perturbations on 1. The perturbations are defined in the following way. A number (N_p) of t values are designated 'knots' or perturbation centres. Each knot acts as the centre for 2 orthogonal perturbation functions. Thus the kth knot at position t_k acts as the perturbation centre for functions $\underset{\sim}{f}_{1k}$ and $\underset{\sim}{f}_{2k}$. Hence $\underset{\sim}{p}(t)$ can be written:

$$\underset{\sim}{p}(t) = \sum_{j=1}^{2} \sum_{k=1}^{N_p} \lambda_{jk} \underset{\sim}{f}_{jk}(t) \qquad (7.3)$$

where the λ_{jk} represent the perturbation amplitudes and:

$$\underset{\sim}{f}_{1k}(t) = f_k \hat{\underset{\sim}{e}}_1 = f(t-t_k)\hat{\underset{\sim}{e}}_1 \qquad (7.4a)$$

$$\underset{\sim}{f}_{2k}(t) = f_k \hat{\underset{\sim}{e}}_2 = f_k(t-t_k)\hat{\underset{\sim}{e}}_2 \qquad (7.4b)$$

$\hat{\underset{\sim}{e}}_1$ and $\hat{\underset{\sim}{e}}_2$ are mutually perpendicular unit vectors. Usually $\hat{\underset{\sim}{e}}_1$ will be the local principal normal to the loop and $\hat{\underset{\sim}{e}}_2$ will be the local binormal. We also require:

$$f_j(t_k) = \delta_{jk} a_j \qquad (7.5)$$

where the a_j are nonzero constants and δ_{jk} is the Kronecker δ. Equation (7.5) thus ensures that the

perturbations are linearly independent.

In this work, damped cubic splines have been used for the functions f_k. So:

$$f_k(t) = e^{-\delta(t-t_k)} g_k(t-t_k) \qquad (7.6)$$

where g_k is a cubic spline function. It can be seen from this equation that the damping factor δ controls the range of t over which an individual perturbation is effective. A detailed description of the perturbation functions is given in Ioannides and Grimes (1986).

The effect of a single perturbation on a circular loop is illustrated in figure 7.2 for 2 different values of δ. The positions of the loop knots are also indicated.

Having defined the perturbation functions, the next step is to express the target field as a function of the amplitudes λ_k. From figure 7.1 and Biot-Savart, we have:

$$\underset{\sim}{B}_T(\underset{\sim}{r}) = \frac{\mu_o I}{4\pi} \oint \frac{dt}{R^3} \left(\frac{d\underset{\sim}{l}}{dt} \times \underset{\sim}{R} \right) \qquad (7.7)$$

$$\underset{\sim}{B}_o(\underset{\sim}{r}) = \frac{\mu_o I}{4\pi} \oint \frac{dt}{R_o^3} \left(\frac{d\underset{\sim}{l}}{dt} \times \underset{\sim}{R}_o \right) \qquad (7.8)$$

It is possible to show that $B_T(r)$ can be expressed as a power series expansion in the perturbation amplitudes (Ioannides and Grimes (1986)). Thus:

$$\underset{\sim}{B}_T(\underset{\sim}{r}) = \underset{\sim}{B}_o(\underset{\sim}{r}) + \sum_{j=1}^{2} \sum_{k=1}^{N_p} \lambda_{jk} \left[\underset{\sim}{G}_{jk}(\underset{\sim}{r}) + \sum_{j'=1}^{2} \sum_{k'=1}^{N_p} \lambda'_{jj'kk'} \left[\underset{\sim}{G}_{jj'kk'}(\underset{\sim}{r}) + \cdots \right] \right] \qquad (7.9)$$

where the perturbation coefficients G_{jk}, $G_{jj'kk'}$ etc.

depend on $\underset{\sim}{R}_o$ and f_k. These coefficients may be derived analytically (Ioannides and Grimes, 1986), however the 1st order terms $\underset{\sim}{G}_{jk}$ can be estimated quite simply by numerical methods. In fact equation (7.9) truncated to 1st order is sufficient for our purpose, so the numerical approach has been adopted here.

At a given value of $\underset{\sim}{r}$, $\underset{\sim}{G}_{jk}$ can be estimated by applying a single, jkth perturbation of known amplitude to the loop and calculating the field change at $\underset{\sim}{r}$. Specifying λ_{jk} as the only non-zero perturbation amplitude and allowing it to have values of +A and -A (where A is known as the unit perturbation amplitude) gives two expressions for the field $\underset{\sim}{B}_{jk}$ at r:

$$\underset{\sim}{B}_{jk}(\underset{\sim}{r},A) = \underset{\sim}{B}_o(\underset{\sim}{r}) + A\,\underset{\sim}{G}_{jk}(\underset{\sim}{r}) + A^2\,\underset{\sim}{G}_{jjkk}(\underset{\sim}{r})$$

$$\underset{\sim}{B}_{jk}(\underset{\sim}{r},-A) = \underset{\sim}{B}_o(r) - A\,\underset{\sim}{G}_{jk}(\underset{\sim}{r}) + A^2\,\underset{\sim}{G}_{jjkk}(\underset{\sim}{r})$$

from which:

$$\underset{\sim}{G}_{jk}(\underset{\sim}{r}) = \frac{\underset{\sim}{B}_{jk}(\underset{\sim}{r},A) - \underset{\sim}{B}_{jk}(\underset{\sim}{r},-A)}{2A} \qquad (7.10)$$

The $\underset{\sim}{G}_{jk}$ values defined in this manner are correct to 2nd order.

In practice we are interested in a single component of $\underset{\sim}{B}(\underset{\sim}{r})$ which I will denote by the subscript z. (In our biomagnetic work, this is the vertical component, although the theory applies equally to any other component). For the single component, equation (7.9) becomes:

$$B_{Tz}(\underset{\sim}{r}) = B_{oz}(\underset{\sim}{r}) + \sum_{j=1}^{2}\sum_{k=1}^{N_p} \lambda_{jk}\left[G_{jkz}(\underset{\sim}{r}) + \sum_{j'=1}^{2}\sum_{k'=1}^{N_p} \lambda_{j'k'}\left[G_{jj'kk'z}(\underset{\sim}{r}) + \cdots\right]\right] \quad (7.11)$$

7.3.2 The loop current

Equation (7.11) implicitly assumes that the current in the reference loop is equal to the target current. Of course, in reality, the current in L is another unknown parameter and should appear explicitly. This can be done quite easily. Let the estimate of the current in l be I_o. Let the actual current in L be I and write :

$$\delta I = I - I_o$$

(7.11) now becomes:

$$B_{Tz}(\underset{\sim}{r}) = \left(1+\frac{\delta I}{I_o}\right)\left\{B_{oz}(\underset{\sim}{r}) + \sum_{j=1}^{2}\sum_{k=1}^{N_p} \lambda_{jk}\left[G_{jkz}(\underset{\sim}{r}) + \sum_{j'=1}^{2}\sum_{k'=1}^{N_p} \lambda_{jk'}\left[G_{jj'kk'z}(\underset{\sim}{r}) + \cdots\right]\right]\right\} \quad (7.12)$$

which can be rewritten as:

$$B_{Tz}(\underset{\sim}{r}) = \mu_o B_{oz}(\underset{\sim}{r}) + \sum_{j=1}^{2}\sum_{k=1}^{N_p} \mu_{jk}\left[G_{jkz}(\underset{\sim}{r}) + \varepsilon_{jk}(\underset{\sim}{r})\right] \quad (7.13)$$

where

$$\mu_o = \left(1+\frac{\delta I}{I_o}\right); \qquad \mu_{jk} = \left(1+\frac{\delta I}{I_o}\right)\lambda_{jk}$$

and ε_{jk} replaces the higher order terms.

Equation (7.12) now forms the basis for a matrix of equations with $2N_p+1$ unknowns (μ_o and μ_{jk}, (k=1,N_p, j=1,2)). In principle, provided $2N_p+1$ values of B_{Tz} are available for different values of $\underset{\sim}{r}$, and ε_{jk} is negligible, the set of equations can be solved for the perturbation amplitudes and the current. Unfortunately, this method does not work well

unless the SRL is very close to the correct solution. The current perturbation parameter u_o dominates the solution and the fit to the loop shape tends to be poor. A more subtle approach is to use the field ratios at two separate positions to eliminate the current entirely from the equation. Thus from equation (7.12), for field points $\underset{\sim}{r}$ and $\underset{\sim}{r}'$:

$$\frac{B_{rz}(\underset{\sim}{r})}{B_{rz}(\underset{\sim}{r}')} = \frac{B_{oz}(\underset{\sim}{r}) + \sum_{j=1}^{2}\sum_{k=1}^{N_p}\lambda_{jk}\left[G_{jkz}(\underset{\sim}{r}) + \varepsilon_{jk}(\underset{\sim}{r})\right]}{B_{oz}(\underset{\sim}{r}') + \sum_{j=1}^{2}\sum_{k=1}^{N_p}\lambda_{jk}\left[G_{jkz}(\underset{\sim}{r}') + \varepsilon_{jk}(\underset{\sim}{r}')\right]}$$

from which:

$$\frac{B_{oz}(\underset{\sim}{r}')}{B_{rz}(\underset{\sim}{r}')} - \frac{B_{oz}(\underset{\sim}{r})}{B_{rz}(\underset{\sim}{r})} = \sum_{j=1}^{2}\sum_{k=1}^{N_p}\lambda_{jk}\left\{\frac{\left[G_{jkz}(\underset{\sim}{r}) + \varepsilon_{jk}(\underset{\sim}{r})\right]}{B_{rz}(\underset{\sim}{r})} - \frac{\left[G_{jkz}(\underset{\sim}{r}') + \varepsilon_{jk}(\underset{\sim}{r}')\right]}{B_{rz}(\underset{\sim}{r}')}\right\} \quad (7.14)$$

Assuming the higher order terms are negligible, at least $2N_p$ equations of this form are needed to solve for the λ_{jk}. The best fit current can then be determined by the method of least squares.

For the method to be useful in analysing experimental data, the gradiometer configuration needs to be considered. An equivalent series expansion to equation (7.11) can be developed substituting the total flux threading the sensing coils for the field (Ioannides and Grimes (1986)). Equivalent equations to (7.12) and (7.14) thus follow.

$$S_r(\underset{\sim}{r}) = \mu_o S_o(\underset{\sim}{r}) + \sum_{j=1}^{2}\sum_{k=1}^{N_p}\lambda_{jk}\left[H_{jk}(\underset{\sim}{r}) + \varepsilon_{jk}(\underset{\sim}{r})\right] \quad (7.15)$$

$$\frac{S_o(\underset{\sim}{r}')}{S_r(\underset{\sim}{r}')} - \frac{S_o(\underset{\sim}{r})}{S_r(\underset{\sim}{r})} = \sum_{j=1}^{2}\sum_{k=1}^{N_p}\lambda_{jk}\left\{\frac{\left[H_{jk}(\underset{\sim}{r}) + \varepsilon_{jk}(\underset{\sim}{r})\right]}{S_r(\underset{\sim}{r})} - \frac{\left[H_{jk}(\underset{\sim}{r}') + \varepsilon_{jk}(\underset{\sim}{r}')\right]}{S_r(\underset{\sim}{r}')}\right\} \quad (7.16)$$

where S_T is the target signal

S_o is the reference loop signal

H_{jk} are the perturbation coefficients given by

$$H_{jk}(\underset{\sim}{r}) = \frac{S(\underset{\sim}{r},A) - S(\underset{\sim}{r},-A)}{2A} \qquad (7.17)$$

as in equation (7.10). Like the coefficients G_{jk}, the H_{jk} can be determined analytically (Ioannides and Grimes, 1986) if desired.

7.4 The iterative perturbative method applied to a 2 dimensional loop (point field measurements)

Although equations (7.15) and (7.16) allow the full inversion process for a 3-dimensional loop and sensing coils of finite area, the basic features of the method are more easily discussed for a simpler case, namely the specification of a 2-dimensional loop from point field measurements. In this section, I will describe the technique for this special case and present several examples of its application.

The set of equations to be solved here is then, from (7.15):

$$B_{rz}(\underset{\sim}{r}_m) = \mu_o B_{oz}(\underset{\sim}{r}_m) + \sum_{k=1}^{Np} \mu_k \left[G_{kz}(\underset{\sim}{r}_m) \right] \qquad (7.18a)$$

where $m = 1, N_d$

$N_d > N_p$

and from (7.16):

$$\frac{B_{oz}(\underset{\sim}{r}_m)}{B_{Tz}(\underset{\sim}{r}_m)} - \frac{B_{oz}(\underset{\sim}{r}'_m)}{B_{Tz}(\underset{\sim}{r}'_m)} = \sum_{k=1}^{N_r} \lambda_k \left\{ \frac{G_{kz}(\underset{\sim}{r}'_m)}{B_{Tz}(\underset{\sim}{r}'_m)} - \frac{G_{kz}(\underset{\sim}{r}_m)}{B_{Tz}(\underset{\sim}{r}_m)} \right\} \qquad (7.18b)$$

where m = 1,N_r (the no. of inversion pairs)

$N_r \geq N_p$

I have dropped the 2nd subscript from the λ_k and the coefficients because in the 2-dimensional case only the perturbations in the direction of the principle normal to the loop are needed.

This set of equations forms an overdetermined linear system for which we wish to find the perturbation amplitudes which minimise the sum of the squares of the residuals. That is, for (7.18a), we need to minimise $\sum_{i=1}^{N_d} E_i^2$, where

$$E_i = B_{Tz}(\underset{\sim}{r}_i) - \left\{ \mu_o B_{oz}(\underset{\sim}{r}_i) + \sum_{i=1}^{N_p} \mu_k G_{kz}(\underset{\sim}{r}_i) \right\}$$

The minimisation condition for (7.18b) is similarly defined.

The minimisation can be carried out by standard matrix techniques (Dalquist and Björck, 1974). The perturbations are then added to the SRL to produce a new loop which may be used as the SRL for a further iteration.

7.4.1 The target data

For the inversions described in this section, the target data were produced by computer simulation. B_z values were calculated for a series of scans in a plane above a horizontal line current loop of arbitrary shape. This loop

was defined by a set of coordinates (the loop points) joined by straight lines. Loop dimensions, scanning area, scanning height and current strength were chosen so that the simulated signals were similar to typical leg data.

Thus the target loop was confined to a region defined by $z = -50mm$; $-60mm \leqslant x \leqslant 60mm$; $-250mm \leqslant y \leqslant 250$ mm. Each scan consisted of a discrete set of data points (between 55 and 61) at 1cm intervals between x = -300 mm and x = 300 mm and there were between 5 and 10 evenly spaced scans in the region $-300mm \leqslant y \leqslant 300mm$. The current strenth I_T was < 50uA and the height of the scanning plane above the loop in all cases was 50mm.

7.4.2 The construction of the starting reference loop

The starting reference loop needs to be sufficiently close to the final solution that the 1st order approximation of (7.18) is valid. In the 2-dimensional case, this can be achieved by observing that the positions of zero B_z on either side of the central maximum for two opposing and parallel line current segments are close to the line currents themselves (see figure 7.3). Each scan thus provides two of these 'field zero' positions which may be used as 'seed points' from which the SRL can be interpolated.

This interpolation could be carried out using an appropriate form of spline function; in practice it was performed by hand and the interpolated loop coordinates were determined using a digitising table. Figure 7.4a shows an example of the interpolation process. In this case, 8 scans

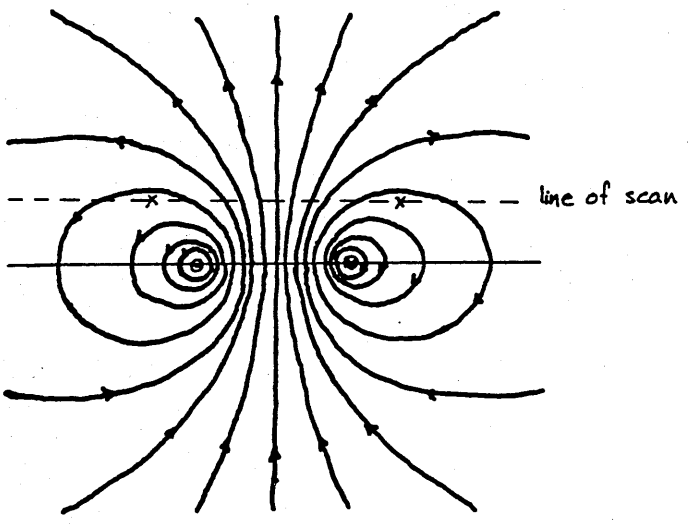

Figure 7.3 Positions of zero B_z (marked x) for a field scan above a horizontal loop.

provide a total of 16 seed points from which the final SRL was constructed. For the examples discussed in this section, the interpolated loops comprised 60 points which provided adequate resolution. Figure 7.4b compares the interpolated loop with the actual target. It can be seen that the overall shape is already roughly correct.

For the purposes of the computational procedures, the parameter t which specifies position on the loop was taken to be the number of the loop point counting round from some arbitrarily chosen origin.

7.4.3 Construction of the perturbations

The perturbations were defined as in section 7.2 with $\sigma = 1$.

The unit perturbation amplitude should be small enough that 2nd order effects are negligible, however the actual value does not appear to be critical. Different amplitudes between 0.05mm and 0.5mm were tried without making any difference to the inversion process. For the results described in this thesis a unit amplitude of 0.2mm was used.

The use of a 60 point loop has the advantage of allowing 15,12 or 10 evenly spaced knots, although there is no necessity for the knots to be evenly spaced. Indeed in some cases it may be advantageous to have greater or smaller knot densities in specific regions. For these 2-dimensional cases, however, ten, evenly spaced knots produced satisfactory results.

If the SRL is not sufficiently close to the target in a particular section of the loop, large amplitudes may be generated in nearby perturbations. Inspection of equation

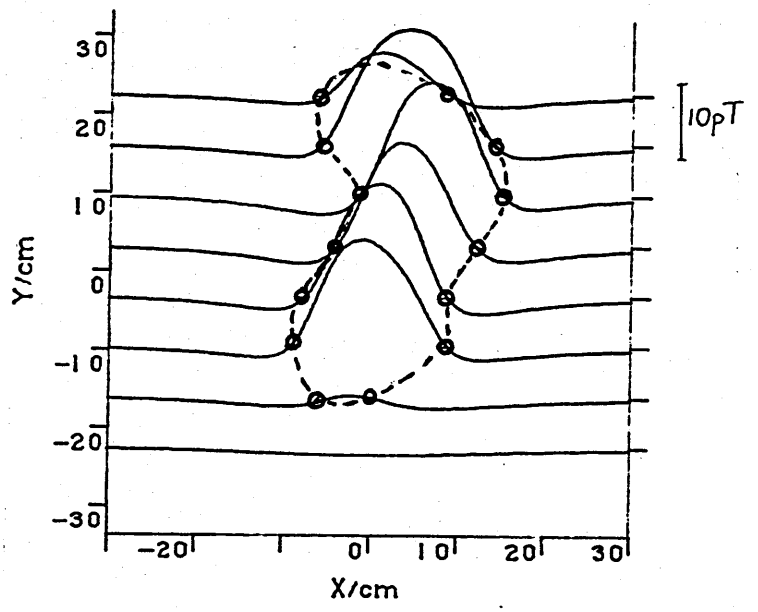

Figure 7.4a) A set of field scans in a plane above a horizontal loop. The field zero positions are marked with open circles. The interpolated loop is shown dashed.

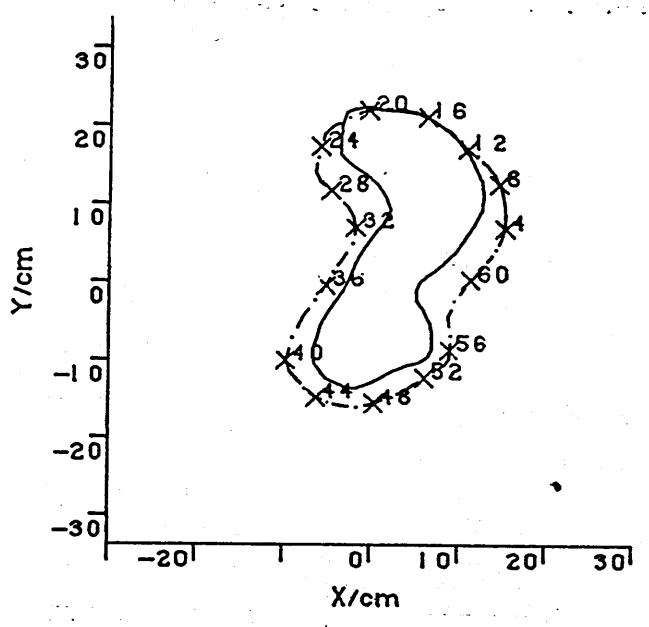

Figure 7.4b) Comparison of the SRL (dashed line) obtained in figure 7.4a with the actual target loop (solid line). Perturbation centres are marked x. The loop point number (t) at each perturbation centre is also indicated.

(7.9) shows that this may give rise to significant 2nd order terms elsewhere and hence corrupt the amplitude estimates. This can cause the calculation to diverge. To avoid this possibility, a damping factor was introduced into the amplitude calculations. Damped amplitudes were derived from the raw estimates according to the equation:

$$\lambda' = \frac{\lambda a^2}{\lambda^2 + a^2} \qquad (7.19)$$

where λ' is the damped amplitude.

Experience of using the method indicates that perturbation amplitudes > 20mm are liable to generate unstable solutions. With a unit amplitude of 0.2mm, this corresponds to $\lambda > 100$. Putting a = 200 in (7.18) provides satisfactory suppression as table 7.1 indicates.

TABLE 7.1

λ	λ'
10	10
50	50
100	80
200	100

At each loop point, the value of $\underset{\sim}{p}(t)$ calculated from equation (7.3) needs to be added in the direction of the principle normal. The principal normal is most easily computed via the tangent to the loop at that point. Writing

$$\underset{\sim}{u}_a(t) = \underset{\sim}{l}(t+1) - \underset{\sim}{l}(t)$$

$$\underset{\sim}{u}_b(t) = \underset{\sim}{l}(t) - \underset{\sim}{l}(t-1)$$

where t is the loop point number. The local tangent is defined by:

$$\hat{\underset{\sim}{q}}(t) = \frac{\underset{\sim}{u}_a(t) + \underset{\sim}{u}_b(t)}{|\underset{\sim}{u}_a(t) + \underset{\sim}{u}_b(t)|} \qquad (7.20)$$

The local binormal is:

$$\hat{\underset{\sim}{b}}(t) = \frac{\underset{\sim}{u}_a(t) \times \underset{\sim}{u}_b(t)}{|\underset{\sim}{u}_a(t) \times \underset{\sim}{u}_b(t)|} \qquad (7.21)$$

And the local principal normal is:

$$\hat{\underset{\sim}{n}}(t) = \frac{\hat{\underset{\sim}{q}}(t) \times \hat{\underset{\sim}{b}}(t)}{|\hat{\underset{\sim}{q}}(t) \times \hat{\underset{\sim}{b}}(t)|} \qquad (7.22)$$

7.4.4 The choice of data points

For N_p perturbations, at least N_p data point pairs are required for the inversion using equation 7.18. The point pairs were distributed over the field map area preferentially where the signal was large in order to maximise the signal to noise ratio. A glance at equation (7.18) shows that regions close to $B_{Tz} = 0$ should be avoided because of singularities. It is also important to choose the points in each pair to be near each other and as close to the reference loop as possible so that each equation is dominated by only one or two perturbations.

A useful guide to inversion point selection was the set of field ratio scans (plotted as $(B_{oz}/B_{Tz} - 1)$ as in figure 7.5). Regions to be avoided because of proximity to $B_{Tz} = 0$ are seen as spikes. Areas of low signal to noise (not shown in this figure) can also be identifed by their high spatial frequency. Optimum results were achieved in many instances

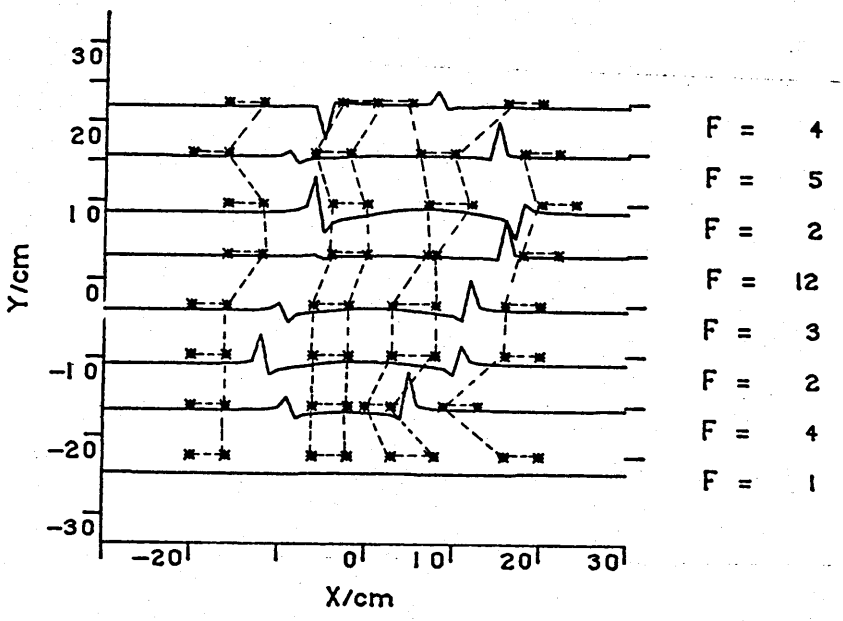

Figure 7.5 Field ratio scans ($B_{oz}/B_{Tz}-1$) for the target and reference loops of figure 7.4. For clarity of presentation, each scan has been scaled down by a factor F. The value of F is shown on the right of each scan.

Field points used in the inversion are shown *. Field point pairs are joined by dashed lines.

when data pairs were chosen to lie approximately in the direction of the local normal to the reference loop. Figure 7.5 also illustrates a suitable choice of inversion points and pairs for this particular example.

7.4.5 Computational procedure

The program to implement the iterative perturbative algorithm described above was written in Fortran using 'Simpleplot' graphics library subroutines and run under the RSX operating system on a DEC-20 mainframe computer.

The program is designed to be interactive. Significant use is made of VDU graphic displays which allow the operator to monitor the progress of the inversion procedure. At various points, the operator may intervene to change parameters and override default sequences depending on the progress of the inversion. This is described in detail below. A block diagram of the program structure is shown in figure 7.6.

At the beginning of each iteration, the reference loop is displayed showing the perturbation knots. At this juncture, the knot positions can be changed if desired, although for 2-dimensional cases, it was not found to be necessary. A second dispay shows scans of the field ratio $(B_{oz}/B_{Tz}-1)$ together with inversion points and pairs. The operator may alter the number of points or pairs or change their positions.

The coefficients G_{kz} are now calculated via equation (7.10) at the inversion points and the inversion is performed. The program allows the choice of inversion either

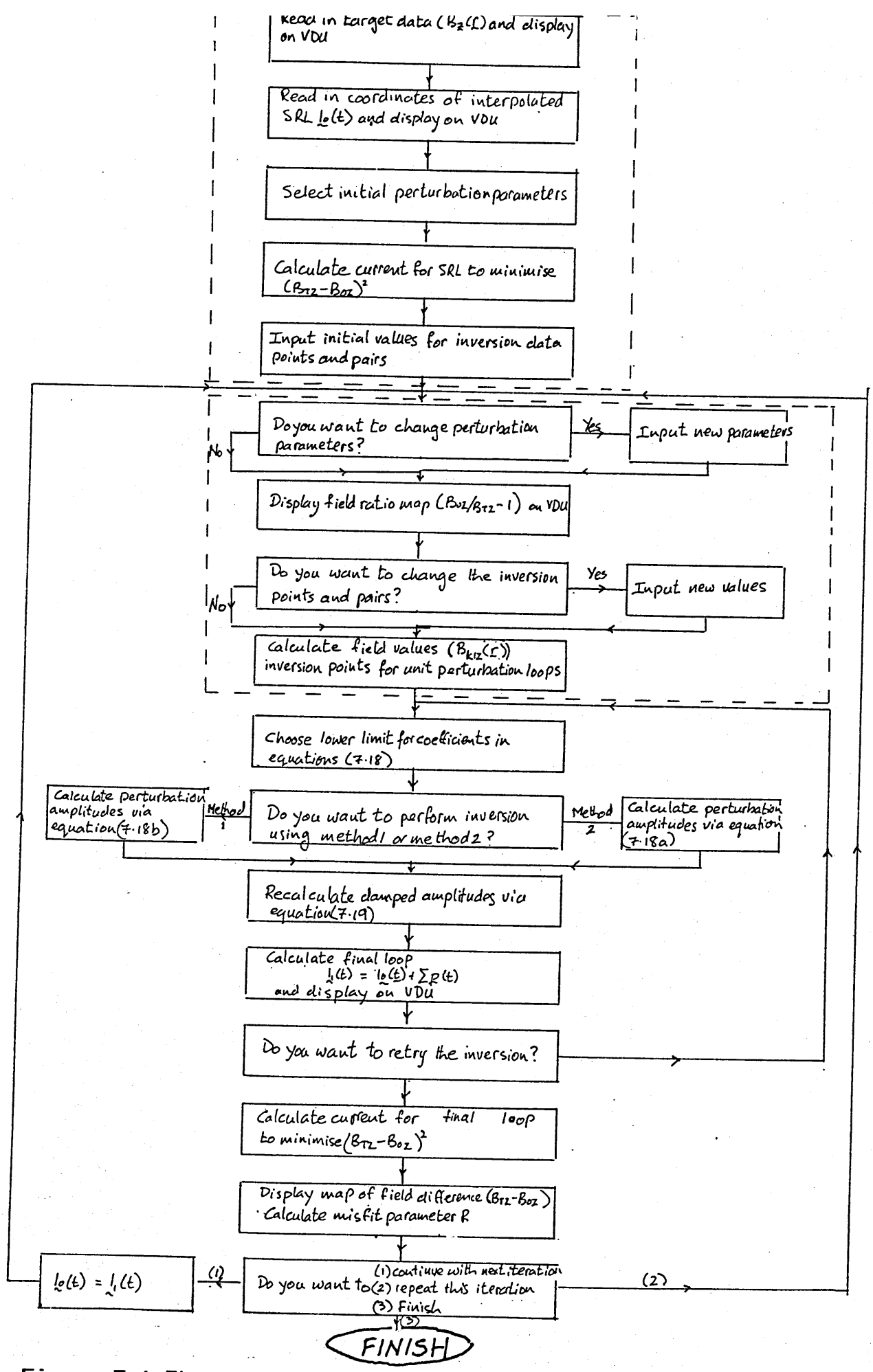

Figure 7.6 The structure of the two dimensional loop fitting program. Dashed sections correspond to dashed boxes in figure 8.2.

via equation (7.18a) (method 2). If necessary, the operator can use both methods and compare the results before deciding how the inversion is to proceed. In almost all of the 2-dimensional cases, the use of method 1 throughout gave satisfactory results.

Very small G_{kz} can lead to spurious λ_k as the kth term ($\lambda_k G_{kz}$) in the summation of (7.18) may be negligible even for large λ_k. This problem is avoided by setting all G_{kz} below a certain threshold equal to zero. The threshold was taken as a fraction T_o of the rms value of G_{kz} for each equation. Typically $T_o = 0.8$ was used, although this could be altered by the operator.

The new SRL is now calculated as the vector sum of the old SRL coordinates and perturbations, after which both old and new loops are displayed on the VDU. As a guide to the overall quality of fit a misfit parameter R is computed. As for the line dipole, this is defined as:

$$R = \left[\frac{\sum_{i=1}^{M} \left(B_{oz}(\underset{\sim}{r}_i) - B_{Tz}(\underset{\sim}{r}_i) \right)^2}{\sum_{i=1}^{M} \left(B_{Tz}(\underset{\sim}{r}_i) \right)^2} \right]^{1/2} \qquad (7.23)$$

where M is the total number of data points. A second parameter R_d is also calculated as in (7.23) but summing only over N_d, the number of inversion points. Large R and small R_d indicates that the inversion is working satisfactorily but the choice of inversion points/pairs could be improved.

If the loop is converging satisfactorily (R decreasing), the new loop is used as the SRL in the next iteration. If the result is unsatisfactory, for instance if R has

increased or unstable oscillations appear to be developing, it is possible to return to the previous SRL and inversion data set and repeat the iteration after altering some parameters.

The whole process is repeated until either the misfit falls below some predetermined level and/or a stable solution is achieved. This is indicated by successive iterations producing very small, random perturbation amplitudes. The field ratio maps may also be used as an indicator of satisfactory convergence as described in the following section.

7.4.6 Examples of the fitting method for 2-dimensional loops

I will illustrate the fitting procedure outlined above with 4 examples. The first is a wide, distorted ellipse shown in figure 7.7a carrying a current of 11.0μA. Figure 7.7b is a set of simulated scans for this loop. Also shown in figure 7.7a is the SRL interpolated from the field zeroes of 7.7b. The field ratio map with inversion points and pairs is shown in figure 7.7c, while 7.7d gives the target and reference loops after 1 iteration.

Figure 7.7e illustrates the stable result achieved after 4 iterations. It will be observed that the target and reference loops are now indistinguishable from each other. The current was correctly estimated at 11.0μA. The misfit R was 0.7%. The field ratio map after 4 iterations is depicted in 7.7f. It can be seen that the spikes associated with the singularities in B_{zo}/B_{zT} have disappeared. This is a useful indicator of an exact match between target and reference

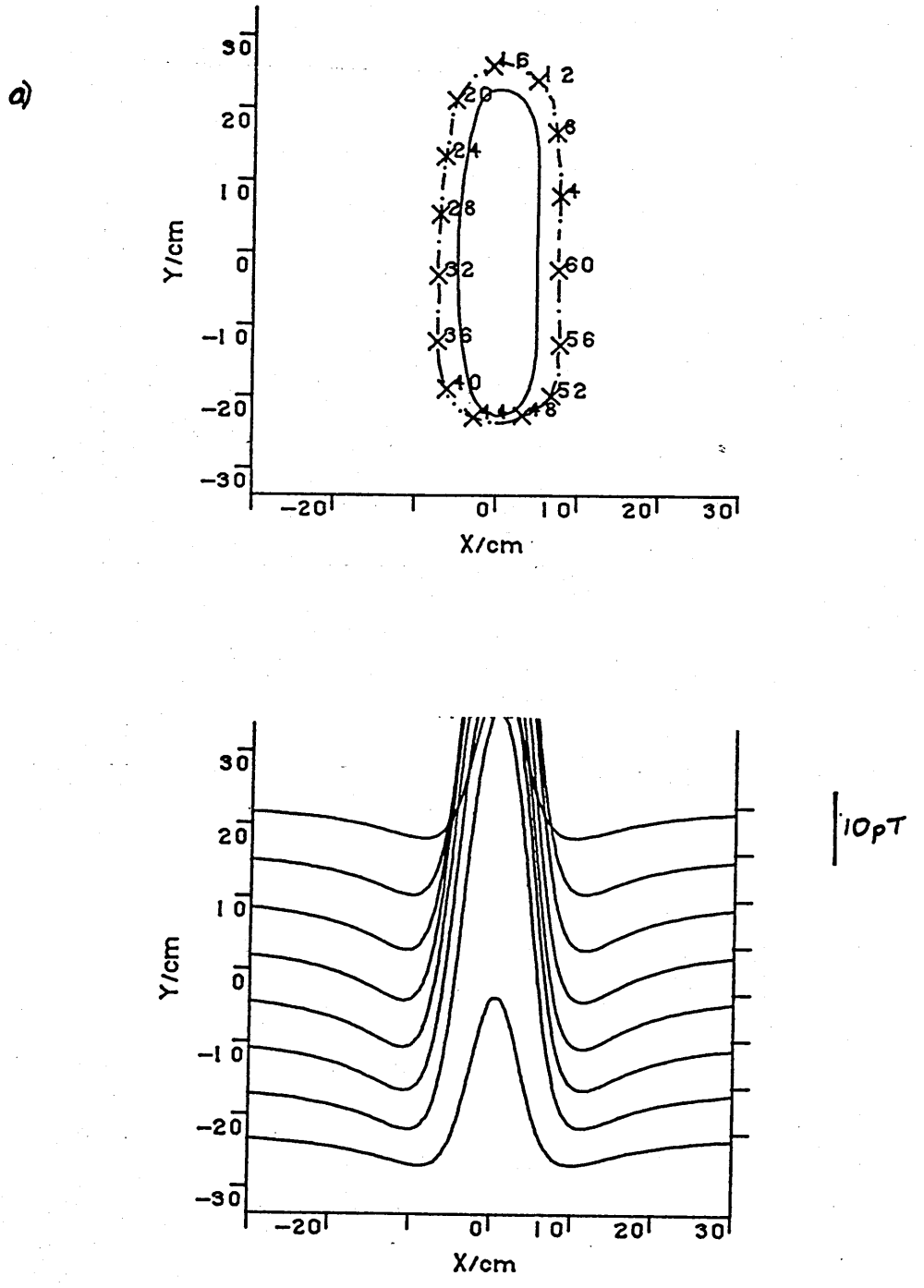

Figure 7.7 Example 1.
a) Target loop (solid line) and SRL computed from field zeroes (dashed line). **b)** Target field from loop in figure 7.7a.

c)

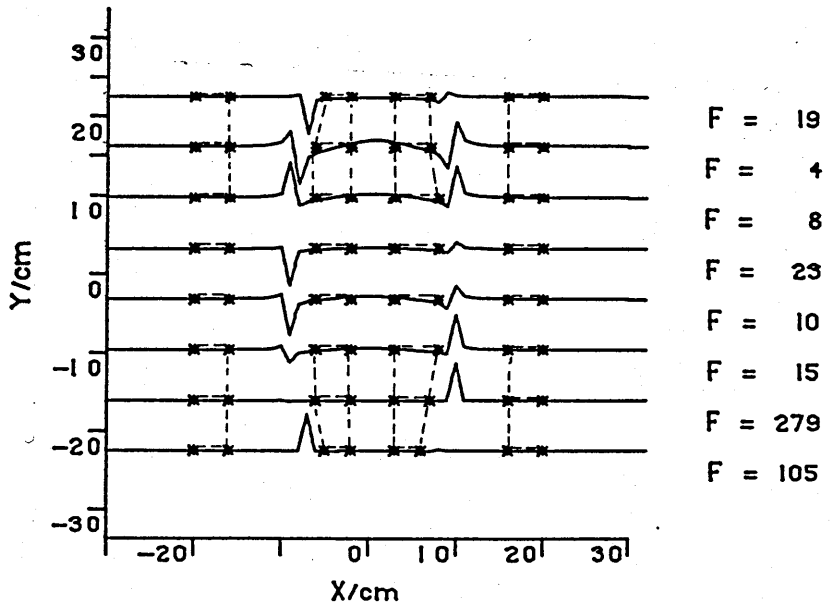

d)

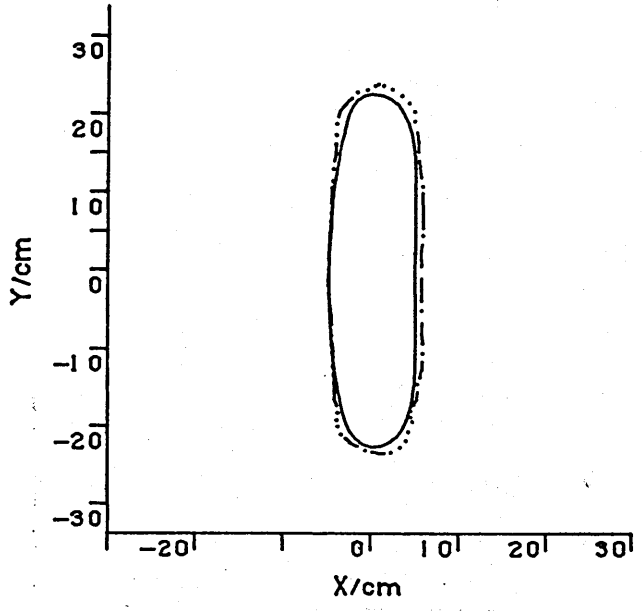

Figure 7.7c) Field ratio map with inversion points and pairs for the target and reference loops shown in 7.7a. **d)** Target and reference loops after 1 iteration.

e)

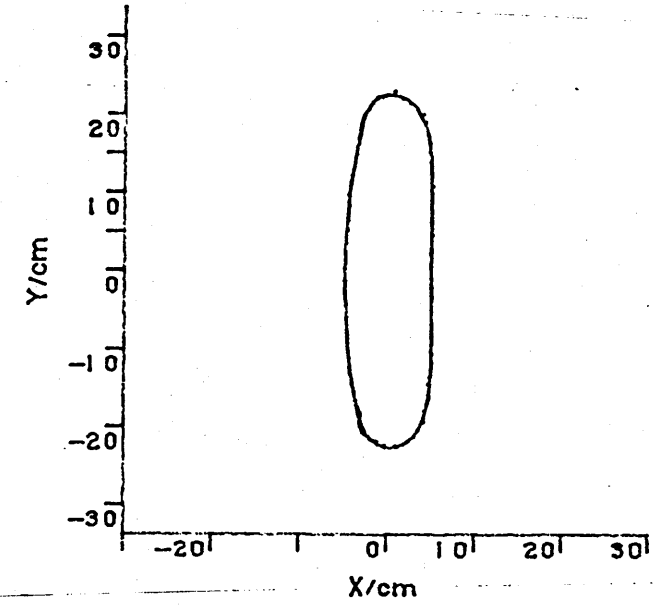

f)

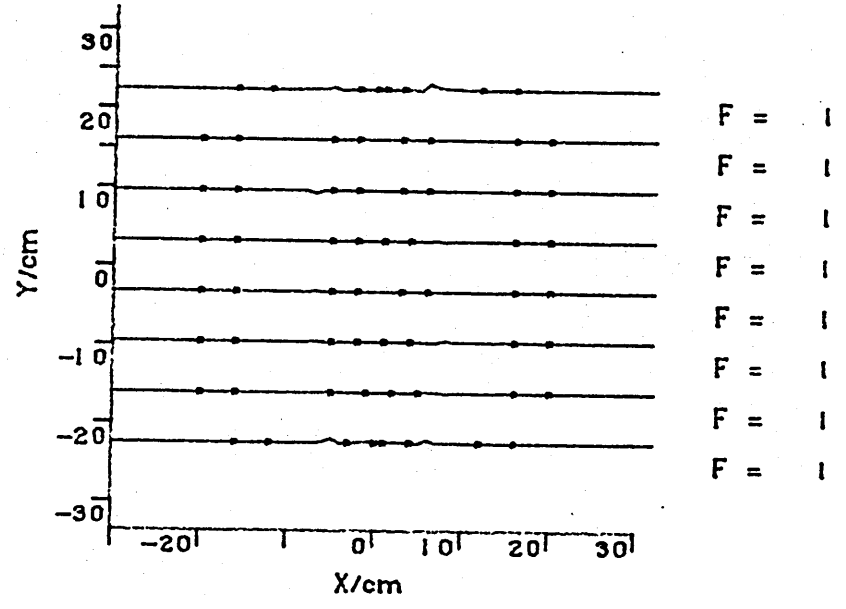

Figure 7.7e) Target and reference loops (indistinguishable from each other) after 4 iterations. **f)** Field ratio map after 4 iterations.

loops.

The second example is a much narrower elliptical loop illustrated in figure 7.8a carrying a current of 20μA. The SRL obtained from the target field of figure 7.8b is also shown. This is a more difficult case as small alterations in the width of a narrow loop (semi-minor axis < 2.5mm) have a very similar effect on the field pattern as small current changes.

This effect may be interpreted in terms of the line dipole model of chapter 4. A narrow loop is well approximated by a line dipole for each scan. Increasing either the current or the loop width will have an identical effect on the dipole moment as defined by equation (4.6). Thus solutions tend to become unstable as the loop narrows.

In this case, switching to inversion method 2 as soon as instabilities began to develop gave a satisfactory solution. Five iterations using method 1, followed by two with method 2 gave the stable final loop of figure 7.8c with I = 18.3μA and R = 0.5%. Once again, the lack of spikes in the field ratio map (figure 7.8d) indicates a good match between target and model loop.

Example 3 is a 'figure of eight' loop with one crossover point (figure 7.9a). This shape is of particular interest as it is the 2 dimensional equivalent of one of the current configurations suggested for the human leg in chapter 6. The SRL is also shown in the figure. In this case the target current was 8μA.

After 6 iterations, the stable solution given in figure 7.9b was achieved. Here difficulty was experienced in fitting the loop in the vicinity of the crossover because of

a)

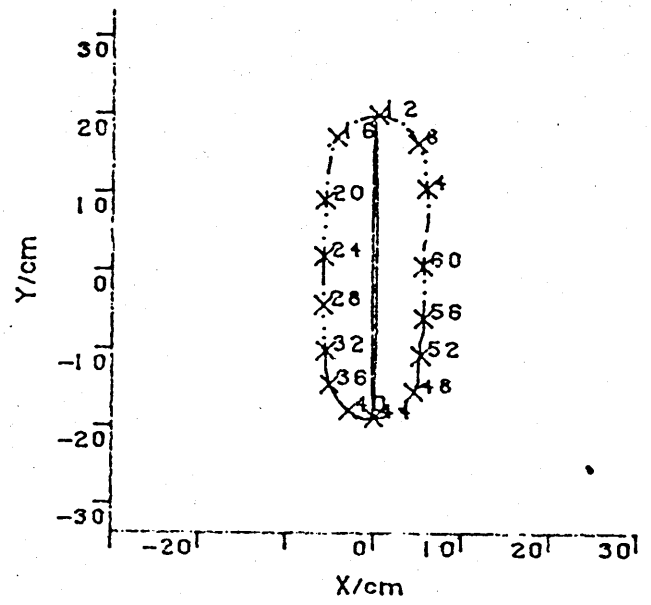

b)

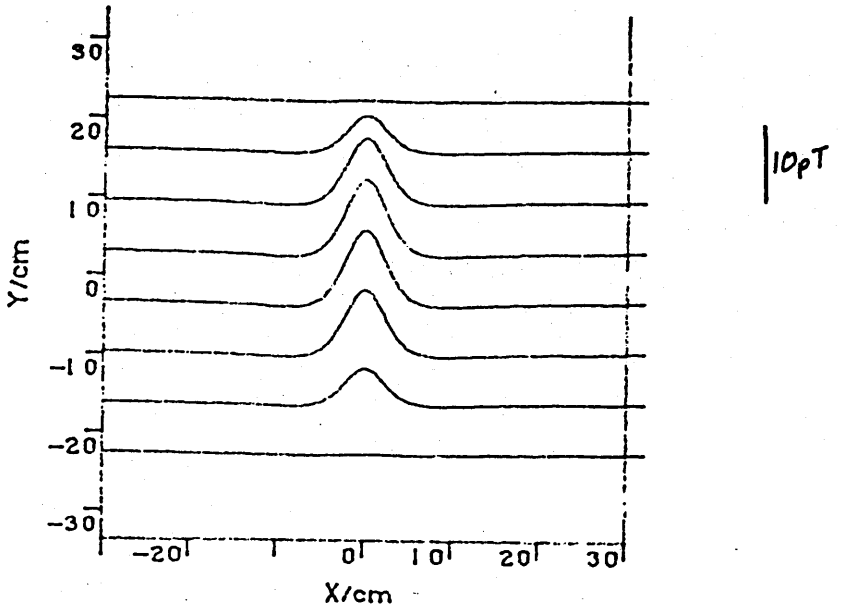

Figure 7.8 Example 2
a) Narrow target loop (solid line) and SRL (dashed line).
b) Target field for the loop in figure 7.8a.

c)

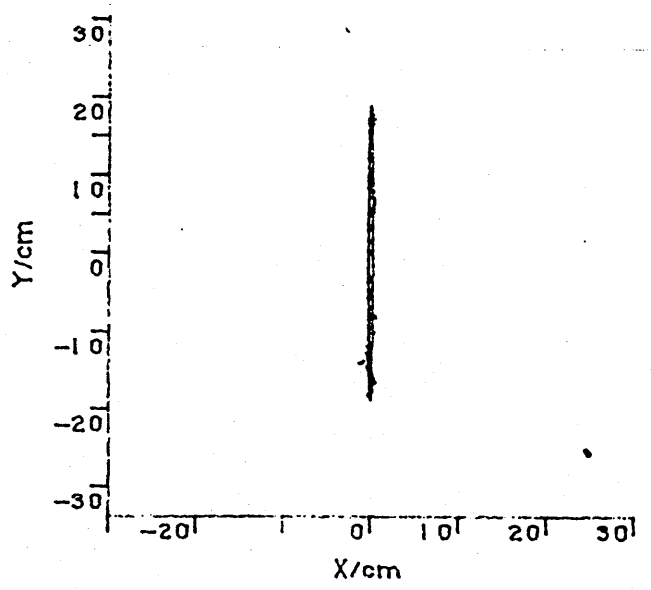

d)

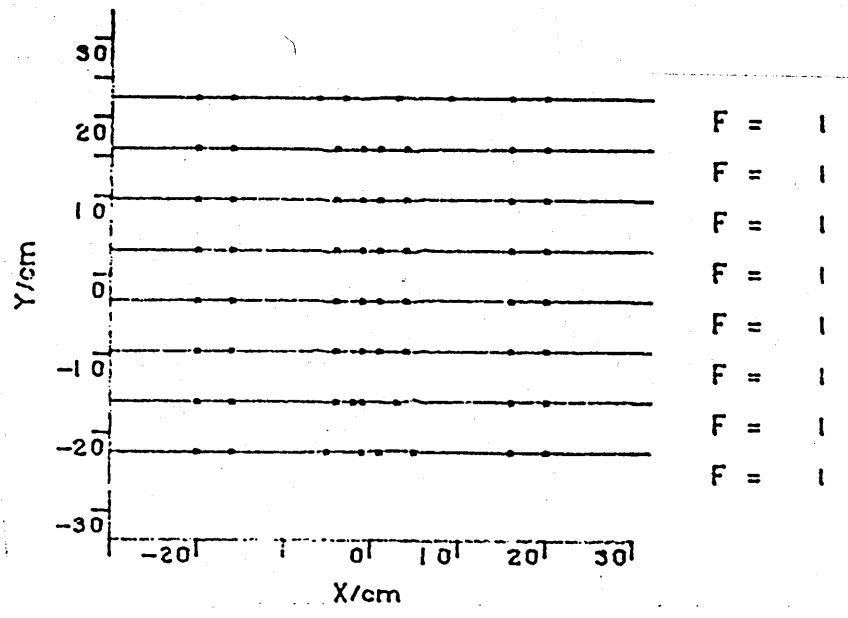

Figure 7.8c) Reference loop and target loop after 7 iterations d) Field ratio map after 7 iterations.

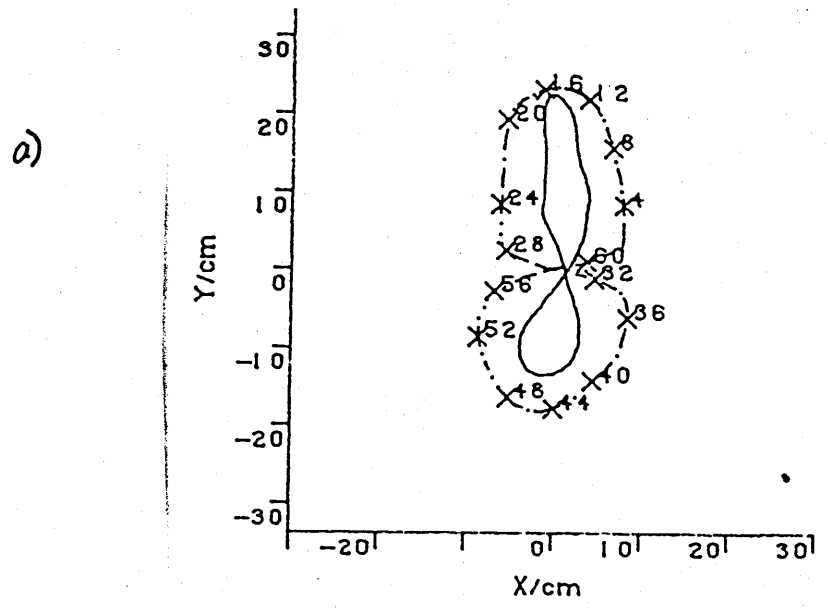

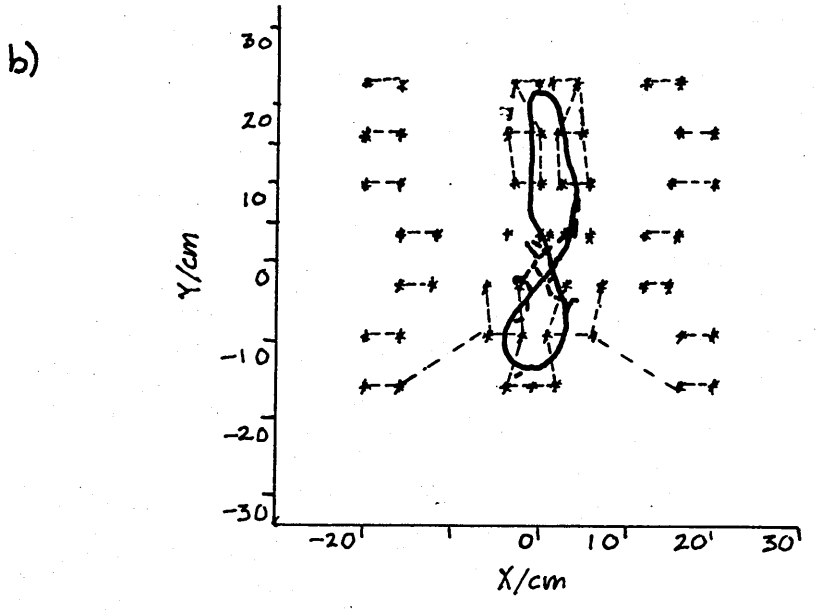

Figure 7.9 Example 3
a) Figure of eight target loop (solid line) and SRL (dashed line) **b)** Target loop and final reference loop after 6 iterations. Inversion points and pairs are also indicated.

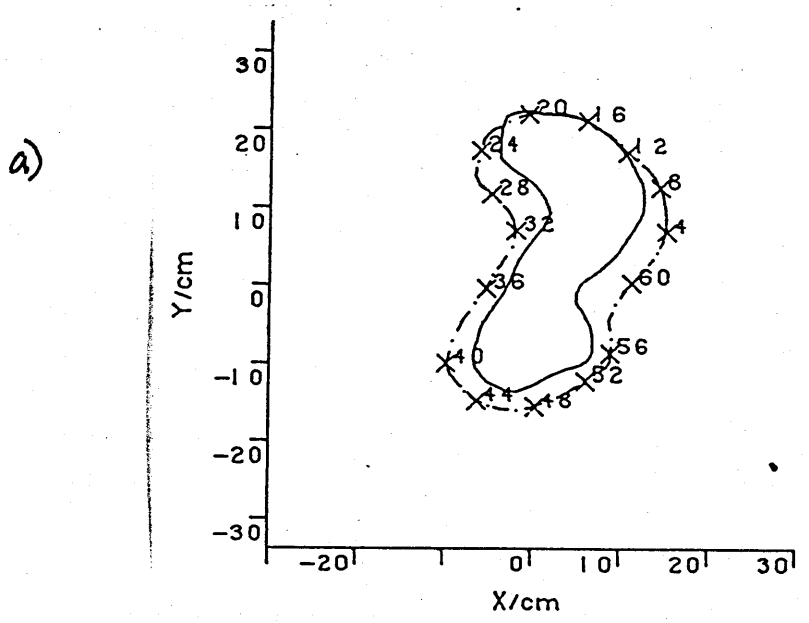

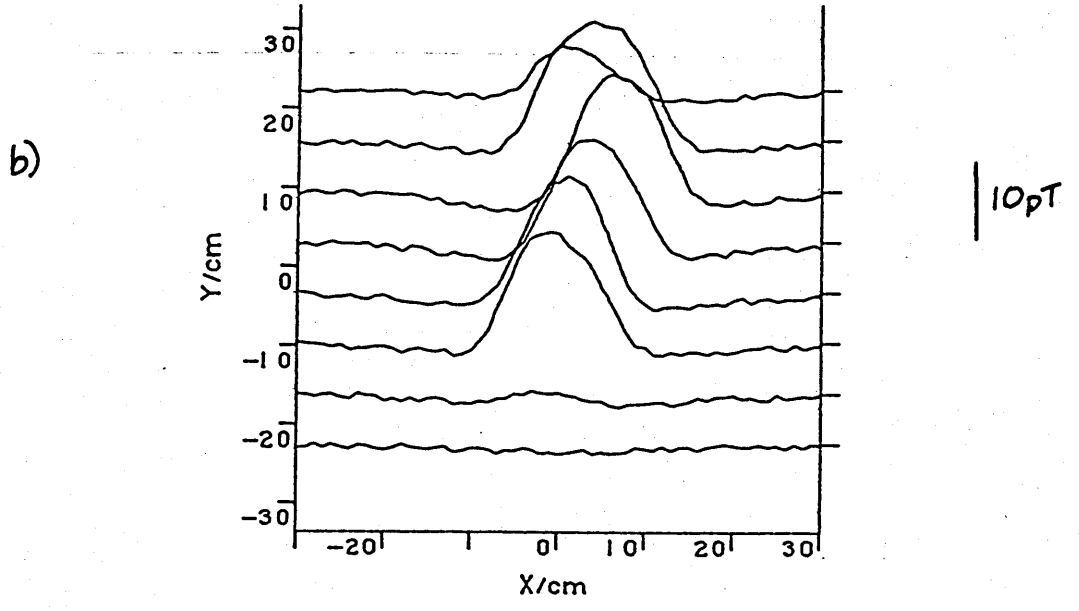

Figure 7.10 Example 4
a) Target loop (solid line) and SRL (dashed line) **b)** Target field with random noise added.

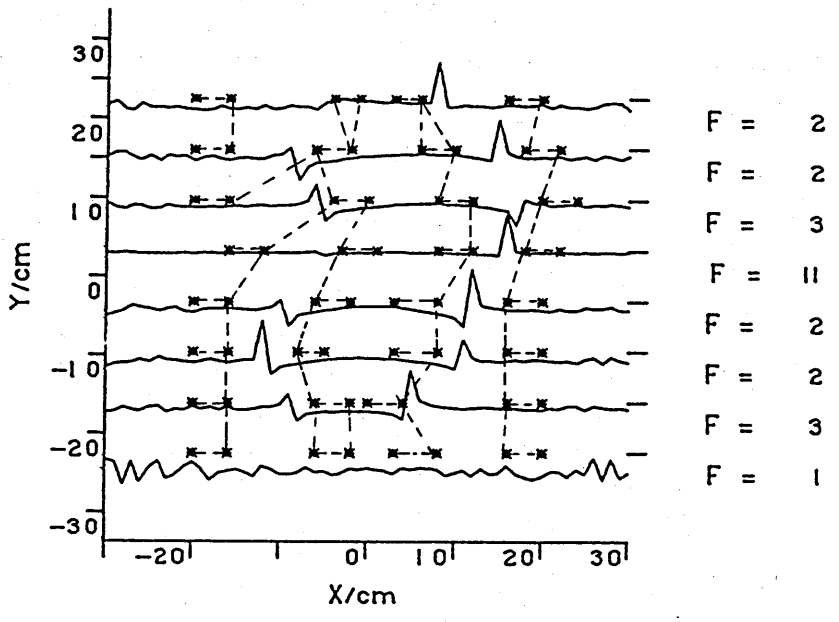

Figure 7.10c) Field ratio map with inversion points and pairs.

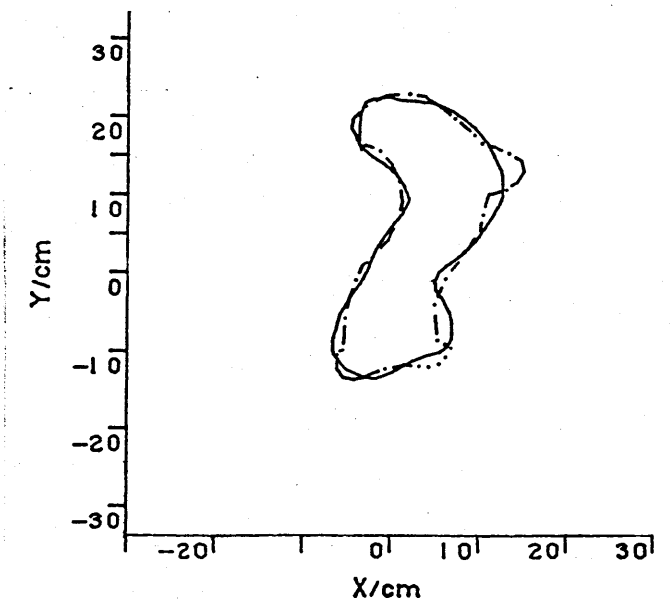

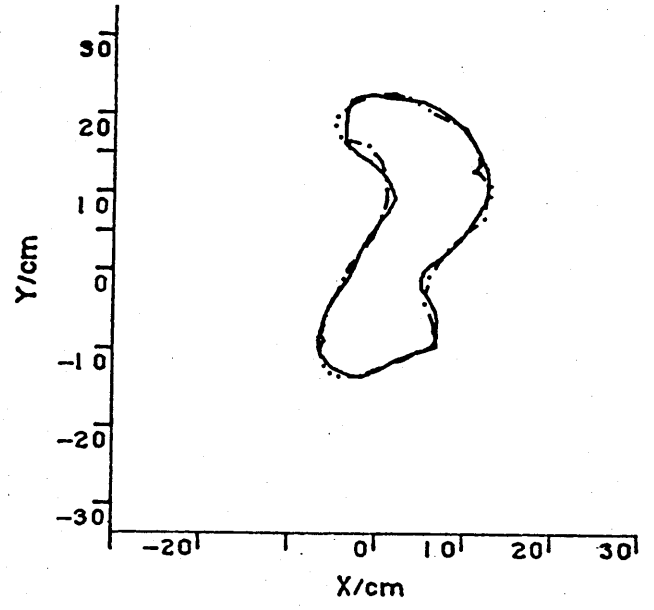

Figure 7.10d) Comparison of reference loop and target after 6 iterations e) Final reference loop after 10 iterations

the conflicting effects of adjacent perturbations. The approximate position of inversion pairs needed to achieve a stable result is also shown in figure 7.9b. Note that the orientation of the pairs is, as far as possible, in the direction of the local normal to the loop.

In the examples discussed so far, the simulated signals were noise free. Example 4 demonstrates the effect of noise on the data. White noise with a peak to peak amplitude of 0.8pT was added to the the target loop field, this being roughly comparable to that expected from experimental leg measurements.

Again, figure 7.10b shows the target field and the SRL is depicted in 7.10a. Figure 7.10c gives the choice of inversion points and pairs, avoiding regions of low signal to noise as evidenced by oscillations of high spatial frequency in the field ratios.

Method 1 was used for the first 6 iterations, the inversion point positions being adjusted as necessary to avoid spikes and noise. The first 6 iterations show a steadily decreasing R. Thereafter no improvement in fit could be achieved with method 1. Switching to method 2 at this point proved successful with a further decrease in misfit, finishing at R = 7.7% after 10 iterations. The situation after 6 iterations is shown in figure 7.10d and the final result after 10 iterations in 7.10e.

Figure 7.10e compares the final best fit loop and the target. The match is remarkably good considering the distortions introduced into the field ratios by the added noise. With the exception of the upper left corner, the

modelled loop is everywhere within 10mm of the target.

Of course, the effect of the noise could be reduced by averaging over adjacent data points or by low-pass filtering the initial field values (see section 7.6), however the purpose of this example is to show that the method is robust enough to give a stable solution even when the data is of poor quality.

CHAPTER 8

THE LINE CURRENT LOOP ITERATIVE-PERTURBATIVE MODEL - FINITE AREA GRADIOMETER AND 3-DIMENSIONAL LOOPS

8.1 Additional features of the algorithm

In order to apply the iterative-perturbative algorithm to experimental data, the model described in the last section needs to be extended to deal with the flux through the sensing coil rather than B_z. It must also take into account the possibilities of perturbations in the third dimension. The full equations incorporating these features have already been given (7.15) and (7.16). For the purposes of computation, these equations are truncated to 1st order:

$$S_T(\underset{\sim}{r}_m) = \mu_0 S_0(\underset{\sim}{r}_m) + \sum_{j=1}^{2}\sum_{k=1}^{N_p} \mu_{jk} H_{jk}(\underset{\sim}{r}_m) \qquad (8.1a)$$

for $m = 1, N_d$

and $N_d > 2N_p+1$

or:

$$\frac{S_0(\underset{\sim}{r}_m)}{S_T(\underset{\sim}{r}_m)} - \frac{S_0(\underset{\sim}{r}'_m)}{S_T(\underset{\sim}{r}'_m)} = \sum_{j=1}^{2}\sum_{k=1}^{N_p} \lambda_{jk}\left[\frac{H_{jk}(\underset{\sim}{r}'_m)}{S_T(\underset{\sim}{r}'_m)} - \frac{H_{jk}(\underset{\sim}{r}_m)}{S_T(\underset{\sim}{r}_m)}\right] \qquad (8.1b)$$

for $m = 1, N_r$

and $N_r > 2N_p$

Incorporation of the terms containing $j = 2$ allows fully

3-dimensional loops.

The magnetometer signal S_T could simply be obtained by numerical integration of B_z over the sensing coil area. In practice, however, this leads to computer run times which are unacceptably long, particularly in view of the interactive nature of the method.

Fortunately, more subtle ways of calculating the total flux through a coil exist. I have used here the method developed by Ioannides and Swithenby (1988). This approach uses Stoke's theorem to express the total flux as the integral of the vector potential around the coil perimeter. The vector potential can then be written as a multipole expansion at the geometric centre of the coil configuration. The symmetry of the d^2B/dz^2 gradiometer means that only a small number of terms in the integrated expansion are needed to achieve high accuracy. Comparison of this method with a simple numerical integration of B_z over the gradiometer coils' surface shows a decrease in computer run time of 1 or 2 orders of magnitude.

8.2 The starting reference loop

For the 3-dimensional case, the field zero positions no longer provide suitable seed points for the interpolation of an SRL and other methods must be sought. With the examples described in this chapter, the most successful approach has been to use a technique suggested by Ioannides (1988). This involves the calculation of a transformation function $\underset{\sim}{V}_z(x,y)$ from the target data. It is defined as:

$$\underset{\sim}{V}_z(x,y) = \frac{\partial S_T}{\partial y}\hat{\underset{\sim}{x}} - \frac{\partial S_T}{\partial x}\hat{\underset{\sim}{y}} \qquad (8.2)$$

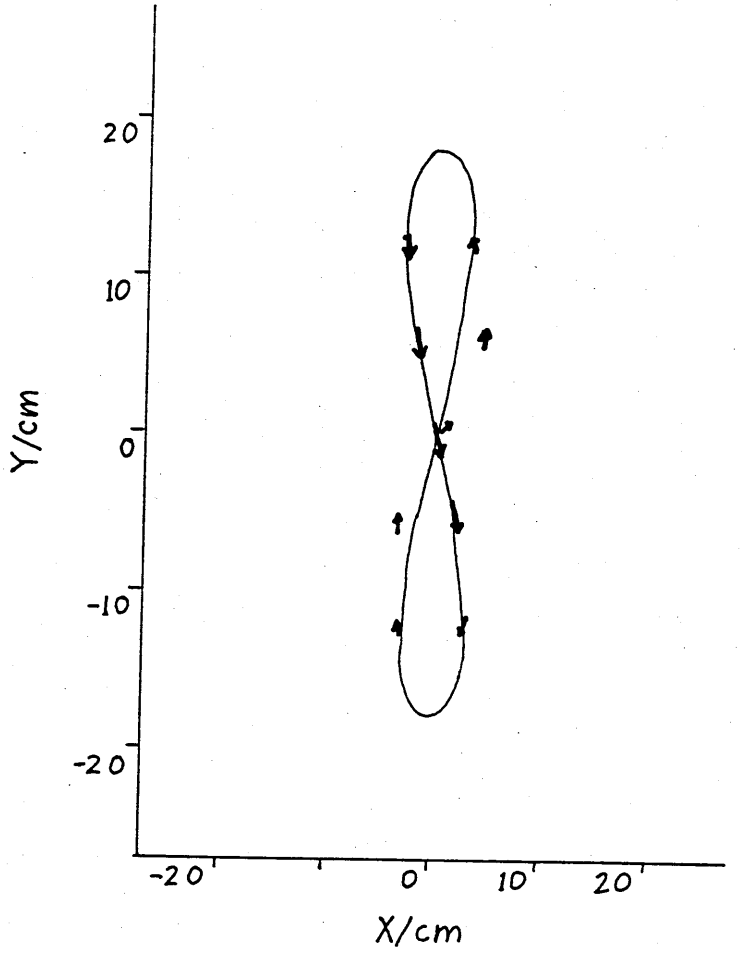

Figure 8.1 Comparison of maximum V_z vectors (arrows) and x-y projection of target loop (solid line). The vectors were derived from the set of scans in figure 8.3b. The limb of the target loop running from bottom right to top left is nearest to the scanning plane. It can be seen that the vectors are very close to the actual loop in this region.

For a single line current element, it can be shown that $\underset{\sim}{V}_z$ computed over the plane of measurement will be a maximum directly above the source and will have the same orientation. If a loop is built up from line current elements, the maximum corresponding to each element is shifted slightly by the contribution from the rest of the loop but the locus of the maxima still provides a useful first order approximation of the projection of the loop in the x-y plane.

For the applications discussed in this chapter, I have simply used the positions of maximum $\underset{\sim}{V}_z$ in each scan to generate a set of seed points from which the full SRL can be interpolated.

Figure 8.1 shows the map of maximum $\underset{\sim}{V}_z$ vectors derived from the set of scans for the 3-dimensional loop discussed in section 8.5.2. The initial SRL (interpolated from figure 8.1) and the target loop may be compared in figures 8.3a and b. It can be seen that the reconstruction is particularly good for the section of the loop closest to the scanning plane.

Of course, the transformation method only gives information pertaining to the x-y plane. It is therefore of most value when the target loop is approximately horizontal.

The best starting z position for the SRL can be determined by searching along the z axis to obtain the least squares best fit between the target and reference fields.

8.3 Problems with the full fitting procedure

Both the finite gradiometer area and the possibility of

perturbations in the z direction tend to make the inverse problem solutions more unstable. The change in the signal for a perturbation in the z direction is much less than for the same sized perturbation in the x-y plane. The result of this is greater instability in the calculated amplitudes which can prevent convergence of the iterative process.

Why the gradiometer configuration also reduces stability is less clear. One possibility is that the more rapid fall off in signal strength with distance reduces the range over which the first order approximation of the algorithm is valid. Thus the perturbation amplitudes are more likely to be corrupted by non-negligible 2nd order terms.

It is probable that both of the above problems could be overcome by retaining the 2nd order coefficients $H_{jj',kk'}$ in equations (8.1) (Ioannides and Grimes (1986)). However this would lead to a significant increase in computer time. Therefore alternative strategies have been adopted which have allowed stable solutions to develop while still only dealing with 1st order calculations. These strategies are outlined below. All strategies are optional and are used at the discretion of the program operator depending on the current state of the inversion.

8.4 Additional features of the SRL

8.4.1 Smoothing the SRL

Instabilities in the solution manifest themselves by high spatial frequencies in the reconstructed loop. As the resolution of the method is limited by the interscan distance, shape changes with a wavelength much shorter than

this are likely to be spurious and may legitimately be removed.

One way of achieving this is by low-pass digital filtering of the calculated perturbations. This is performed by convolving the components of the perturbation vector p(t) with an appropriate window function w(t). In all the work described here, w(t) was a simple 'top hat' function.

Thus:

$$p_x'(t) = p_x(t) * w(t)$$

$$p_y'(t) = p_y(t) * w(t) \qquad (8.3)$$

$$p_z'(t) = p_z(t) * w(t)$$

where $w(t+a) = 1$ for $-b/2 \leqslant a \leqslant b/2$

$w(t+a) = 0$ for $a < -b/2$ and $a > b/2$

b represents the length of the 'top hat'

$p'_x(t)$ represents the smoothed $p_x(t)$ etc.

Once more, the filtering is an interactive process. The decision on whether filtering is desirable and the choice of b are made by the operator after inspection of the reconstructed SRL.

8.4.2 Rejection of small coefficients

As described in section 7.4.4 for the G_{kz}, very small H_{jk} can lead to artificially large μ_{jk} or λ_{jk} in equations (8.1). This problem is avoided by setting to zero all H_{jk} below a threshold given by $T_o H_{jk}(rms)$. Choosing $T_o = 0.8$ usually gave acceptable results although the chosen value of T_o could be altered during any iteration.

8.4.3 Perturbation partitioning

For a starting SRL determined as in section 8.2, the x,y loop coordinates are likely to be more accurate than the z coordinates. A useful initial approach is to hold the x,y components (l_x,l_y) fixed and allow perturbations in the z direction only until a minimum R is reached. At this point, one can revert to the full fitting procedure or hold l_z fixed and allow only horizontal perturbations. Alternating between vertical and horizontal perturbations was often found to be the quickest way of reaching a solution.

8.4.4 Data partitioning

If particular sections of the loop develop unstable perturbations, they can be effectively ignored by removing their perturbation knots. A fit is then sought for the remaining sections, using only data local to those areas. Once a stable solution is achieved here, a fit using the whole data set is tried, this time only allowing perturbations in the unstable areas. Eventually, when a solution appears close, a global approach may be attempted once more, using all perturbations and the whole inversion data set.

8.4.5 Current fixing

Solutions for narrow target loops tend to collapse, giving a zero width loop with very large currents. This can be prevented by fixing the current at a suitable estimated value and then using method 2 with spatial perturbations only. A 'suitable' current estimate can be found by

identifying a section of the data which fits well and calculating a least squares best fit current from that section of the data alone. The identification of such a section of data is best performed by inspection of field difference and field ratio displays.

8.4.6 Linearity checking

Linearity can be checked for individual perturbation amplitudes. After the amplitude λ_{jk} has been determined, its contribution to the field change at the inversion points may be estimated, assuming linearity and unit current, as:

$$S_{jk}(r) = \lambda_{jk} H_{jk}(r) \qquad (8.4)$$

The actual contribution to the field change at the inversion points can be obtained by constructing a loop with a single jkth perturbation of amplitude $_{jk}$ and computing the new field. Writing this as $S'_{jk}(r)$, the validity of the linearity assumption can be checked by calculating the coefficient

$$c_{jk}(r) = \frac{S'_{jk}(r)}{S_{jk}(r)} \qquad (8.5)$$

For c_{jk} significantly different from unity, the perturbation amplitude may be ignored or heavily damped.

8.5 The full inversion procedure in practice

8.5.1 General remarks

A successful inverse problem solution for a particular target usually involves a combination of the strategies

described above. The choice of strategy is guided by the change in the misfit parameter R after each iteration. A particular strategy may be pursued until it no longer causes a reduction in R. Alternative strategies can then be tried until R begins to reduce once more. This continues until no further decrease can be achieved.

It was found in general that the value of R for a fit using the gradiometer signal was appreciably higher than for a visually similar fit using point field values. This can be attributed to the more rapid attenuation of signal with distance for the gradiometer. A small inaccuracy in part of the loop thus causes a proportionately greater mismatch between target and reference loop data. Experience shows that R < 15% indicates an acceptable fit, with a final loop of the correct shape and almost everywhere within 10mm of the target.

A block diagram showing the structure of the 3-dimensional fitting procedure allowing for the gradiometer configuration is shown in figure 8.2.

For all the examples described here, the SRL was constructed via the signal transformation method described in section 8.2.

8.5.2 Example of the full fitting procedure (computer simulation)

Figure 8.3a and b show a 3-dimensional 'figure of eight' target loop together with the SRL. As in the 2 dimensional case, this loop shape is selected as an example because of its similarity to the suspected leg current configuration.

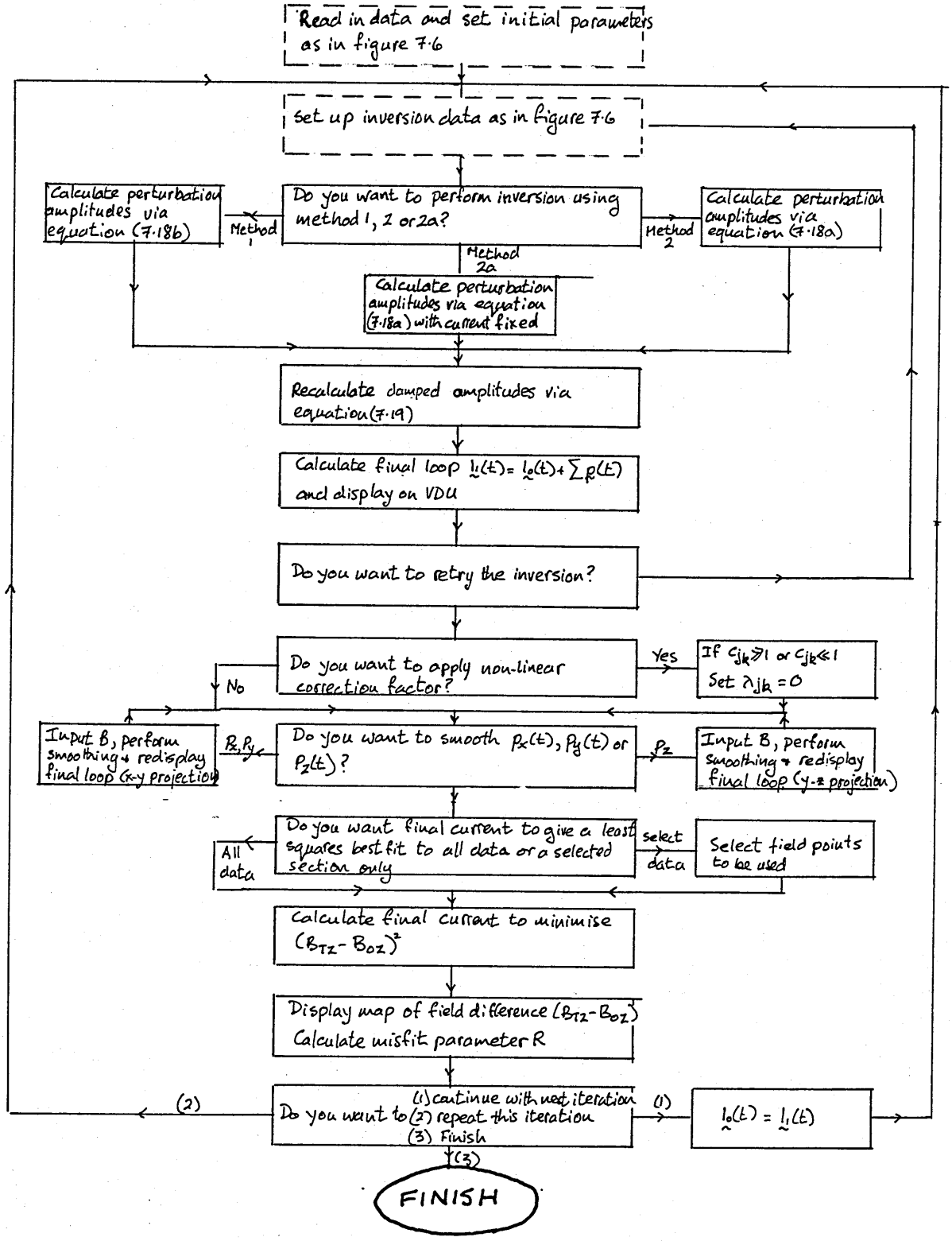

Figure 8.2 The structure of the full, three dimensional fitting program. Dashed boxes correspond to dashed sections in figure 7.6.

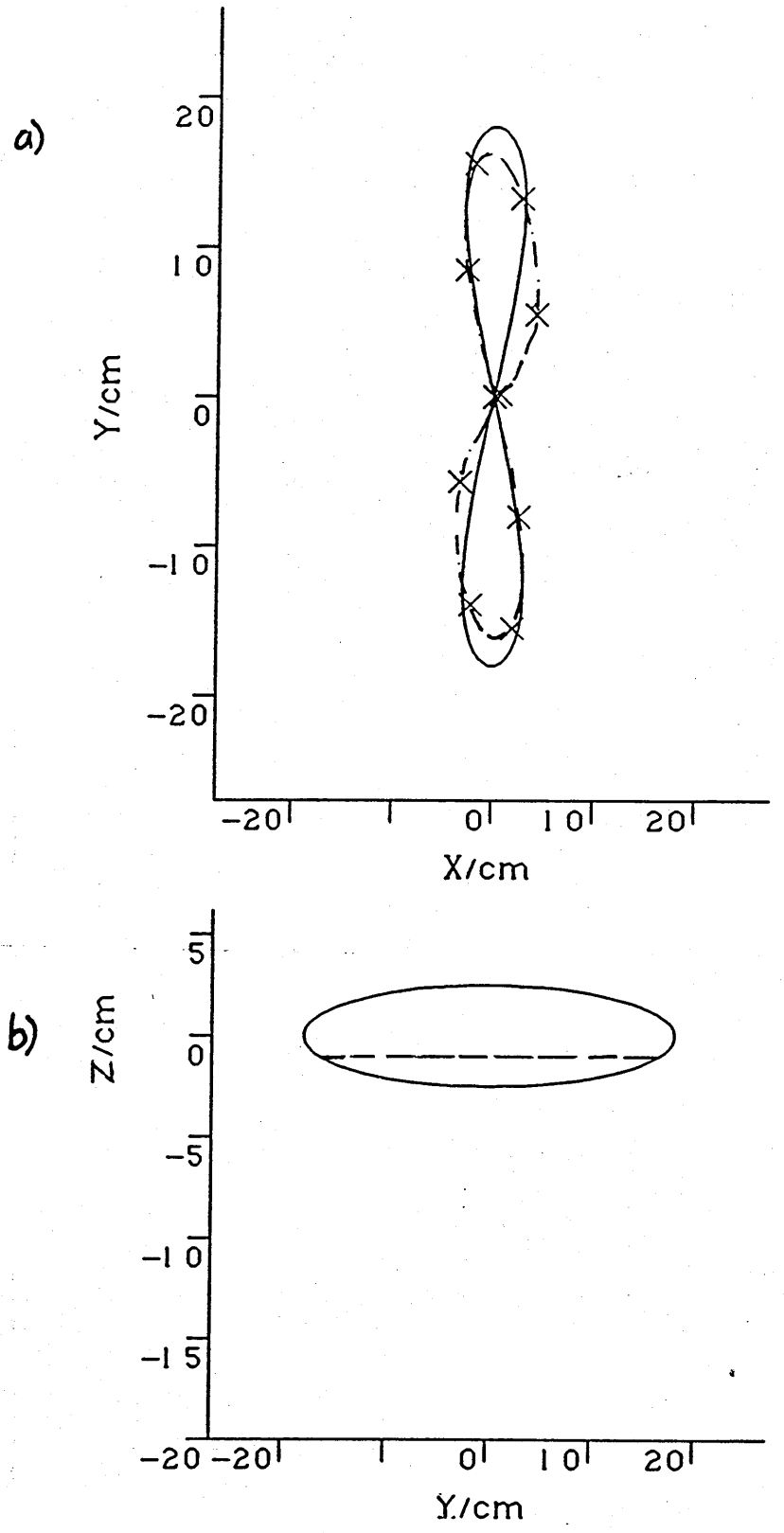

Figure 8.3 Example 1. Modelling a three dimensional figure of eight loop (simulation). a) Comparison of target loop (solid line) and initial SRL (dashed line) (x-y projection). b) Comparison of target loop (solid line) and initial SRL (dashed line) (y-z projection).

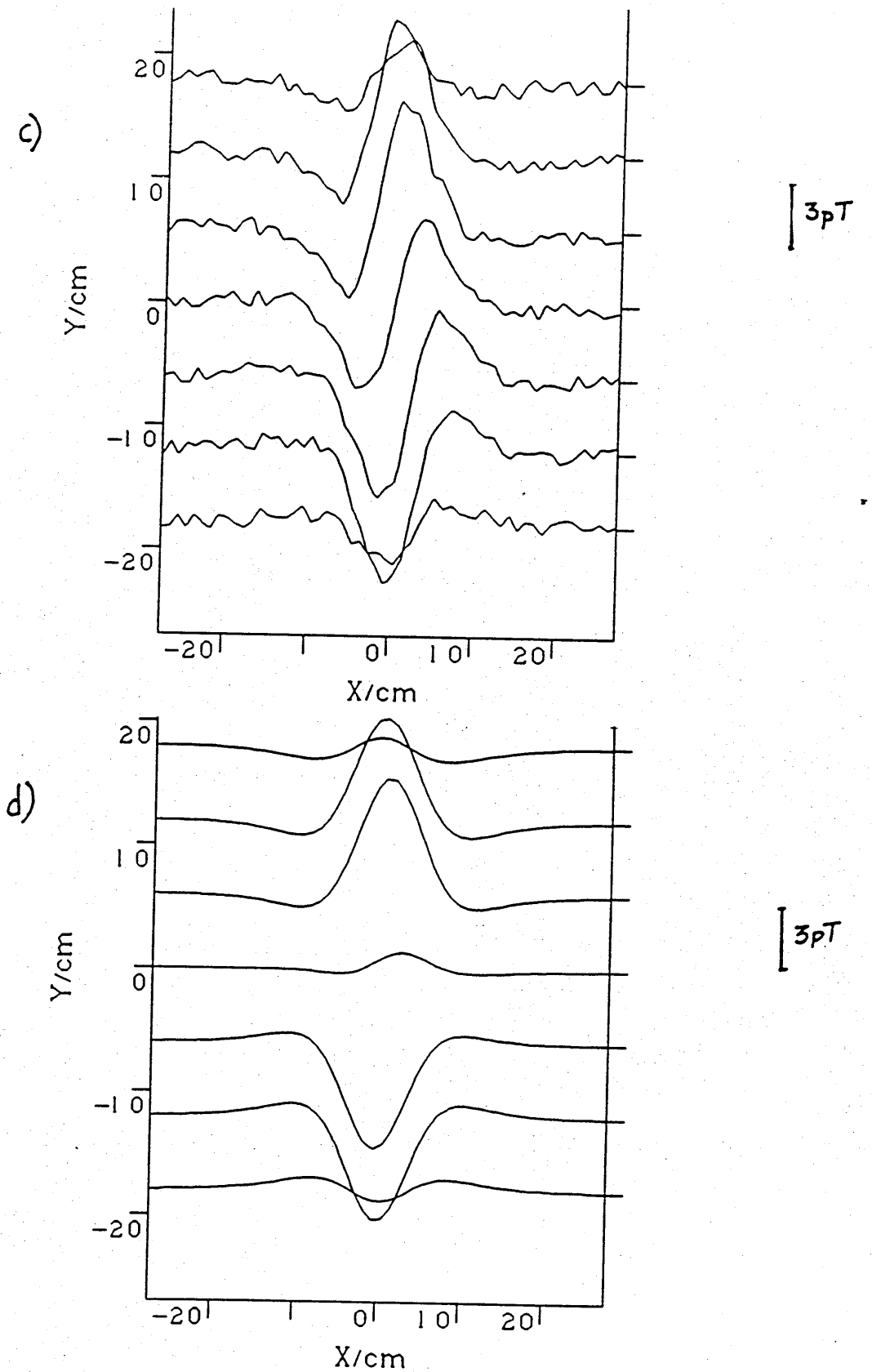

Figure 8.3c) Simulated gradiometer signal from the target loop in figure 8.3a,b. d) Simulated gradiometer signal from the SRL in figure 8.3a,b.

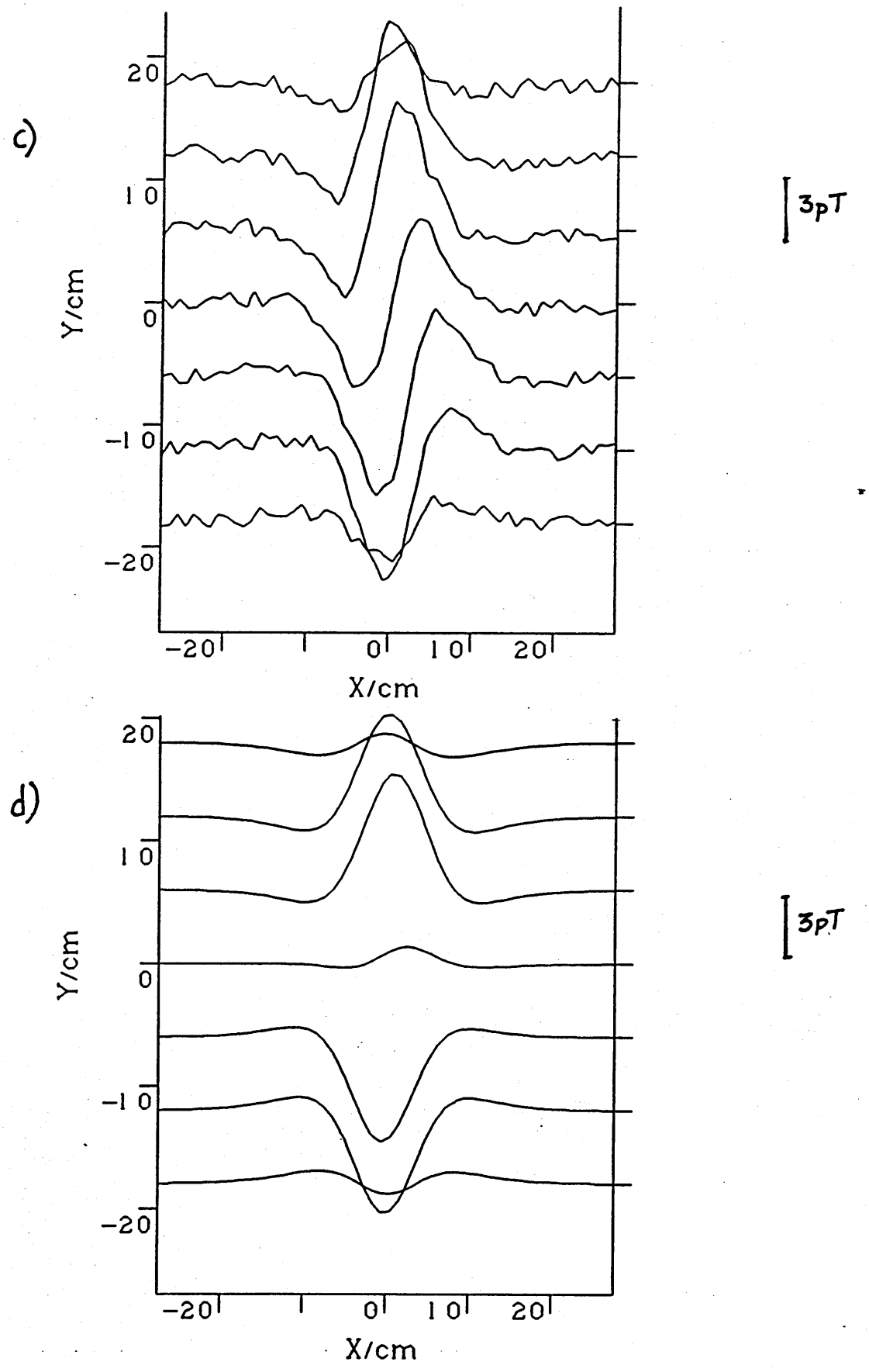

Figure 8.3c) Simulated gradiometer signal from the target loop in figure 8.3a,b. d) Simulated gradiometer signal from the SRL in figure 8.3a,b.

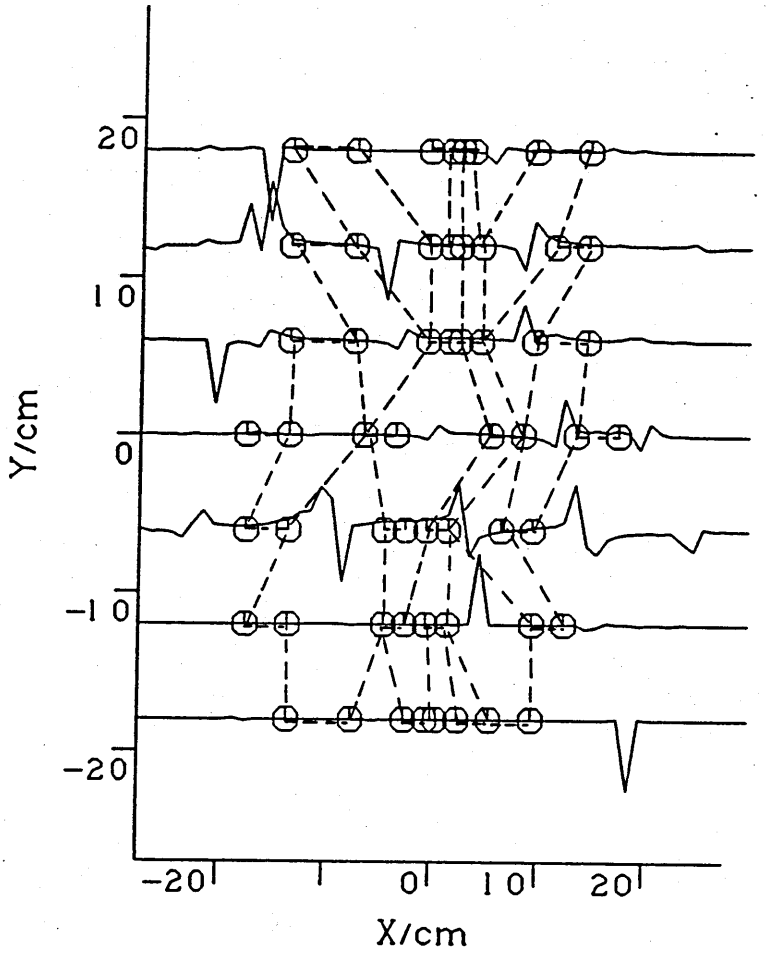

Figure 8.3e) Field ratio map ($B_{oz}/B_{Tz}-1$) also showing inversion points and pairs.

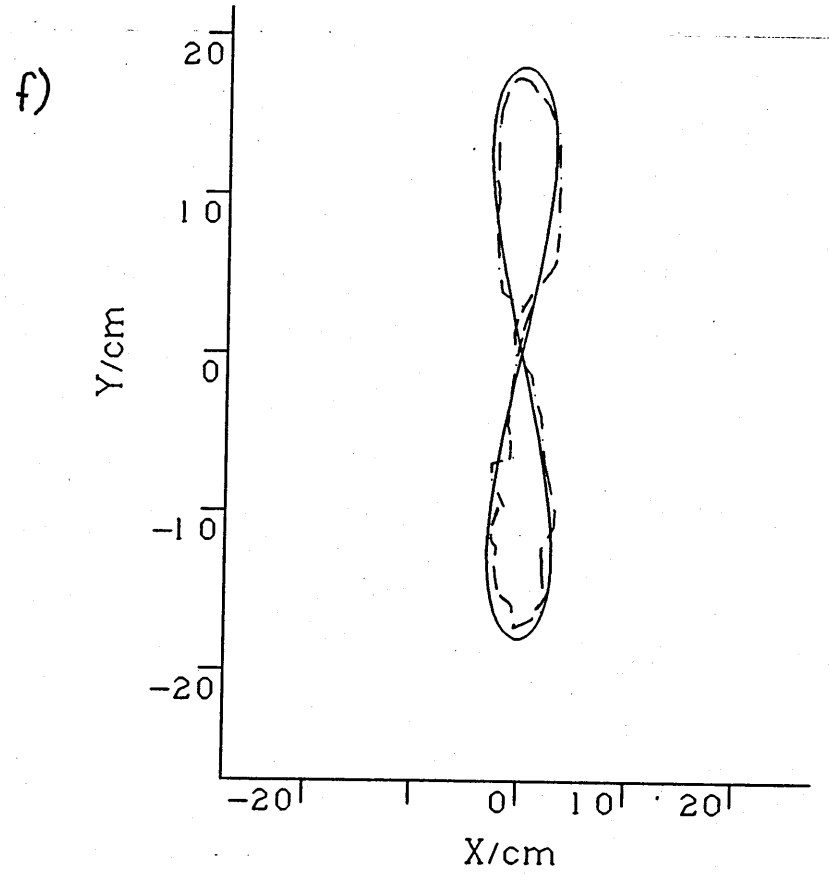

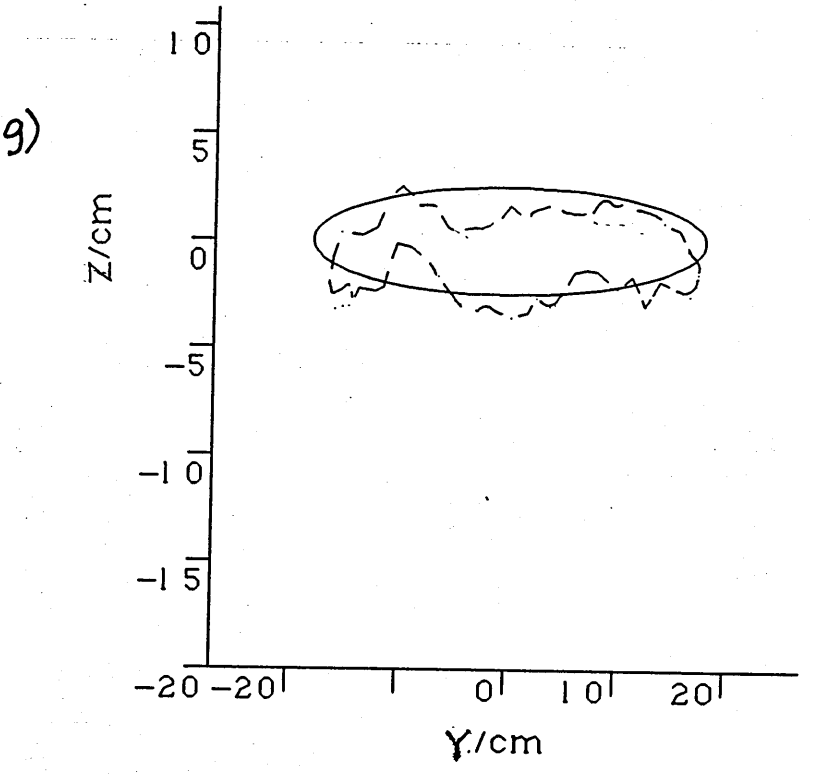

Figure 8.3f) Comparison of target loop (solid line) and final reference loop (dashed line) after 6 iterations, before smoothing (x-y projection). **g)** Comparison of target loop (solid line) and final reference loop (dashed line) after 6 iterations, before smoothing (y-z projection).

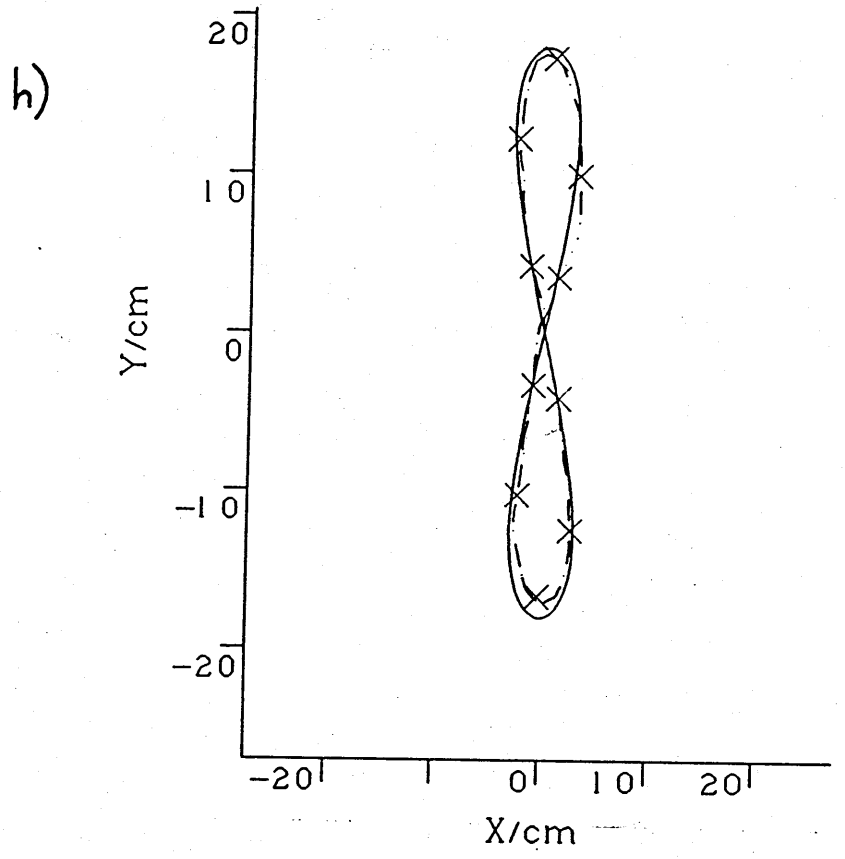

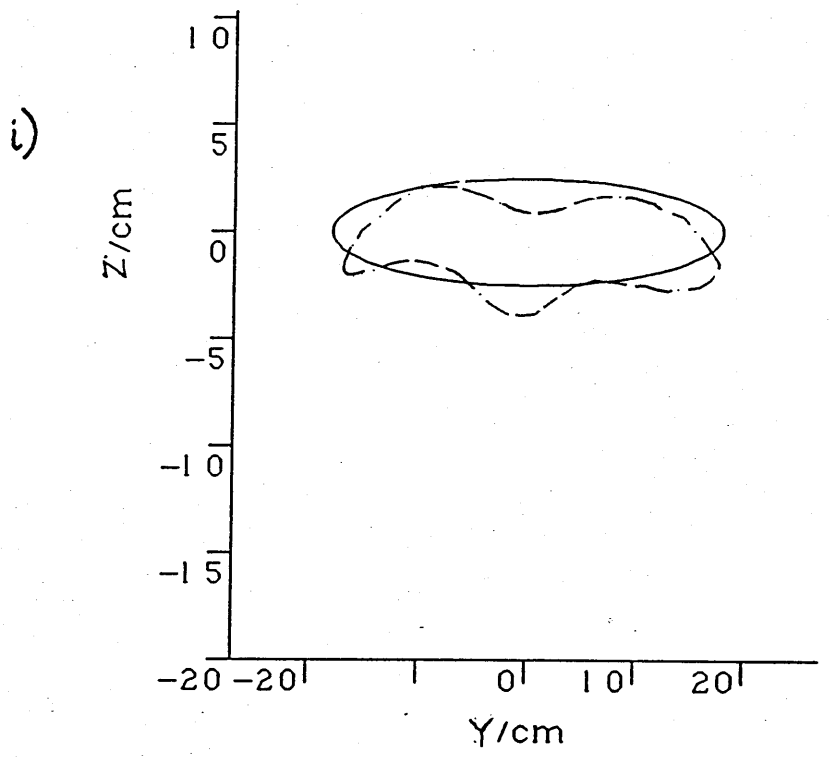

Figure 8.3h) Comparison of target loop (solid line) and final reference loop (dashed line) after 6 iterations, after smoothing (x-y projection). **i)** Comparison of target loop (solid line) and final reference loop (dashed line) after 6 iterations, after smoothing (y-z projection).

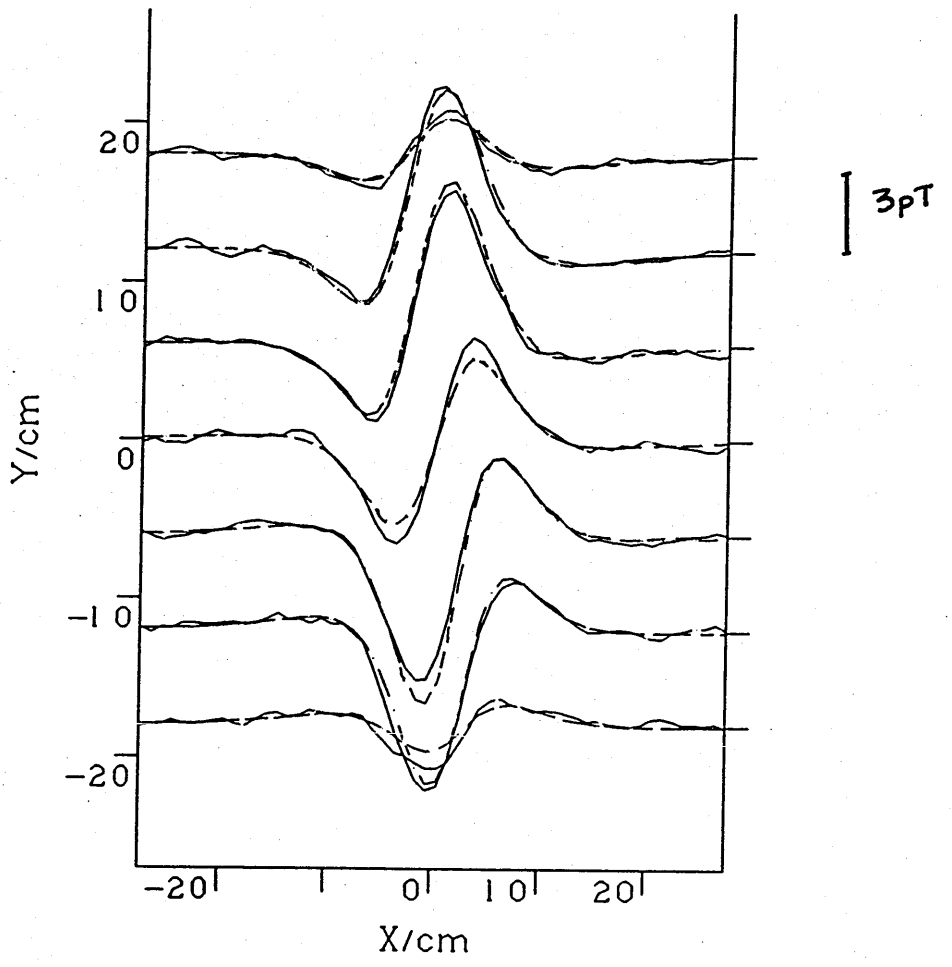

Figure 8.3j) Comparison of target field (solid line) and final reference loop signal(dashed line).

The simulated gradiometer scans produced by a 7.0μA current in the loop are shown in figure 8.3c.

The scanning plane was 80mm above the geometric centre of the target. As usual, each scan comprised 57 data points at 10mm intervals. White noise of 0.8pT peak to peak amplitude was added to the signal to simulate experimental conditions. In this case the raw data were smoothed prior to fitting by convolution with a 'top hat' function of length 50mm.

The SRL was defined by 60 loop points with 10 evenly spaced knots and was initially placed at a depth of 90mm below the scanning plane. The simulated set of reference loop scans is plotted in figure 8.3d. At this point the misfit between target and model field data was 57%. Figure 8.3e gives the field ratio map with inversion points and pairs indicated.

Table 8.1 shows the inversion process in full. T_o gives the rejection level for coefficients H_{jk} (section 8.4.2). b_z is the length of the filtering window for z perturbations and b_h is the window length for horizontal perturbations. Method 2a indicates the use of equation 8.1a with the current held fixed (that is, <u>not</u> included as a perturbation).

Initially the x,y coordinates were assumed to be well approximated by the SRL, hence only z perturbations were used. When no further reduction in R could be achieved with this strategy, the z perturbations and the current were held fixed while the horizontal perturbations were used.

Alternating between the various strategies as detailed in table 8.1 produced an optimum fit with R = 14% after 6

iterations. Figure 8.3f and g show the final loop compared with the target after 6 iterations before smoothing. Figure 8.3h and i show the result of the smoothing operation.

Overall the fit is good. In the x-y plane (figure 8.3h), the model loop is within 10mm of the target everywhere except at the extreme bottom edge. In the y-z plane (figure 8.3i), the approximate dimensions and position are correct, although inaccuracies are apparent in the middle and at the ends. These areas are likely to be the most difficult to fit. There is less information in the scans relating to the loop ends and the difficulty of achieving a good fit near the crossover have already been pointed out in section 7.4.5.

TABLE 8.1

Iteration	Perturbations	Method	T_o	b_h	b_z	R%	R_d%
1	z	1	0.8	-	-	30	21
2	z	1	0.8	-	9	22	20
3	x,y	2a	0.8	9	-	17	13
4	z	1	0.8	-	7	16	12
5	z	2a	0.8	-	7	16	12
6	all	2a	0.8	7	7	14	8

The target and final model fields are plotted for comparison in 8.3j. The discrepancy between the two sets of scans are of the same order as the noise amplitude. This would seem to indicate that the maximum information has been extracted from the data and inaccuracies in the loop shape reflect the noise level and possibly the 'smearing' effect

of the gradiometer coils.

8.5.3 Example of the full fitting procedure (experimental data)

A wire loop was formed by passing a wire tightly around a number of small wooden pegs positioned in a long wooden beam. The positions of the pegs and the height of the wire above the beam at each peg were recorded so that the loop shape could be digitised and stored in the computer for reference.

A current of 0.522mA was passed through the wire and it was scanned using the experimental technique described in chapter 2. The geometric centre of the loop was at approximately z = -55mm. As for the tests described in section 5.3, the SQUID electronics system was set to a sensitivity of $2\times10^{-8}TV^{-1}$ (100x less sensitive than for biological measurements). This ensured a signal of comparable amplitude to the leg measurements but with negligible noise. Each scan consisted of 57 data points at 10mm intervals. The scans are plotted in figure 8.4a.

The initial SRL (shown in figure 8.4b) consisted of 60 loop points with 10 evenly spaced knots. The best initial misfit between target and SRL fields was 39% obtained at z = -60mm. Field points and pairs are indicated in figure 8.4c.

An optimum fit was achieved after 8 iterations. Again a mixture of the strategies outlined in section 8.4 was used to obtain the final solution. Table 8.2 gives the details of the procedure. The final and target loops are compared in figures 8.4d and e and the target and model scans are shown in 8.4f.

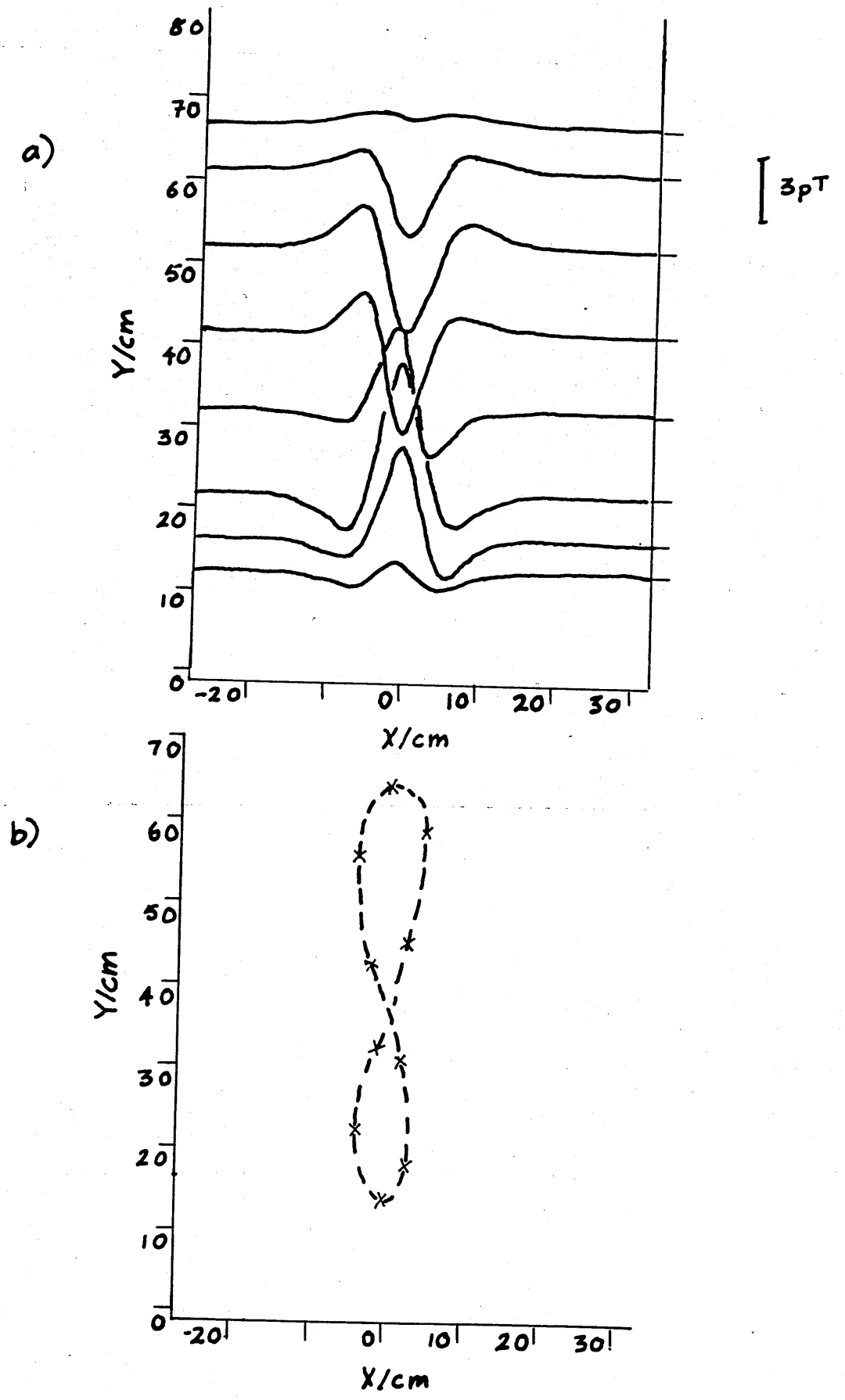

Figure 8.4 Example 2. Modelling a three dimensional figure of eight loop (experimental data).
a) Target scans **b)** Initial SRL. Perturbation centres are shown as crosses.

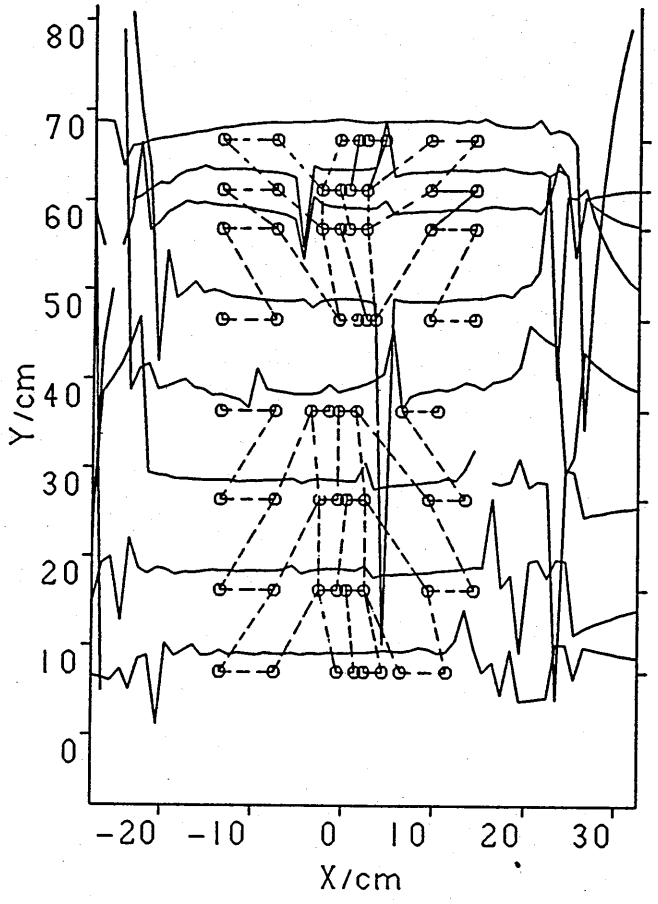

Figure 8.4c) Field ratio map ($B_{oz}/B_{Tz}-1$) also showing inversion points and pairs.

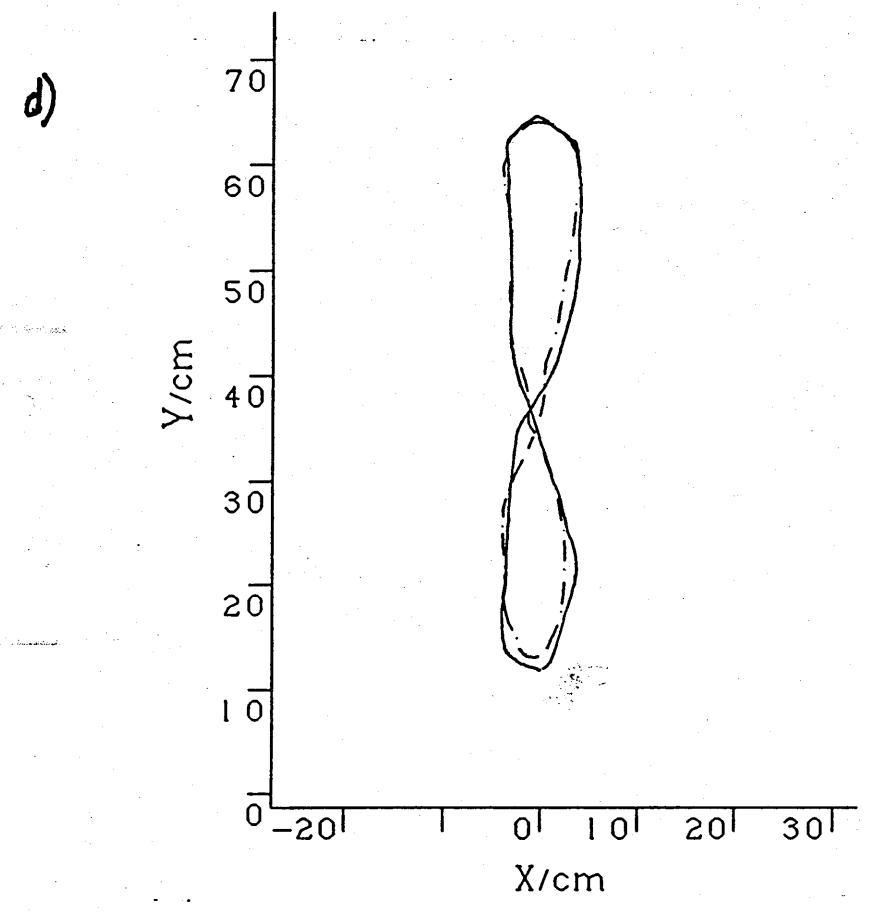

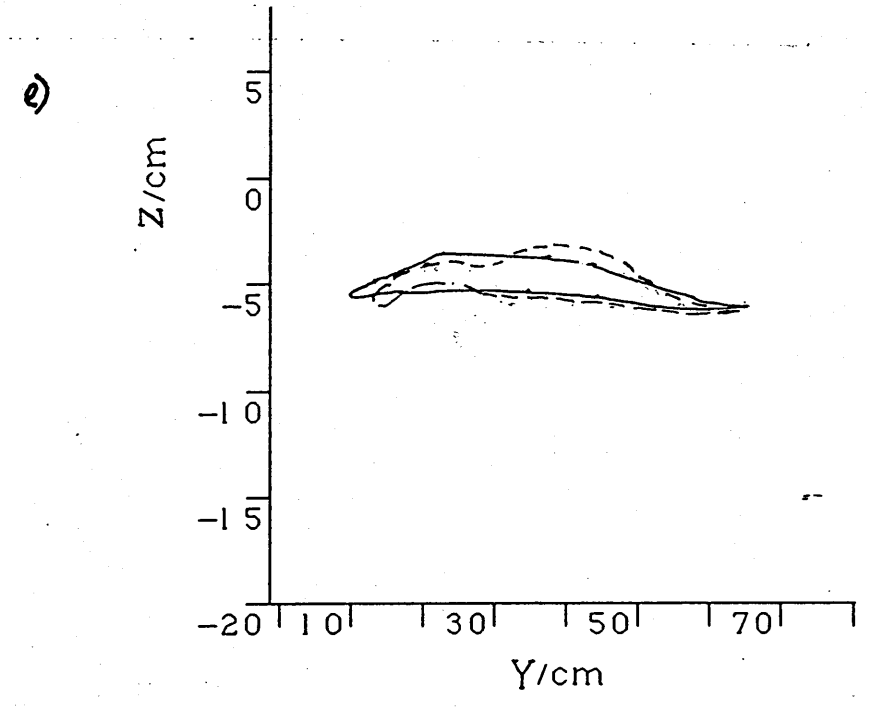

Figure 8.4d) Comparison of target loop (solid line) and final reference loop (dashed line) after 8 iterations, (x-y projection). **e)** Comparison of target loop (solid line) and final reference loop (dashed line) after 8 iterations, (y-z projection).

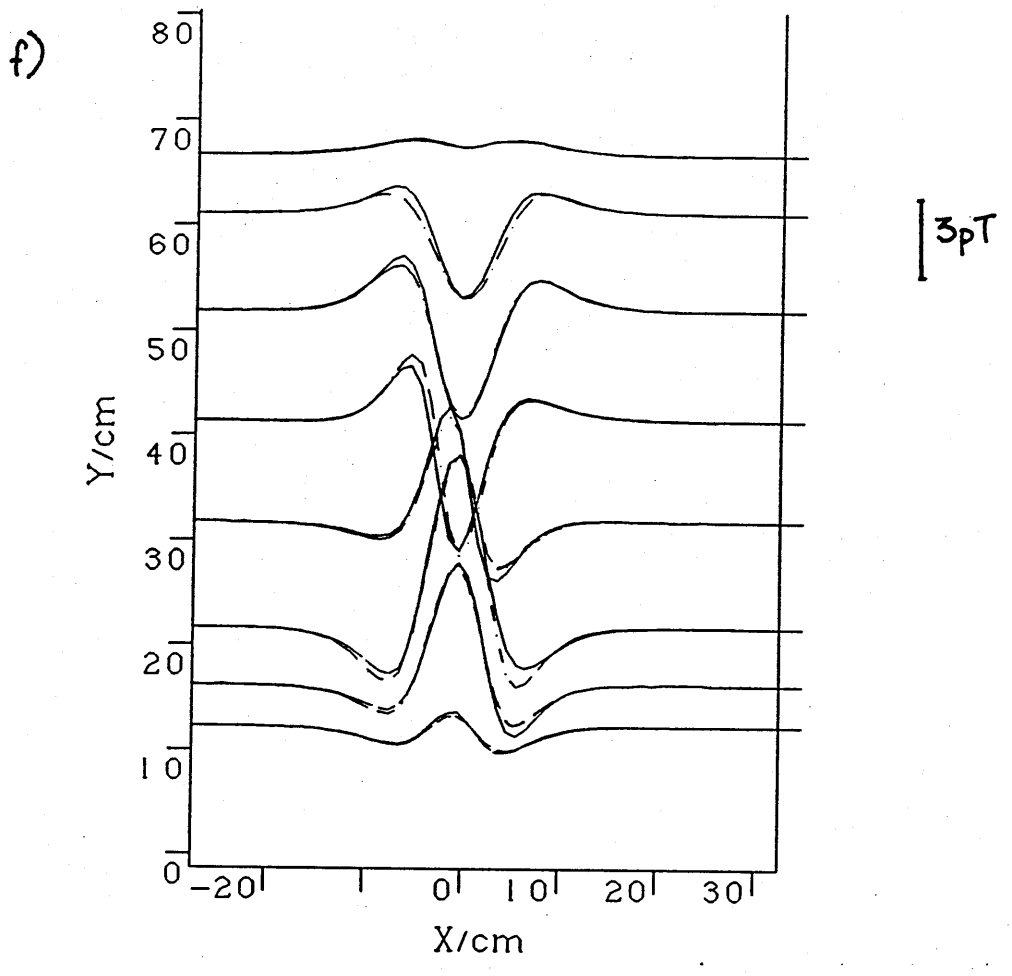

Figure 8.4f) Comparison of target loop scans (solid line) and final reference loop scans (dashed line)

TABLE 8.2

Iteration	Perturbations	Method	T_o	b_h	b_z	R%	R_d%
1	z	1	0.8	-	-	37	32
2	x,y	2a	0.8	-	-	24	19
3	x,y	2a	0.8	7	-	20	15
4	z	1	0.8	-	7	18	12
5	x,y	2a	0.8	7	-	18	9
6(1)	all	1	0.8	7	7	14	6
7	all	2a	0.8	7	7	13	5
8(2)	all	1	0.8	5	-	11	7

(1) Perturbations all moved one loop point anticlockwise

(2) Data partitioned - only bottom 4 scans used. Current fixed.

Once again the overall fit is good. In this case, the accuracy is a little more difficult to judge as the wire loop shape was only measured to within ±2mm. The best fit current was computed at 0.42mA.

This value for the current seems to be a substantial underestimate, however inspection of figure 8.4e indicates that the model loop is, on average, too high. As the current is calculated by a least squares best fit after the loop coordinates have been determined, one would expect the underestimate of depth to cause a compensatory underestimate of current. Because of the distance-sensitivity response of the gradiometer, even a small discrepancy in z could produce a large error in I.

8.6 The line current loop model applied to leg data

8.6.1 Leg data from normal subjects

The iterative-perturbative approach has produced high quality fits to data from a number of line current loops of different shapes, however its application to the leg field data has been somewhat less successful. The misfit between the simulated scans from the initial SRL (calculated from $\underset{\sim}{V}_{\equiv}$ vector positions) and the target field is in general much higher (around 80%) and the model loop shows a greater tendency to develop instabilities. It has not been possible to achieve a final best fit configuration with $R < 40\%$.

Nevertheless, the best fit loops are broadly consistent with the line dipole results of chapter 6 and I will show later in this section that the poor fit to the data is consistent with a physiologically likely model of the current generators.

The results of a typical inversion process are shown in figure 8.5. Figure 8.5a illustrates the target data for a set of scans above the lateral surface of the left leg of subject DG. The scans correspond to anatomical positions 1 to 8. It should be noted that the scans in this and subsequent figures are plotted in the opposite order to those in chapter 6.

The lateral aspect was chosen as the dipole vectors from the analysis in chapter 6 indicate that the loop should be predominantly horizontal in this orientation. Furthermore, the leg geometry allows data to be collected in a plane while remaining close to the leg surface. Although not essential, this simplifies the analysis somewhat.

The initial SRL is given in figure 8.5b and the data

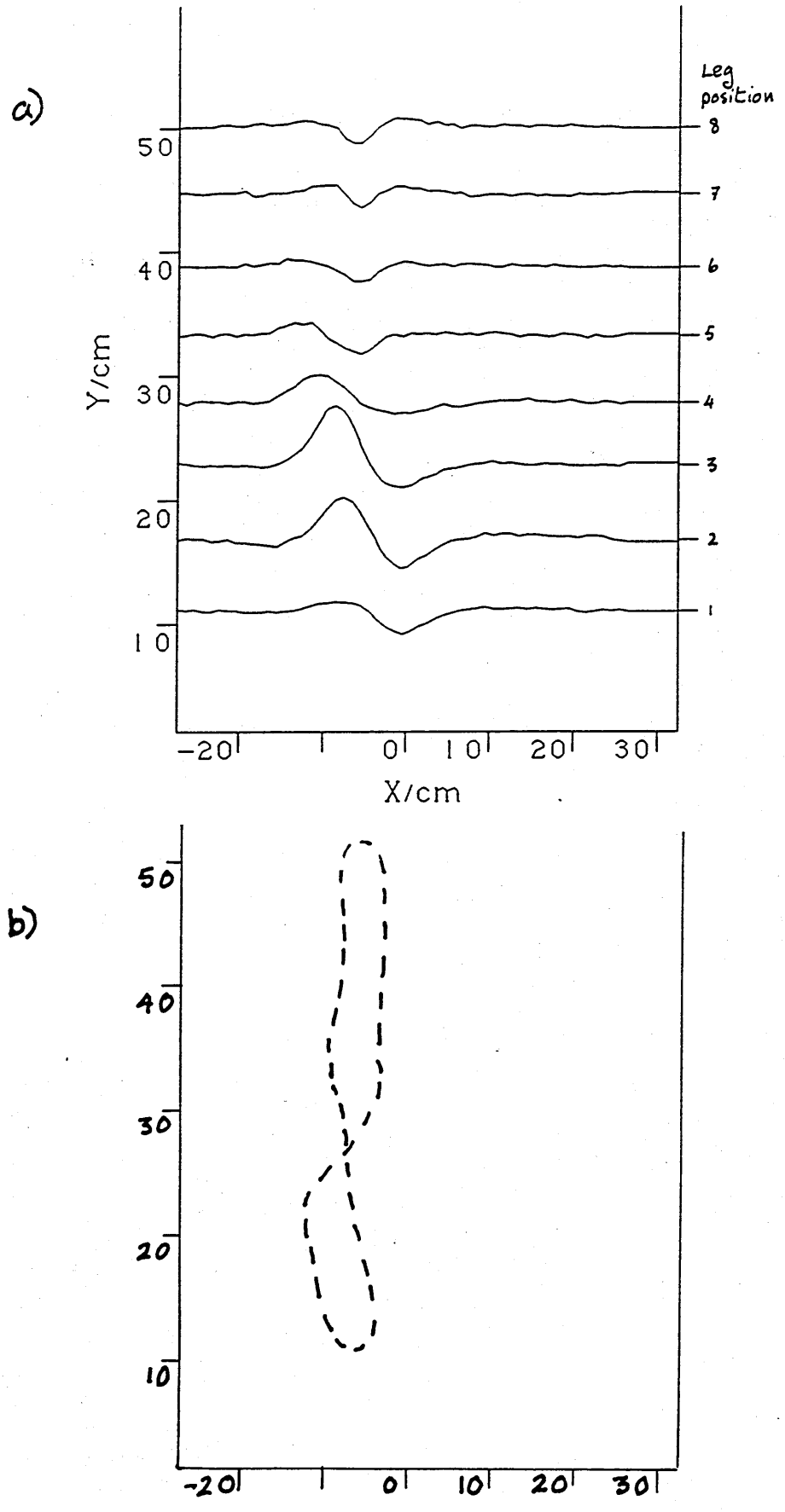

Figure 8.5 Example 3. Modelling the leg data.
a) Set of scans in a plane above the lateral surface of the leg for subject DG. b) Initial SRL derived from the data in figure 8.5a.

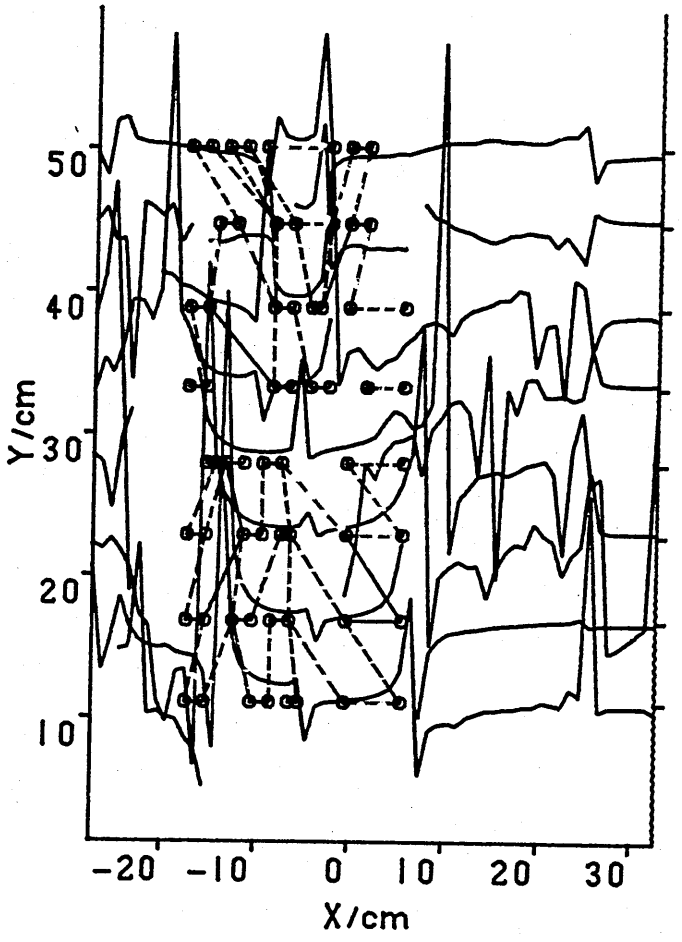

Figure 8.5c) Field ratio map ($B_{oz}/B_{Tz}-1$) showing inversion points and pairs.

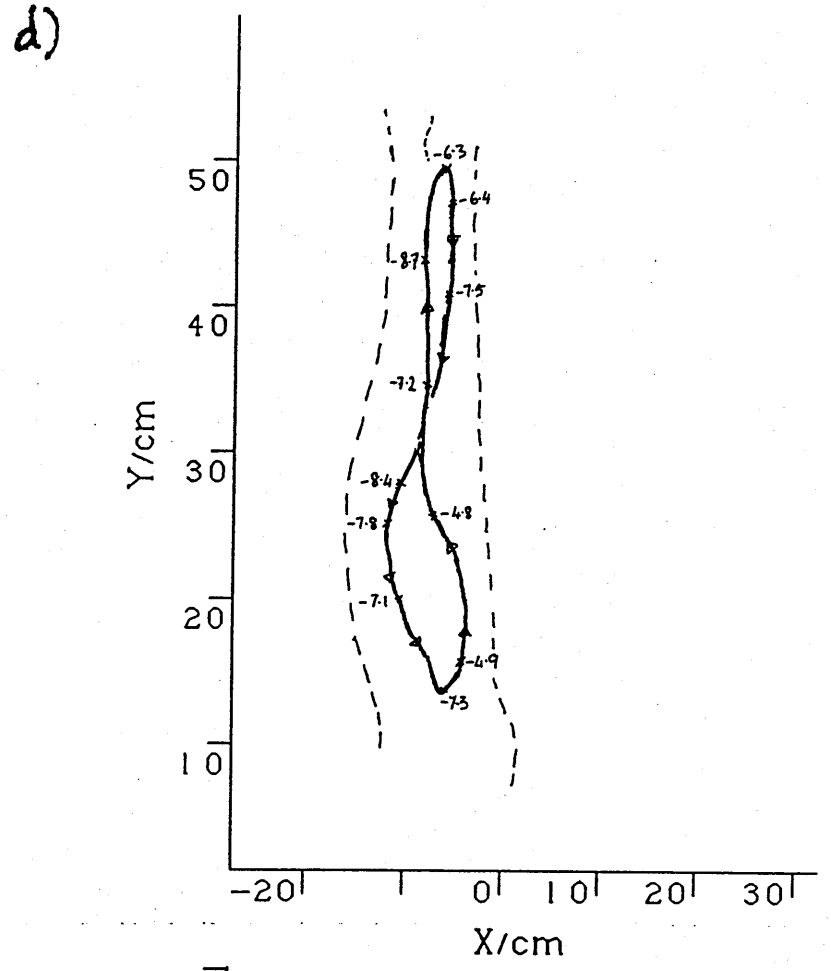

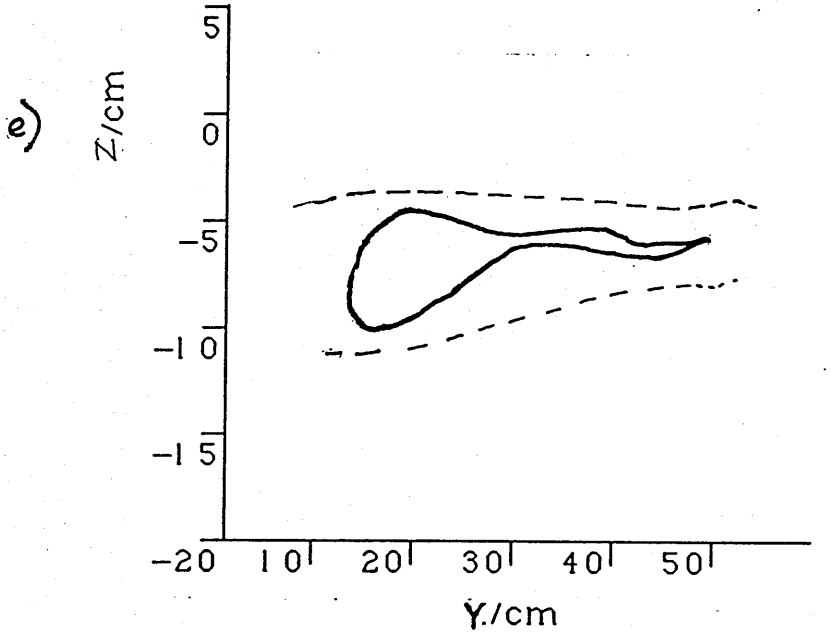

Figure 8.5d) Best fit loop for leg data (x-y projection). z coordinates are given at various points to indicate the three dimensional nature of the loop. Arrows indicate current direction. Approximate leg outline is shown dashed.**e)** Best fit loop for leg data (y-z projection).

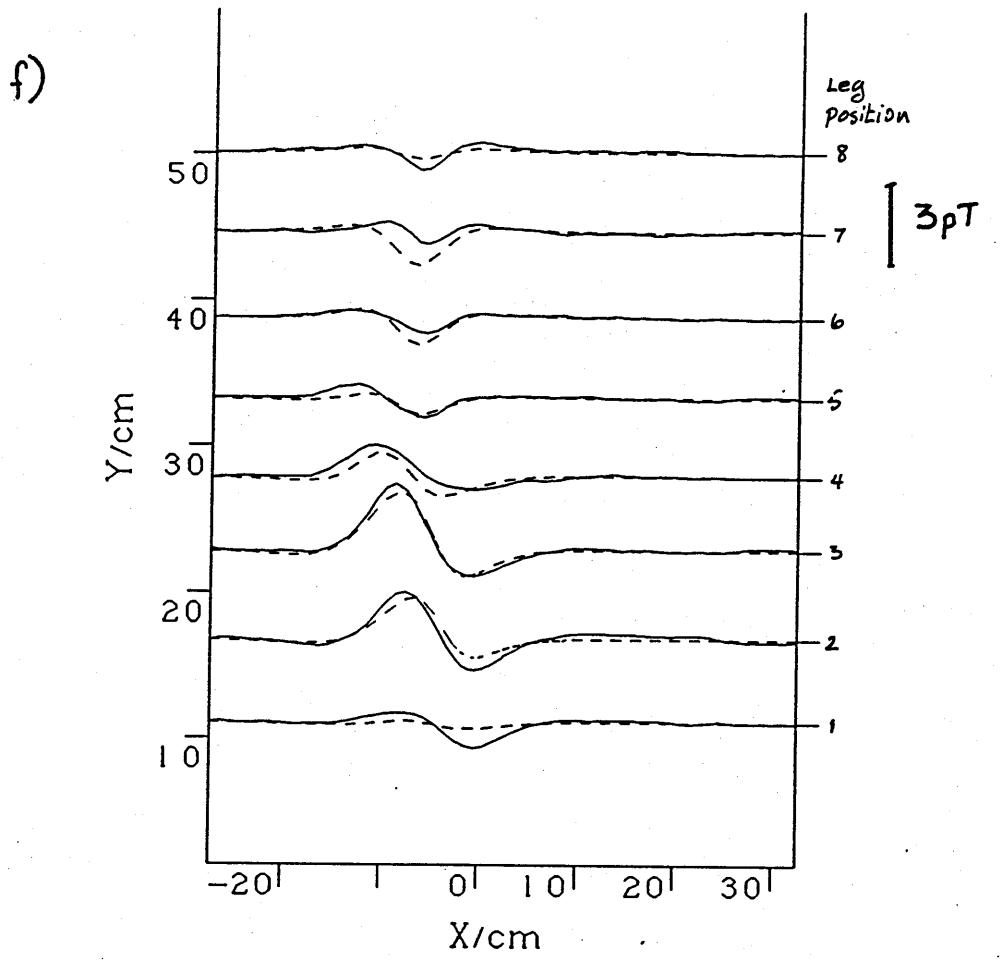

Figure 8.5f) Comparison of leg data with best fit loop signal.

here, particularly in the light of the good fits achieved with line current loops described above. Various approaches have been tried with these and other leg current data. The number and positions of perturbation nodes have been varied as have the number and positions of inversion data points and pairs. Different combinations of iteration methods have been used and yet in no case has it been possible to achieve a value of R < 40%.

It might be thought that a better fit could be achieved with a more accurate initial SRL. The initial SRL interpolated from $\underset{\sim}{V}_z$ maxima only gives information about the x-y loop coordinates, whereas the final loop shows considerable variation in the z direction (figure 8.5d). However further consideration of table 8.3 suggests that this is unlikely to be the cause of the eventual high misfit.

It can be seen from the table that the first three iterations were restricted to z perturbations only and gave a consistent decrease in R. As experience shows that the $\underset{\sim}{V}_z$ method provides a reasonable approximation of the x-y projection of the loop, the addition of improved z estimates obtained during these initial iterations means that we should expect to have a reasonable starting point for the 4th iteration. In spite of this, convergence is poor and only a 20% reduction in R is achieved between the 4th iteration and the final solution.

I have pursued the point further by using an alternative method to produce an initial SRL. Best fit line-dipole vectors have been calculated for each scan and positions of centres of upward and downward current have been estimated

points and pairs in 8.5c. Table 8.3 illustrates the development of the solution. The final value of the current was 2.2μA and the best obtainable value for R was 47% after 8 iterations. Figure 8.5d and e give the final loop shape with an approximate leg outline and a comparison of model and target data is shown in figure 8.5f. The whole inversion process is set out in table 8.3.

The final loop appears physiologically reasonable in that it broadly follows the muscle bulk of the lower leg. The shape agrees well with the dipole analysis (cf figure 6.9 and 6.5b). The indication is of a fairly wide loop (50mm) in the soleus/gastrocnemius muscle compartments and a narrower distal loop (30mm) in the anterior or lateral crural compartments. The width of the loop in the region of scan 3 is also of the same order as the suggested value of δl in section 6.3.

TABLE 8.3

Iteration	Perturbations	Method	T_o	b_h	b_z	R%	R_d%
1	z	1	0.8	-	9	71	66
2	z	1	0.8	-	9	61	57
3	z	1	0.8	-	9	60	56
4	x,y	2a	0.8	7	-	58	52
5	x,y	1	0.8	7	-	55	48
6	z	2a	0.8	-	9	54	42
7	all	2a	0.8	7	11	48	43
8	all	2a	0.8	5	9	47	39

Some consideration needs to be given to the large misfit

by assuming a current of 5μA and calculating the current separation δl from the line-dipole moment via equation 4.6. The remaining loop points were interpolated using a quadratic spline. The resultant SRL was then moved along the z-axis until a position of minimum R was found. Although the average misfit for each scan was 10%, the overall SRL misfit at optimum depth was 80%.

These results suggest strongly that the eventual poor fit to the data is not the result of a poor choice of SRL and one is led to the conclusion that the model is, in some way, inappropriate for the leg data. Thus the high misfit of the initial SRL is a symptom rather than a cause of the limitations of the current loop model in this particular situation.

I will consider three possible reasons why the current loop model may be inappropriate. Firstly, the measured field may arise not only from currents in the lower leg but also from currents in the thigh and foot. Certainly scans at positions 1 and 8 might be affected in this case, and indeed the fit is particularly poor at these positions (figure 8.5f). However, given the rapid attenuation of gradiometer response with distance, it is unlikely that the remaining scans are affected and therefore unlikely that this is a primary cause of the overall high misfit.

Secondly, it might be that two loops rather than a single 'figure of eight' would provide a better model. This would be consistent with the pattern suggested by the line-dipole analysis (figure 6.10). It can also be seen by inspection of figure 8.5f that a better fit could be

by assuming a current of 5μA and calculating the current separation δl from the line-dipole moment via equation 4.6. The remaining loop points were interpolated using a quadratic spline. The resultant SRL was then moved along the z-axis until a position of minimum R was found. Although the average misfit for each scan was 10%, the overall SRL misfit at optimum depth was 80%.

These results suggest strongly that the eventual poor fit to the data is not the result of a poor choice of SRL and one is led to the conclusion that the model is, in some way, inappropriate for the leg data. Thus the high misfit of the initial SRL is a symptom rather than a cause of the limitations of the current loop model in this particular situation.

I will consider three possible reasons why the current loop model may be inappropriate. Firstly, the measured field may arise not only from currents in the lower leg but also from currents in the thigh and foot. Certainly scans at positions 1 and 8 might be affected in this case, and indeed the fit is particularly poor at these positions (figure 8.5f). However, given the rapid attenuation of gradiometer response with distance, it is unlikely that the remaining scans are affected and therefore unlikely that this is a primary cause of the overall high misfit.

Secondly, it might be that two loops rather than a single 'figure of eight' would provide a better model. This would be consistent with the pattern suggested by the line-dipole analysis (figure 6.10). It can also be seen by inspection of figure 8.5f that a better fit could be

achieved if the current in the distal region (scans 6,7 and 8) were increased, while that in the remainder of the leg were decreased. A two loop model would, of course, allow independent current strengths in these regions.

Allowing for two loops in the model would involve considerable rewriting of the computer code, however it is possible to test the hypothesis by modelling each section of the leg separately with a single loop. This has been done and the results show no increase in stability of solution or quality of fit over the whole leg approach. For scans 1 to 4, it was not possible to achieve a value of $R < 40\%$. For scans 5 to 8, the lowest R obtainable was 70%.

Seen in the context of the results described in the remainder of this thesis, these misfit values are surprising. The scan morphology suggests a simple current structure and the line dipole analysis indicate that single centres of proximally and distally directed currents provide an adequate model. The results of section 8.5 indicate that, if the current pattern approximates to a continuous loop, the algorithm should find a satisfactory, convergent solution with a small misfit. The fact that such a solution cannot be found, either for the whole leg or the separate proximal and distal sections, indicates that a continuous loop or loops do not provide an appropriate model for these data.

This leads to a third possible explanation of the poor fit to the leg data. The physiological model for the current sources described in section 6.8. suggests that the measured field pattern is the summed effect of a large number of individual current generators in individual muscle cells

each with its own return path. In that case, one would expect that proximally and distally directed currents through any transverse plane would balance but one would not necessarily expect current strength to be maintained in either direction along the leg. This would explain why a good fit is achieved with the line dipole model while a successful solution with the current loop model is exceedingly difficult. In the latter case, the algorithm insists on current continuity throughout the loop.

8.6.2 Data from subject with fibula fracture

Unfortunately it has not been possible to attempt to fit the data from the fractured fibula (subject TR). These data were collected with a view to line dipole analysis and, while the depth of the leg below the detector was noted for each scan, there was no common z reference. Therefore the z positions cannot be correlated between scans as is required for the loop fitting procedure.

8.7 Summary of the line current loop model

An iterative perturbative approach to modelling unknown current sources with a line current loop has been developed. It has been successfully applied to computer simulations of both point field and 2nd order gradiometer (d^2B/dz^2) data from line current loop sources. It has also been successful in modelling experimental measurements from a SQUID gradiometer (again d^2B/dz^2) passed over current-carrying wire loops.

The method involves the initial estimate of a starting

reference loop followed by the application of an iterative perturbative algorithm to converge on a best fit loop.

A feature of the method is its interactive nature. This allows a high degree of flexibility in approach. The program operator can adopt various strategies depending on the results of previous iterations. Individual iterations can be rejected and repeated in modified form and sections of the data can be treated in isolation as circumstances dictate. Perturbation centres may be repositioned during the procedure and a subset of perturbations may be selected for a particular iteration. The linearity assumptions built into the algorithm can be checked for individual perturbation amplitudes.

The method works extremely well in the simple situation of single-component (B_z) point field data relating to a 2-dimensional loop at a known depth. When a finite area gradiometer is included in the algorithm and the loops are 3-dimensional, the method is less robust and more prone to instabilities. However, careful application of the strategies outlined in this chapter allows reasonable accuracy to be achieved even in the case of 'figure of eight' loops where the crossover may confuse the amplitude estimates.

The leg data were less well fitted than the data from actual current loops. However the best fit model agrees broadly with the results of the line dipole method (chapter 6) in terms of current location. The difficulty of achieving a high quality fit may be due to the current system being more complex than is allowed for in a single loop model.

In particular, the high misfit values suggest that the

requirement for current continuity between scans is inappropriate for the leg data. This is consistent with the physiological model described in section 6.8 which suggests that the observed fields may be caused by many individual current loops associated with individual muscle cells.

CHAPTER 9

CONCLUSIONS AND DISCUSSION

9.1 Summary of the modelling methods

Two methods of analysing magnetic field data to obtain information about the associated current distribution have been described in this thesis. In each case the algorithm has been designed assuming that the target data consists of a set of horizontal scans made by a finite area gradiometer above the current pattern. The scans are parallel to the x-axis of a cartesian coordinate system. The x-y plane is horizontal.

The two techniques have been successfully applied to computer simulations of current systems and to actual measurements made by scanning across current-carrying wire loops. Gradiometer measurements of the B-field in the vicinity of the human leg have also been analysed for a number of normal subjects and for one subject with a fractured fibula.

9.2 The line dipole technique

9.2.1 Simplifying assumptions of the line dipole model

The line dipole method is based on certain simplifying assumptions regarding current structure. These are:

1) Currents are predominantly parallel to the y-axis of the coordinate system.

2) The x-z current cross-section is assumed to be approximately line-dipolar. The term 'line-dipolar' is defined in chapter 4.

3) The data in each scan are determined by the currents in the immediate vicinity of the scan. It follows that, for the purposes of analysis, the current cross-section in the x-z plane directly below the scan can be assumed to extend to $\pm\infty$ in the y direction.

These assumptions allow the currents to be modelled by the dipole term in a multipole expansion. This dipole term may be physically represented by a pair of oppositely directed line currents parallel to the y-axis with infinitessimal separation. The problem is thus reduced to two dimensions since the dipole position is specified by x,z coordinates only.

9.2.2 Tests on the line-dipole model

The algorithm gives results which are exactly correct when the input data is purely line-dipolar - thus demonstrating its internal consistency. Tests have also been carried out to ascertain the response of the model when the target currents deviate from the above assumptions.

In order to determine the effect of a non-line-dipolar cross section, the technique was applied to a pair of oppositely oriented currents parallel to the y-axis and the separation between the currents was varied.

With a small separation, the best fit model parameters accurately reflected the position and strength of the currents. At larger separations, a convergent solution was easily achieved, although there were discrepancies between

the best fit line-dipole positions and the actual parameters of the target configuration. The discrepancies showed a cyclical variation with Ø, the dipole vector angle. The amplitude of this variation depended on δl, the current separation, and the depth of the currents below the scanning plane. It is possible to use the amplitude of this variation with Ø to recalculate the parameter values corrected for the discrepancies.

One interesting result of these tests was that, for current pairs with large δl, the model dipole may produce a good fit to the target data yet have large parameter discrepancies. Thus a small misfit is not necessarily a guarantee of accurate parameter values. This may be because the algorithm finds a location for the dipole at which the quadrupole term is zero, rather than a location which reflects the true position of the line current pair.

Assumption (3) has been tested by modelling current systems which vary in the y direction. The region over which the effect of such a non-uniformity is detectable increases with depth, so these tests were performed at a the greatest depth at which leg currents are likely to be detected (about 80mm).

By calculating the simulated gradiometer response for a truncated line dipole, it has been possible to compute the rate at which the gradiometer response falls off with distance measured in the horizontal plane. In particular, it may be calculated that more than 90% of the gradiometer signal is generated within 90mm of the line of scan. Furthermore the position and orientation of a truncated line

dipole which extends only 10mm on either side of the scan position can be accurately located using the infinite line dipole model. These results suggest that line-dipole-like currents that are approximately constant for a few cm on either side of the line of scan may be adequately modelled with the line dipole approach.

Empirical tests with various three dimensional configurations corroborate these findings. The model dipole location was correct to within 10mm provided the line of scan was more than 10mm from the end of a loop or more than 70mm from an abrupt 180° twist.

Tests on non-parallel wire pairs (assumption (1)) indicate that small deviations from parallel (included angle 5°) have little effect. Again the model dipole location discrepancy is less than 10mm provided the line of scan is more than 10mm from the crossover point for the currents.

9.2.3 Analysis of leg data

Data from 25 normal subjects and one with a fractured fibula have been analysed. The normal subject fields all follow a similar pattern with large, reproducible signals from positions 2 and 4 consistent with a distally directed current in the anterior/lateral crural compartments and a proximally directed current in the gastrocnemius or soleus.

At positions 6 and 7, the currents are smaller and more varied. For most subjects, both upward and downward currents are probably in the anterior or lateral crural compartments. The whole pattern is consistent with a single 'figure of eight' loop extending the length of the lower leg, or two separate loops, one in the muscle bulk of the calf and the

other in the distal section of the anterior crural compartment.

Experiments have also been carried out at position 3 with the leg rotated about its long axis so that in turn anterior, lateral, posterior and medial surfaces were scanned. The variation of dipole parameters with angle of rotation is consistent with a separation of several cm between the upward and downward centres of current. With this separation, the current strength would be a few microamps. These results have suggested the possibility of modelling the leg data with a continuous line current loop.

9.2.4 Physiological source of the leg currents

The dipole parameters indicate that at least some of the current is in the muscle bulk but the dipole locations have not been determined with sufficient accuracy to rule out the possibility of part of the current path being in the tibia. The most likely physiological mechanism for producing tibial currents would be stress related potentials in the bone, however mechanically stressing the tibia had no effect on the observed fields.

Other experiments have shown that the signals are not related to blood flow, while the probable location of the current path makes it unlikely that ionic transport within the main nerves of the leg is involved. Thus the most likely hypothesis is that the currents are produced by some mechanism involving the muscle fibres themselves. This is supported by results indicating that the signal strength decays if the leg muscles are kept relaxed.

A possible explanation is that an inhomogeneous arrangement of Cl^- channels in the muscle fibre cell membranes gives rise to a nonuniform Cl^- density in the extra cellular fluid. The observed current is then the result of a longitudinal ionic flow acting to restore equilibrium.

9.2.5 Analysis of leg fracture signals

The line dipole vectors provide a useful means of characterising the normal leg signals and also give some indication of the physiological source. If the current pattern within a naturally healing, fractured limb is significantly different, the line dipole model should provide a useful method of analysing the differences. Unfortunately, it has only been possible to look at one subject with a fibula fracture. These results are encouraging in that substantial differences were evident between the healthy and the fractured limb signals, however more subjects need to be investigated before any meaningful conclusions can be drawn.

9.3 The iterative perturbative line current loop technique

9.3.1 Description of the model

While the line-dipole model works well on a scan by scan basis, the simplifying assumptions described above are somewhat restrictive. The line current loop model is an attempt to loosen some of these restrictions.

The approach is to model the current pattern as a continuous, closed line current loop. Continuity of current strength between scans is required but there are no

restrictions on current direction. This model is consistent with the evidence mentioned above that centres of upward and downward current may be separated by several centimetres.

The method requires the definition of an initial reference loop as the starting point for an iterative-perturbative process. Each iteration proceeds by adding a set of perturbations of suitable amplitude to the reference loop. Estimates of the perturbation amplitudes are derived from the differences between the target data and the simulated reference loop signal.

The reconstructed loop is then used as a starting point for the next iteration and the process continues until an optimum fit is found. The method is interactive in that the operator may intervene at various points to guide the course of the iterations.

9.3.2 Application of the iterative perturbative technique to current loops

The application of the method to simulations of point field data from 2-dimensional sources has been highly successful. Difficulties have arisen only in the case of very narrow loops (where changes in current strength and loop width have almost identical effects on the field) and in 'figure of eight loops' (where fitting is problematic close to the crossover point).

In the more realistic situation of a gradiometer signal generated by a 3-dimensional loop, obtaining an accurate fit has proved more difficult. However, various interactive strategies have been developed which are helpful in avoiding

non-convergent iterations and regions of instability. With the implementation of these strategies, the technique has been successfully applied to 3-dimensional 'figure of eight' loops similar in shape to the postulated current path in the human leg.

9.3.3 Application of the iterative perturbative technique to leg data

The application of the technique to human leg data has been less successful. It has proved difficult to obtain a solution with a misfit much better than 50%. This suggests that a single, continuous loop requiring current continuity is not an approppriate model for the currents in the leg. Attempts to fit the data with two, separate loops also produce large misfits.

It seems highly probable that the difficulty in achieving acceptable solutions is attributable to the fact that continuity of current strength around the average current path is not maintained in the leg. This is entirely consistent with the measured field being due to the cumulative effect of currents in individual muscle fibres.

In spite of the relatively high misfit values for the line current loop method, the results are in broad agreement with the line-dipole analysis. The modelled current path comprises a wide loop within the gastrocnemius/soleus compartments and a smaller loop in the distal region, probably in the anterior and/or lateral crural compartment. Unfortunately it has not yet been possible to model data from a fibula fracture using this technique.

9.4 Future work

The main purpose of the overall research project to which these studies have contributed is to investigate the possibility of the existence of currents related to naturally healing fractures. The overriding priority at this stage is to make more measurements of such fractures. To this end a collaboration has been established with Leicester Royal Infirmary. Leicester Royal Infirmary acts as a trauma centre for the East Midlands and it is hoped that a significant number of patients with fibula fractures will be examined in the next few months. It should also be possible to examine patients suffering from non-union of a tibial fracture to see if there is any deviation from the normal field pattern.

A further medical application of the modelling techniques may lie in the assessment of muscle damage. If the leg currents are generated by, and flow parallel to, the muscle cell membranes, it is likely that severe damage to the muscle will disrupt the curremt paths (This has already been suggested in chapter 6 as a possible reason for the anomalous features of the scans associated with the fibula fracture). As the normal field patterns are well characterised, it may be possible to assess the extent of muscle damage by analysis of the magnetic field data. This would be very useful as the optimum treatment regime for a limb fracture depends on the extent of muscle damage, yet, at present, there is no non-invasive way of assessing such damage. In order to develop these ideas, we intend to examine subjects with severe leg muscle damage but no

fractures.

The results from the current loop method suggest the need for an algorithm which can map subtle current density variations arising from currents distributed throughout the muscle bulk of the lower leg. A novel approach recently suggested by Ioannides et al (1989) uses a probability weighting technique to allow for just such distributed sources and it is hoped to apply this technique to the leg data in the near future.

At present, the current loop method is interactive. While this allows flexibility and permits decisions on the iterative procedure to be made during the course of the inversion, it is time consuming and tedious. A development here may be the introduction of 'expert systems' techniques which can make the appropriate strategic decisions automatically. Research into the application of expert systems approaches to data analysis is currently being pursued by the Biomagnetism Research Group at the Open University (Palfreyman et al,1989).

APPENDIX 1

Calculation of flux through a sensing coil from a truncated line dipole.

In this appendix, I wish to show that the flux through a sensing coil from a truncated, axially uniform current distribution such as that shown in figure 5.10 can be represented by a multipole expansion similar in form to the line multipole expansion described in chapter 4. I will also derive an expression for the dipole term of this expansion.

Consider a distribution of currents, uniform with respect to y and everywhere parallel to the y-axis. The current is nonzero only for $-L < y < L$. Figures 5.10 and A1 illustrate the situation. $\underset{\sim}{r}'$ ($= x'i + z'k$) defines the position of a current element with strength $\delta I = J(r')\,\delta a'$, where $\delta a'$ is an element of area.

A horizontal, sensing coil G of radius c is positioned with its centre at r_o directly above the x-axis. In order to obtain a value for the flux S_T through the sensing coil due to the current element at $\underset{\sim}{r}'$, the surface integral

$$S_{T1} = \iint_G \underset{\sim}{B}\cdot\hat{\underset{\sim}{n}}\, da \qquad \text{(A1)}$$

must be evaluated, where n is the unit vector perpendicular to the element of area a and B is the field due to the current element.

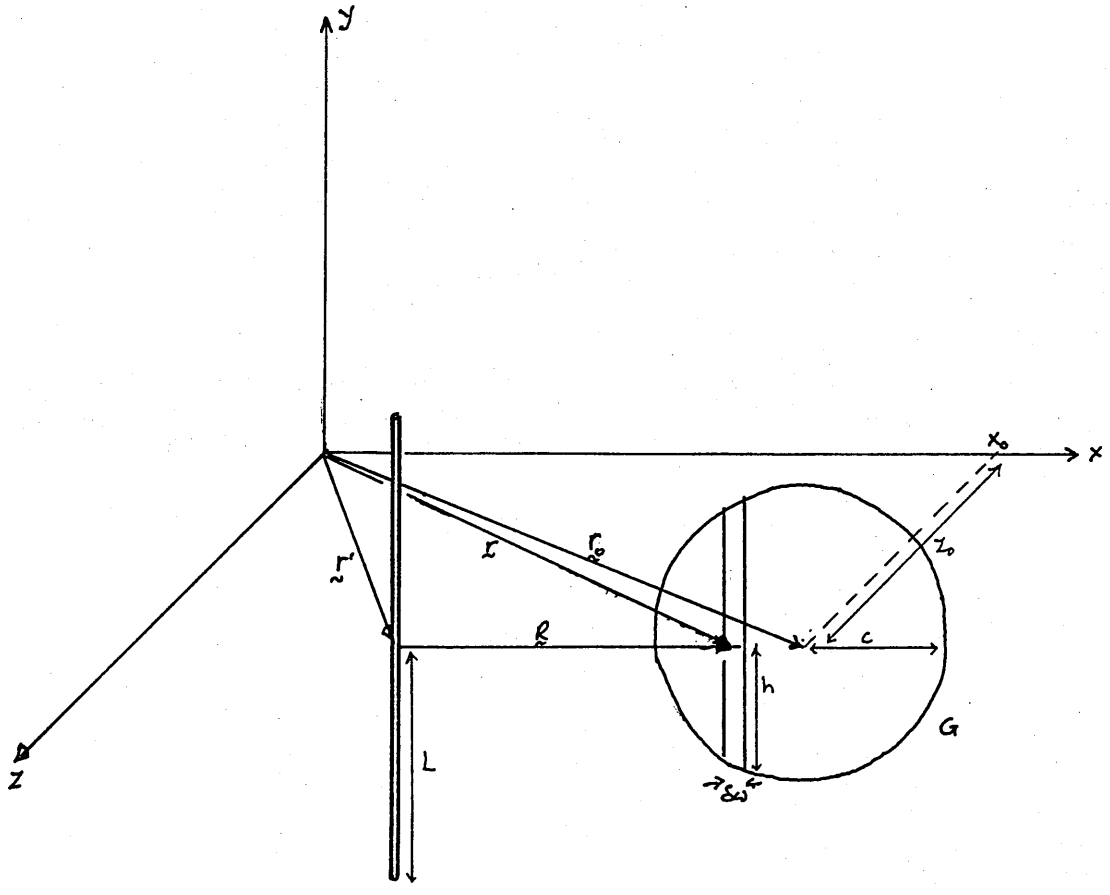

Figure A1 The coordinate system used to discuss the truncated line dipole. A truncated line element of half-length L lies parallel to the y-axis. A gradiometer coil G is positioned in an x-y plane with centre at $r_o = (x_o, z_o)$. The integration is performed by summing the flux over a series of strips of length h and width w parallel to the y-axis.

In this case

$$S_{T1} = \iint_G B_z \, dx\,dy \qquad \text{(A2)}$$

The integral with respect to y can in fact be performed analytically. Thus the flux through a strip of width δw parallel to the y-axis (such as that shown in figure A1) can be evaluated, leaving the integration with respect to x to be carried out numerically.

We proceed by calculating the field at some point $\underset{\sim}{r}$. From Biot-Savart, this is (using the notation of figure A1):

$$\underset{\sim}{B}(\underset{\sim}{r}) = \frac{\mu I}{4\pi r^2}\left\{\frac{1}{\sqrt{l^2+R^2}} + \frac{(2L-l)}{\sqrt{(2L-l)^2+R^2}}\right\} \underset{\sim}{j} \times \underset{\sim}{R} \qquad \text{(A3)}$$

Rather than integrate (A3) with respect to y to obtain the flux through the strip, it is easier to use the variable l. This is equivalent to holding $\underset{\sim}{r}$ fixed and shifting the current element in the y direction by an amount equal to the strip length.

Thus the total flux $\delta\Phi_T$ through the strip is:

$$\delta\Phi_T = \frac{\mu I}{4\pi R^2}\,\delta w\,\underset{\sim}{\hat{k}}\cdot(\underset{\sim}{j}\times\underset{\sim}{R})\int_{L-h}^{L+h}\frac{I\,dl}{\sqrt{l^2+R^2}} \qquad \text{(A4)}$$

which yields:

$$\delta\Phi_T = \frac{\mu I}{4\pi}\,\delta w\,\underset{\sim}{\hat{k}}\cdot(\underset{\sim}{\hat{j}}\times\underset{\sim}{\hat{R}})\,2\left[\left((L+h)^2+R^2\right)^{\frac{1}{2}} - \left((L-h)^2+R^2\right)^{\frac{1}{2}}\right] \qquad \text{(A5)}$$

The average B-field z-component across the strip is then:

$$\delta B_z = -\frac{\mu I X}{4\pi R^2 h}\left[((L+h)^2+R^2)^{1/2} - ((L-h)^2+R^2)^{1/2}\right] \qquad (A6)$$

which can be written:

$$\delta B_z = -\frac{\mu I}{4\pi h} f(\underset{\sim}{R}) \qquad (A7)$$

where

$$f(\underset{\sim}{R}) = \frac{X}{R^2}\left[((L+h)^2+R^2)^{1/2} - ((L-h)^2+R^2)^{1/2}\right] \qquad (A8)$$

The multipole expansion for the current distribution can be derived by replacing the current element at $\underset{\sim}{r}'$ with a series of terms at the origin. This can be done using a Taylor series expansion for $f(\underset{\sim}{R})$.

$$f(\underset{\sim}{R}) = f(\underset{\sim}{r}-\underset{\sim}{r}') = \left(1 + (-r'\cdot\nabla_r) + \frac{(-r'\cdot\nabla_r)^2}{2} + \cdots\right) f(\underset{\sim}{r}) \qquad (A9)$$

The second term is the dipole term. Writing this as f_1 we have:

$$f_1(\underset{\sim}{r}) = -\left(x'\frac{\partial}{\partial x} + z'\frac{\partial}{\partial z}\right)\left\{\frac{X}{r^2}\left[((L+h)^2+r^2)^{1/2} - (L-h)^2+r^2)^{1/2}\right]\right\} \qquad (A10)$$

After some algebra this gives:

$$f_1(\underset{\sim}{r}) = \frac{\hat{x}}{r^4}\cdot\left\{x(\underset{\sim}{r}\cdot\underset{\sim}{r}')\left[\frac{r^2+2(L+h)^2}{((L+h)^2+r^2)^{1/2}} - \frac{r^2+2(L-h)^2}{((L-h)^2+r^2)^{1/2}}\right]\right.$$

$$\left. - x\, r^2\left[((L+h)^2+r^2)^{1/2} - ((L-h)^2+r^2)^{1/2}\right]\right\} \qquad (A11)$$

$$S_{T1} = -\frac{\mu m}{2\pi}\frac{1}{\pi c^2}\sum k_i \int_{-c}^{c} \frac{ds}{((s+X_{iD})^2+Z_{iD}^2)} \left\{ \left[\frac{(Z_{iD}^2-(X_{iD}+s)^2)(L+h)^2 + Z_{iD}^2(Z_{iD}^2+(X_{iD}+s)^2)}{[(X_{iD}+s)^2+Z_{iD}^2+(L+h)^2]^{1/2}} \right.\right.$$

$$\left.\left. - \frac{(Z_{iD}^2-(X_{iD}+s)^2)(L-h)^2 + Z_{iD}^2(Z_{iD}^2+(X_{iD}+s)^2)}{[(X_{iD}+s)^2+Z_{iD}^2+(L-h)^2]^{1/2}} \right] \sin\phi \right.$$

$$\left. - (X_{iD}+s) Z_{iD} \left[\frac{((X_{iD}+s)^2+Z_{iD}^2+2(L+h)^2)}{[(X_{iD}+s)^2+Z_{iD}^2+(L+h)^2]^{1/2}} - \frac{((X_{iD}+s)^2+Z_{iD}^2+2(L-h)^2}{[(X_{iD}+s)^2+Z_{iD}^2+(L-h)^2]^{1/2}} \right] \cos\phi \right\} \quad \text{(A15)}$$

This equation reduces to (4.20) as $L \to \infty$.

The dipole term in the multipole expansion for the whole current distribution is simply obtained by combining (A7) and (A11) and integrating over a'.

$$\delta B_{z1} = -\frac{\mu I}{4\pi h}\,\hat{\underset{\sim}{z}}\cdot\left\{\underset{\sim}{r}(\underset{\sim}{r}\cdot\underset{\sim}{r}')\frac{(r^2+2(L+h)^2)}{((L+h)^2+r^2)^{1/2}}-\frac{(r^2+2(L-h)^2)}{((L-h)^2+r^2)^{1/2}}\right.$$

$$\left.-\underset{\sim}{r}'r^2\left[((L+h)^2+r^2)^{1/2}-((L-h)^2+r^2)^{1/2}\right]\right\} \qquad \text{(A12)}$$

As before, the dipole moment is defined as $\underset{\sim}{m} = \int_{a'}\underset{\sim}{r}'J(\underset{\sim}{r}')da'$, so

$$B_{z1} = -\frac{\mu}{4\pi h}\,\hat{\underset{\sim}{z}}\cdot\left\{\underset{\sim}{r}\left(\int\underset{\sim}{r}'J(\underset{\sim}{r}')\,da'\right)\left[\frac{(r^2+2(L+h)^2)}{((L+h)^2+r^2)^{1/2}}-\frac{(r^2+2(L-h)^2)}{((L-h)^2+r^2)^{1/2}}\right]\right.$$

$$\left.-r^2\int\underset{\sim}{r}'J(\underset{\sim}{r}')da'\left[((L+h)^2+r^2)^{1/2}-((L-h)^2+r^2)^{1/2}\right]\right\} \qquad \text{(A13)}$$

Using the notation of equations (4.16) and (4.17), (A13) can be rewritten for the laboratory system in terms of the defining dipole parameters m,Ø, and the coordinates x_D, z_D.

$$B_{z1} = \frac{\mu m}{4\pi h r_0^4}\left\{\left[\frac{(Z_0^2-X_0^2)(L+h)^2+Z_0^2(X_0^2+Z_0)^2}{((L+h)^2+r^2)^{1/2}}-\frac{(Z_0^2-X_0^2)(L-h)^2+Z_0^2(X_0^2+Z_0^2)}{((L-h)^2+r^2)^{1/2}}\right]\sin\phi\right.$$

$$\left.-X_0Z_0\left[\frac{r_0^2+2(L+h)^2}{((L+h)^2+r_0^2)^{1/2}}-\frac{r_0^2+2(L-h)^2}{((L-h)^2+r_0^2)^{1/2}}\right]\cos\phi\right\} \qquad \text{(A14)}$$

Note that here $\underset{\sim}{r}_D = \underset{\sim}{r}_0-\underset{\sim}{r}_1$.

Finally, the expression for the total flux through the sensing coil can be obtained by multiplying (A14) by 2h and integrating with respect to x beteen x_0+c and x_0-c. Summing over the sensing coils in the usual manner gives the required gradiometer signal:

REFERENCES

Barker A. T., Lunt A. W. The effects of pulsed magnetic fields of the type used in the stimulation of bone fracture healing. Clin. Phys. Physiol. Meas. 4(1): 1-27. 1983.

Barker A.T., Dixon R.A., Sharrard W.T.W., Sutcliffe M.L. Pulsed magnetic field therapy for tibial nonunion: interim results of a double blind trial. Lancet No 384. May 5th, 1984.

Basset C.A.L. The development and application of pulsed electromagnetic fields for ununited fractures and arthrodeses. Clinics in Plastic Surgery 12(2): 1985

Betz W.J., Caldwell J.H., Ribchester R.R., Robinson K.R., Stump K.F. Endogenous fields around muscle fibres and the Na^{+}-K^{+} pump. Nature 287: 5779. 235-237. 1980

Betz W.J., Caldwell J.H., Kinnamon S.C. Physiological basis of a steady endogenous current in rat lumbrical muscle. J. Gen. Physiol. 83: 57-92. 1984.

Blumlein H., McDaniel J., Perren S.M. Electrical Stimulation of Bone Growth and Repair. pages 41-44. Springer Verlag, Berlin. 1978.

Borgens R.B. What is the role of naturally produced electric currents in vertebrate regeneration and healing? Internat. Rev. Cytology 76: 1982.

Borgens R.B., Vanables J.W., Jaffe L.F. Bioelectricity and regeneration. Bioscience 298: (8) 468-473. 1979.

Brighton C.T. J. Bone and Joint Surgery. 63A: 847-851. 1981.

Brighton C.T., Friedenburg Z.B., Mitchell E.I., Booth R.E. Clin. Orthop. 124: 106-123. 1977.

Brighton C.T., Black J., Friedenburg Z.B., Esterhai J.L., Day J.L., Connolly J.F. J. Bone and Joint Surgery. 63A(1): 2-13. 1981.

Chapman R.M., Ilmoniemi R.J., Barbarena S., Romani G.L. Electroenceph. Clin. Neurophysiology. 1984

Cuffin B.N., Cohen D. Magnetic fields produced by models of biological current sources. J. App. Phys.. 48(9). 3973. 1977.

Dalquist G., Bjorck A. Numerical Methods. Prentice Hall, Englewood Cliffs, New Jersey. 1974.

de Vahl Davis G. Numerical Methods in Science and Engineering. p95 Allen and Unwin, London. 1986.

Dubois-Reymond E. Ann. Phys. Chem. (Leipzig) 58: 1-30. 1843.

Enzler M.A., Waelchi-Suter E., Perren S.M. Unfallheilkunde 83: 188-94. 1980.

Friedenberg Z.B., Harlow M.C., Brighton C.T. J. Trauma 11: 883-5. 1971

Friedenberg Z.B., Brighton C.T. Bioelectric potential in bone. J. Bone and Joint Surgery 48A: 915-923. 1986.

Fuentes A.E.R., de Souza J.P.H., Valeri V., et al Experimental models of electrical stimulation of Pseudarthrosis healing. Clin. Orthop. 183: 267-275. 1984

Fukada E., Yasuda I. On the piezoelectric effect in bone J. Physiol. Soc. Japan 12: 1158-1162. 1957.

Geselowitz D.B. IEEE Trans. Mag. MAG-6: 346-347. 1970.

Gifford R.P., Webb R.A., Wheatley J.C. Principles and methods of low frequency electric and magnetic measurements using an rf biased, point contact, superconducting device. J. Low Temp. Physics 6(5/6). 1972

Gonelli R.S., Sicuro M. Use of the current multipole model for the cardiac source localisation of normal subjects. Biomagnetism '87. Atsumi K., Kotani M., Ueno S., Katila T. Williamson S.J. (eds.) Tokyo Denki University Press. 1988.

Gonelli R.S., Agnello M. Simulation of an excitation wavefront spreading through an anisotropic myocardium: an analytic study of the heart magnetic field during ventricular activity. Biomagnetism '87. Atsumi K., Kotani M., Ueno S., Katila T., Williamson S.J. (eds.) Tokyo Denki University Press, Tokyo. 1988.

Grimes D.I.F, Ioannides A.A. Reconstructing 3-dimensional line current sources from magnetic field data Biomagnetism '87. Atsumi K., Kotani M., Ueno S., Katila T., Williamson S.J. (eds.) Tokyo Denki University Press, Tokyo. 1988.

Grimes D.I.F., Lennard R.F., Smith T.B., Swithenby S.J. Multipole analysis of biomagnetic signals from the human leg IEEE Trans. Mag. MAG-21(3). May, 1985.

Grimes D.I.F., Lennard R.F., Swithenby S.J. Macroscopic ionic currents in the human leg. Phys. Med. Biol. 30(10). 1101-1112. 1985.

Grynszpan F., Geselowitz D.B. Model studies of the magnetocardiogram. Biophys. J. 13:. 911-925. 1973.

Harrop R., Weinberg H., Brickett P., Dylestra C. Phys. Med. Biol. 32(1) 1984.

Helmholtz H. Ueber einige Gesetze der Vertheilung elektrische Stroeme in Koerperlichen Leitern mit Anwendungen auf die thierischen-elektrischen Versuchen. Ann. Physik u. Chemie 165(89). 211-33. 1853.

Hyde I.H. Difference in electrical potential in developing eggs. Am. J. Physiol. 12: 241-275. 1905.

Ioannides A.A. Graphical solutions and representations for the biomagnetic inverse problem. Advances in Electronics and Electron Physics. Supplement 19, Inverse Problems: An Interdisciplinary Study. Sabatier P.C. ed. Academic Press, Orlando. 1987.

Ioannides A.A., Clarke C.J.S, Bolton J.R. Localised and distributed source solutions for the biomagnetic inverse problem. submitted to the 7th International Conference on Biomagnetism. New York, 1989

Ioannides A.A., Grimes D.I.F. A method for reconstructing line current sources from magnetic field data. Inverse Problems 2: 331-352. 1986.

Ioannides A.A., Janday B.S., Swithenby S.J. The identification of multipole current dipole sources using spatial partitioning of data. Abstracts of the 6th International Conference on Biomagnetism. Tokyo, 1987.

Ioannides A.A., Macintosh R.S. A method for S-matrix potential inversion at fixed energy. Nucl. Phys. A 438: 1985.

Ioannides A.A., Swithenby S.J. A fast and accurate method for calculating the flux through gradiometers. Biomagnetism '87. Atsumi K., Kotani M., Ueno S., Katila T., Williamson S.J. (eds.) Tokyo Denki University Press, Tokyo. 1988.

Jaffe L. Electrical currents through the developing Fucus egg. Proc. Natl, Acad. Sci. USA 56: 1102-1109. 1966

Jaffe L. The role of ionic currents in establishing development. Phil. Trans R. Soc. Lond. B 295:

Jaffe L.F., Nuccitelli R. Ultrasensitive vibrating probe for measuring steady, extracellular currents. J. Cell. Biol. 63: 614-28. 1974.

Jaffe L.F., Nuccitelli R. Electrical controls of development. Ann. Rev. Biophys. Bioeng 6: 445-476. 1977.

Katila T.E., Maniewski R., Makijarvi M., Nenonen J., Siltanen P. Phys. Med. Biol. 32(1) 125-31. 1987.

Katila T.E., Karp P. Magnetocardiography - morphology and multipole presentations. Biomagnetism - An Interdisciplinary Approach. Williamson S.J., Romani G.L., Kaufman L., Modena

I. (eds.) Plenum Press N.Y. 1983.

Katila T.E. On the current multipole expansion for the biomagnetic field. Acta Polytechn. Scanda., 1983.

Kellaway P.E.C. The part played by electric fish in the early history of bioelectricity and electrotherapy. Bull. Hist. Med. 20: 112-137. 1946.

Kraus W., Lechner F. Die Heilung von Pseudarthrosen und Spontanfrakturen durch strukturbildende elektrodynamische Potentiale. Muench. med. Wschr. 114: 1814-19. 1972.

Lennard R.F. The Measurement of Small Ionic Currents in Living Organisms by Sensitive Magnetometry. PhD thesis. The Open University. 1984.

Lokietek W., Pawluk R.J., Basset L.A. Muscle injury potentials, a source of voltage in the undeformed rabbit tibia. J. Bone and Joint Surgery 56B(2): 361-369, 1974.

Lorrain P.,Corson D.R. Electromagnetism : Principles and Applications. W.H. Freeman and Co., New York. 1978.

Lund E.J. Electrical control of organic polarity in the egg of Fucus. Bot. Gaz. 76: 288-301. 1923.

Meijs J.W.H., Peters M.J. Various models of the head and their influence on MEGS. Biomagnetism '87. Atsumi K., Kotani M., Ueno S., Katila T., Williamson S.J. (eds.) Tokyo Denki University Press, Tokyo. 1988.

Nicolas P., Germain V., Thomas T., Duret D. MEG representation based on piecewise circular models. Biomagnetism : Applications and Theory. Weinberg H., Stroink G., Katila T.E. (eds.) Pergamon Press. 1985.

Nobili C.L. Comparison entre les deux galvonometres les plus sensibles, La grenouille et les multiplicateurs a deux aiguilles, suivie de quelques resultats nouveaux. Ann. Clin. Phys. 38: 225-245. 1828.

Nuccitelli R. Ooplasmic segregation and secretion in the Pelvetia egg is accompaneid by membrane generated electric current. Dev. Biol. 62: 13-33. 1978.

Okada Y. Neurogenesis of evoked magnetic fields in Biomagnetism, an Interdisciplinary Approach. Williamson S.J., Romani G.L., Kaufman L., Modena I. (eds.). Plenun Press. 1983.
Okada Y. Discrimination of localised and distributed sources and localised single and multiple sources. Biomagnetism : Applications and Theory. Weinberg H., Stroink G., Katila T.E. (eds.) Pergamon Press. 1985.

Palfreyman N.M., Ioannides A.A. Expert techniques in inverse problem solving. Abstracts of the 6th International Conference on Biomagnetism. Tokyo. 1987.

Palfreyman N.M., Singh K.D., Swithenby S.J. Rule based location of multiple dipole sources from biomagnetic data. submitted to 7th International Conference on Biomagnetism. New York, 1989.

Pienkowski D., Pollack S.R. The origin of stress generated potentials in fluid saturated bone. J. Orthop. Res. 1: 30-41.

Romani G.L., Williamson S.J., Kaufman L. Science 216: 1339-41. 1982.

Sabatier P.C. Inverse problems - an introduction. Inverse Problems 1: 1985.

Sarvas J., Hamalainen M.S., Jarvi A.T. Bayesian parameter estimation in the neuromagnetic inverse problem. Abstracts of the 6th International Conference on Biomagnetism. Tokyo. 1987.

Sarvas J. Basic mathematical and electromagnetic concepts of the biomagnetic inverse problem. Phys. Med. Biol. 32(1): 11-22. 1987.

Shamos M.H., Lavine L.S., Shamos M.I. Piezoelectric effect in bone. Nature 197: 81. 1963.

Smith T.B. Best fit multipole expansions for fields from static currents. Inverse Problems 1: 173-179. 1985.

Stern C.D. A simple model for early morphogenesis. J. Theor. Biol. 107: 229-242. 1984

Stern C.D. Do ionic currents play a role in the control of development? Bioesays 4(4): 180-183. 1986.

Stern C.D., Jaffe L.F. Large electric currents leave the primitive streak of early chick embryos. Science 206: 569. 1979.

Sturmer K.H., Schmit Neuerburg K.P. Quantitative determination of the influence of induced alternating current on the integration of autologous spongiosa grafts. Unfallchirugie 11(4): 168-173. 1985a.

Sturmer K.H., Schmit Neuerburg K.P. Indications and clinical results of electromagnetically induced ac stimulation of pseudarthroses showing poor reaction. Unfallchirugie 11(4): 197-203. 1985b.

Swithenby S.J., Janday B.S. Analysis of magneto-encephalographic data using the homogeneous sphere model: empirical tests. Phys. Med. Biol. 32(1): 105-113.

Swithenby S.J. SQUIDS and their applications in the measurement of weak magnetic fields. J. Phys E. Sci. Instrum. 13:. 1980.

Tripp J.H. in Biomagnetism an Interdisciplinary Approach p138. Williamson S.J., Romani G.L., Kaufman L., Modena I. (eds.). Plenum Press. 1983.

Weinberg H., Brickett P., Coolsma F., Baff M. Topography of simulated MEG and EEG generated by multiple intracranial dipoles. Biomagnetism : Applications and Theory. Weinberg H., Stroink G., Katila T.E. (eds.). Pergamon Press. 1985.

Williamson S.J., Kaufman L. Magnetic fields of the cerebral cortex. Biomagnetism. pages 353-399. Walter de Gruyter and Co., Berlin. 1981.

Yasuda I. Fundamental aspects of fracture treatment. J.Kyoto Med. Soc. 4: 395-406. 1953.

this are likely to be spurious and may legitimately be removed.

One way of achieving this is by low-pass digital filtering of the calculated perturbations. This is performed by convolving the components of the perturbation vector p(t) with an appropriate window function w(t). In all the work described here, w(t) was a simple 'top hat' function.

Thus:

(8.3)

where $w(t+a) = 1$ for $-b/2 \leqslant a \leqslant b/2$

$w(t+a) = 0$ for $a < -b/2$ and $a > b/2$

b represents the length of the 'top hat'

$p'_k(t)$ represents the smoothed $p_k(t)$ etc.

Once more, the filtering is an interactive process. The decision on whether filtering is desirable and the choice of b are made by the operator after inspection of the reconstructed SRL.

8.4.2 Rejection of small coefficients

As described in section 7.4.4 for the G_{kz}, very small H_{jk} can lead to artificially large μ_{jk} or λ_{jk} in equations (8.1). This problem is avoided by setting all H_{jk} below $t_h H_{jk}$ to zero. Choosing $t_h = 0.8$ usually gave acceptable results. t_h could be altered during any iteration.